Charles University in Prague
Faculty of Mathematics and Physics

MASTER THESIS

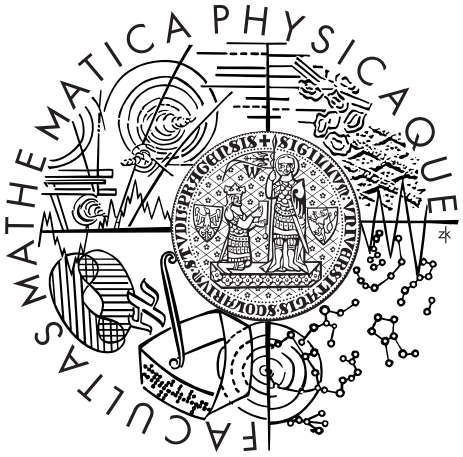

Michal Zajaček

Neutron stars near a galactic centre

Astronomical Institute of the Charles University in Prague

Supervisor of the master thesis: Prof. RNDr. Vladimír Karas, DrSc.
Study programme: Physics
Specialization: Astronomy & Astrophysics

Prague 2014

Acknowledgements. First, I would like to thank my supervisor Prof. Vladimír Karas for the careful supervision of this thesis. I really appreciate that he has always found time to discuss various problems despite his busy schedule as the director of the Astronomical Institute, Academy of Sciences of the Czech Republic. The discussions with him have been always helpful and enriching in many ways.

Second, I am grateful to Dr. Miroslav Brož for advice and various suggestions to improve the thesis. I would also like to thank post-doctoral researcher Dr. Devaky Kunneriath for her help concerning the processing of interferometry data and fruitful discussions about the Galactic centre. I also appreciate Prof. Ladislav Šubr's, Dr. Jaroslav Haas's, and Mr. František Dinnbier's critical, constructive comments. I thank the whole team of the Relativistic Astrophysics group in Prague for advice and a friendly attitude.

Moreover, I am grateful for many helpful comments to Prof. Andreas Eckart and other members of his group at the University of Cologne/Max Planck Institute for Radioastronomy. My stays in the Galactic centre group at the University of Cologne helped me to comprehend basic observational aspects of the Galactic centre research.

I thank Prof. Hagai B. Perets (Technion – Israel Institute of Technology) and Prof. Francis Wilkin (Union College) for very helpful comments concerning the preparation of the paper (Zajaček, Karas & Eckart, Astronomy and Astrophysics 2014, accepted) on which Chapter 4 of the thesis is based.

Last but not the least, I would like to thank my parents for all the support during my studies at the Charles University in Prague.

The work on this thesis has been financially supported by the Grant Agency of the Charles University in Prague (GAUK 879113).

I declare that I carried out this master thesis independently, and only with the cited sources, literature and other professional sources.

I understand that my work relates to the rights and obligations under the Act No. 121/2000 Coll., the Copyright Act, as amended, in particular the fact that the Charles University in Prague has the right to conclude a license agreement on the use of this work as a school work pursuant to Section 60 paragraph 1 of the Copyright Act.

In Prague, 10 April 2014 Michal Zajaček

Title: Neutron stars near a galactic centre

Author: Michal Zajaček

Department: Astronomical Institute of the Charles University in Prague

Supervisor: Prof. RNDr. Vladimír Karas, DrSc., Astronomical Institute of the Academy of Sciences of the Czech Republic

Abstract: In this work we study the processes near the Galactic centre, which serves as a paradigm for low-luminosity galactic nuclei. The introductory part of the thesis is a brief review on the radio source Sagittarius A* in the Galactic centre and on its immediate surroundings. The main part of the thesis focuses on the hypothetical population of neutron stars that should be present in large numbers in this region. We analyse the predictions concerning the encounters of this observationally unexplored population with the ambient interstellar medium and we discuss the distribution of their interaction modes with respect to the parameters of the system. We find out that this distribution is strongly dependent on the density of the ambient medium, whereas only weakly dependent on its temperature. The effect of the prolongation of rotational period is negligible on the time-scale of about ten thousand years. In the second part, we predict the evolution of the high-eccentricity passages of clouds and dust-enshrouded stars (with pericentre distances at about 1000 Schwarzschild radii from the black hole). In all studied cases a major part of the matter is diverted from the original path.

Keywords: Galaxy: centre, Stars: neutron, ISM: kinematics and dynamics

---

Název práce: Neutronové hvězdy v okolí galaktického jádra

Autor: Michal Zajaček

Katedra: Astronomický ústav Univerzity Karlovy v Praze

Vedoucí diplomové práce: Prof. RNDr. Vladimír Karas, DrSc., Astronomický ústav Akademie věd České republiky, v. v. i.

Abstrakt: Tato práce se zabývá procesy probíhajícími v blízkosti jádra Galaxie, jež slouží jako příklad jader galaxií s velmi nízkou luminozitou. Úvodní část práce je stručnou reserší soudobých poznatků o radiovém zdroji Sagittarius A* v jádru Galaxie a o jeho bezprostředním okolí. Hlavní část práce se zabývá dosud hypotetickou populací neutronových hvězd, jež by měla být v jádru Galaxie zastoupena s poměrně vysokou četností. Rozebíráme předpovědi týkající se průchodu této dosud observačně neprobádané populace okolním mezihvězdným prostředím a diskutujeme rozdělení interakčních módů v závislosti na parametrech systému. Zjistili jsme, ze toto rozdělení je značně ovlivněno hustotou prostředí, naopak závislost na teplotě se jeví jako poměrně nevýrazná. Vliv prodlužování rotační periody je zanedbatelný na časové škále řádu desítek tisíc let. Dále se pak věnujeme předpovědím pro vývoj plynných oblaků a hvězd s pracho-plynnou obálkou pohybujících se po vysoce excentrických trajektoriích (pericentrum ve vzdálenosti přibližně 1000 Schwarzschildových poloměrů od centra). Ve všech zkoumaných případech se během průchodu pericentrem převážná část hmoty významně odklonila od své původní dráhy.

Klíčová slova: Galaxie: centrum, Hvězdy: neutronové, Mezihvězdná hmota: kinematika a dynamika

Contents

Prologue

"Astronomy, the queen of science for:

1. *its exclusivity,*
2. *effect on the solution of philosophical-religious problems,*
3. *enormous significance in a practical life."*

Milan Rastislav Štefánik (1880-1919)
Slovak astronomer, winner of Janssen's prize in astronomy, and politician

The constellation of Sagittarius is a frequent object of interest for amateur as well as professional astronomers. The reason why it is so interesting is that it lies in the direction of the centre of the Milky Way (Eckart et al. 2005; Melia 2007). Thus, the stellar field is very dense and contains a variety of picturesque nebulae and stellar clusters attractive for amateur astronomers. In fact, the Sagittarius constellation contains the largest sample of Messier objects (15). Besides amateurs, astrophysicists are often attracted to the Sagittarius because of the possibility to study the processes near the nucleus of the Milky Way, which is the closest galactic nucleus to us and therefore can be studied with the highest resolution. The view to the centre is obstructed by gaseous-dusty clouds located mainly in three spiral arms (Sagittarius-Carina, Scutum-Crux, Norma), see Fig. 1. Hence, the extinction in visible wavelengths is very high and other wavebands have to be used, mainly in radio, infrared, and X-ray part of the spectrum.

From a historical point of view, the understanding of the centre of the galaxy or the system in which we live changed dramatically. First, since antiquity to the Middle Ages it had been associated with the Earth. After the Copernican revolution in the half of the 16^{th} century it switched to the Sun. In 1610 Galileo Galileo was able to resolve individual stars in the Milky Way using a telescope. Utilising these observations Thomas Wright put forward and idea in the half of the 18^{th} century that the Milky Way is a disk of a large number of stars mutually bound by gravitational forces and consequently it produces an observable band on the sky seen from the Earth embedded in the disk. Towards the end of the 18^{th} century William Herschel produced the first shape of the Milky Way based on stellar counts in different directions. In this scheme the Sun was near the centre of the system. In 1920 Jacobus Kapteyn presented the model of a small ellipsoidal galaxy (diameter $\sim 15\,\text{kpc}$[1]) with the Sun near the centre, as well. By studying the distribution of globular clusters, Harlow Shapley came with the model of a flat disk with the Sun further from the centre than previously thought (Shapley 1918a). A few years later Robert Julius Trumpler took into account the absorption of light by interstellar dust by analysing open clusters (Trumpler 1930), which was not done in the previous analysis. Consequently, a model close to the current view of the Milky Way had been emerging.

It is useful to briefly mention the determination of the distance to the Galactic centre and the angular distances we are going to work with. In fact, the distance

[1] pc represents parsecs, $1\,\text{kpc} = 1000\,\text{pc} \approx 3 \times 10^{21}\,\text{cm}$.

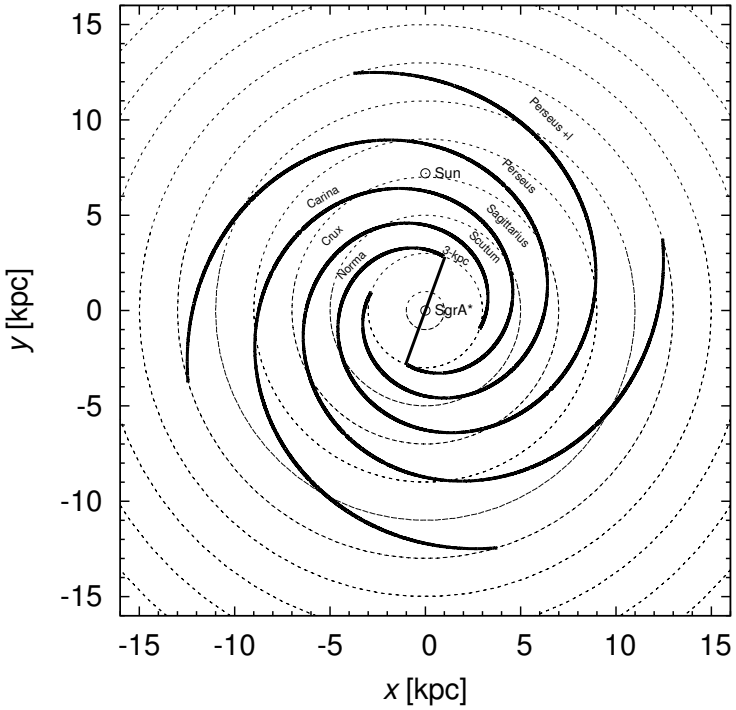

Figure 1: The spiral structure of the Milky Way galaxy, modelled by logarithmic curve model using the following parameters: pitch angle $p = 12°$ inward and 4 spiral arms altogether. The positions of the Sun and compact radio source Sgr A* are labelled. The central $3-$ kpc bar is inclined by 20° with respect to the Sun-Sgr A* axis. The concentric circles mark the distance from the centre, starting from 1 kpc, incrementing by 2 kpc.

to the centre is a fundamental parameter in all models of the Milky Way. Moreover, it sets a length scale for other distances and mass estimates and influences distance determinations of extragalactic sources based on period-luminosity relations (Genzel et al. 2010). One of the first determinations of the distance to the Galactic bulge was performed by observing the globular clusters. Shapley (1918b) assumed correctly that the higher concentration of globular clusters in Sagittarius represents the central bulge. Consequently, he used the luminosities of standard candles to set the distance to the bulge equal to 13 kpc. During the 20^{th} century many studies followed that improved the calibration of luminosities of standard candles. One of the newer works (McNamara et al. 2000) used the RR Lyrae and the high-altitude δ Scuti variable stars to determine the distance to the Galactic centre. They obtained the value 7.9 ± 0.3 kpc.. The determination of the distance is being continually updated. We may distinguish the following methods (Genzel et al. 2010):

1. direct: trigonometric orbital parallax, 3D stellar orbits, statistical parallax,
2. indirect: globular clusters, RR Lyrae stars, Cepheids, Mira variables, red giants, characteristic magnitudes of stellar populations in HR diagram,
3. model-based estimates: cluster parallax distance, Jeans modelling
4. others.

Genzel et al. (2010) use previous computations of the distance to determine their weighed mean. They obtain $8.15 \pm 0.14 \pm 0.35$ kpc where the first uncertainty is the variance of the weighed mean and the second one is the weighed sample variance. Additionally, using only direct measurements yields $8.23 \pm 0.20 \pm 0.19$ kpc and considering the maser data from Reid et al. (2009) changes the value to $8.25 \pm 0.19 \pm 0.19$ kpc. All of these values imply $1'' \approx 0.04$ pc near the centre.

In the half of the 20$^{\text{th}}$ it became obvious that the Galactic centre is connected with the strong source of radio continuum emission known as Sgr A (Piddington & Minnett 1951). A decade later Schmidt (1963) reports the discovery of a distant luminous stellar-like object QSO (quasar). Consequently, large luminosities and energy densities of these objects were explained best by the conversion of the gravitational energy of matter accreting onto massive black holes to radiation (Lynden-Bell 1969). Lynden-Bell (1969) and Lynden-Bell & Rees (1971) used the theory of quasars powered by the supermassive black hole (hereafter denoted as SMBH) to argue that the SMBH is responsible for the extensive gas ionization and a strong hot wind in most galaxies, including the Milky Way. Later Balick & Brown (1974) reported the discovery of a strong radio emission compact source within an arcsecond of the Galactic centre. Its brightness temperature was estimated $\gtrsim 10^7$ K and it was unresolved at $\lesssim 0.1''$. As a result, since the discovery of the radio source Sgr A* a broad scientific community started to consider it as a SMBH. Direct proofs of a concentrated source of gravity came with the observations of NeII and OI emissions, which revealed supersonic speeds of compact clouds of ionized gas implying a Keplerian mass of the central object to be $\sim 3 \times 10^6 M_\odot$ (for instance, Lacy et al., 1982). Another method of the determination of the central mass is a measurement of stellar proper motions and radial velocities. The best results come from direct observations of the *S-stars*, which are tightly bound to the central object (for instance, Ghez et al., 2003a inferred mass $3.6 \pm 0.4 \times 10^6\, M_\odot$).

This thesis deals with the processes in the environment close to Sgr A*, namely the interaction of stars with the gaseous-dusty environment. Specifically, we analyze the interaction of neutron stars with the gas near the SMBH. In this sense, the thesis broadens the current knowledge of the processes near the Galactic centre.

Motivation and Outline

The observations of the close vicinity of the Galactic centre revealed a large number of young, massive stars orbiting the SMBH as close as $\sim 0.1\,\mathrm{pc}$ (Bartko et al. 2010; Nayakshin & Sunyaev 2005). In fact, the nuclear star cluster is one of the densest concentrations of young massive stars in the Galaxy (Genzel et al. 2010). In comparison, there is an observable dearth, or rather a flat distribution, concerning the population of late-type stars with the radius of as much as $10''$ (Bartko et al. 2010; Buchholz et al. 2009; Do et al. 2009). It is thought that a steep relaxed Bahcall-Wolf cusp of stars with the slope of 7/4 or 3/2 (Bahcall & Wolf 1976, 1977) is missing. The stellar mass function reflecting the initial mass function (IMF) is top-heavy for disk stars (Wolf-Rayet, O and B stars) (Bartko et al. 2010). In general, it is complicated to explain the *in situ* formation of these stars because of a strong tidal shear from the SMBH that is thought to suppress the formation of low-mass stars (Morris 1993; Krabbe et al. 1995; Levin & Beloborodov 2003; Ghez et al. 2005)[2]. Nayakshin & Sunyaev (2005) show that the *in situ* formation in a massive disc with the top-heavy IMF gives results consistent with X-ray observations, whereas the formation in a massive cluster further away from Sgr A* is inconsistent with the X-ray data regardless of the IMF (classical disk-population Salpeter IMF or top-heavy). For further studies of the Galactic centre it is important to keep in mind the interplay between the gaseous-dusty medium, stars, and the activity of the supermassive black hole manifesting itself as the compact radio source Sgr A*. The overall structure and the physics of the region is thus very complex, see Fig. 2.

The top-heavy IMF combined with the mass segregation over the age of the bulge ($\sim 10\,\mathrm{Gyr}$) implies a large number of stellar remnants (neutron stars and stellar black holes) present in the nuclear star cluster. It has been previously advocated that a large population of stellar mass black holes ($\sim 10^4$) should exist in the Galactic centre (e.g., Morris, 1993; Miralda-Escudé & Gould, 2000). A similar number is expected for neutron stars (Wharton et al. 2012). Having used the total X-ray luminosity of the inner parsec, Deegan & Nayakshin (2007) set the upper limit to the number of compact remnants ($N \lesssim 40000$).

So far the presence of a presumed large population of neutron stars/pulsars within 1 pc of the Galactic nucleus has not been observationally confirmed despite continuing efforts (e.g., the observations with the Effelsberg radio telescope at 18.95 GHz, Eatough et al., 2012). It is thought that a lack of detections is due to a profound interstellar dispersion and scattering near Sgr A*. However, there are observational hints that such a population is present. Johnston et al. (2006) report the discovery of two highly dispersed pulsars with the angular separation less than 0.3° from the Galactic centre. Deneva et al. (2009) confirm the detection of three new pulsars with large dispersion measures and the angular distance $\sim 10' - 15'$ from Sgr A*. Recently, a magnetar PSR J1745-2900 has been discovered (Kennea et al. 2013; Mori et al. 2013; Eatough et al. 2013a) at the projected distance of $\sim 2.4 \pm 0.3''$ and having a period of 3.7635537(2) (Rea et al. 2013).

[2]Ghez et al. (2005) discusses three scenarios: (1) Old stars appearing young, (2) *in situ* formation, (3) Formation at greater distances in a massive cluster and coming closer due to a dynamical friction.

Figure 2: Multi-wavelength image; combination of infrared (Spitzer telescope), near-infrared (Hubble telescope), and X-ray (Chandra satellite) images of the Galactic centre region. The Galactic centre represented by the compact radio source Sgr A* is the bright, white region to the right of the image. In the east direction (left) from Sgr A* one can find: the Arches cluster, the Quintuplet cluster surrounded by the Sickle with the Pistol star, and a bluish X-ray binary (1E 1743.1-2843). The angular width of the image approximately corresponds to that of the Moon, $\sim 30'$. Credit: NASA, ESA, SSC, CXC, and STScI.

Utilising pulsar surveys and the current detection of a magnetar near the Galactic centre, Chennamangalam & Lorimer (2013) set an upper limit on the pulsar population ~ 950 in the inner parsec using a Bayesian and Monte Carlo approach. This estimate is still consistent with an expected large population of neutron stars. The observations of pulsars near the SMBH would significantly contribute to:

- comprehension of the starbursts and related star formation near the Galactic centre using their number and age distribution (Hartmann 1995),
- mapping the gravitational potential near the SMBH based on their period derivatives,
- constraining the electron density profile in the Galactic centre using their dispersion measures.

There are continuing efforts to find pulsars even closer to the event horizon, where relativistic effects become visible. While propagating through moderate- and strong-field regime of the SMBH near the Galactic centre, their beams could be deflected. The detection and long-term precision timing of such radio pulses from a pulsar with orbital periods $\lesssim 100\,\mathrm{yr}$ would enable us to study the properties of the spacetime near the SMBH (Stovall et al. 2012).

It has also not been determined yet if the nucleus accelerates particles in the form of a bipolar, precisely collimated jet (Yusef-Zadeh et al. 2012) as we observe in active galaxies. We can certainly exclude massive jets typical of some active galactic nuclei (AGN). However, a smaller or transient jet outflow may

exist, which is supported by a small rate of accretion onto the SMBH. The study of the dynamics of magnetized neutron stars near the SMBH and their interaction with the ionized environment is significant for the understanding of particle acceleration in this region.

Recently, an infrared-excess source G2/DSO (Dusty S-cluster object)[3] has been reported to fall directly into the accretion zone of the supermassive black hole (SMBH) in the Galactic centre (Gillessen et al. 2012; Eckart et al. 2013c). It was discovered in 2011 in near-infrared images produced by ESO VLT. Due to a large Doppler shift, it is well-recognized in the hydrogen recombination lines Brackett-γ and Paschen-α. This object is expected to lose a fraction of matter while passing close to the SMBH. It should trigger an enhanced activity of Sgr A* in the near future when a fraction of material comes close to the event horizon. Hence, G2/DSO provides a unique opportunity to study the hydrodynamics and accretion properties on the order of 100 AU from the SMBH.

Gillessen et al. (2012) obtained L'-band (3.8 μm) images of the thermal emission of the dust (~ 600 K) with the adaptive optics NACO instrument as well as images using deep integral field spectroscopy obtained by SINFONI at the VLT. A new set of observations was published, which enabled to update the orbital elements of the cloud structure (Gillessen et al. 2013a) using the L'-continuum emission and thus predict the pericentre passage in September 2013. Using the Br-γ line emission, Phifer et al. (2013) infer another set of orbital elements resulting into an offset from the cloud trajectory inferred by Gillessen et al. (2013a) and a later pericentre passage in 2014. The object has also been detected in VLT K_s-band and Keck K'-band as a $\sim 19^m$ continuum source (Eckart et al. 2013b).

So far it has also not been observationally confirmed if there is a compact source inside the structure or not. Only the upper limits were determined for an embedded stellar core (Gillessen et al. (2012): $m_K > 17.8$, Phifer et al. (2013): $m_K > 20$). Thus, a number of models of the cloud and its origin have been proposed. Gillessen et al. (2012, 2013a) find out that the inclination of the cloud is close to that of the clockwise disk of young massive stars that lies in the range from 0.04 pc to 0.5 pc. In relation to the clockwise disk, one of the origin scenarios involves a thermal instability of colliding stellar winds of nearby Wolf-Rayet stars (Gillessen et al. 2012; Burkert et al. 2012; Cuadra et al. 2006) or the interaction of the accreting gas with the jet-driven outflow from Sgr A* (Gillessen et al. 2013a; Yusef-Zadeh et al. 2012). Other theories include a recent nova outburst which ejected a ring-like shell of gas (Meyer & Meyer-Hofmeister 2012), a young planetary nebula (Gillessen et al. 2012), a protoplanetary disc that gradually evaporates (Murray-Clay & Loeb 2012), and a collision between a low-mass main-sequence star and a stellar mass black hole (Miralda-Escudé 2012). Gillessen et al. (2012, 2013a) performed a simple test-particle simulation, which matched the observations at the time of publication, so it seems that hydrodynamical effects are negligible at greater distances from the SMBH and tidal shearing prevails. Moreover, hydrodynamical simulations without a compact source discussing various scenarios of origin have also been performed (Schartmann et al. 2012; Burkert et al. 2012). These models show that hydrodynamic

[3]Named G2 by Burkert et al. (2012). Another cloud structure G1 was reported by Clénet et al. (2005). Acronym DSO is proposed by Eckart et al. (2013c) since it describes the nature of the source better with respect to a dust content.

effects due to the interaction with the hot and dense environment will profoundly effect the evolution of the cloud near the pericentre.

The compact source scenario has gradually been extended by new theories and models. Scoville & Burkert (2013) propose that the cloud is a result of a mass-loss from a low-mass T Tauri star. In their model, an inner, thin, and cold bow shock is formed that is responsible for the observed emission. Ballone et al. (2013) perform hydrodynamic simulations of the compact source scenario and find out that the model fits the observations best when the mass-loss by wind and a wind velocity are compatible with those of a young T Tauri star. Eckart et al. (2013b) discuss higher luminosities up to $\sim 30\,L_{\odot}$, implying masses $10 - 20$ $M_{\odot}$ for stellar cores of spectral types AF or AGB stars.

Content of the thesis. We discuss and study the interaction of neutron stars with the gaseous-dusty environment near a galactic centre. We focus on our Galaxy, the Milky Way, for which we have the most observational constraints. However, the results we present here may be also applied to other nuclei.

First, we constrain the neutron star population using the power-law initial mass function (IMF) and the assumption of the plausible mechanism of the dynamical friction taking place in the Galactic centre region over the age of the bulge, $\sim 10\,\mathrm{Gyr}$. Then we revisit the study of the possible interaction of compact objects with a single, G2-like cloud, analysing the neutron star population in more detail (Bartos et al., 2013 and de la Fuente Marcos & de la Fuente Marcos, 2013 mostly consider stellar and intermediate black holes). We compare the number of encounters for different spatial distributions of neutron stars (Bahcall-Wolf-like cusp or uniform distribution).

Consequently, we study the interaction of magnetized neutron stars with the ionized gas medium close to Sgr A*, namely the 'Minispiral'. We analyse the modes of interaction of neutron stars (ejector, propeller, accretor, Lipunov, 1992) given the external conditions - the electron density, temperature, and velocity profile of the gaseous medium.

Given the current passage of the dusty S-cluster object G2 close to Sgr A* and its significance for the study of physical processes and material transport near a low-luminosity galactic nucleus, we perform several simulations that are in several ways complementary to already published works. We compare three scenarios: a core-less cloud, a dust-enshrouded star, and a dust-embedded binary. We model pericentre passages for a different set of parameters (presence of a star, binary, different mass-loss rate and terminal wind speed) and explore under what conditions these encounters can lead to an enhanced accretion activity. The most significant results of this analysis were accepted for publication (see Zajaček et al., 2014).

Outline. The thesis is organized as follows: in chapter 1 we briefly review the current knowledge about the Galactic centre, focusing on Sgr A*, the Nuclear star cluster, and gaseous-dusty environment. Then we study the distribution of gas in the close vicinity of Sgr A* making use of radiointerferometric observations in chapter 2. In chapter 3, we study the population of neutron stars near the Galactic centre, focusing on their general observed characteristics in section 3.1 and we constrain their number in section 3.2. Finally, we study their interaction

with the gaseous medium near the Galactic centre in section 3.4, focusing on the distribution of interaction modes of magnetized neutron stars and their possible observational effects in section 3.5. In chapter 4, we analyse the passages of clouds and dust-enshrouded stars near the supermassive black hole. In section 4.1, we summarize the main accretion phenomena in galactic nuclei; in section 4.2 we set up the model and describe the numerical procedure to explore the mutual interaction between the star and its environment. In section 4.3, we present the main results of the simulations of pericentre passages, which is followed by the discussion of the results in section 4.4 and the summary in section 4.5. The last chapter is dedicated to the conclusion of the thesis.

1. A Brief Review on the Galactic Centre

The compact radio source Sgr A* is the closest galactic nucleus. Therefore, we can study the physical processes with a much higher resolution than in case of other galactic nuclei. In fact, the observations stretch over about 18 magnitudes of electromagnetic radiation (Genzel et al. 2010). Besides observations in radio, infrared, X-ray, and γ parts of spectrum, theoretical and computer studies have become more important in unveiling the physics of the close vicinity of Sgr A*. In this brief review, we start with the account of the supermassive black holes that reside in most galaxies, with the focus on Sgr A*. Then we proceed with the discussion of the dense nuclear star cluster surrounding the black hole and the processes in it. Finally, we discuss the gaseous-dusty environment in the inner parsec. This review was in many ways inspired by a detailed account by Genzel et al. (2010), where the reader finds more information about phenomena that are beyond the scope of this thesis.

1.1 Sgr A* – supermassive black hole

The proof that a massive object is a black hole requires a detailed mapping of the potential up to the event horizon using test particles, i.e. gas clouds or stars. In reality, the dynamical resolution at the scale of the event horizon is currently not possible for any black hole, not even Sgr A*. However, in case of the Milky Way and several nearby galaxies it has been possible to show that a non-stellar massive object dominates the potential of the nucleus - other alternatives would be more extended (cluster of stellar remnants) or would produce more light.

It is shown in several works that the mass distribution in our Galaxy centre (and presumably in other similar galaxies) is dominated by *dark compact mass* surrounded by the extended *nuclear star cluster* up to several parsecs (e.g., Genzel & Townes, 1987, Mezger et al., 1996, Melia & Falcke, 2001).

Radial velocity measurements. The proof for the central concentration of mass came first with the measurements of radial velocities of ionized gas clouds (12.8 μm line of [NeII]) that increase to a few hundred km/s in the inner parsec (Wollman et al. 1977). It was shown by the virial analysis that these velocities imply a mass of 2–4 million solar masses. Such a massive central core could be hardly explained by the presence of stars. Several studies put forward an idea that the compact radio source Sgr A* is a supermassive black hole (Lacy et al. 1980, 1982). Although further studies of gas dynamics in the central 'cavity' confirmed the central concentration of mass, some authors doubted the results since the gas motion may be easily affected by other, non-gravitational forces, for instance, the interaction with the ambient medium, magnetic field, and radiation. Besides that the infrared and X-ray detection of Sgr A* was missing (Allen & Sanders 1986; Rieke & Rieke 1988; Kormendy & Richstone 1995).

The strengthened evidence for the central mass of the order of million solar masses came with the analysis of stellar motions. The spectroscopy measure-

ments and the first determination of the velocity dispersion based on $2\,\mu$m CO absorption in late-type giants and supergiants (Rieke & Rieke 1988; McGinn et al. 1989) and observations of 18 cm OH maser emission stars (Lindqvist et al. 1992b,a) confirmed the results of the observations of gaseous clouds. However, the larger distance of the objects ($\gtrsim 5\,$pc) from the centre gave only weak constraints on the distribution of the central mass. With the detection of the first blue supergiant stars in the central $10''$ (Forrest et al. 1987; Allen et al. 1990) it became possible to constrain the mass distribution at this distance using the virial analysis, which favoured the existence of the central, dark mass of the order of million solar masses (Krabbe et al. 1995).

The number of the observed late-type as well as early-type stars continually increased and it was possible to use the statistical projected mass estimators (virial and Bahcall-Tremaine) as well as the modelling based on the Jeans equation. Genzel et al. (1996) apply these methods separately for late-type and early-type stars and obtain the mass for the central, dark core ($\sim 3 \times 10^6\,M_\odot$) and simultaneously the mass of the nuclear star cluster ($\sim 10^6\,M_\odot$) with the core radius of 0.4 pc. Similarly, by employing the Jeans modelling, Haller et al. (1996) infer the dark central mass of 1.5–1.8 $\times\, 10^6\,M_\odot$ and the nuclear star cluster mass of 1–2.5 $\times\, 10^6\,M_\odot$. This analysis assumes circular, isotropically distributed orbits. However, if it does not hold, the central mass may be actually much smaller to explain the distribution of radial velocities.

S-cluster. An important advance in the study of the mass distribution came with the detection of the proper motions of the fast-moving 'S'-stars (Eckart & Genzel 1996, 1997; Genzel et al. 1997) with the velocities as much as $\sim 10^3\,\mathrm{km\,s^{-1}}$ and angular distances $\lesssim 1''$ from Sgr A*. The detection was achieved using the near-infrared speckle imaging performed with 3.5 m ESO NTT. The observations were later complemented with the higher resolution speckle imaging performed by 10 m Keck telescope (Ghez et al. 1998). The analysis of the data confirmed the Keplerian increase in the velocity dispersion $\sigma \propto r^{-1/2}$ and the average velocity field was reported to be close to isotropic. Consequently, the measurement of the first accelerations for 'S'-stars was an important step towards the determination of their orbits (Ghez et al. 2000; Eckart et al. 2002). The first orbit determination was achieved for the star S2 (S02, Schödel et al., 2002, Ghez et al., 2003b). It moves on a highly elliptical orbit ($e \sim 0.88$) around the dark mass of $4.4 \times 10^6\,M_\odot$ with the period of 15.8 yr and the pericentre distance of $1400\,\mathrm{r_s}$. The employment of the adaptive optics (near-infrared wavefront sensing or laser guide star) has contributed significantly to the increase in the orbit determinations of the S-cluster members (~ 30, Gillessen et al. (2009b,a)). The analysis of the orbits of S1, S8, S12, S13, and S14 stars yields the updated values for the distance r_0 to the Centre as well as the central mass $M_\bullet$ (Gillessen et al. 2009b):

$$r_0 = 8.28 \pm 0.15 \pm 0.29\,\mathrm{kpc}\,,$$
$$M_\bullet = 4.30 \pm 0.20 \pm 0.30 \times 10^6\,M_\odot\,,$$

where the first uncertainty is the statistical fit error and the second one is the systematic error. Furthermore, the full orbit monitoring of S2 star (Gillessen et al. 2009a) leads to the result that the extended mass within its orbit (stars, stellar

remnants and possibly diffuse, dark matter) contributes less than 4% to 6.6% of the central dark mass (Gillessen et al. 2009b; Genzel et al. 2010). Recently, Meyer et al. (2012) report the detection and full phase coverage of an 'S'-star denoted as S0-102 with the shortest-known period of 11.5 years and the periapse passage in 2009.5 ± 0.3. We may expect that high-resolution imaging of this star and other 'S'-stars will significantly contribute to the constraining and the mapping of the gravitational potential close to Sgr A*. For illustration, we plot the projected orbits on the sky plane for chosen S-cluster stars, see Fig. 1.1.

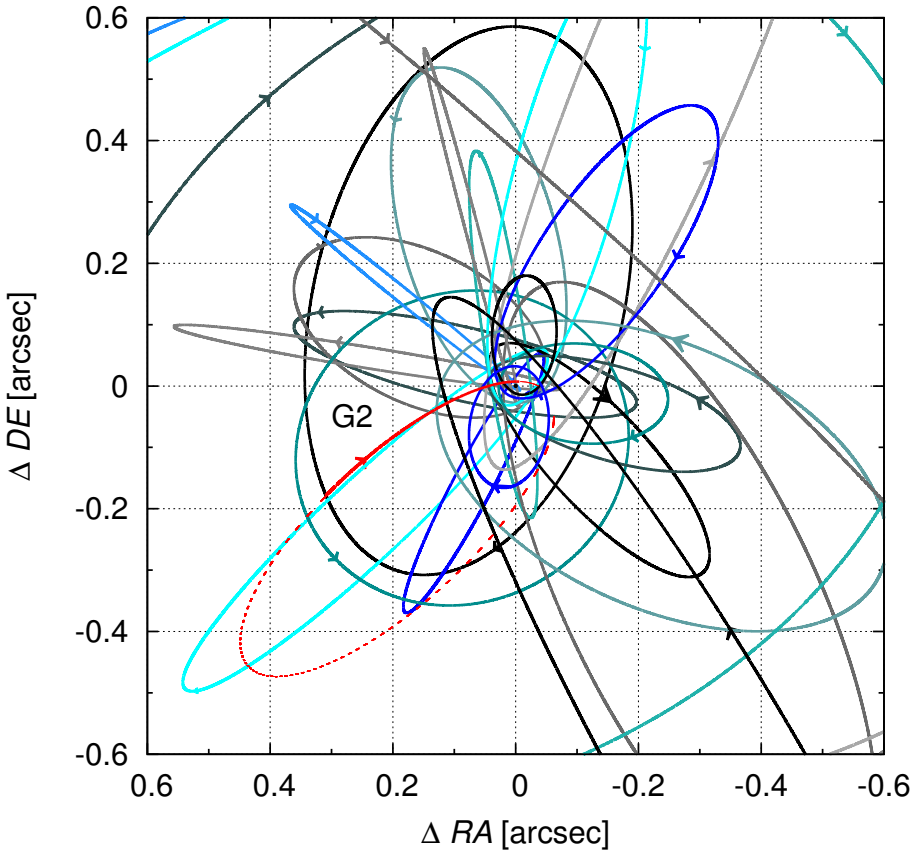

Figure 1.1: The projected orbits of 'S' stars as seen from the Earth. The axes show the angular offset from Sgr A* (the east is to the left with the increasing right ascension offset, the north is upwards with the increasing declination offset). The nominal trajectory for the highly eccentric dusty 'S'-cluster object G2 is also shown. The data for this plot were taken from Gillessen et al. (2009a), Gillessen et al. (2013b), and Meyer et al. (2012).

The fitted orbits as well as the temporal evolution of radial velocities for the two shortest-period-known stars, S2 and S102, are plotted in Fig. 1.2. In the radial velocity plot, we show the temporal evolution of radial velocities for other 'S'-cluster members, G2 cloudy object included.

To sum up, inferred stellar orbits require the central concentration of dark mass ~ 4 million solar masses within the pericentre of S2 star ($\sim 125\,\mathrm{AU}$). The determined minimum density is $5 \times 10^{15}\,\mathrm{M_\odot pc^{-3}}$ and hence, it cannot correspond to an extended stellar cluster or a cluster of stellar remnants. The centre of mass is coincident with the compact radio source Sgr A* within $\pm 2\,\mathrm{mas}$ uncertainty.

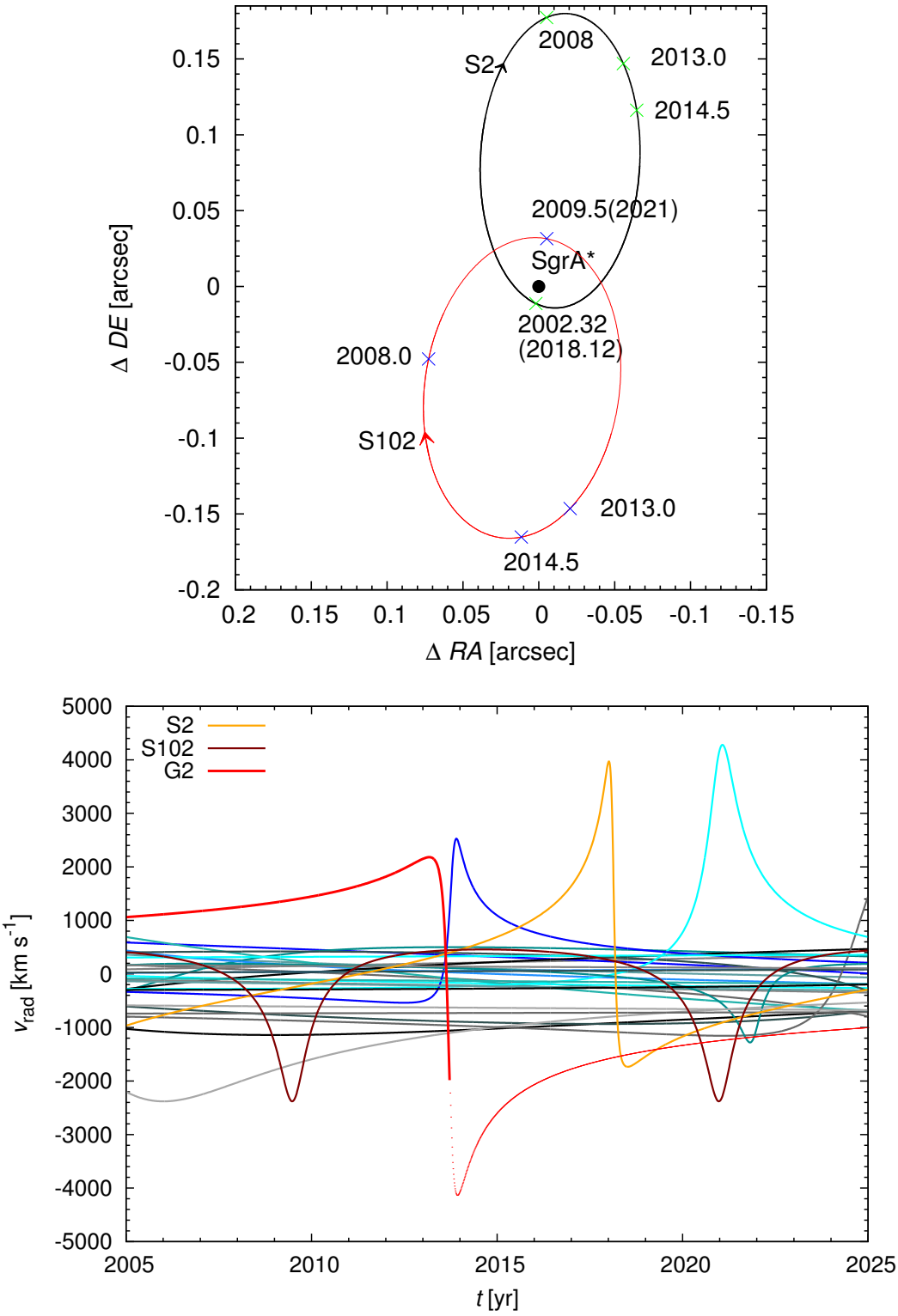

Figure 1.2: The projected orbits on the sky of the two shortest-period-known stars, S2 and S102 (Top panel). The temporal evolution of radial velocities (Bottom panel) for S2, S102, and G2 object (reddish colors) and other 'S'-cluster members (bluish colors). The data for these plots were taken from Gillessen et al. (2009b), Gillessen et al. (2013b) and Meyer et al. (2012).

In addition, the non-thermal, compact radio source Sgr A* has an apparent size $< 1\,\mathrm{AU}$ (Shen et al. 2005; Bower et al. 2006; Doeleman et al. 2008). Combined with the lower mass limit, the lower limit on its density is $6.5\times10^{21}\,\mathrm{M_\odot pc^{-3}}$ (Shen et al. 2005). Furthermore, near-infrared and X-ray flares have been observed that are best explained by the variations in the accretion flow. Based on these arguments, the supermassive black hole associated with Sgr A* is one of the best proven astrophysical black holes.

Studies of the accretion flow and variability. The proximity of Sgr A* makes it an ideal target for studying the accretion flow structure up to the event horizon. In fact, the SMBH in the Galactic centre is believed to have the largest angular size among black holes and it is thus the best canditate for its silhouette imaging (e.g., Falcke et al., 2000). At the distance $\sim 8\,\mathrm{kpc}$, the event horizon for a Schwarzschild black hole ($r_s = 2GM_\bullet/c^2 \approx 0.08\,\mathrm{AU}$) has a characteristic angular size of $\sim 10\,\mu\mathrm{as}$.

It is supposed that the emission from Sgr A* is fuelled by accretion processes, which is supported by its spectrum, observations of variability and flares, very long baseline interferometry (VLBI) observations, surrounding environment, and polarization measurements. The spectrum of Sgr A* extends from radio to gamma rays. It has a peak in the submillimeter range, where it changes from inverted power-law to optically thin spectrum. In general, the spectrum is similar to those of AGN. However, the bolometric luminosity is very low. It is widely accepted that AGN nuclei exhibit a radiatively efficient accretion mode that is currently well-described by the standard theory of thin discs or slim discs (Shakura & Sunyaev 1973; Abramowicz et al. 1988). In this mode the accretion rate approaches and sometimes even exceeds the *Eddington limit* $\dot{M}_{\mathrm{Edd}} \simeq L_{\mathrm{Edd}}/(0.1c^2)$, where L_{Edd} is the Eddington luminosity:

$$L_{\mathrm{Edd}} = \frac{4\pi G M_\bullet m_{\mathrm{p}} c}{\sigma_{\mathrm{T}}}\,, \tag{1.1}$$

with m_{p} proton mass, σ_{T} Thomson cross-section.

The accretion rates in low-luminosity nuclei are much smaller than the Eddington rate ($\dot{M}_\bullet \ll \dot{M}_{\mathrm{Edd}}$)(Eckart et al. 2013a). This may be explained by the lack of material falling on the black hole and the radiatively inefficient accretion modes at certain stages. Sgr A* in its current stage is a paradigm of low-luminosity, inactive nucleus with the accretion rate $\dot{M}_\bullet \approx 10^{-8}\,\mathrm{M_\odot yr^{-1}}$ that can be understood in terms of advection-dominated accretion flows (Narayan & McClintock 2008).

One may ask if Sgr A* has an event horizon or a hard surface instead. In case of the hard surface scenario, infalling gas would hit it and consequently would get shocked and thermalized. The surface radiation would be thermal, but as we know there is no thermal component observed. The thermal component might be hidden in the observed quiescent, non-thermal radiation, but that would require radiative efficiencies close to 100%, which is not the case even for AGNs, X-ray binaries, or gamma-ray bursts ($\sim$ 10%, Kato et al. (2008)). In addition, as was already described, the radiative efficiency is expected to be much smaller for Sgr A* ($\sim$ 0.01%-1%, Narayan & McClintock (2008)) as a result of the weak coupling between ions and electrons present in the accretion flow. Hence, the

presence of a hard surface is ruled out (Broderick et al. 2009).

Very Long Baseline Interferometry (VLBI) with its high resolution enables to resolve structures on the sub-mas scale. It has been determined from several VLBI observations in cm- and mm-bands (Bower et al. 2004, 2006; Doeleman et al. 2008; Shen et al. 2005) that the intrinsic size of Sgr A* decreases with decreasing wavelength, specifically as λ^{α} ($\alpha = 1.44 \pm 0.07$, 1σ, Doeleman et al. (2008)) based on VLBI measurements at 1.3mm where the apparent scattering size is smaller than the intrinsic size. This dependence confirms that the Sgr A* emission region is spatially stratified and thus observations with different wavelengths explore different, spatially detached layers. The intrinsic size of Sgr A* inferred from 1.3-mm VLBI data is $37^{+16}_{-10}(3\sigma)$ μas, which is only 3.7 times the size of the event horizon of $4.3 \times 10^6\, M_{\odot}$ black hole (Doeleman et al. 2008; Genzel et al. 2010). It is even smaller than the apparent diameter of the horizon (48–55 μas, depending on spin) due to broadening by lensing effects. The explanation according to Doeleman et al. (2008) is that the emission comes from the accretion flow surrounding Sgr A* and the asymmetry arises from inhomogeneities ('hot spots') or simply relativistic beaming of the incoming radiation.

The main problems with the measurements of the intrinsic size of Sgr A* are related to its low luminosity, small size, interstellar scattering, and the opacity of the accretion flow at wavelengths longer than 1.3 mm. The foreground scattering and limited uv-coverage of interferometry has not enabled to produce a two-dimensional image yet. As a consequence, it is necessary to make assumptions of circular or elliptical brightness distribution. However, with the increased angular resolution at short mm-wavelengths and denser uv-coverage, it is expected that more complex structures in the accretion flow will be observed (Genzel et al. 2010).

Based on multiwavelength measurements of Sgr A* variability and its intrinsic size combined with the mass determinations inferred from orbital motions of stars bound to dark, central mass, there is currently no reasonable doubt that Sgr A* is a single supermassive black hole in the low-luminosity mode. In addition to the arguments above, Sgr A* has a very small intrinsic motion orthogonal to the Galactic plane ($-0.4 \pm 0.9\,\mathrm{kms}^{-1}$, (Reid & Brunthaler 2004)), which is in agreement with the analysis of the motion of the SMBH embedded in the dense nuclear star cluster. There is also no empirical proof for the presence of a second massive black hole, which may be excluded from dynamical reasons. However, observations do allow the presence of an intermediate black hole $(10^3, 10^{4.5})\, M_{\odot}$ that is either very close to the SMBH ($\lessapprox 1\,\mathrm{mpc}$) or further away from Sgr A* ($\gtrapprox 100\,\mathrm{mpc}$)(Genzel et al. 2010).

1.2 Nuclear Star Cluster

The first infrared observations of the Galactic centre region revealed a large number of bright stars (IRS 7,13,16, Becklin & Neugebauer, 1975; Becklin et al., 1978). Infrared spectroscopy revealed that these stars are late-type (red) giants, supergiants (IRS7) and asymptotic giant branch (AGB) stars that form an old stellar cluster (Genzel et al. 2010). The discovery of 'Allen-Forrest (AF)' star (Forrest et al. 1987; Allen et al. 1990) was a breakthrough in the studies of the Galactic centre stellar population. More HeI- and H-emission stars had been

discovered and it was shown that these are early-type, post-main-sequence blue supergiant stars and Wolf-Rayet stars (O/WR) that formed a few Myr ago with ZAMS masses 30–100 $M_{\odot}$ (Najarro et al. 1994, 1997). Martins et al. (2008) analysed young massive stars in the dense Arches cluster. Another high concentration of young massive stars is found in the Quintuplet and the 'S'-cluster. As we already pointed out, the Galactic centre hosts one of the densest concentrations of young massive stars in the Galaxy. It is still being explored theoretically if these young stars formed *in situ* or whether they moved from more distant regions.

The composition of the nuclear star cluster varies with the distance from the centre. The earliest seeing-limited observations detected a decrease in CO absorption strength (e.g., Allen et al., 1990). This was explained either by the presence of bright early-type stars or by the drop in the density of late-type stars. Later the adaptive optics observations with a high spatial resolution confirmed that both mentioned factors occur in the central arcseconds (e.g., Eisenhauer et al., 2005, Lu et al., 2009, Buchholz et al., 2009). It was proposed that star-star or star-black hole collisions in the central arcsecond may partially contribute to the dearth of giants by destroying their envelopes (Dale et al. 2009).

Observed stellar populations. Majority ($\sim 96\%$) of the observed stars are late-type ($> 1\,$Gyr) M, K, and G metal-rich giant stars. There are also He-burning stars ('red clump') observed that are detected with the lower magnitude limit (Maness et al. 2007). The distribution of velocities is random and nearly isotropic. The rotation of the late-type system is close to the solid-body rotation and there is no significant deviation from the rotation of the whole Galactic Bulge system.

There is also a population of AGB stars (Krabbe et al. 1995; Blum et al. 2003) that formed during one of the recent star-formation events ($\gtrsim 100\,$Myr). They are distinguished from late-type stars based on H_2O absorption bands in their spectra. A small number of supergiants, such as IRS 7, are also observed in the innermost parsec.

Several infrared excess sources with featureless spectra (IRS1W, 3, 9, 10W, and 21) were detected (Becklin et al. 1978; Krabbe et al. 1995; Genzel et al. 1996) that were later resolved with high-resolution imaging. These sources are mostly young, bright mass-losing stars interacting with the surrounding medium, the 'Minispiral', which results in the bow-shock formation (Perger et al. 2008; Mužić et al. 2010).

A distinct population of HeI- and H-emission stars was detected in the innermost half parsec. These are thought to be young, massive stars formed during a recent star-formation epoch 3-7 Myr ago (e.g., Krabbe et al., 1995). It was reported that these stars are also found in IRS 13 and 16 associations (Eckart et al. 2004; Maillard et al. 2004; Lu et al. 2005). It was suggested that the most luminous stars of this young stellar population are in the transitional phase from O supergiants to Wolf-Rayet stars (WN9/Ofpe according to, e.g., Allen et al. (1990)) with high mass-loss rates (e.g., Najarro et al., 1994, Krabbe et al., 1995, Najarro et al., 1997, Paumard et al., 2001, Moultaka et al., 2005). These O/WR stars are responsible for the major part of the luminosity of the NSC and supply the central parsec with about half of the excitation/ionizing luminosity (e.g., Najarro et al., 1997, Paumard et al., 2006, Martins et al., 2007).

A substantial fraction ($\approx$ 55–60 %) of young, massive stars forms a clockwise (the projection on the sky), coherently rotating disc structure (CWS) (Levin & Beloborodov 2003). It extends from the inner edge of $\approx$ 0.03 pc, which is quite sharp, to $\approx$ 0.5 pc. The stellar surface density profile changes with the radius as $\Sigma(R) \sim R^{-\beta}$, where $\beta \in (1.5, 2.3)$. However, there are now several indications that a single power-law profile is not adequate and a broken power-law profile seems to be more suitable to fit observations (flatter inner profile and steeper outer profile, Buchholz et al., 2009; Do et al., 2013a). The mean plane of the disc is characterized by its inclination $i \approx 127°$ with respect to the plane of the sky and the longitude of the ascending node $\Omega \approx 99°$ measured from the north (see Paumard et al. (2006) for more details). Levin & Beloborodov (2003) propose that the disc was formed in a massive self-gravitating accretion disc during a recent star-formation event (6 ± 2 Myr ago) of a short duration. Genzel et al. (2003) and Paumard et al. (2006) report the existence of a second, counter-rotating, coherent stellar disc (CCWS) that is supposed to be formed by fewer stars. It is more narrow, located around $\gtrsim$ 0.15 pc. The existence of this second disc is still debated. By fitting individual stellar orbits, Lu et al. (2009) confirm only CWS disc, while a similar number of stars form a random, off-disc population. On the other hand, by adding new O/WR and B stars, Bartko et al. (2009, 2010) claim that there is a coherent structure, but it appears to be more like a dissolving disc, stellar filament, stream, or a small cluster. Some authors claim that the distribution of young, massive stars may be more irregular and the two-disc theory is just an approximation (Kocsis & Tremaine 2011).

In the immediate vicinity of Sgr A* ($\lesssim$ 0.3 pc) there is a cluster of B stars – 'S'-cluster, which was already discussed for its importance for weighting the central, dark mass (see Figs. 1.1, 1.2). These stars are lighter than O/WR stars ($\sim$ 3.5–20 $M_\odot$) and could be older ($\gtrsim$ 6 Myr). The orbits, or rather angular momentum vectors, are distributed isotropically, see Fig. 1.4. The eccentricities of 'S'-stars are non-zero (≥ 0.1) and their distribution is consistent with a thermal isotropic distribution $n(e)\mathrm{d}e = e\mathrm{d}e$, see Fig. 1.3. The members of 'S'-cluster are classified as main-sequence OB stars and hence, it is problematic to explain their formation *in situ* due to strong tidal fields in the vicinity of the SMBH. Unless they just appear to be young, they plausibly migrated from more distant regions of the NSC.

Absence of the central cusp. In the studies of the environment of the SMBHs, it was first predicted that the SMBHs will manifest themselves through a rising stellar density (Peebles 1972). The radius, at which we may expect the onset of this rise, may be approximated by the gravitational influence radius of the SMBH (Merritt 2013):

$$r_\mathrm{h} \equiv \frac{GM_\bullet}{\sigma^2} \approx 10.8 \left(\frac{M_\bullet}{10^8\,M_\odot}\right) \left(\frac{\sigma}{200\,\mathrm{km s^{-1}}}\right)^{-2} \mathrm{pc}\,, \tag{1.2}$$

where σ is a velocity dispersion along any direction. In case of the isotropic velocity distribution, it is related to the rms stellar velocity as $\sigma = v_\mathrm{rms}/\sqrt{3}$. The presence of such a cusp is expected from the *adiabatic growth model*, according to which $\rho \sim r^{-3/2}$ near the SMBH, or the *Bahcall-Wolf cusp* for equal stellar masses ($\rho \sim r^{-7/4}$, Bahcall & Wolf, 1976) and unequal stellar masses ($\rho \sim r^{-3/2}$,

Bahcall & Wolf, 1977), which is a result of the exchange of orbital energy between stars in the potential of the SMBH.

The Milky Way nucleus exhibits a rise in the luminosity density inside the influence radius, scaling roughly as $j \sim r^{-\gamma}$, where $\gamma \approx 1 - 1.5$ Genzel et al. (2003), but as was already stressed, the majority of the luminosity is attributed to young, massive stars. The time-scale for the formation of the Bahcall-Wolf cusp is much longer than the inferred age of a few million years for observed OB stars. In fact, the density profile of late-type stars is flat and nearly constant inside the innermost 0.5 pc. According to Merritt (2013), there is no convincing evidence for the presence of the steep, dense stellar cusp in any observed nucleus. In contrast, the presence of the SMBH is often manifested by a low-density core. However, the concentration of stellar remnants in the core may still be high, based on the detection of four X-ray transients in the central parsec that are in excess with respect to the broader Galactic centre region (Muno et al. 2005).

Fundamental parameters of the NSC. Recent studies (Fritz et al. 2013; Chatzopoulos et al. 2014; Schödel et al. 2014) confirm that the nuclear star cluster is nearly spherical, slightly elongated along the Galactic plane, centred on the central dark potential of Sgr A*, and embedded in the much larger flattened nuclear star disk. Schödel et al. (2014) investigate the parameters of the NSC in MIR ($4.5\,\mu$m) by correcting images for PAH emission as well as for extinction. They find that in the inner few parsecs the density follows the already established density profile $\rho \propto r^{-2}$, but it becomes steeper, $\rho \propto r^{-3}$, further away at projected distances of ~ 5 pc. They infer a half-light radius of 4.2 ± 0.4 pc, a total luminosity of $L_{\mathrm{NSC},4.5\,\mu\mathrm{m}} = 4.1 \pm 0.4 \times 10^7\,L_\odot$, and a mass of $M_{\mathrm{NSC}} = 2.1 \pm 0.4 \times 10^7\,M_\odot$. The rotation of the NSC is parallel to the rotation of the Galactic Bulge, which is consistent with its flattened shape and the supply of material into the NSC from the Galactic plane. Using the isotropic spherical Jeans modelling Fritz et al. (2013) determine the NSC mass within $100''$, $M_{100''} = (6.11 \pm 0.52|_{\mathrm{fixR_0}} \pm 0.97|_{R_0}) \times 10^6\,M_\odot$, which implies the total mass of the NSC of $M_{NSC} = (13.08 \pm 2.51|_{fixR_0} \pm 2.08|_{R_0}) \times 10^6\,M_\odot$. They also calculate the mass-to-light ratio, $M/L = 0.50 \pm 0.12\,M_\odot/\mathrm{L}_{\odot,\mathrm{Ks}}$, for the central $100''$. It seems that the nuclear star cluster of the Milky Way has a typical size, but it appears to be brighter and more massive than nuclear star clusters observed in other galaxies.

Relaxation. The formation of the Bahcall-Wolf cusp of old stars and stellar remnants is only possible in a relaxed system whose age is greater than the relaxation time T_r or time during which random gravitational encounters cause stars to change orbital energy and angular momentum. This time-scale is given by a standard relation (e.g., Spitzer, 1987, Merritt, 2013):

$$T_r = \frac{0.34\sigma^3}{G^2 m_\star \rho \ln\Lambda} \approx 0.95 \times 10^{10} \left(\frac{\sigma}{200\,\mathrm{km\,s^{-1}}}\right)^3 \left(\frac{\rho}{10^6 M_\odot \mathrm{pc}^{-3}}\right)^{-1} \left(\frac{m_\star}{M_\odot}\right)^{-1} \left(\frac{\ln\Lambda}{15}\right)^{-1} \mathrm{yr}\,, \tag{1.3}$$

where σ is the one-dimensional velocity dispersion of the stars, $m_\star$ is the mass of a single star, ρ is the stellar density, and $\ln\Lambda$ is the Coulomb logarithm. Within

the influence radius of the SMBH, the Coulomb logarithm may be approximated $\ln \Lambda \approx \ln (M_\bullet / m_\star) \approx \ln (N_h)$, with N_h denoting the number of stars whose mass equals $M_\bullet$.

In general, we may distinguish *collisionless* and *collisional* nuclei that are older than one relaxation time. The former have $T_r(r_\mathrm{h}) \gtrsim 10^{10}\,\mathrm{yr}$ and collisional nuclei have $T_r(r_\mathrm{h}) \lesssim 10^{10}\,\mathrm{yr}$. The nucleus of the Milky Way, which exhibits a flat core of late-type stars, is probably near the collisionless state, so the collisional steady-state was not yet established, but "initial conditions" may have been partially erased by random encounters (Merritt 2013).

The disc of young O/WR stars as well as the 'S'-cluster are probably not completely relaxed systems, since their age is just a few million years. However, relative velocities in the coherently rotating thin stellar disc are small enough to significantly shorten the relaxation time, eq. (1.3). Šubr & Haas (2014) show that the relaxation time of the young stellar disc in the Galactic centre is comparable to its estimated young age of a few million years. The two-body relaxation seems to have affected the radial density profile mainly in the inner, densest part of the disc, while the outer parts may keep imprints of the initial distribution; hence, the broken power-law is a natural consequence of the two-body relaxation in the disc with an increasing density towards the centre.

Moreover, there are faster relaxation processes in the vicinity of the SMBH than two-body relaxation, namely scalar and even faster vector resonant relaxations (Rauch & Tremaine 1996; Hopman & Alexander 2006). These cause the change of the value and the direction of the angular momentum, respectively. The vector resonant relaxation is so short that a complete randomization of 'S'-cluster orbits could have occurred. However, the age of 'S'-stars is not long enough for them to undergo the scalar relaxation, so the thermalization of their orbits have not taken place except for the lightest ones. Hence, it is plausible that the current distribution of their eccentricities (see Fig. 1.3) reflects the initial distribution, so their origin seems to be connected to the process favouring higher eccentricities (Genzel et al. 2010). It was proposed that high eccentricities may be caused by the Kozai resonance due to the presence of a fossil accretion disc (Šubr & Karas 2005), although the Kozai mechanism is expected to be more efficient for intermediate-mass black holes rather than supermassive ones.

1.3 Gaseous-dusty environment

Besides the supermassive black hole – Sgr A* and the nuclear star cluster, an important component of the Galactic centre environment is the gaseous-dusty environment that is strongly linked to the observed accretion phenomena as well as star formation. The fundamental properties of the Galactic centre region may be described by the distinction of the *ionized cavity* that extends from 1 to 1.5 pc that is surrounded by a region of a dense molecular gas and warm dust, the *circum-nuclear disk* (CND), which ranges from 1.5 to $\sim 4\,\mathrm{pc}$ (e.g., Christopher et al., 2005). Further away from Sgr A* complex, there are several massive '$+20\,\mathrm{km\,s^{-1}}$' and '$+50\,\mathrm{km\,s^{-1}}$' molecular clouds (see Mezger et al. (1996) for a review).

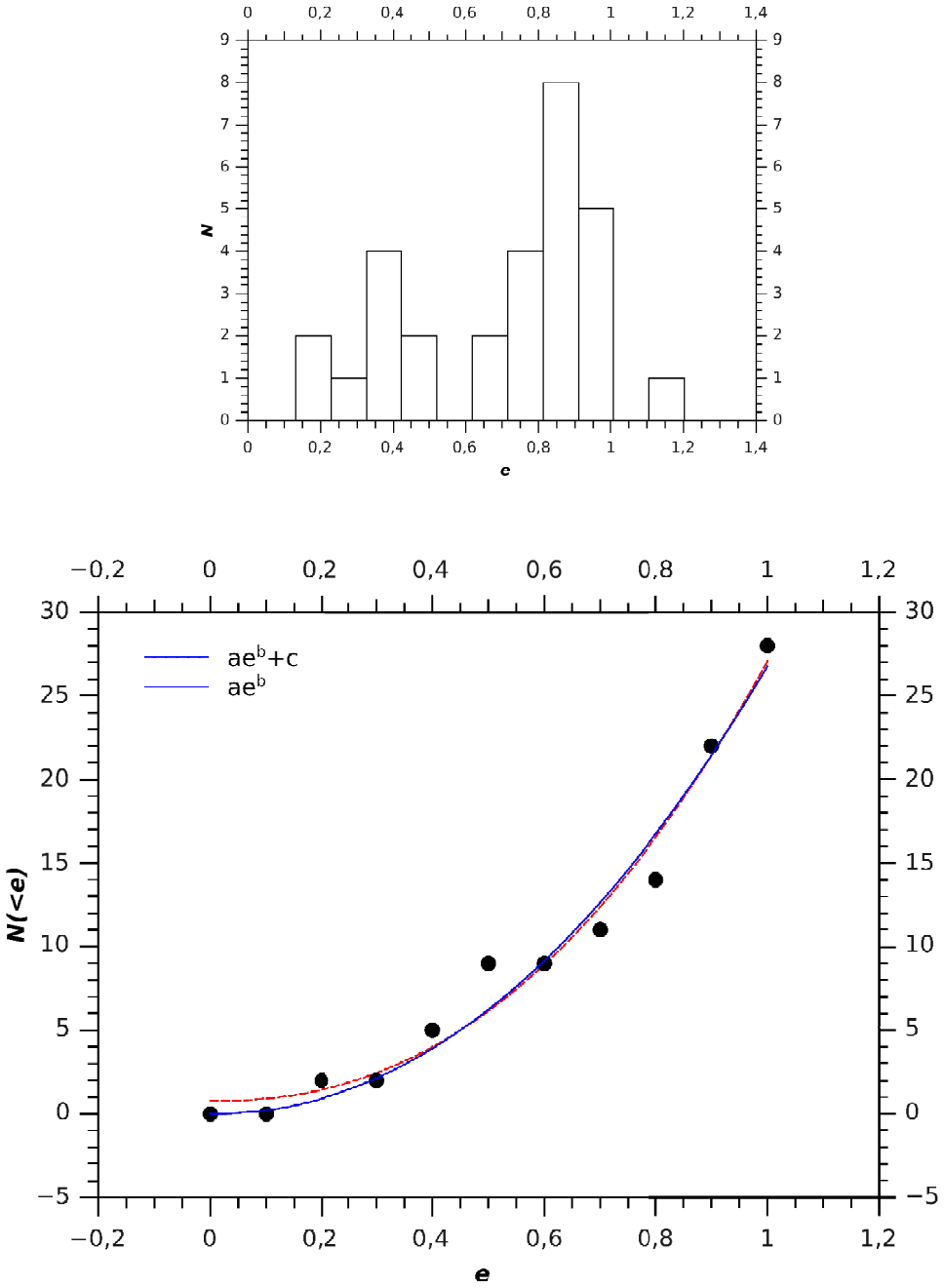

Figure 1.3: (*Top panel*) The histogram of the distribution of eccentricities for 29 'S'-stars. Fourteen 'S'-cluster members have eccentricities in the interval $(0.6, 1)$. The data were taken from Gillessen et al. (2009b); Meyer et al. (2012). (*Bottom panel*) The cumulative number of 'S'-stars for a given eccentricity. The data were fitted with $N(< e) = ae^b + c$ (red-dashed line, best fit:$a = 26 \pm 1$, $b = 2.3 \pm 0.3$, and $c = 0.8 \pm 0.9$) and $N(< e) = ae^b$ (blue solid line, best fit: $a = 27 \pm 1$ and $b = 2.1 \pm 0.2$). The fitted differential distribution is thus: $n(e)\mathrm{d}e \propto e^{\gamma}\mathrm{d}e$, where $\gamma = b - 1$ and in our case $\gamma = 1.3 \pm 0.3$ and $\gamma = 1.1 \pm 0.2$, respectively. This is consistent with a thermal isotropic distribution $n(e)\mathrm{d}e = e\mathrm{d}e$. The data were taken from Gillessen et al. (2009b); Meyer et al. (2012).

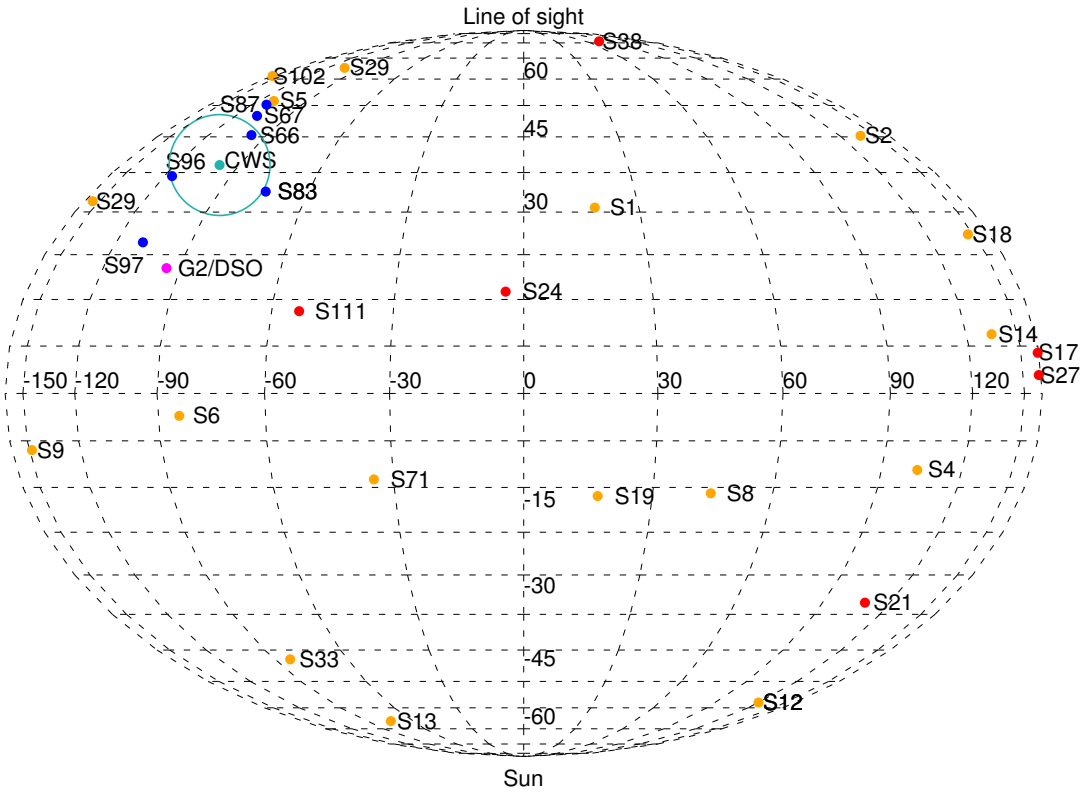

Figure 1.4: The distribution of the orbits of 'S'-stars in the all-sky plot, where the vertical coordinate is the inclination of the orbit i and the horizontal coordinate corresponds to the longitude of the ascending node Ω. The distribution is given by the orbital angular momentum perpendicular to the orbit, whose components are related to the inclination and the longitude of the ascending node: $n_x = \sin i \cos\Omega$, $n_y = -\sin i \sin\Omega$, $n_z = -\cos i$. The face-on, clockwise orbits are at the top of the graph, edge-on orbits at the equator, and counter-clockwise orbits at the bottom. We label the clockwise disc of O/WR stars (CWS) ($\Omega \approx 98°$, $i \approx 129°$, blue circle) and the 'S'-stars of the same spectral type that are located at the inner edge of the disc: S66, S67, S83, S87, S96, S97. Red points mark the late-type stars and orange ones stand for B stars. The purple point labels the dusty 'S'-cluster object G2. The data for this plot were taken from Gillessen et al. (2009b), Gillessen et al. (2013b), and Meyer et al. (2012).

The Circum-Nuclear Disk – CND. The CND was first observed as a double-lobed emission at 50 and 100 μm (Becklin et al. 1982). Consequently it has been observed across radio and infrared wavelengths (Vollmer & Duschl 2001). It is a ringlike structure containing clouds and filaments of dense (10^5–$10^8\,\mathrm{cm}^{-3}$) molecular and atomic gas and dust of high temperature (several 100 K). It extends from at ≈ 1.5 pc up to 3–4 pc and the inclination range is $\approx 50°$–$75°$ (Christopher et al. 2005). The kinematics of the CND can be mostly described by a circular rotation at $\approx 110\,\mathrm{km\,s}^{-1}$ (Marr et al. 1993). However, non-circular patterns have also been detected that are explained by a clumpy structure of the CND consisting of gas streamers infalling from more distant massive molecular clouds (Jackson et al. 1993) or a warped structure caused by a collision of two clouds (Guesten et al. 1987). By analysing the observations in HCN(J=1–0) and HCN^+(J=1–0)

Christopher et al. (2005) find a core structure having densities of 10^7–$10^8\,\mathrm{cm}^{-3}$. Moreover, they infer the core masses of a few $10^4\,M_\odot$. Šubr et al. (2009) analyse the precession rate of the orbits of young O/WR stars that is strongly dependent on the inclination of the stellar disc with respect to the CND and the mass of CND. They also constrain the mass of the CND and find out that if it were more massive than $10^6\,M_\odot$, the clockwise disc would be dissolved by the gravitational torque of the CND within its lifetime ($\approx 6\,\mathrm{Myr}$).

The 'Minispiral' – ionized gas in Sgr A West. The CND sharply ends at $\sim 1.5\,\mathrm{pc}$ which is caused by the radiation field of young, massive stars that ionizes gas. The 'Minispiral' comprises a few streamers of gas and dust from the inner boundary of the CND. The most prominent four parts are denoted as the Northern Arm, the Western Arc, the Eastern Arm, and the Bar (Ekers et al. 1983; Lo & Claussen 1983; Kunneriath et al. 2012). The three streams can be successfully fitted with a bundle of Keplerian orbits; the northern and eastern arm streams have high eccentricities, whereas the western arc is nearly circular (Zhao et al. 2009, 2010). However, there are also deviations from Keplerian motion caused probably by the interaction with stellar winds from O/WR stars. The studies of SgrA West are multiwavelength, ranging from NIR, through MIR, up to millimetre observations (see Kunneriath et al. (2012) and references therein).

The 'Mini-spiral' region needs to treated in the context of complex plasma, i.e., the mixture of gas having electron densities of the order $\sim 10^4\,\mathrm{cm}^{-3}$ and dust that can be charged by photoionization. Hot and cold phases coexist, with dust temperatures of a few hundred Kelvins and the plasma component of $10^4 \div 10^5\,\mathrm{K}$ (Moultaka et al. 2005). Dust can even have an icy coat (Moultaka et al. 2012). Based on MIR observations, the dust mass is estimated $\sim 0.25\,M_\odot$ (Kunneriath et al. 2012). The emission mechanisms in the region range from non-thermal inverted synchrotron radiation of Sgr A* ((+) spectral index $\alpha \approx 0.5$), thermal free-free emission ($\alpha \approx -0.1$), and a possible dust emission ($\alpha \approx 1.0$) (Kunneriath et al. 2012).

2. Radio-interferometry of the gaseous medium near Sgr A*

2.1 Principles and importance for the study of Sgr A*

The angular resolution A for observations with a single radio telescope with a parabolic antenna of diameter D is given by simple relation $A \propto \lambda/D$. This limits the resolution to about 10 arcsec for the largest single-dish radiotelescopes ($D \sim 300\,\mathrm{m}$) observing at the shortest wavelengths ($\lambda \sim 1\,\mathrm{cm}$). This is enough for the mapping of the large-scale structure of the Galactic nucleus (CND). In order to resolve the fine structure of the gaseous medium and the immediate vicinity of Sgr A*, one has to combine output signals of several individual antennas separated by distance B, which is the basic principle of interferometry. The resolution is then given by the largest baseline B and diameters of individual dishes determine the field of view (FOV). Radio interferometry observations of the Galactic centre are necessary for the study of scales on the order of one arcsec and below.

In principle, we can measure only the *correlation function* $R(\mathbf{B})$, which is a function of the baseline vector $\mathbf{B}$. Consequently, *aperture synthesis* is used to recover intensity distribution $I(x, y)$, where x and y are coordinates in the sky plane. The measured correlation function is expressed in terms of the visibility $V(u, v)$ that is a function of two orthogonal coordinates u and v in the projected plane of telescope baselines as seen from the target. The visibilities are linked to intensity distribution in the sky plane I via a Fourier transform:

$$V(u,v) = \int\int A(x,y) I(x,y) \exp\left[i2\pi(ux+vy)\right] \mathrm{d}x\mathrm{d}y\,, \tag{2.1}$$

where $A(x, y)$ is the primary beam shape. The integral in 2.1 goes formally from $-\infty$ to ∞, supposing that $A(x, y) = 0$ for $x^2 + y^2 > l^2$, where l denotes the full width of the primary telescope beam. The fundamental step to recover the modified intensity distribution $I'(x, y)$ is to perform the inverse Fourier transform:

$$I'(x,y) = A(x,y) I(x,y) = \int\int V(u,v) \exp\left[-i2\pi(ux+vy)\right] \mathrm{d}x\mathrm{d}y\,. \tag{2.2}$$

Consequently, the true intensity distribution $I(x, y)$ is obtained by the division of $I'(x, y)$ by the primary beam shape $A(x, y)$ point by point. The integral goes over the whole range in uv-plane. However, the coverage is sparse due to a limited number of telescopes in real measurements. For N measured visibilities,the discrete Fourier transform is employed:

$$I'(x,y) = \sum_{i=1}^{N} g(u_i,v_i) V(u_i,v_i) \exp\left[-i2\pi(u_i x + v_i y)\right], \tag{2.3}$$

where $g(u, v)$ is named *grading* or *apodization* and serves as a weight. Several weighting functions are used and their choice is arbitrary to alter effective beam

shape and side lobe level. The measured intensity distribution $I'(x, y)$ is referred to as *dirty map* and represents the convolution of real intensity distribution $I(x, y)$ with *dirty beam* $DB(x, y)$:

$$I'(x, y) = I(x, y) \bigotimes DB\,. \tag{2.4}$$

The dirty beam represents the response of an interferometer to a point source. It is simply given by $DB(x, y) = \sum_{i=1}^{N} g(u_i, v_i) \exp\left[-i2\pi(u_i x + v_i y)\right]$. It consists of a central component and side lobes that result from the response to a point source due to a discrete coverage of uv-plane.

The final "clean" image is obtained through `CLEAN` algorithm (Högbom 1974). The actual clean intensity distribution $I(x, y)$ is modelled as a sum of point sources with unknown positive intensities $A_i(x_i, y_i)$. Cleaning is performed in the image plane and proceeds iteratively. First, the peak intensity of the dirty map is located, then the fraction $\gamma \in (0, 1)$ having the shape of the dirty beam is subtracted from the image. This is repeated several times until the intensities of the remaining peaks are below some threshold. Finally, the resulting point source model is convolved with a clean beam, usually given by Gaussian distribution having the *full width at half peak* (FWHP) similar to that of dirty beam.

This process starting from visibilities in the Fourier plane and ending with clean intensities in the image plane is today done fully digitally. In this subtask of the thesis, we used the software `CASA` developed by National Radio Astronomy Observatory in the USA (NRAO), where the necessary steps are fully implemented. The visibility data are stored in table format in *Measurement Set* files that are directories of tables. `CASA` uses the *Measurement Equation* (Hamaker et al. 1996) for finding clean intensity distribution:

$$\underbrace{V_{ij}(u, v)}_{\text{START}} = M_{ij} B_{ij} G_{ij} D_{ij} \int E_{ij} P_{ij} T_{ij} F_{ij} S \underbrace{I(x, y)}_{\text{GOAL}} \exp\left[i2\pi(ux + vy)\right] \mathrm{d}x\mathrm{d}y + A_{ij}\,, \tag{2.5}$$

where ij represents baseline between antennas i and j and other terms denote the following:

- M_{ij} – multiplicative baseline error,
- B_{ij} – bandpass response,
- G_{ij} – generalised electronic gain,
- D_{ij} – D-term (polarization leakage),
- E_{ij} – antenna voltage pattern,
- P_{ij} – parallactic angle,
- T_{ij} – tropospheric effects,
- F_{ij} – Faraday rotation, and
- A_{ij} – additive baseline error.

The measured visibility V_{ij}^{m} for a given baseline ij differs from an ideal one V_{ij}^{ideal} due to atmospheric and instrumental effects, which may be written as $V_{ij}^{\mathrm{m}}(\nu, t) = B_{ij} G_{ij} D_{ij} P_{ij} T_{ij} F_{ij} V_{ij}^{ideal}(\nu, t) = G_{ij}(\nu, t) V_{ij}^{ideal}(\nu, t)$, where the frequency and time-dependent gain term $G_{ij}(\nu, t)$ is determined through frequency or *bandpass* calibration and gain (amplitude and phase) calibrations. We briefly describe these calibrations using the interferometric observations of the mini-spiral region and the final image is produced.

2.2 Observations and Pre-calibration phase

Observations of Sgr A that we make use of were performed by the Combined Array for Research in mm-wave Astronomy (CARMA) in California. The total integration time is ≈ 18000 seconds. The observed sources – target and calibrators – are summarized in Table 2.1.

ID	Name	RA	DE	Epoch
0	NOISE	16 : 42 : 58.810000	+39.48.36.99400	J2000
1	3C273 (bandpass calibrator)	12 : 29 : 06.700000	+02.03.08.59800	J2000
2	NOISE	17 : 33 : 02.706000	−13.04.49.54800	J2000
3	1733-130 (gain calibrator)	17 : 33 : 02.706000	−13.04.49.54800	J2000
4	SGRAOFF (target)	17 : 45 : 40.040000	−29.00.28.10000	J2000
5	NOISE	21 : 54 : 44.258679	−13.06.36.62717	J2000
6	NEPTUNE (flux calibrator)	21 : 54 : 44.259104	−13.06.36.62540	J2000

Table 2.1: Observed sources: Sgr A (target) and calibrators (3C273, 1733-130, Neptune).

The CARMA interferometer comprises 15 antennas: six antennas with diameters 10.4 m (id 1 – 6) and nine 6.1 m (id 7 – 15). Our observations were taken at 3 mm (100 GHz in the C configuration that is intermediate between the most extended A configuration (0.25–2 km) and the most compact E configuration (8–66 m). The example of antenna configuration is in Fig. 2.1. For calibrations we always pick the antenna near the centre of the array that also has to have a stable performance (in this case antenna 11).

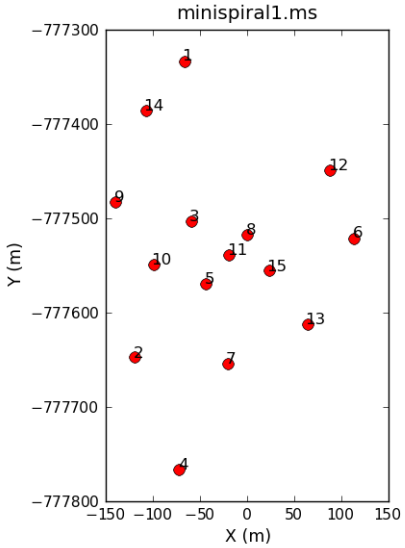

Figure 2.1: An example of array configuration for CARMA.

For illustration, we plot the *uv*-coverage for the target source and calibrators, see Fig. 2.2.

We investigate the plots of amplitude and phase vs. time and channel (or frequency). In Fig. 2.3, we see usual behaviour before calibration, amplitude

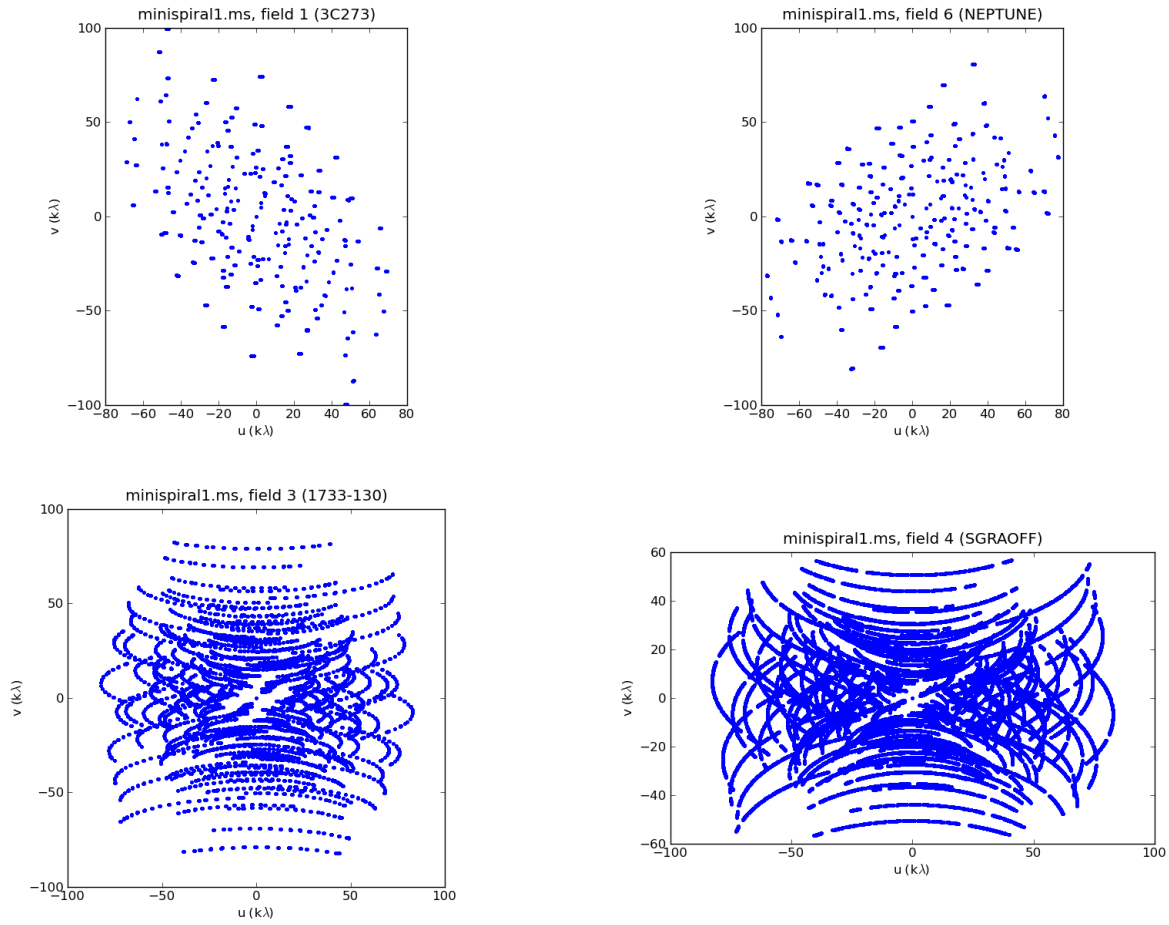

Figure 2.2: The *uv*-coverage for target source (SGRAOFF) and three calibrator sources (3C273, Neptune, 1733-230).

varies with time and frequency and phase is highly scattered in both types of plots. However, for calibrators as point sources, amplitude should be constant and phase close to zero, so we have to perform the corresponding calibrations in time and frequency to find corresponding gain terms $G_{ij}(\nu, t)$ that distort these dependencies.

Flagging. Before proceeding with the calibration, we check for bad data to flag them. The only flagging we perform is removing shadowing effects and autocorrelation, since we are only interested in cross-correlation.

2.3 Calibration

For more detailed, step-by-step procedures, the reader is asked to look at the `PYTHON` script in the attachment, including all necessary parameters (attachment A).

First, we proceed with bandpass calibration using bright point source 3C273, which was observed during one scan before all other scans. This is sufficient due to its high flux, which secures a good signal-to-noise ratio. We understand bandpass as a relative gain (amplitude and phase) of an antenna (or baseline)

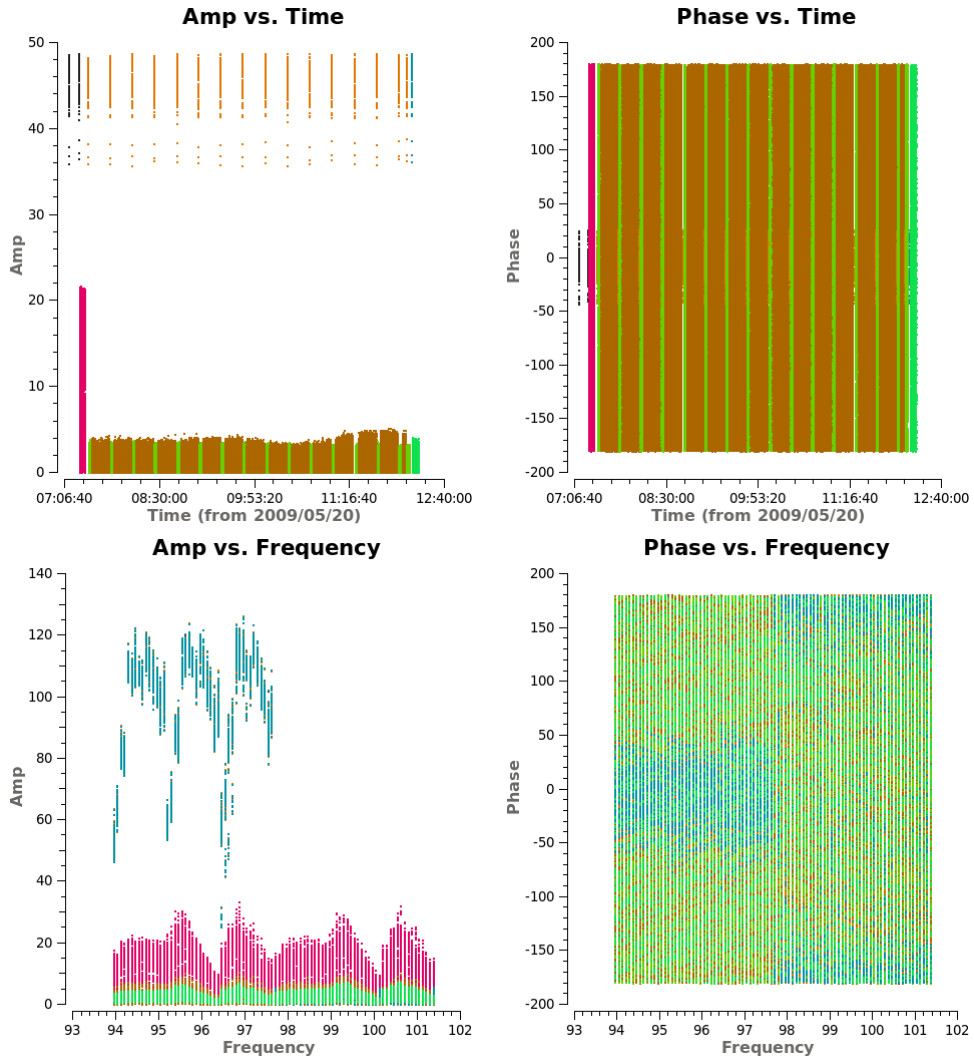

Figure 2.3: Amplitude vs. time and frequency and phase vs. time and frequency before calibration. Frequency is expressed in GHz.

with respect to frequency (channel). After the bandpass calibration we continue with the flux calibration using the flux calibrator Neptune. Consequently, we simultaneously calibrate phase and amplitude. During this process we apply the bandpass calibration table. The phase and amplitude calibrator 1733–130 was scanned regularly. Finally, we bootstrap its flux to the flux of Neptune. Finally, we apply calibrations to the target, Sgr A, as well as to calibrators.

The amplitude-time, amplitude-frequency, amplitude-uv-distance, phase-time, and phase-frequency graphs of Sgr A after applying calibrations are displayed in Fig. 2.4. We see that there are still some deficiencies , for instance, in amplitude-time plot, there is a high peak at the beginning. In principle, we could flag the bad data and calibrate the measurement set again until everything seems right.

2.4 Imaging

Finally, we produce images of calibration sources and that of Sgr A using the `CLEAN` algorithm. Calibrator sources are imaged to make sure that they appear

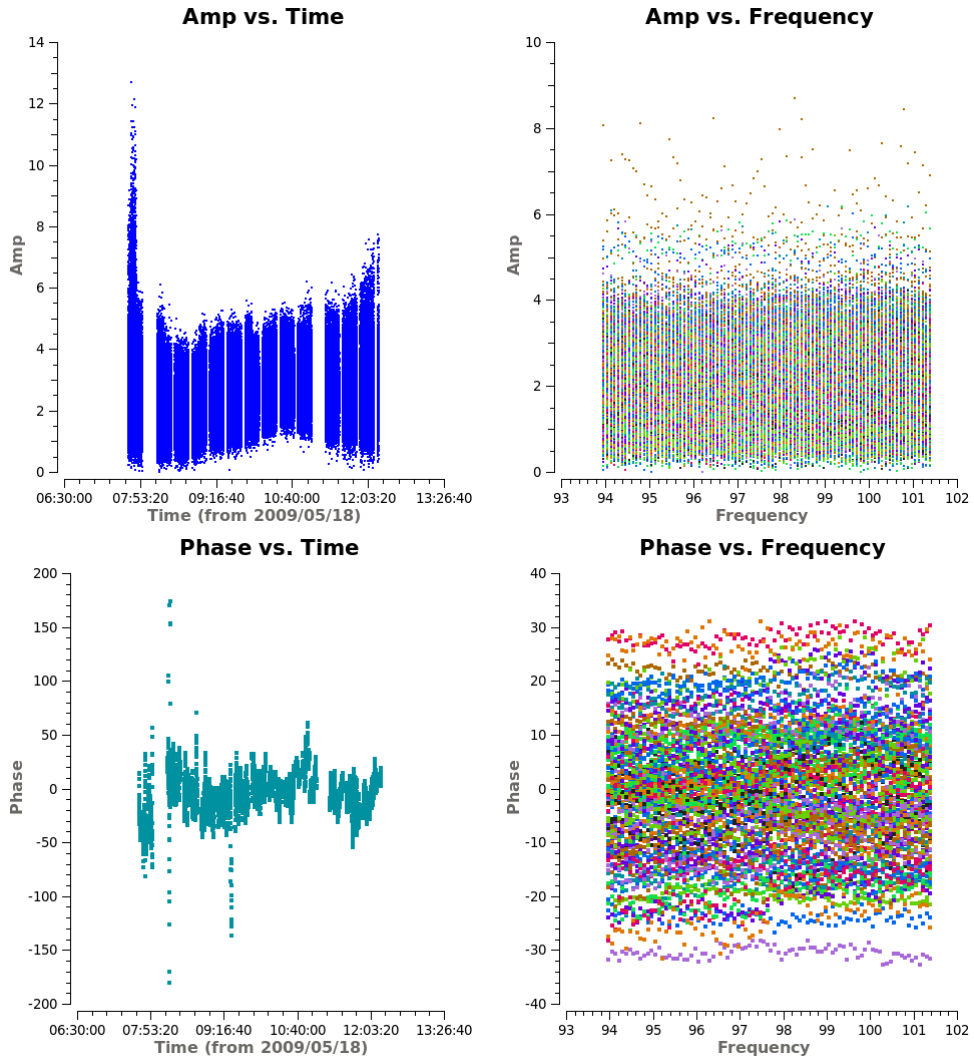

Figure 2.4: Amplitude vs. time and frequency and phase vs. time and frequency for Sgr A after applying bandpass and gain calibrations. Amplitude vs. frequency and phase vs. frequency are colorised by baselines.

as point sources. We use the `CASA` task `imview` for displaying images as well as `ds9` software, see Fig. 2.6

Finally, we produce combined raster and contour images of the ionized environment - Sgr A West or the mini-spiral, see Fig. 2.7. It consists of several streamers of gaseous and dusty material that are infalling from the more distant and colder circum-nuclear disk. The most distinct features are the Northern Arm, the Eastern Arm, the Bar (labelled in Fig. 2.7), and the Western Arc (not visible). For further information see Kunneriath et al. (2012).

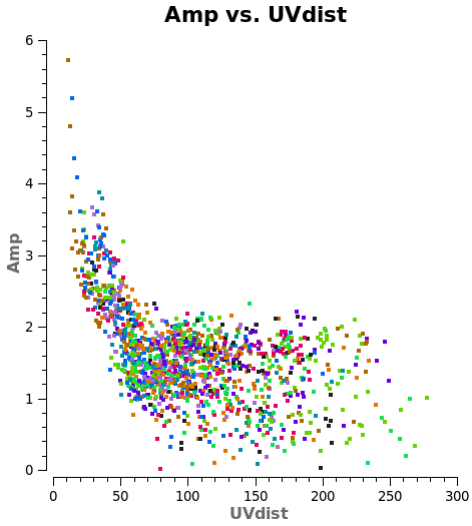

Figure 2.5: Amplitude vs. *uv*-distance for the target source Sgr A after calibration. Colorised by baselines.

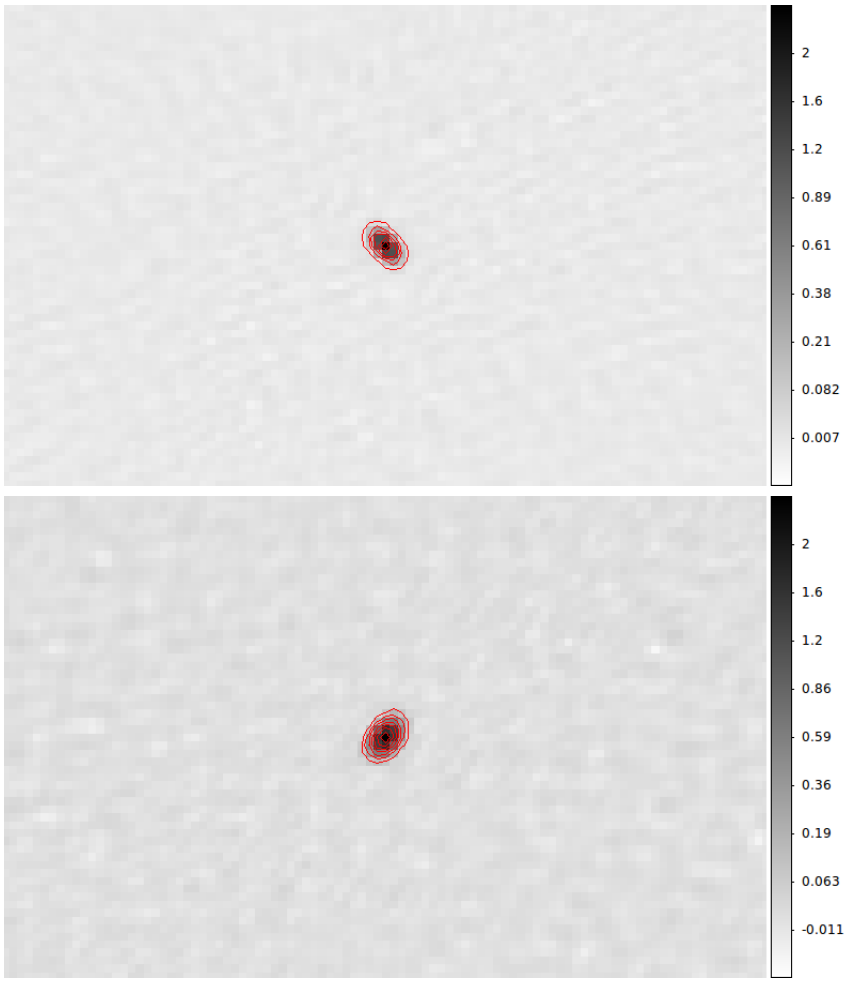

Figure 2.6: (*Top panel*) The image of the gain (amplitude and phase) calibrator 1733-130. The contours correspond to flux density values 0.03, 0.19, 0.44, 0.80, 1.26, 1.83, 2.49 Jy/beam. (*Bottom panel*) The image of the flux calibrator Neptune. The contours correspond to flux density values 0.09, 0.24, 0.46, 0.73, 1.07, 1.47, 1.93, 2.45 Jy/beam.

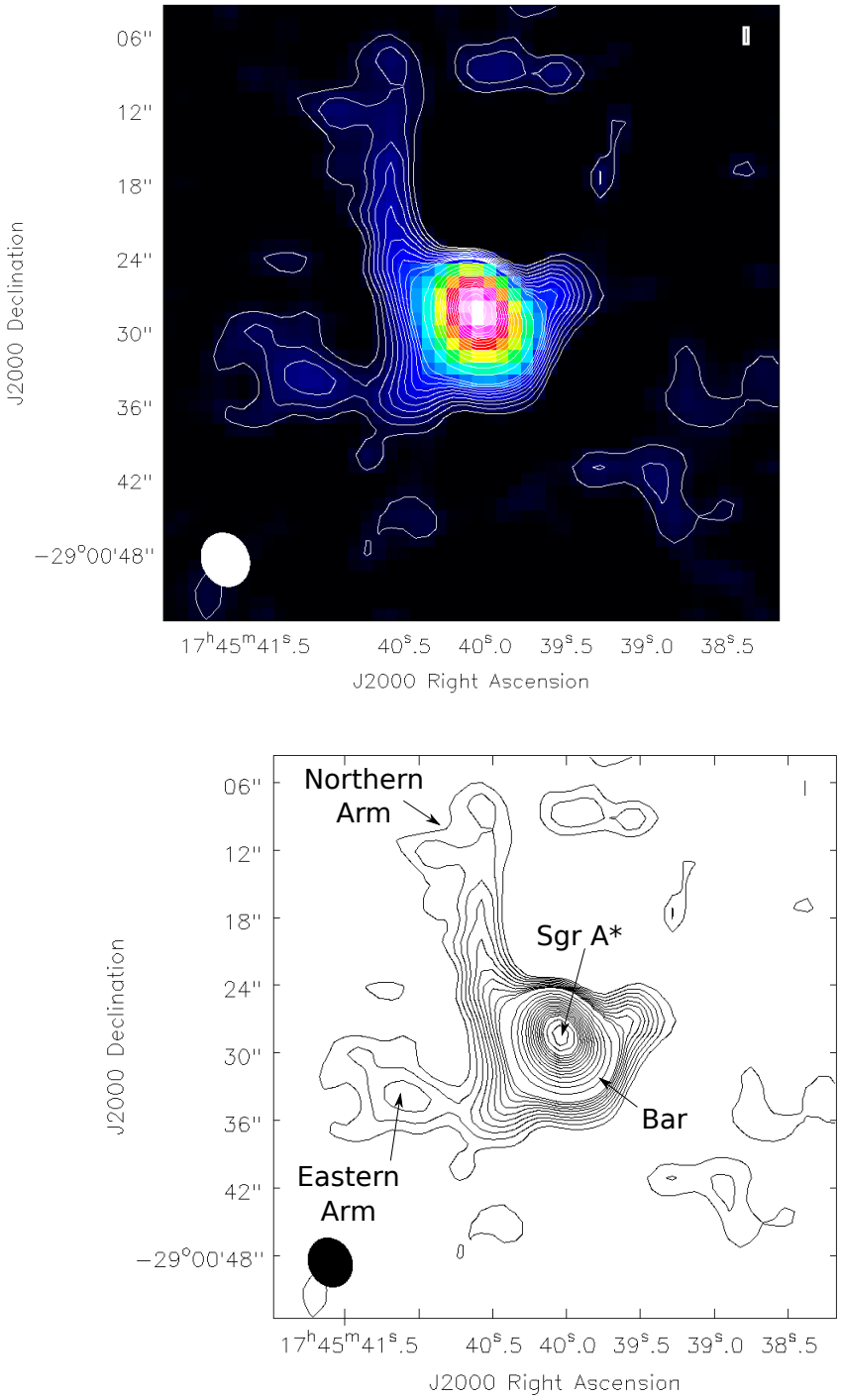

Figure 2.7: (*Top panel*) The image of Sgr A West. The contour levels correspond to 0.01, 0.02, 0.03, 0.04, 0.05, 0.06, 0.07, 0.08, 0.09, 0.1, 0.15, 0.2, 0.25, 0.3, 0.35, 0.4, 0.45, 0.5, 0.55, 0.60, 0.65, 0.7, 0.8, 0.9, 1.0 Jy/beam. The beam is denoted by a white ellipse. (*Bottom panel*) The same contour image with the labels of important components of the Galactic centre mini-spiral: the Nothern Arm, the Eastern Arm, the Bar, and the compact radio source Sgr A*.

3. Interaction modes of neutron stars near the Galactic centre

Before analysing the interaction of neutron stars with the gaseous environment near the centre of the Milky Way or the centres of other galaxies, we will discuss some fundamental properties of neutron stars inferred mainly from the observations of pulsars.

Neutron stars were first predicted theoretically and represent one of the final stages of the stellar evolution formed in supernova explosions (Baade & Zwicky 1934). Their progenitors have lost an internal source of energy and the mass of collapsing stars exceeds the Chandrasekhar limit (Lipunov 1992):

$$M_{\rm Ch} \approx \frac{3.1}{\mu_{\rm e}^2}\left(\frac{hc}{G}\right)^{3/2} \approx 5.83\mu_{\rm e}^{-2}M_\odot \overset{\mu_{\rm e}\to 2}{\approx} 1.46\,M_\odot\,, \tag{3.1}$$

where $\mu_{\rm e}$ is the average number of nucleons per electron and h, c, and G denote the Planck constant, speed of light, and the gravitational constant, respectively.

As the progenitor star collapses, it spins up, atomic nuclei get very close to each other and eventually, a large atomic nucleus of density $\sim 10^{14}$–$10^{15}\,{\rm gcm}^{-3}$ and diameter $\sim 10\,{\rm km}$ is formed. If we assume the conservation of angular momentum, the spin-up leads to very short final periods $P_{\rm f} = P_{\rm i}(R_{\rm f}/R_{\rm i})^2 \approx 10\,{\rm days}\,(10\,{\rm km}/10^6\,{\rm km})^2 \approx 10^{-4}\,{\rm s}$. The collapsed core exhibits high electrical conductivity. For the limit of infinite electrical conductivity, the magnetic flux $\Phi \propto BR^2$ is conserved. Given the initial magnetic field of the order $B_{\rm i} \approx 100\,{\rm G}$, the final value rises to $B_{\rm f} = B_{\rm i}(R_{\rm i}/R_{\rm f})^2 \approx 10^{12}\,{\rm G}$.

Neutron stars reveal themselves as periodic radio sources - pulsars (first observation by Hewish et al. (1968)) or as gas-accreting X-ray sources (Giacconi et al. 1962; Davidson & Ostriker 1973). There are three main arguments that classify pulsars as rotating neutron stars:

- short periods ranging from milliseconds,
- the slowdowns of pulsars over time manifesting the conversion of rotational energy into electromagnetic radiation (exceptions are very short events of spin-ups, "glitches", and accreting pulsars)
- stability of their rotational periods, enabling one of the most precise measurements in astronomy (periods as precise as 13 significant digits).

3.1 Observed characteristics of neutron stars

Observed spatial distribution of pulsars. Figure 3.1 shows the distribution in the Galactic coordinate system. It is apparent that pulsars are mostly located close to the Galactic equator ($\approx \pm 8^\circ$ from the plane). If we look at particular types, anomalous X-ray pulsars and soft gamma-ray repeaters (AXP, SGR, green) have low Galactic latitudes, whereas spin-powered pulsars with pulsed emission from radio to infrared or higher frequencies (HE, orange), binary systems (red), and isolated neutron stars with pulsed thermal X-ray emission but no detectable

radio emission (XINS, purple) are more scattered and reach also high Galactic latitudes. We note that there is another category of bursting, transient neutron stars, rotating radio transients (RRAT, McLaughlin et al., 2006; Hyman et al., 2005), which are not separately labelled here. They seem to have similar intrinsic properties (period and magnetic field) as AXP, SGR, and XINS.

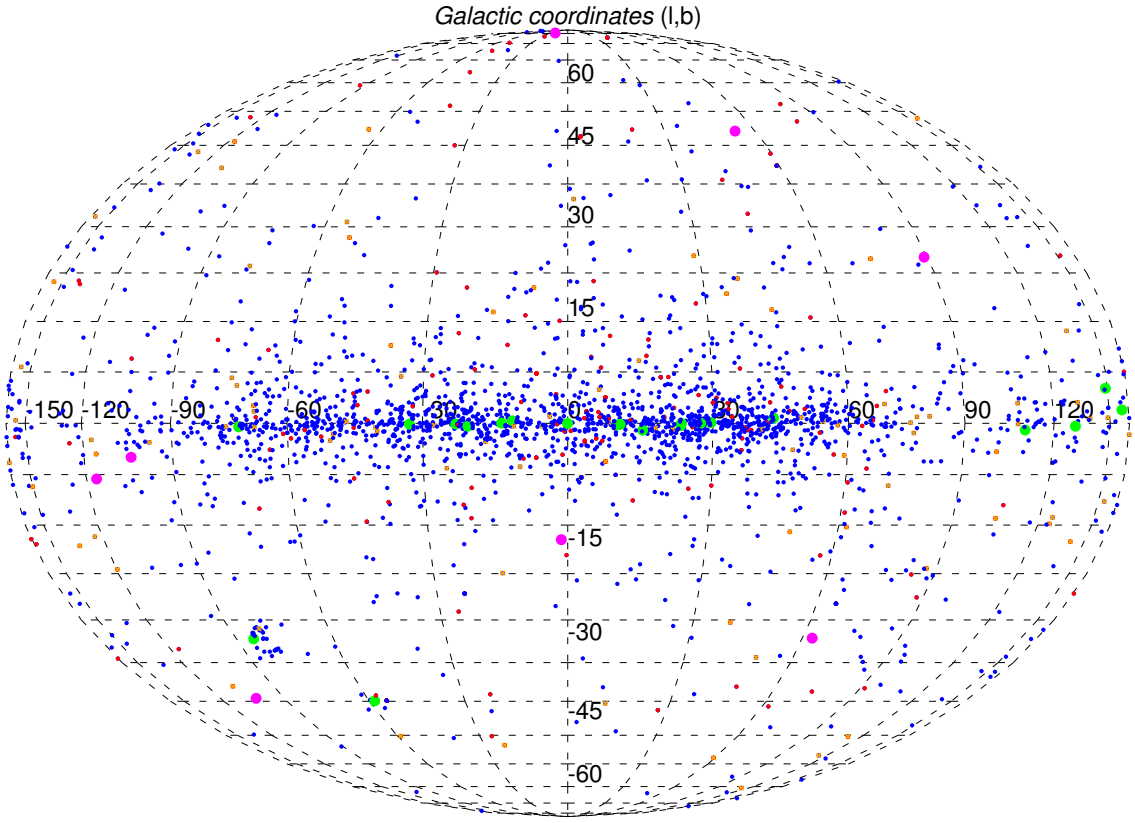

Figure 3.1: The distribution of neutron stars in Galactic coordinates (l, b). The plot depicts 2302 pulsars (blue). Binary systems are denoted as red points, spin-powered pulsars with pulsed emission from radio to infrared or higher frequencies (HE, orange), anomalous X-ray pulsars or soft gamma-ray repeaters with detected pulsations (AXP, green), and isolated neutron stars with pulsed thermal X-ray emission but no detectable radio emission (XINS, purple). The data are taken from ATNF Pulsar Catalogue, `http://www.atnf.csiro.au/research/pulsar/psrcat`, Manchester et al. (2005).

Pulsars are apparently concentrated towards the Galactic plane, which implies their origin in Galactic stellar populations, see Fig. 3.2. The distribution of pulsars with respect to the Galactic latitude is fit well with the exponential decay law $N(b) = N_0 \exp(-b/\beta)$ up to $b \approx \pm 20°$. The best-fit coefficients are $N_0 = 1444 \pm 27$ and $\beta = (5.6 \pm 0.2)°$. Similarly, we investigate the dependence with respect to the Galactic z coordinate. The fitting function is $N(z) = N_0 \exp(-z/z_0)$, where z_0 is a scale-height. First, both parameters are allowed to vary and the best-fit parameters are $N_0 = 201 \pm 7$ and $z_0 = (225 \pm 10)$ pc. Second, we set $N_0 = 250$, which is the value in the histogram for $z = 0$ kpc, and vary just the scale-height, which yields $z_0 = (172 \pm 7)$ kpc. In the first case, the wings of the distribution

are better described, whereas in the second case the peak of the distribution. We choose the first case, because we need to describe the character of the distribution for increasing $|z|$. The normalized density distribution $\rho = \rho(z)$, $\int_{-\infty}^{+\infty} \rho(z)dz = 1$, has the form $\rho(z) = 1/(2z_0)\exp(-z/z_0)$, where the scale-height $z_0 = 225 \pm 10$ is consistent with previous findings by Taylor & Manchester (1977)

Distances to pulsars are inferred from the pulse arrival times at different frequencies. Radio waves emanating from the pulsar propagate through conducting interstellar medium that exhibits variable density and various inhomogeneities. The phase velocity of an electromagnetic wave with wave number k is

$$v_{\rm ph} = \frac{\omega}{k} = \frac{c}{\epsilon^{1/2}}\,, \tag{3.2}$$

where ϵ denotes the dielectric constant and $\epsilon = [1 - (\omega_{\rm p}/\omega)^2)^{1/2}$ with $\omega_{\rm p}$ the plasma frequency, for which

$$\omega_{\rm p} = \left(\frac{4\pi n_{\rm e} e^2}{m_{\rm e}}\right)^{1/2}\,, \tag{3.3}$$

where $n_{\rm e}$ is the electron density. Inserting the dielectric constant ϵ into the relation for phase velocity (3.2), we obtain the dispersion relation for the plasma environment $\omega^2 = \omega_{\rm p}^2 + c^2k^2$, from which the group velocity follows as

$$v_{\rm g} = \frac{{\rm d}\omega(k)}{{\rm d}k} = c\epsilon^{1/2} \overset{\omega>>\omega_{\rm p}}{\simeq} c\left(1 - \frac{\omega_{\rm p}^2}{2\omega^2}\right)\,. \tag{3.4}$$

The arrival time for a pulse centred at the frequency $\omega = 2\pi\nu$ that is coming from a source at the distance D is

$$\begin{aligned} t_{\rm a}(\omega) &= \int_0^D \frac{{\rm d}l}{v_{\rm g}} \\ &\simeq \frac{1}{c}\int_0^D \left(1 + \frac{\omega_{\rm p}^2}{2\omega^2}\right){\rm d}l \\ &= \frac{D}{c} + \frac{2\pi e^2}{m_{\rm e}c\omega^2}\int_0^D n_{\rm e}{\rm d}l\,. \end{aligned} \tag{3.5}$$

Rewritten in terms of frequencies ν we finally get

$$t_{\rm a}(\nu) = \frac{D}{c} + \frac{e^2}{2\pi m_{\rm e}c}\nu^{-2}\underbrace{\int_0^D n_{\rm e}{\rm d}l}_{DM}\,, \tag{3.6}$$

where DM denotes *dispersion measure*, which may be easily expressed in terms of the mean electron density $\overline{n}_{\rm e}$,

$$DM = \int_0^D n_{\rm e}{\rm d}l = \overline{n}_{\rm e}D\,. \tag{3.7}$$

Dispersion measure DM is inferred from dispersive time delays $\Delta t_a(\nu)$ of different frequency components of a pulse. From (3.6) we get

$$\frac{\Delta t_{\rm a}(\nu)}{\Delta\nu} = -\frac{e^2}{\pi m_{\rm e}c}\nu^{-3}DM\,. \tag{3.8}$$

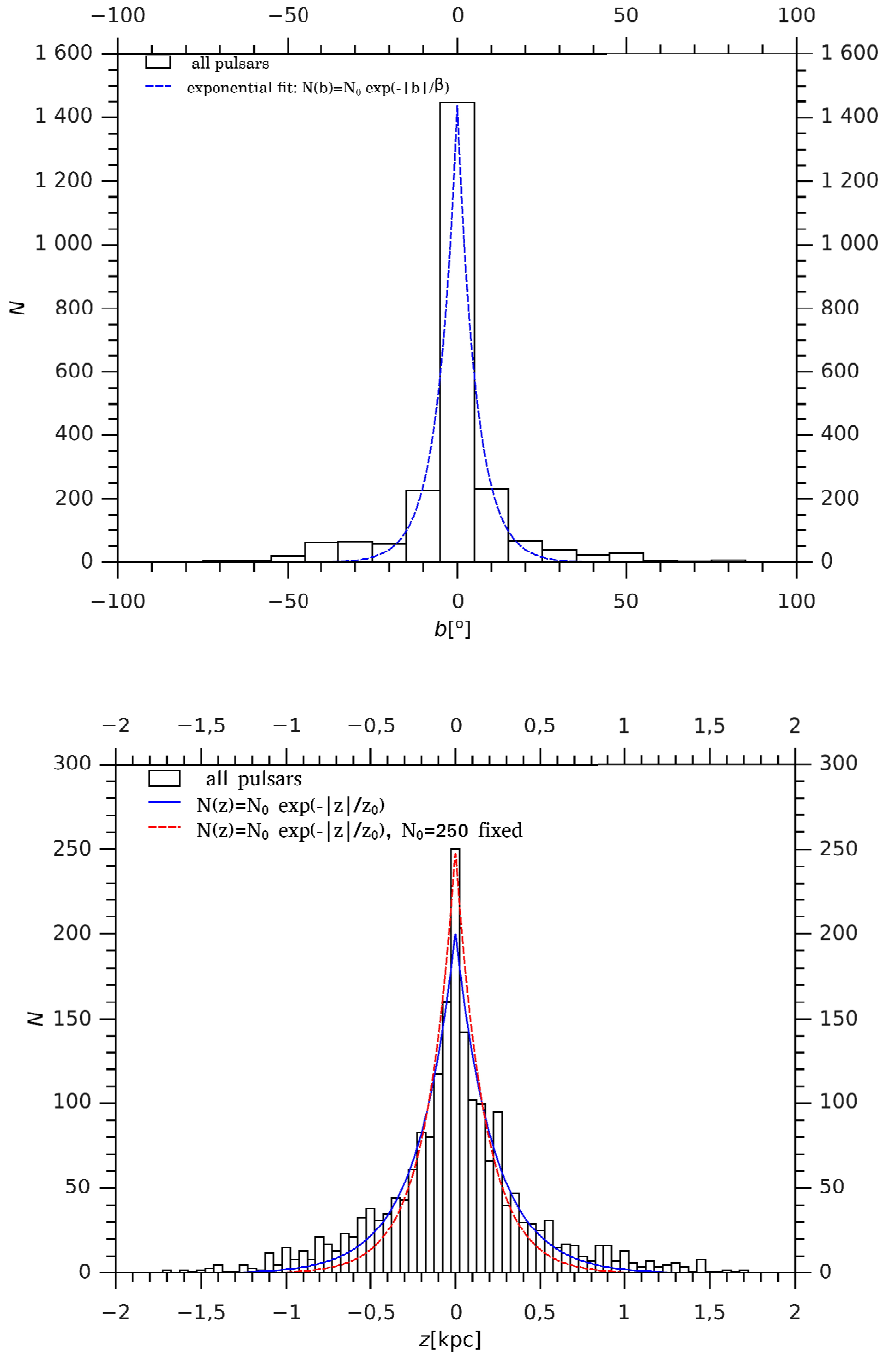

Figure 3.2: (*Top panel*) The histogram showing the distribution of pulsars with respect to the Galactic latitude. The majority of pulsars (1446 out of 2302) is concentrated towards the Galactic plane, $b = 0° \pm 5°$. The distribution is fit well with the exponential decay law up to $\pm 20°$. For higher latitudes, the number of observed pulsars is larger than the number predicted from exponential distribution. (*Bottom panel*) The distribution of pulsars with respect to Galactic z coordinate expressed in kiloparsecs (kpc). The blue line shows the exponential decay fit with two parameters N_0 and z_0, whereas the red line shows the fit with just one parameter z_0. The data are taken from ATNF Pulsar Catalogue, `http://www.atnf.csiro.au/research/pulsar/psrcat`, Manchester et al. (2005).

The distribution of dispersion measures of observed pulsars is depicted in Fig. 3.3. The highest number of pulsars have dispersion measures around ≈ 25–$35\,\mathrm{pc\,cm^{-3}}$. The distribution is decreasing for higher values of dispersion measures, having just few pulsars above $1000\,\mathrm{pc\,cm^{-3}}$. This is plausibly a consequence of the lack of observational sensitivity for the environment of large electron densities, especially the Galactic centre region. In the same figure, we plot the relation between the dispersion measure and the Galactic latitude. We see that the dispersion measure reaches large values $\gtrsim 500\,\mathrm{pc\,cm^{-3}}$ for pulsars observed near the Galactic plane, which may be explained by higher electron densities in comparison with higher Galactic latitudes and the halo region.

For known mean electron densities $\overline{n}_\mathrm{e}$ it is possible to compute distances D of pulsars using (3.7). Inversely, electron density of $0.03\,\mathrm{cm^{-3}}$ in the solar neighbourhood has been determined for sources of known distances (inferred from parallax measurements, Spitzer, 1978). From (3.7), the uncertainty of the distance D is given by the uncertainty of the density $\overline{n}_\mathrm{e}$. Deviations of $\overline{n}_\mathrm{e}$ from actual values n_e may lead to a factor-of-2 errors in determinations of pulsar distances.

We show the distribution of pulsars in space and the distribution of their distances in several ways. First, we compare the distribution of pulsars in the xy Galactic plane and the histogram of their distances from the Sun, see Fig. 3.4. It is obvious from both plots in Fig. 3.4 that observed pulsars are located near the Sun, the peak in the histogram is in the range ~ 2–$5\,\mathrm{kpc}$. This asymmetry is apparently caused by observational bias.

The asymmetry is even more prominent in the surface plots of the pulsar distribution in xy, xz, and yz planes, see Fig.3.5. The Galactic centre region around $(0, 0, 0)$ seems to be devoid of pulsars, which is visible in xy and yz cuts. This is caused by observational bias, namely lack of sensitivity of current instruments. In the next section we show that actually a large number of neutron stars and hence pulsars may be expected in the central parsec.

Mass. Some of the observed neutron stars are found in binary systems. Through precise timing it is possible to determine the masses of radiopulsars with high accuracy. A historical example is PSR 1913+16 (Hulse-Taylor pulsar), for which periastron advance has been detected. In case of binary X-ray pulsars, which consist of optical companion and X-ray emitting neutron star, there exists a simple relation between the masses of components M_o, M_x and $\sin i$ on one side and observable quantities, namely half-amplitudes of radial velocities v_o, v_x and orbital period T, on the other, (Lipunov 1992):

$$f_\mathrm{o}(M) = \frac{(M_\mathrm{x}\sin i)^3}{(M_\mathrm{x}+M_\mathrm{o})^2} = \frac{T v_\mathrm{o}^3}{2\pi G}\,,$$
$$f_\mathrm{x}(M) = \frac{(M_\mathrm{o}\sin i)^3}{(M_\mathrm{x}+M_\mathrm{o})^2} = \frac{T v_\mathrm{x}^3}{2\pi G}\,. \qquad (3.9)$$

The function $f(M)$ is called the *mass function*. By measuring half-amplitudes v_o and v_x for the components and having some estimate of the inclination of the binary $\sin i$ (usually brings the highest uncertainty), we can compute the masses of components using (3.9). Precise measurements have been performed in case

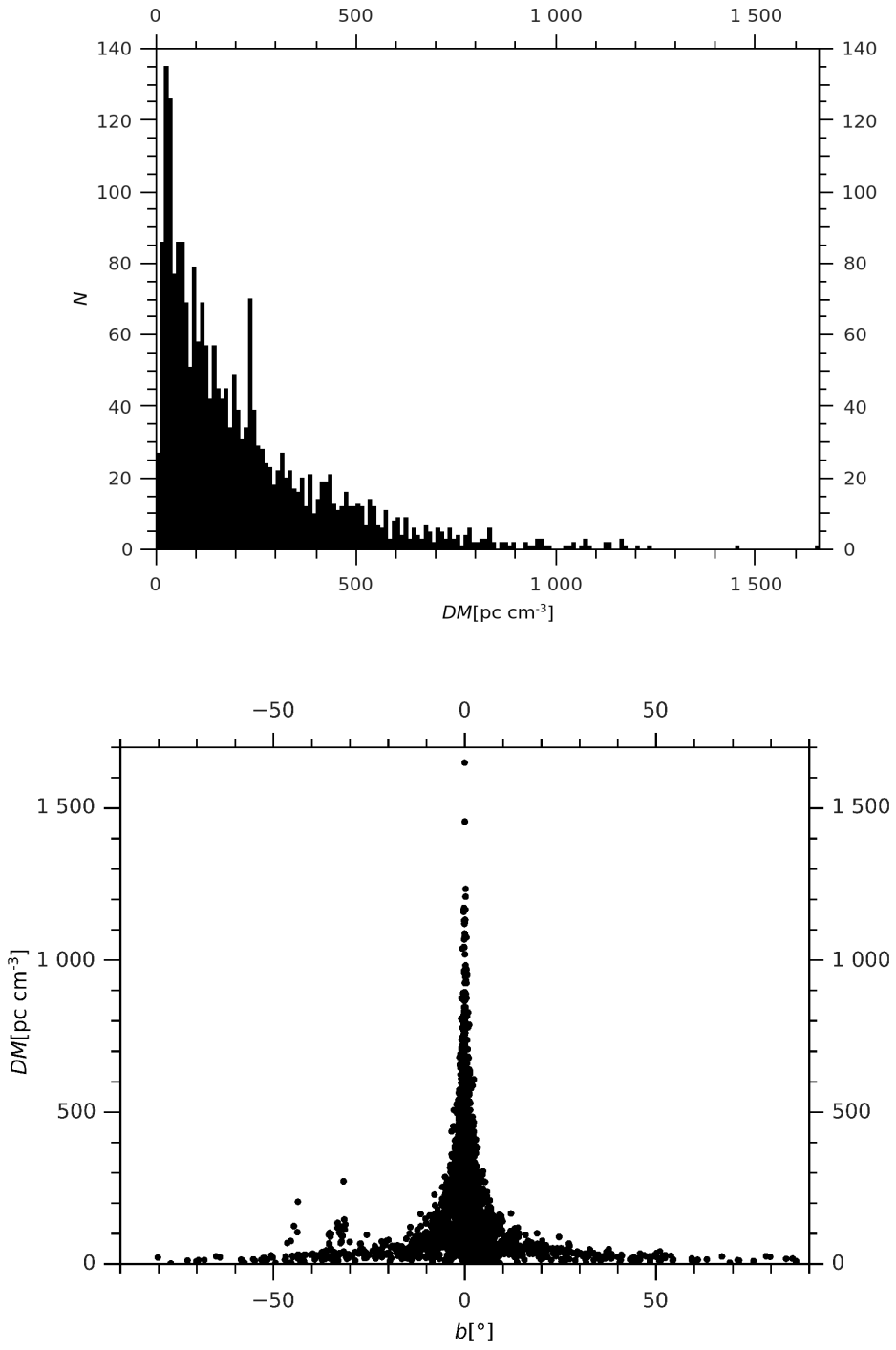

Figure 3.3: (*Top panel*) The histogram showing the distribution of dispersion measures of pulsars. The peak of the distribution is for values ≈ 25–$35\,\mathrm{pc\,cm^{-3}}$. For higher dispersion measures, the distribution decreases and reaches small values above $1000\,\mathrm{pc\,cm^{-3}}$. (*Bottom panel*) Relation between dispersion measure DM and Galactic latitude b. Large values of DM ($\gtrsim 500\,\mathrm{pc\,cm^{-3}}$) are found near the Galactic plane, whereas for higher Galactic latitudes $\gtrsim 10°$, DM drops to $\lesssim 150\,\mathrm{pc\,cm^{-3}}$. The data are taken from ATNF Pulsar Catalogue, `http://www.atnf.csiro.au/research/pulsar/psrcat`, Manchester et al. (2005).

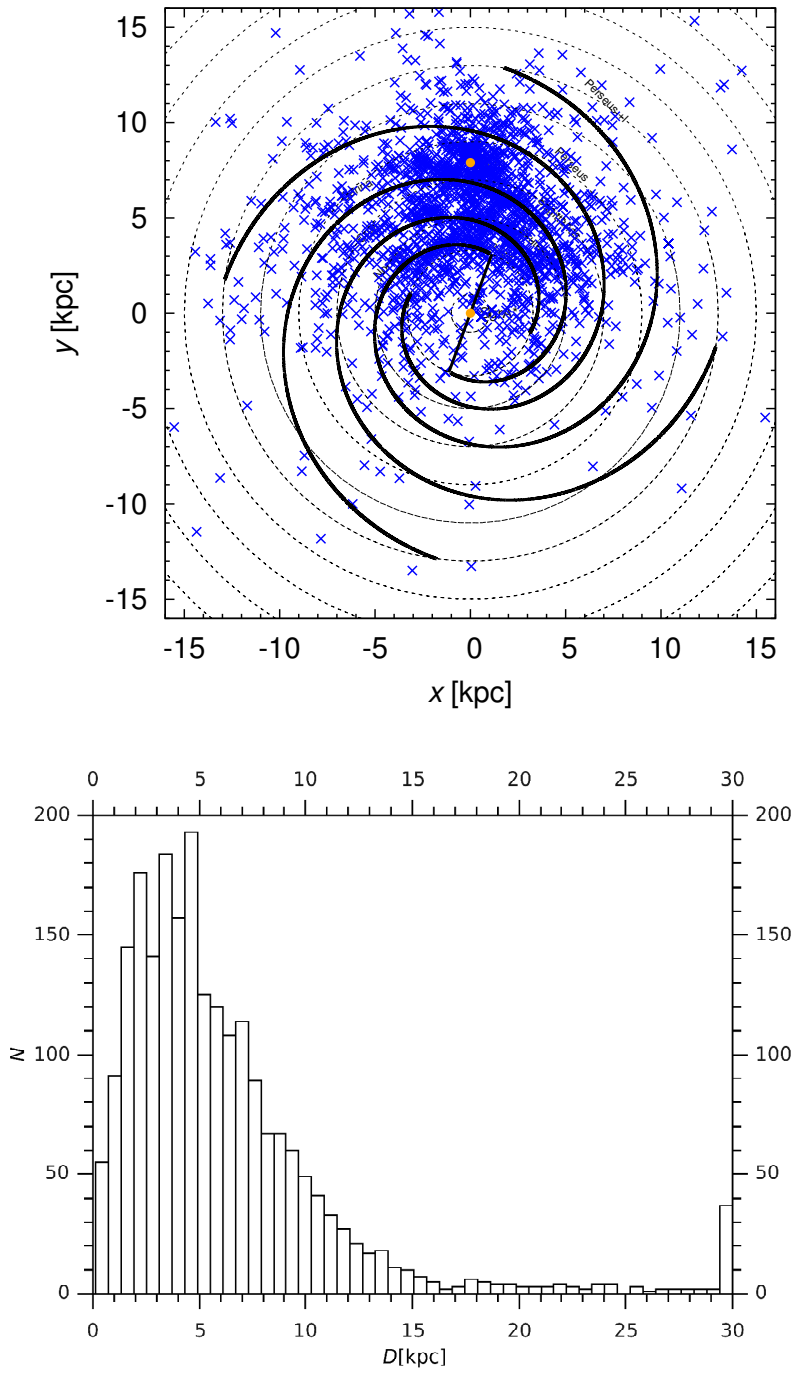

Figure 3.4: (*Top panel*) The distribution of 2302 pulsars in the xy Galactic plane. The four spiral arms are modelled as logarithmic spirals. The distance of the Sun from the Galactic centre is 7.9 kpc. (*Bottom panel*) The histogram of pulsar distances from the Sun (in kpc). Most pulsars are located $\sim$ 2–5 kpc from the Sun. The minimum distance is 130 pc and the maximum is 30 kpc. The bin width is 597.40 pc. The data are taken from ATNF Pulsar Catalogue, `http://www.atnf.csiro.au/research/pulsar/psrcat`, Manchester et al. (2005).

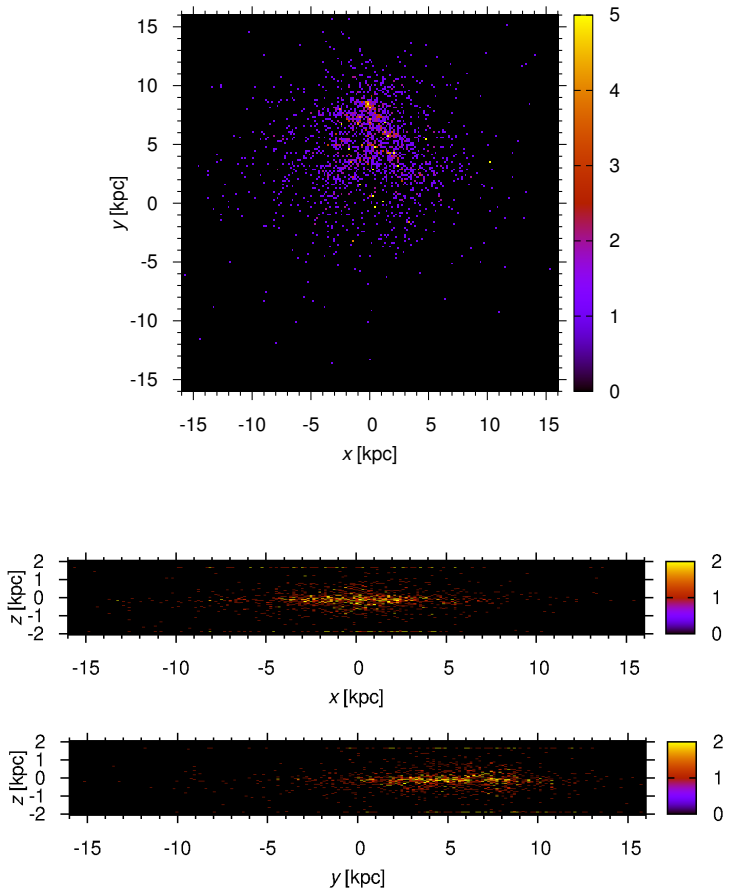

Figure 3.5: Surface plots of the distribution of pulsars in xyz Galactic coordinate system. The asymmetry is obvious for xy and yz plots. The data are taken from ATNF Pulsar Catalogue, `http://www.atnf.csiro.au/research/pulsar/psrcat`, Manchester et al. (2005).

of double systems, mainly neutron star – neutron star (NS – NS), neutron star – white dwarf (NS – WD) binary systems, see Fig. 3.6.

We see that the range of the masses is very narrow. According to Özel et al. (2012), there is a slight difference in the mean mass among neutron stars in double neutron star systems ($1.33 \pm 0.05\,M_\odot$), neutron stars near their birth masses ($1.28 \pm 0.24\,M_\odot$), and neutron stars that have undergone episodes of accretion ($1.48 \pm 0.20\,M_\odot$).

Rotational periods. Rotational periods are generally short (ranging from milliseconds to a few seconds) and stable for pulsars, which makes them one of the basic observational characteristics of rotating neutron stars. Using the values published in the ATNF Pulsar Catalogue (Manchester et al. 2005) we plot the histogram (see Fig. 3.7) for all available values (white columns), consequently distinguishing subsets of anomalous X-ray pulsars (AXP) and soft gamma-ray repeaters (green columns), spin-powered pulsars with pulsed emission from radio to infrared or higher frequencies (HE, orange columns), binary systems (blue columns), and isolated neutron stars with pulsed thermal X-ray emission but no detectable radio emission (XINS, olive columns).

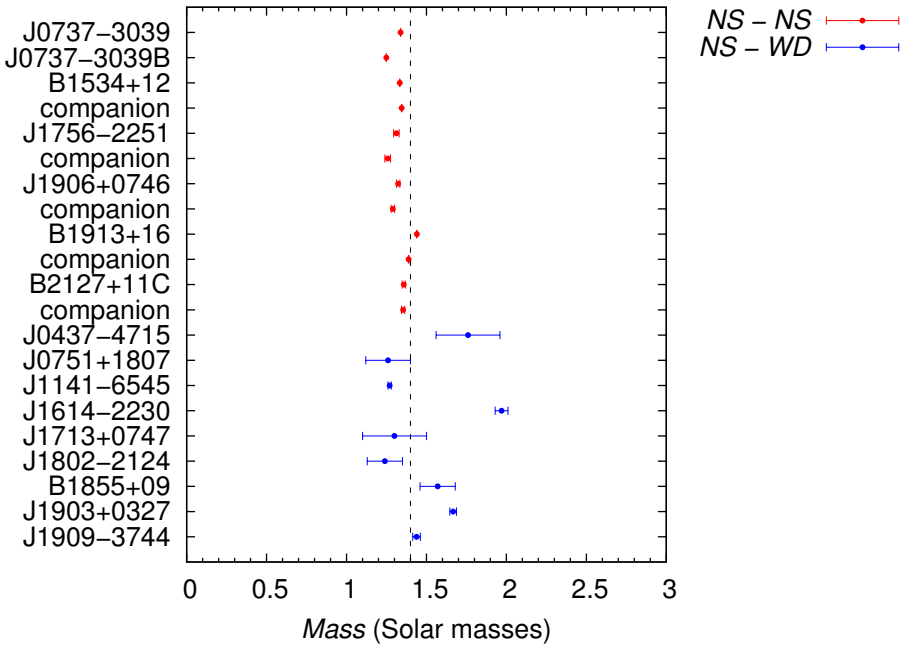

Figure 3.6: The plot depicts precisely determined neutron star masses in binary *neutron star – neutron star* systems (NS – NS) and *neutron star – white dwarf* (NS – WD) systems. The value of $1.4\,M_\odot$ corresponding approximately to the Chandrasekhar limit is depicted by a dashed line. The data are taken from Özel et al. (2012).

We fit the distribution in Fig. 3.7 by double-peak Gaussian function of the following form:

$$N(\log P_0) = N_0 + A_1 \frac{1}{(2\pi)^{1/2}\sigma_1} \exp\left(-\frac{(\log P_0 - \mu_1)^2}{2\sigma_1^2}\right) + A_2 \frac{1}{(2\pi)^{1/2}\sigma_2} \exp\left(-\frac{(\log P_0 - \mu_2)^2}{2\sigma_2^2}\right), \tag{3.10}$$

where N_0, $A_{1,2}$, $\sigma_{1,2}$, and $\mu_{1,2}$ are free parameters. The best-fit values are in Table 3.1.

Parameter	Millisecond peak (MSP)	Normal peak (SP)
N_0	17.7 ± 0.4	
$A_{1,2}$	35.9 ± 0.5	345.9 ± 0.9
$\sigma_{1,2}$	0.145 ± 0.002	0.3478 ± 0.0008
$\mu_{1,2}$	-2.406 ± 0.002	-0.2189 ± 0.0007
$P_{\mathrm{MSP,SP}}$[s]	$(3.93 \pm 0.02) \times 10^{-3}$	0.604 ± 0.001

Table 3.1: Best-fit parameters of the double-peak Gaussian function (3.10).

The mean values for the period peaks are thus $P_{\mathrm{MSP}} = 3.93 \pm 0.02\,\mathrm{ms}$ and $P_{\mathrm{SP}} = 0.604 \pm 0.001\,\mathrm{s}$.

We see these prominent features in Fig. 3.7:

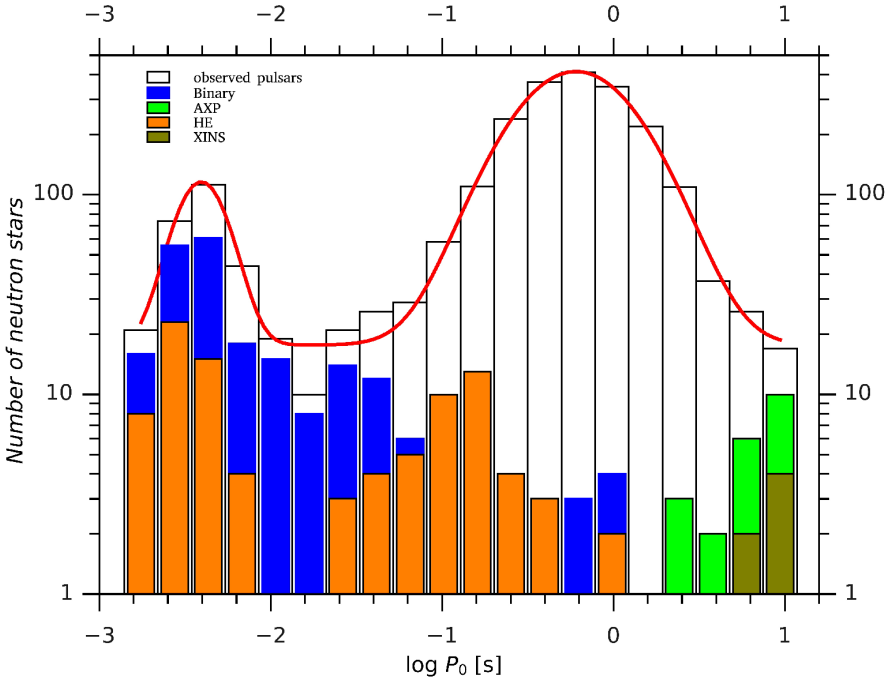

Figure 3.7: The histogram of the periods for observed neutron stars. There are different subsets presented (see the key) besides the whole sample of 2302 pulsars. The data are taken from ATNF Pulsar Catalogue, `http://www.atnf.csiro.au/research/pulsar/psrcat`, Manchester et al. (2005).

- binary systems are located in the millisecond part ,
- anomalous X-ray pulsars (AXP) and isolated X-ray pulsars (XINS) are located in the long-period part of the histogram.

A possible explanation for millisecond periods of pulsars found in binary systems is that they have been spun up by the accretion of material from the other component. On the other hand, AXP and XINS may be manifestations of old neutron stars that have lost a substantial amount of their rotational energy.

Period–Period derivative (P–$\dot{P}$) diagram. For several pulsars it has been possible to measure the period derivative $\dot{P}$ or change of period with time. We plot P–$\dot{P}$ diagram from available data by combining ATNF Pulsar Catalogue (Manchester et al. 2005) and SNR catalogue (`http://www.physics.umanitoba.ca/snr/SNRcat`; Ferrand & Safi-Harb,2012), see Fig. 3.8.

Various lines in Fig. 3.8 are derived from the lowest order of approximation of neutron stars - rotating magnetic dipoles emitting magnetic dipole radiation. Assuming that the magnetic dipole is inclined by angle α from the rotation axis and that its temporal changes are harmonic with the rotational period P ($\Omega = 2\pi/P$), $\mathbf{m} = \mathbf{m_0}\exp(-i\Omega t)$, its radiation is emitted at a rate given by Larmor formula:

$$\frac{\mathrm{d}E_{\mathrm{rad}}}{\mathrm{d}t} = \frac{2}{3c^3}|\ddot{\mathbf{m}}| \overset{|\mathbf{m}|=BR^3}{=} \frac{2}{3c^3}B^2\Omega^4R^6\sin^2\alpha\,. \tag{3.11}$$

In this derivation, we assume that a neutron star may be represented as a uniformly magnetized sphere with surface magnetic field B and radius R. This radiation may be associated with the loss of rotational energy

$$\dot{E}_{\rm rot} = I\Omega\dot{\Omega} = -4\pi^2 I\dot{P}/P^3\,, \tag{3.12}$$

where I is the moment of inertia of the neutron star that is often approximated by the uniform-density sphere ("canonical" neutron star: $M_{\rm NS} = 1.4\,M_\odot$, $R_{\rm NS} = 10^6\,{\rm cm} \rightarrow {\rm I} \approx 10^{45}\,{\rm g\,cm^2}$). We use this simple relation for energy losses to label spin-down power lines $\dot{E}$ in Fig. 3.8 (in ${\rm erg\,s^{-1}}$).

By setting the radiation power of rotating dipole equal to losses of rotational energy ($-\dot{E}_{\rm rot}$), one can estimate the lower limit [1] for the surface magnetic field $B \gtrsim B\sin\alpha$:

$$B \gtrsim \left(\frac{3c^3 I}{8\pi^2 R^6}\right)^{1/2} (P\dot{P})^{1/2} \approx 3.2\times 10^{19}\left(\frac{P\dot{P}}{\rm s}\right)^{1/2}\,. \tag{3.13}$$

Equation (3.13) is used to depict minimum magnetic field in P–$\dot{P}$ plane in Fig.3.8 (in Gauss). Finally, assuming that $B\sin\alpha$ does not change significantly over time, equation (3.13) implies $P\dot{P} = {\rm const}$. By integrating $P{\rm d}P = P\dot{P}$ over the lifetime τ of the pulsar (from initial period P_0 to current value P and from 0 to τ, respectively) and assuming $P_0 \ll P$, we get the characteristic age of the pulsar

$$\tau \equiv \frac{P}{2\dot{P}}\,. \tag{3.14}$$

Equation (3.14) is used to plot lines of constant characteristic age.

P–$\dot{P}$ diagram may be looked at as an *evolutionary diagram* for neutron stars (analogous to HR diagram). As Baade & Zwicky (1934) predicted, neutron stars seem to be born in supernova explosions, which is hinted by their presence in or near the remnants. These young pulsars with age $\lesssim 100\,{\rm kyr}$ (see Fig. 3.8) have small P and higher $\dot{P}$. Assuming that their magnetic field does not change significantly, they move along lines of constant B towards lower right corner of P–$\dot{P}$ diagram, consequently having longer periods and smaller $\dot{P}$. In case of binaries, they may attain angular momentum through accretion resulting in their spinning-up. During this process, they move towards lower left corner, having shorter periods (on the order of milliseconds) and smaller magnetic fields. The spinning-up is possible up to the spin-up limit marked by red line in Fig. 3.8. This line is determined from the condition that the flux of angular momentum towards the neutron star is possible if the angular velocity (presumably Keplerian) of the accreting material at the capture radius is higher than the angular velocity of the rotating star. The spin-up is thus halted if these velocities are approximately equal, which is near the spin-up line. The assumption of the constant magnetic field may not be quite correct. There may be processes leading to the magnetic field decay, causing pulsars to move straight down towards *death lines* and below, where their radiation mechanism is turned off and it is not possible to observe them.

[1] We usually do not know the magnetic dipole inclination α or we have its estimate with large uncertainty.

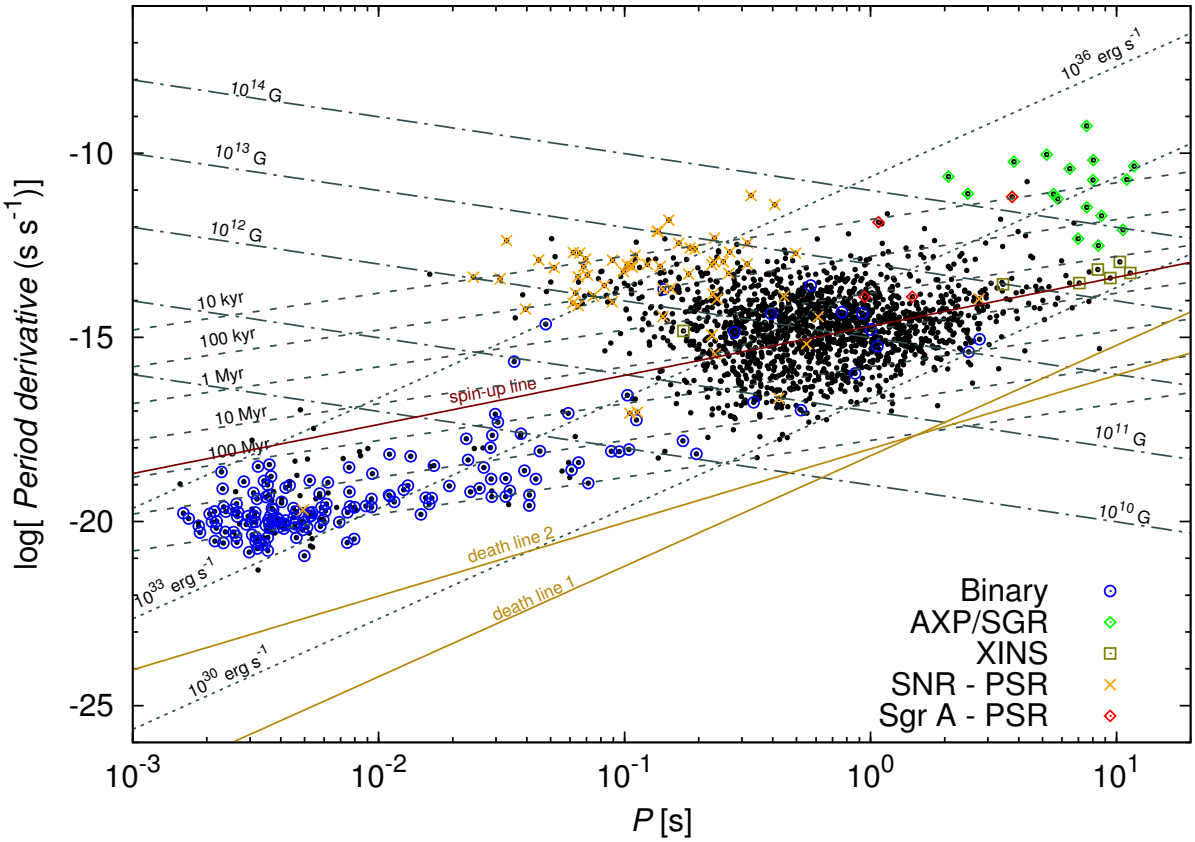

Figure 3.8: The period (P) – period derivative ($\dot{P}$) diagram for 2302 observed neutron stars. The lines of constant characteristic age (3.14), minimum magnetic field (3.13), and spin-down power (3.12) are depicted for several values. The spin-up limit line (red) for binaries and death lines (gold), which separate the regions where radio emission is and is not possible, are labelled, as well. For the description of possible evolutionary tracks, see the text. The data are taken from ATNF Pulsar Catalogue, `http://www.atnf.csiro.au/research/pulsar/psrcat`, Manchester et al. (2005), and SNR catalogue (`http://www.physics.umanitoba.ca/snr/SNRcat`; Ferrand & Safi-Harb,2012).

Magnetic field. The magnetic field of neutron stars is often approximated by a dipole magnetic field. This has two reasons:

- The rotating magnetic dipole model matches the observations well, see P – $\dot{P}$ diagram, Fig. 3.8. Based on the observed combination of these two quantities, we may estimate the lower limit of the dipole magnetic field using (3.13), which yields a typical value of 10^{12} Gauss for younger pulsars and lower values for older pulsars or accreting pulsars in binary systems.

- During the core collapse, higher multipoles decrease in magnitude and the field is cleansed, making the dipole component the most representative part.

We plot the histogram of the estimates of the dipole magnetic field (in Gauss) from the available database, see Fig. 3.9. In the histogram, we plot all observed pulsars (white), binaries (blue), spin-powered pulsars with pulsed emission from radio to infrared or higher frequencies (HE, orange), anomalous X-ray pulsars or soft gamma-ray repeaters with detected pulsations (AXP, green), and isolated neutron stars with pulsed thermal X-ray emission but no detectable radio emission (XINS, olive). We see the same tendency as in P–$\dot{P}$ diagram: pulsars in binaries have smaller magnetic fields, while AXP and XINS are concentrated towards the stronger tail. Most pulsars have dipole magnetic fields around 10^{12} Gauss.

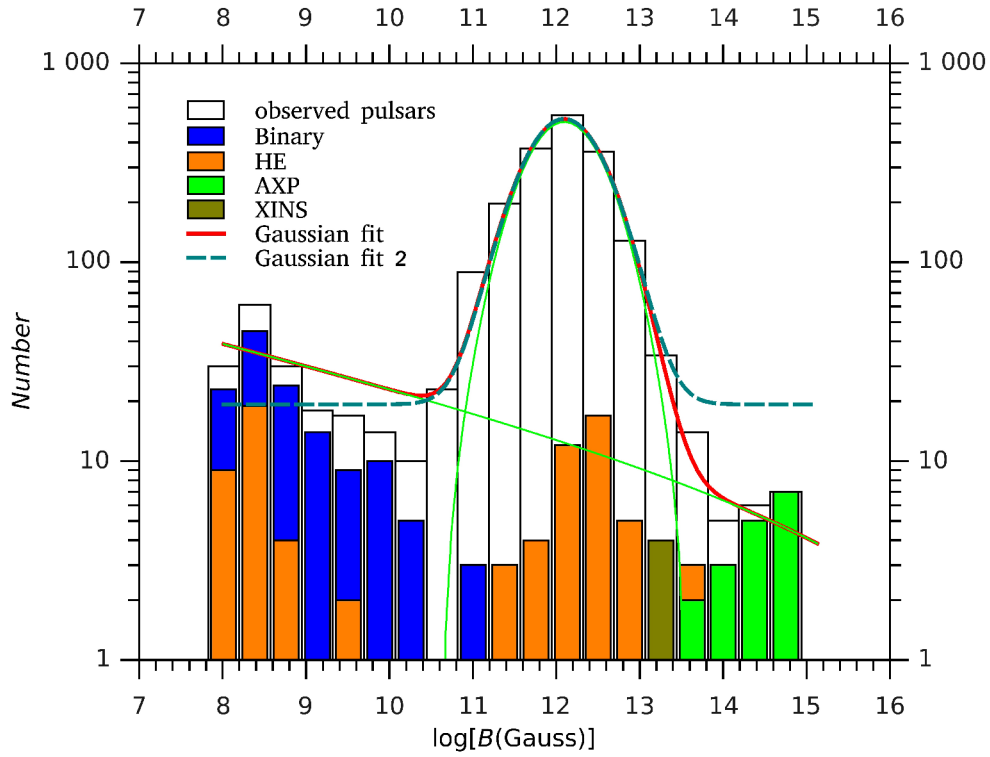

Figure 3.9: The histogram of the distribution of pulsars according to surface dipole magnetic field computed from P and $\dot{P}$. Particular subsets (binaries, HE, AXP, XINS) are denoted according to the key. The data are taken from ATNF Pulsar Catalogue, `http://www.atnf.csiro.au/research/pulsar/psrcat`, Manchester et al. (2005).

As in the case of the pulsar period distribution (see 3.7), we recognize two peaks. We attempt to fit this distribution using double-peak Gaussian function (see (3.10)). However, the χ^2 is an order of magnitude higher, hence we fit only the stronger peak around 10^{12} G with a one-peak Gaussian with N_0, A, $\sigma_{\log \mathrm{B}}$, and $\log B$ as free parameters. Results are summarized in Table 3.2.

Parameter	Best-fit value
N_0	19 ± 6
A	593 ± 25
$\sigma_{\log \mathrm{B}}$	0.47 ± 0.02
μ_B	12.09 ± 0.02

Table 3.2: Parameters for a one-peak Gaussian fit of the distribution in Fig. 3.9.

Compactness parameter. For typical values of mass M_{NS} and radius R_{NS} ($M_{\mathrm{NS}} \approx 1.4\,M_\odot$, $R_{\mathrm{NS}} \approx 10\,\mathrm{km}$) we may compute the *compactness parameter*, which characterizes the energy released during accretion processes:

$$\epsilon = \frac{2GM}{Rc^2} \approx 0.4\,, \tag{3.15}$$

The compactness parameter for the Sun is about 10^5 times smaller. Thus, neutron stars are capable of releasing much more energy through accretion than main sequence stars.

3.2 Constraints for the number of neutron stars near Sgr A*

It has been previously advocated that a large population of stellar remnants should exist in the Galactic centre (e.g., Morris, 1993; Miralda-Escudé & Gould, 2000). Morris (1993) supports this claim by arguing that massive stars are preferably formed near the Galactic centre. It can be shown that adiabatic diffusion time scale is longer than orbital/dynamical time scale near galactic nuclei (by more than a factor of ten). Therefore, clouds are more likely to be compressed by external agents, such as supernova shocks, collisions with other clouds or winds from nearby stars and Sgr A* than by spontaneous gravitational contraction. Consequently, they lose their angular momentum while contracting. This is because of the following factors:

- magnetohydrodynamic winds maintained by the global magnetic field on the order of a milligauss,
- higher metallicity, yielding higher opacity, which prolongs the contraction period and thus the cloud has enough time to get rid of its angular momentum and/or to accrete additional matter from its surroundings before radiation pressure and winds cause it to halt.

Hence, due to the angular momentum loss the cloud does not fragment and more massive stars are favoured in comparison with the disk population.

Mass segregation and relaxation. Heavier stellar remnants, mainly black holes formed as a result of a core collapse of massive stars ($M_\star \approx 30 - 100\,M_\odot$), concentrate towards the galactic centre due to the dynamical friction since they are more massive than field stars. In case of neutron stars, the distribution towards the centre is probably not so steep, because they are comparable to other field stars concerning the mass ($\sim 1.4\,M_\odot$). The relaxation time within 1 pc is short enough for heavy members of the nuclear star cluster to sink inwards ($\lesssim 3 \times 10^8$ yr, Morris, 1993).

While heavy remnants (mainly black holes) move towards the centre, the low-mass, older stars are ejected outwards due to relaxation (see Fig. 3.10, Miralda-Escudé & Gould, 2000). Miralda-Escudé & Gould (2000) predict that about 24 000 stellar black holes having a mass of $\sim 5\,\%$ of Sgr A* moved towards the centre. These heavy remnants should still be present there since the time scale of a direct capture by the SMBH or the capture through gravitational wave losses is much longer than the Hubble time.

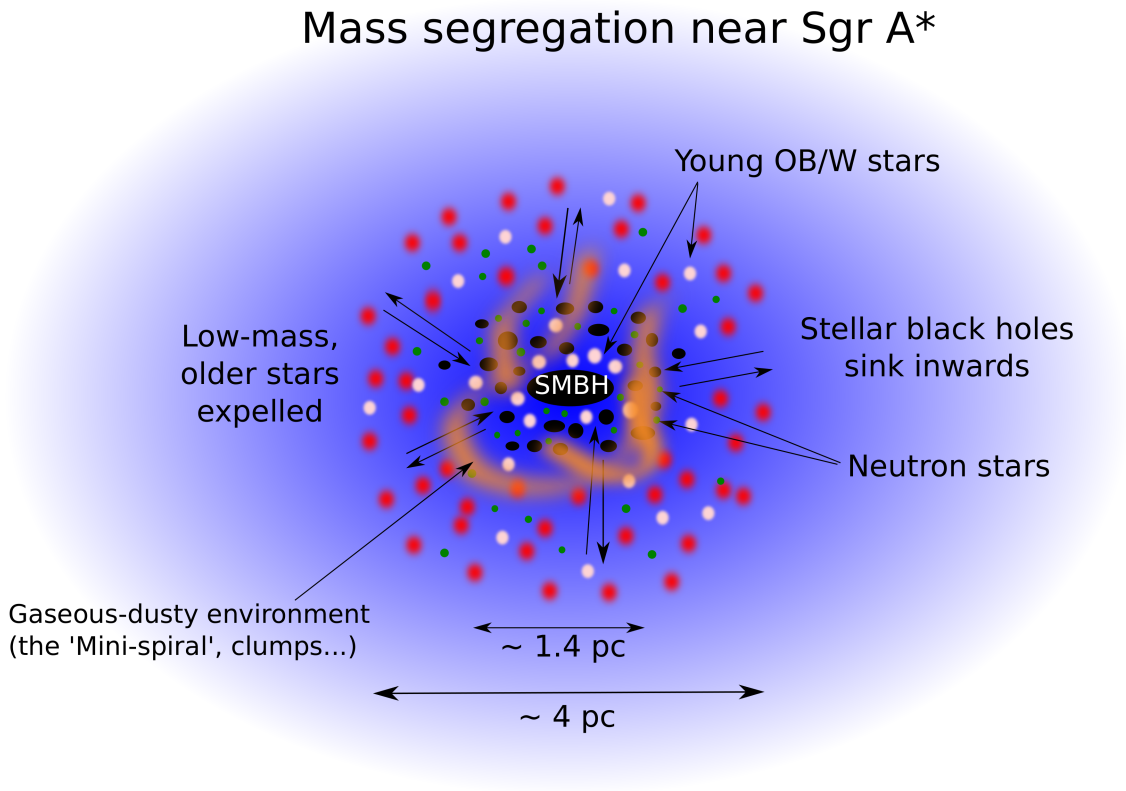

Figure 3.10: Segregation process near Sgr A* and other similar nuclei as proposed by Miralda-Escudé & Gould (2000). The estimated radius of the expelled older population is ~ 2 pc, while the black hole cusp should occupy the inner ~ 0.7 pc.

The time scale $t_{\rm df}$ for stellar remnants (and normal stars as well) having mass M to reach the core region is estimated from the deceleration due to dynamical friction by field stars having mass m (Binney & Tremaine 2008):

$$t_{\rm df} = 10^9 \left(\frac{V_{\rm M}}{100\,{\rm km\,s^{-1}}}\right)^3 \left(\frac{R_{\rm gc}}{1\,{\rm pc}}\right)^{1.8} \left(\frac{1\,M_\odot}{M+m}\right) \times \left[{\rm erf}\,(X) - \frac{2X}{\sqrt{\pi}}\exp\left(-X^2\right)\right]^{-1} {\rm yr}\,, \tag{3.16}$$

where $V_{\rm M}$ is the velocity of the remnant with mass M with respect to the local standard of rest at distance $R_{\rm gc}$ from the galactic centre. The last term contains error function erf (X) and $X = V_{\rm M}/(\sqrt{2}\sigma)$.

From relation (3.16), we plot the dependence of the migration radius $R_{\rm gc}$ on the remnant mass M, see Fig.3.11. We set $t_{\rm df} \approx 10^{10}\,{\rm yr}$, which is an estimate of the bulge age, and the mass of field stars m is set to $1\,M_\odot$. This simple calculation assumes constant deceleration due to dynamical friction from the start radius to the core cluster. As is discussed by Morris (1993), the computed radii may be underestimates since the field density towards the centre is supposed to rise.

Specifically, for neutron stars having an average mass of $1.4\,M_\odot$, the migration radius is estimated to be 1.6 pc.

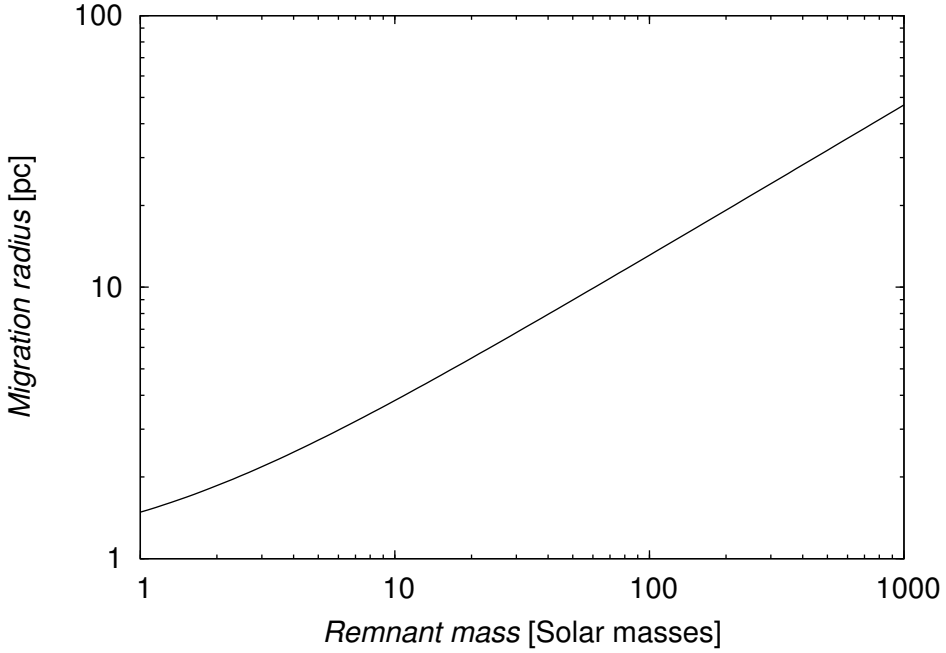

Figure 3.11: The radius in pc from which a remnant object migrates in $10^{10}\,{\rm yr}$ to the core cluster versus its mass in Solar masses. Computed according to (3.16) (Morris 1993).

Estimates from Initial Mass function. The estimate of the number of compact remnants is possible through observations of massive stars near the Galactic Centre. A significant parameter is the enclosed dynamical mass inferred from velocity measurements of stars (Wharton et al. 2012).

Furthermore, the functional form of the initial mass function (IMF) is crucial as well as the stellar mass limits that determine the number of stars that turn

into white dwarfs, neutron stars, and black holes. It is also important to include the low-mass stars that are still on the main sequence and contribute to the total mass.

First, we embark upon a simple approach that includes just the observed dynamical mass in the central parsec, the mass limits for stars that turn into neutron stars we are interested in, and the functional form of the IMF. The IMF is usually assumed to have the following power-law form (Salpeter 1955; Morris 1993; Kroupa 2012):

$$\frac{\mathrm{d}N}{\mathrm{d}m} = Cm^{-\alpha}\,, \tag{3.17}$$

where $\mathrm{d}N$ stands for the number of stars with initial masses having the span of $\mathrm{d}m$ and the exponent α depends on considered stellar populations. Let us denote the total mass in the inner parsec M_{TOT} and the mass limits m_{min} and m_{max} for the minimum and maximum initial masses of stars. We neglect the differences of the IMF before and after the bulge formation as well as its change over time.

By evaluating a simple integral:

$$M_{\mathrm{TOT}} = C\int_{m_{\mathrm{min}}}^{m_{\mathrm{max}}} m^{1-\alpha}\mathrm{d}m\,, \tag{3.18}$$

we get a general formula for the constant C:

$$C = \frac{(2-\alpha)M_{\mathrm{TOT}}}{m_{\mathrm{max}}^{2-\alpha} - m_{\mathrm{min}}^{2-\alpha}}\,. \tag{3.19}$$

We evaluate the number of neutron stars N_{NS} using IMF (3.17). We denote m_{NS1} and m_{NS2} the mass limits of stars that finally become neutron stars. Finally, we get

$$N_{\mathrm{NS}} = \frac{2-\alpha}{1-\alpha}\frac{m_{\mathrm{NS2}}^{1-\alpha} - m_{\mathrm{NS1}}^{1-\alpha}}{m_{\mathrm{max}}^{2-\alpha} - m_{\mathrm{min}}^{2-\alpha}}M_{\mathrm{TOT}}. \tag{3.20}$$

We take the value of the extended mass $M_{\mathrm{TOT}} = 0.5 - 1.5 \times 10^6\,M_\odot$ in the central parsec from Schödel et al. (2009). The adopted values for α and mass limits and subsequent calculations using (3.20) are summarized in Table 3.3.

The mass limits m_{min} and m_{max} for stars are $0.1\,M_\odot$ and $100\,M_\odot$ that are often assumed for the disk population (Wharton et al. 2012; Zane et al. 1996). However, as was already mentioned, the star formation may be quite different in the Galactic centre (Morris 1993), specifically it is thought that the top-heavy IMF is valid with the low-mass cutoff at about $1\,M_\odot$ (Zane et al. 1996). This is also justified by near-infrared observations Maness et al. (2007); Nayakshin & Sunyaev (2005); Ghez et al. (2005). Therefore we increase the value m_{min} in some calculations.

The limits m_{NS1} and m_{NS2} for the stars to collapse into neutron stars are assumed to be $9\,M_\odot$ and $25\,M_\odot$ (Heger et al. 2003), respectively. However, due to rotation and mass losses by wind, the progenitor mass may be higher by about two orders of magnitude to collapse into neutron star Muno et al. (2006); Zane et al. (1996). Hence, we vary these limits, as well.

α	$m_{\mathrm{NS1}}\,[M_\odot]$	$m_{\mathrm{NS2}}\,[M_\odot]$	$m_{\mathrm{min}}\,[M_\odot]$	$m_{\mathrm{max}}\,[M_\odot]$	$M_{\mathrm{TOT}}\,[10^6\,M_\odot]$	N_{NS}
2.35	9	25	0.1	100	0.5	2449
	9	25	0.1	100	1.0	4899
	9	25	0.1	100	1.5	7348
	9	25	1.0	100	1.0	12479
	9	30	0.1	100	1.0	5258
	9	40	0.1	100	1.0	5673
	9	40	1.0	100	1.0	14452
	10	50	0.1	100	1.0	5032
	10	50	1.0	100	1.0	12820
2.01	9	25	0.1	100	0.5	5071
	9	25	0.1	100	1.0	10142
	9	25	0.1	100	1.5	15213
	9	25	1.0	100	1.0	15391
	9	30	0.1	100	1.0	11086
	9	40	0.1	100	1.0	12264
	9	40	1.0	100	1.0	18611
	10	50	0.1	100	1.0	11378
	10	50	1.0	100	1.0	17267
1.70	9	25	0.1	100	0.5	6757
	9	25	0.1	100	1.0	13515
	9	25	0.1	100	1.5	20272
	9	25	1.0	100	1.0	15776
	9	30	0.1	100	1.0	15065
	9	40	0.1	100	1.0	17142
	9	40	1.0	100	1.0	20011
	10	50	0.1	100	1.0	16608
	10	50	1.0	100	1.0	19387
0.45	9	25	0.1	100	0.5	2826
	9	25	0.1	100	1.0	5652
	9	25	0.1	100	1.5	8478
	9	25	1.0	100	1.0	5656
	9	30	0.1	100	1.0	7039
	9	40	0.1	100	1.0	9530
	9	40	1.0	100	1.0	9538
	10	50	0.1	100	1.0	11306
	10	50	1.0	100	1.0	11315

Table 3.3: Table summarizing the computation of the number of neutron stars within the inner parsec using the relation (3.20). The values of parameters α, m_{NS1}, m_{NS2}, m_{min}, m_{max}, and M_{TOT} are also included.

The average value of the number of neutron stars computed from Table 3.3 is 11 200 with the standard deviation 5 200. This result is consistent with previous estimates based on recent pulsar searches (Wharton et al. 2012).

Second, we proceed with a more careful analysis of the IMF (3.17), since we take into account the mass distribution $\rho = \rho(r)$ within 1 pc. So the number of stars with a mass in the range $\mathrm{d}m$ is distance-dependent $\mathrm{d}n{=}\mathrm{d}n(r)$ as well as the

factor $C = C(r)$ and in this context $\mathrm{d}n$ expresses number density of stars per a unit of volume (pc^{-3}). We also add more parameters besides the exponent of the IMF α and maximum and minimum mass limits m_{max} and m_{min}. Using the approach of Morris (1993), we assume that all stars with initial masses $(m_{\mathrm{B}}, m_{\mathrm{max}})$ collapse into black holes with the mass m_{BH}, those in the range $(m_{\mathrm{N}}, m_{\mathrm{B}})$ turn into neutron stars with the mass m_{NS}, and stars in the mass range $(m_{\mathrm{W}}, m_{\mathrm{N}})$ are assumed to end up as white dwarfs having the mass m_{WD}. Finally, there are light stars in the range $(m_{\mathrm{min}}, m_{\mathrm{W}})$ that are still on the main sequence and are thought to keep their initial masses.

Using the known density distribution $\rho(r)$, we can find the expression for $C(r)$. From relation (3.17) we can express the mass density of the black hole population:

$$\rho_{\mathrm{BH}} = \frac{C(r)}{1-\alpha}(m_{\mathrm{max}}^{1-\alpha} - m_{\mathrm{B}}^{1-\alpha})m_{\mathrm{BH}}\,. \tag{3.21}$$

Expressions for the mass density of neutron stars ρ_{NS} and white dwarfs ρ_{WD} are analogous to (3.21). The mass density of lighter main-sequence stars is

$$\rho_{\mathrm{MS}} = \frac{C(r)}{2-\alpha}(m_{\mathrm{W}}^{2-\alpha} - m_{\mathrm{min}}^{2-\alpha})\,. \tag{3.22}$$

From the equation $\rho_{\mathrm{BH}} + \rho_{\mathrm{NS}} + \rho_{\mathrm{WD}} + \rho_{\mathrm{MS}} = \rho(r)$, we may easily express the factor $C(r)$:

$$C(r) = (1-\alpha)(2-\alpha)\rho(r)/\{(1-\alpha)(m_{\mathrm{W}}^{2-\alpha} - m_{\mathrm{min}}^{2-\alpha}) + (2-\alpha)[(m_{\mathrm{max}}^{1-\alpha} - m_{\mathrm{B}}^{1-\alpha})m_{\mathrm{BH}} + (m_{\mathrm{B}}^{1-\alpha} - m_{\mathrm{N}}^{1-\alpha})m_{\mathrm{NS}} + (m_{\mathrm{N}}^{1-\alpha} - m_{\mathrm{W}}^{1-\alpha})m_{\mathrm{WD}})]\}\,. \tag{3.23}$$

To compute numbers of stellar remnants per a unit of volume, we integrate relation (3.17). For instance, the number density of neutron stars n_{NS} can be expressed in the following way:

$$n_{\mathrm{NS}}(r) = \frac{C(r)}{1-\alpha}(m_{\mathrm{B}}^{1-\alpha} - m_{\mathrm{N}}^{1-\alpha})\,. \tag{3.24}$$

In order to obtain the number of compact remnants within the core cluster, to which they migrated from the radius R_{gc} in 10 Gyr, we integrate the number density $n(r)$ from the tidal disruption radius R_{dis} to the corresponding radius R_{gc} obtained from (3.16) and plotted in Fig. 3.11. In general, the number of compact remnants (CR) in the core cluster may be estimated by

$$N_{\mathrm{CR}} = 4\pi \int_{R_{\mathrm{dis}}}^{R_{\mathrm{gc}}} n_{\mathrm{CR}}(r) r^2 \mathrm{d}r\,. \tag{3.25}$$

Mass density distribution. The first attempt to infer the mass density distribution $\rho = \rho(r)$ of stellar objects is from the deprojected brightness profile measurements. The basic assumption is that the mass follows the light, which may not be true for compact remnants and smaller bodies (brown dwarfs, planets, and asteroids).

Authors	r_b [pc]	γ	δ	γ_0
Do et al. (2013b)	$1.56^{+0.26}_{-0.25}$	$0.05^{+0.29}_{-0.60}$	$6.87^{+2.10}_{-2.65}$	$5.94^{+2.68}_{-2.11}$
	$1.53^{+0.28}_{-0.25}$	$0.16^{+0.25}_{-0.30}$	$6.83^{+2.08}_{-2.55}$	$5.88^{+2.68}_{-2.10}$
	$1.51^{+0.27}_{-0.24}$	$0.22^{+0.22}_{-0.30}$	$6.81^{+2.16}_{-2.62}$	$6.31^{+2.47}_{-2.19}$
Antonini & Perets (2012)	0.5	$0.5^{(\mathrm{i})}$, $1.8^{(\mathrm{ii})}$	2	1.8

Table 3.4: The parameters for the deprojected density profile. (i) corresponds to the observed distribution of stars, (ii) stands for a relaxed cusp.

The mass density profile for $r \lesssim 10\,\mathrm{pc}$ is modelled as power-law $\rho \propto r^{-\alpha}$, where $\alpha \approx 2$ from infrared observations (Becklin & Neugebauer 1968; Sanders & Lowinger 1972; McGinn et al. 1989). Bahcall & Wolf (1976, 1977) showed that a dynamically relaxed cluster of stars surrounding the black hole has a power-law density profile with the exponent $\alpha = 7/4$ and $\alpha = 3/2$ for equal mass and unequal mass stars, respectively. However, the steep Bahcall-Wolf cusp is not observed in the inner parsec of the Galactic centre.

The mass near Sgr A* is dominated by metal-rich old stellar population of spectral types M,K, and G (Merritt 2010). In the work of Buchholz et al. (2009), they find the core radius of $\sim 0.5\,\mathrm{pc}$ with a constant or even declining surface density of old stars. Moreover, they report the steep power law of young stars near the SMBH. Recently, Do et al. (2013b) confirm by analysing 3D kinematic observations of late-type stars that the surface density profile is shallower than expected for a dynamically relaxed cusp.

For the spatial density profile of stars near Sgr A*, it is, therefore, necessary to consider a broken power law (Lauer et al. 1995; Do et al. 2013b):

$$\rho(r) = \rho_0 \left(\frac{r}{r_\mathrm{b}}\right)^{-\gamma} \left[1 + \left(\frac{r}{r_\mathrm{b}}\right)^{\delta}\right]^{(\gamma-\gamma_0)/\delta} , \tag{3.26}$$

where the inner power law slope is expressed by γ, γ_0 stands for the outer slope, r_b is the break radius, and δ defines the sharpness of the transition between the two slopes.

The values of the parameters used for the estimates of the number of compact remnants are summarized in Table 3.4 and the corresponding profiles are plotted in Fig. 3.12.

While evaluating the integral (3.25). the upper bound R_gc is evaluated using the dynamical friction time-scale (3.16). For the lower bound, we take the tidal disruption radius R_dis estimated as (Hills 1975):

$$R_\mathrm{dis} \approx R_\star \left(\frac{M_\bullet}{M_\star}\right)^{1/3} , \tag{3.27}$$

where we plug in Solar values for the radius and mass, which leads to the value $r_\mathrm{dis} \approx 160\,R_\odot$. Although the tidal disruption radius may seem unreasonable for inspiralling stellar black holes, it approximately marks the radius where relativistic effects leading to black hole mergers take place.

In our calculations of stellar remnant numbers near the Galactic centre based on (3.25), we assume $m_\mathrm{min} = 0.1\,M_\odot$, $m_\mathrm{max} = 100\,M_\odot$, $m_\mathrm{WD} = 0.6\,M_\odot$, $m_\mathrm{NS} = 1.4\,M_\odot$, and $m_\mathrm{BH} = 7\,M_\odot$. All other parameters are varied. The mass density

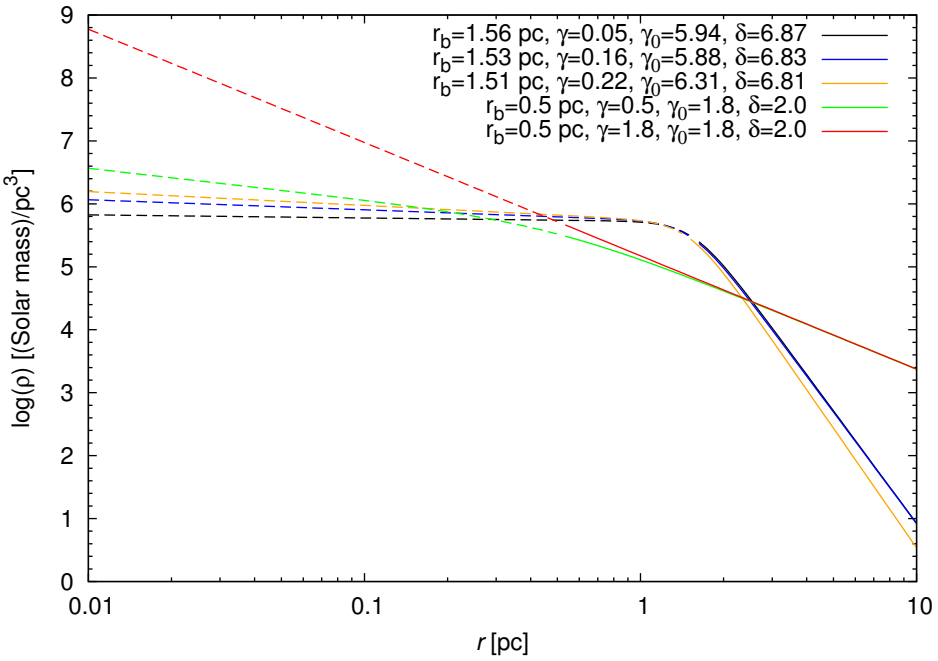

Figure 3.12: The mass density profiles for the parameters summarized in Table 3.4.

ρ_0 is varied in such a way that the dynamical mass within 1 pc is in the interval $(0.5, 1.5) \cdot 10^6\, M_\odot$ (Schödel et al. 2009).

α	$\rho_0\,[10^5\,\mathrm{M_\odot pc^{-3}}]$	$m_{\mathrm{min}}\,[M_\odot]$	$m_{\mathrm{W}}\,[M_\odot]$	$m_{\mathrm{N}}\,[M_\odot]$	$m_{\mathrm{B}}\,[M_\odot]$	$m_{\mathrm{max}}\,[M_\odot]$	r_{b} [pc]	γ	γ_0	δ	N_{WD}	N_{NS}	N_{BH}
2.30	3.0	0.1	1.0	8.0	25.0	100.0	1.56	0.05	5.94	6.87	502159	45461	18861
2.30	3.0	0.1	1.0	8.0	25.0	100.0	1.53	0.16	5.88	6.83	527009	46265	18495
2.30	3.0	0.1	1.0	8.0	25.0	100.0	1.51	0.22	6.31	6.81	536121	45626	16944
1.70	3.0	0.1	1.0	8.0	25.0	100.0	1.56	0.05	5.94	6.87	919141	250804	215547
1.70	3.0	0.1	1.0	8.0	25.0	100.0	1.53	0.16	5.88	6.83	964626	255235	211354
1.70	3.0	0.1	1.0	8.0	25.0	100.0	1.51	0.22	6.31	6.81	981305	251713	193636
0.45	3.0	0.1	1.0	8.0	25.0	100.0	1.56	0.05	5.94	6.87	110419	230467	955679
0.45	3.0	0.1	1.0	8.0	25.0	100.0	1.53	0.16	5.88	6.83	115883	234539	937089
0.45	3.0	0.1	1.0	8.0	25.0	100.0	1.51	0.22	6.31	6.81	117887	231302	858535
2.30	3.0	0.1	1.0	8.0	25.0	100.0	0.50	0.50	1.80	2.00	157515	12448	8000
2.30	3.0	0.1	1.0	8.0	25.0	100.0	0.50	0.50	1.80	2.00	157515	12448	8000
2.30	5.0	0.1	1.0	8.0	25.0	100.0	0.50	0.50	1.80	2.00	262525	20747	13334
2.30	7.0	0.1	1.0	8.0	25.0	100.0	0.50	0.50	1.80	2.00	367535	29046	18668
2.30	5.0	0.1	1.0	8.0	30.0	100.0	0.50	0.50	1.80	2.00	263467	22114	10000
2.30	5.0	0.1	1.0	8.0	40.0	100.0	0.50	0.50	1.80	2.00	264574	23722	6081
1.70	5.0	0.1	1.0	8.0	25.0	100.0	0.50	0.50	1.80	2.00	480520	114459	152379
0.45	5.0	0.1	1.0	8.0	25.0	100.0	0.50	0.50	1.80	2.00	57726	105177	675609
2.30	5.0	0.1	1.0	8.0	25.0	100.0	0.50	1.80	1.80	2.00	385692	28036	15372

Table 3.5: Number of compact remnants based on the radial mass density profile and the initial mass function.

Although the values depend strongly on the initial mass function, the number of neutron stars is always of the order 10^4 – 10^5 and not less than 10^3. The order of magnitude 10^5 is reached by decreasing the slope of the IMF from the standard Salpeter 2.3 (Salpeter 1955) to 1.7 and top-heavy IMF 0.45 (Morris 1993). We consider the configurations with the number of stellar black holes exceeding $\sim 5 \times 10^5$ improbable, since the total mass of the nuclear star cluster in the innermost parsec would be larger than the one based on the observations, $M_{1\,\mathrm{pc}} \simeq 1.5 \times 10^6\, M_\odot$ (Schödel et al. 2009; Fritz et al. 2013). After the exclusion of the estimates with the high abundance of stellar black holes the average number

of neutron stars computed from Table 3.2 is $N_{\rm NS} = 83\,000 \pm 26\,000$, which is higher than the previous estimate based on the total enclosed mass, not taking the actual density distribution into account, eq. (3.20). For further computations and analysis, we assume the conservative number of $10\,000 \pm 5000$ for neutron stars within 1 pc.

3.3 Observed pulsars near the Galactic centre

The main motivation for searching pulsars near the Galactic centre is their big potential for space-time mapping in the immediate vicinity of Sgr A*. Furthermore, an ensemble of observed pulsars would provide new insights into magneto-hydrodynamical properties of the medium within the inner parsec of the Galactic nucleus. These findings could be then extrapolated to other, mainly low-luminosity, nuclei.

Despite predictions based on the initial mass function and the mass segregation presented in the previous chapter, where the number of neutron stars is estimated to be of the order of $\sim 10^4$ in the inner parsec and even higher for a certain set of parameters, there have been only a few detections in the inner $\sim 15'$ and just one pulsar/magnetar in the inner $\sim 25''$, see Table 3.6 for their basic parameters and Fig. 3.8 for their position in P-$\dot{P}$ diagram (labelled as red points).

Object	Discoverer	P[s]	$\dot{P}$[ss^{-1}]	DM[pc cm^{-3}]	Spectral index α
J1745-2900	Rea et al. (2013)	3.7635537(2)	$6.61(4) \times 10^{-12}$	1750 ± 50	-
J1746-2850	Deneva et al. (2009)	1.0771014910(4)	$1.34311(2) \times 10^{-12}$	962.7(7)	-0.3
J1746-2849	Deneva et al. (2009)	1.478480373(2)	$1.27(6) \times 10^{-14}$	1456(3)	-1.1
J1745-2910	Deneva et al. (2009)	0.982	-	1088	-
J1745-2912	Johnston et al. (2006)	0.1873794(2)	-	1130(20)	-
J1746-2856	Johnston et al. (2006)	0.945224316(3)	$12.5(3) \times 10^{-15}$	1168(7)	-

Table 3.6: The list of detected pulsars in the inner $15'$ minutes of the Galactic centre region. The basic characteristics include period, period derivative, dispersion measure, and spectral index. The data is taken from discovery papers cited in the table.

There may be several explanations for the discrepancy between a predicted and observed number of neutron stars. Without going into technical details, it is important to realize that more distant regions in the Galactic plane are prone to interstellar scattering, which causes a one-sided broadening of the observed pulse profile with a frequency dependence of $\sim \nu^{-4.4}$ (Lorimer & Kramer 2004). In the Galactic disk, there is also a high background temperature that also results in decreasing the sensitivity of the instrument. In fact, the minimum detectable flux density $S_{\rm min}$ is proportional to the sum of background sky temperature, $T_{\rm sky}$, and system noise temperature, $T_{\rm sys}$. For a pulsar having period P, the following relation holds (Lorimer & Kramer 2004):

$$S_{\rm min} = \epsilon n_\sigma \frac{T_{\rm sys} + T_{\rm sky}}{G\sqrt{N_{\rm p}\Delta t \Delta\nu_{\rm MHz}}} \sqrt{\frac{W_{\rm e}}{P - W_{\rm e}}}\,{\rm mJy}\,, \tag{3.28}$$

where n_σ is the minimal signal-to-noise ratio S/N that is taken into account, G denotes the gain of the telescope (in K/Jy), Δt represents integration time (in

seconds), N_p stands for the number of polarizations, and $\Delta\nu_\mathrm{MHz}$ is the bandwidth (in MHz). The factor $\epsilon \sim 1.5$ stands for additional losses while reducing data. The effective pulse width W_e depends on the intrinsic pulse width W, the time resolution of the detection facility δt, the broadening of the pulse caused by the plasma environment – dispersion – δt_DM, and the broadening caused by inhomogeneities – scattering – δt_scatt,

$$W_\mathrm{e} = \sqrt{W^2 + \delta t^2 + \delta t_\mathrm{DM}^2 + \delta t_\mathrm{scatt}^2}\,. \tag{3.29}$$

By looking at Table 3.6, all of the detected pulsars have dispersion measures of the order of $\gtrsim 1000\,\mathrm{pc\,cm^{-3}}$. However, high dispersions can be dealt with by subdividing the observing bandwidth into many channels (mostly using a filterbank system), whereas scattering caused by inhomogeneities distorts the pulse in a way that cannot be properly treated. The only solution is to observe at higher frequencies, which has been also applied in case of the Galactic centre surveys (see e.g., Eatough et al., 2013b). Nonetheless, for high-frequency searches, the flux is lower (typically steep spectra, $S_\nu \propto \nu^{-1.7}$, Lorimer & Kramer, 2004) and the beam size also decreases. The latter may be solved by multibeam receivers and the former by selecting an optimum frequency so that we get a sufficient signal-to-noise ratio on one hand and a low scatter-broadening on the other.

The lack of observed pulsars in the Galactic centre region may be explained by the following hypotheses:

(a) low sensitivity of current instruments,

(b) natural processes that lead to the depletion of the neutron star population near the Galactic centre (e.g., big natal kicks, disruptions of binaries resulting in hypervelocity, escaping neutron stars),

(c) most neutron stars in the Galactic centre are old and isolated with a decayed magnetic field ($B \approx 10^9\,\mathrm{G}$). They are located beyond death lines (see Fig. 3.8) and thus inactive. However, they can slowly accrete the denser ISM material near the Galactic centre and contribute to the diffuse X-ray emission (2.5–7 keV) (possible observational effects studied by Ostriker et al., 1970; Zane et al.; 1996).

The true explanation why the currently observed population is small may be, of course, a combination of these hypotheses. The reason (a) should be weakened by future observational facilities, e.g. Square Kilometre Array (SKA), whereas (b) and (c) are probably valid for a smaller or a larger fraction of the Galactic centre neutron star population.

3.4 Interaction with gaseous medium near Sgr A*

3.4.1 Collisions with a single cloud

First, we consider the uniform density distribution of neutron stars within 1 pc. With the assumed number of 10 000, this leads to $n_\mathrm{NS} \approx 2400\,\mathrm{pc^{-3}}$. When we assume the G2/DSO radius of the order $R_\mathrm{cloud} = 10^{-3}\,\mathrm{pc}$, there may be as many as $N_\mathrm{NS} = 4/3\pi R_\mathrm{cloud}^3 n_\mathrm{NS} = 10^{-5}$ neutron stars at any time. For the mean number

of encounters from the apocentre to pericentre[2], we need to evaluate the integral (e.g., Bartos et al., 2013):

$$\langle N_{\rm NS}\rangle \approx \int_S n_{\rm NS}(r)\sigma_{\rm cloud}v_{NS}(r){\rm d}t\,, \tag{3.30}$$

where $\sigma_{\rm cloud} \approx \pi R_{\rm cloud}^2 \approx 10^{-6}\,{\rm pc}^2$ is the cross-section of the cloud, $v_{\rm NS}(r) = (GM_\bullet/r)^{1/2}$ is the circular velocity of a neutron star at the distance r and ${\rm d}t$ is the time interval between r and $r + {\rm d}r$.

In comparison with Bartos et al. (2013) and other previous works, we assume the uniform distribution of neutron stars in the innermost parsec. This assumption may be plausible in case of Sgr A, since the observed mass density distribution is flatter than expected for a relaxed Bahcall-Wolf cusp and the dynamical friction for neutron stars is not so large as for stellar black holes since their mass is comparable to the field stars.

Using (3.30) and assuming uniform distribution yielding $(10\,000 \pm 5\,000)$ neutron stars in the inner parsec, we calculate

$$\langle N_{\rm NS}\rangle = (5.6 \pm 2.8) \times 10^{-4}.$$

For the uniform distribution, the probability of encounter of an infalling cloud with a neutron star is low.

Second, we assume the density distribution that falls off with the distance from the Galactic centre as $\sim r^{-3/2}$ (Pfahl & Loeb 2004). For the already assumed number of neutron stars $N_{\rm NS} \approx 10\,000$ in the inner parsec, we get the distribution:

$$n(r) = \frac{3}{8\pi}N_{\rm NS}\left(\frac{r}{1{\rm pc}}\right)^{-3/2}\,{\rm pc}^{-3}. \tag{3.31}$$

For this dependence, the mean number of encounters rises significantly during the infall, but it is still below one:

$$\langle N_{\rm NS}\rangle = 0.3^{+0.2}_{-0.1}.$$

For an optimistic estimate of the number of neutron stars (1000 within 0.017 pc, Pfahl & Loeb, 2004) and the distribution according to (3.31), we get $\langle N_{\rm NS}\rangle \approx 35$ encounters, most of them close to the pericentre, as is also evident in Fig. 3.13. In this figure, we also compare the mean number of cloud – neutron star encounters for a different total number of neutron stars in the inner parsec as well as different distributions. In case of a uniform distribution, the mean number of encounters stays low (< 1) even for the largest number.

In Fig. 3.14, we illustrate the number of neutron stars that are inside the cloud with radius $R_{\rm cloud} = 10^{-3}\,{\rm pc}$. In this case we use the Pfahl & Loeb distribution (3.31) with $N_{\rm NS} = 10^5$.

[2]In this case, we do not take into account the post-pericentre evolution, since the cross-section of the cloud changes and its semi-major axis and eccentricity are expected to decrease.

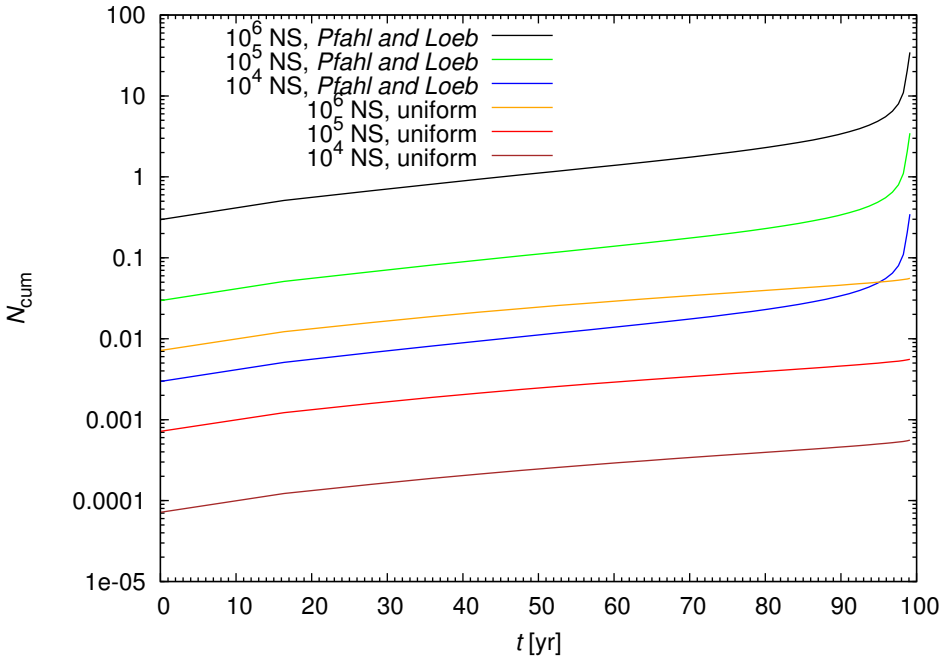

Figure 3.13: The total number of encounters as a function of time - case of G2/DSO from the apocentre ($t = 0.0\,\mathrm{yr}$) to the pericentre ($t = 99\,\mathrm{yr}$); orbital elements adopted from (Gillessen et al. 2012). In case of Pfahl & Loeb distribution (3.31) we see a rapid increase near the pericentre. For the uniform distribution, the mean number of encounters stays low (< 1) even for a large number of neutron stars in the inner parsec.

Mapping the Minimal Orbit Intersection Distance (MOID) for an infalling extended object. Besides the number density distribution (uniform or distance-dependent) and the total number of neutron stars in the core population, one should also determine the distribution of orbital elements of neutron stars that collide with an eccentric cloud that falls toward the Galactic centre.

For this purpose, we adopt the method similar to de la Fuente Marcos & de la Fuente Marcos (2013) and develop a Monte Carlo code based on it. We do not make any special assumptions on the distribution of neutron stars. They are distributed uniformly in the space of orbital elements, specifically having a uniform distribution of semi-major axes $a \in (2.0 \times 10^{-4}\,\mathrm{pc} \approx 40\,\mathrm{AU}, 0.5\,\mathrm{pc} \approx 100000\,\mathrm{AU})$, eccentricities $e \in (0.0, 0.99)$, inclinations $i \in (0°, 180°)$, longitudes of ascending node $\Omega \in (0°, 360°)$, and arguments of pericentre $\omega \in (0°, 360°)$. The motion of each neutron star is assumed to be Keplerian around the SMBH ($\approx 4 \times 10^6\,M_\odot$), not taking into account the influence of other bodies. While this approach may seem simplistic, one should realize that we are only interested in the statistics of possible interactions. Furthermore, the region of our interest is within the sphere of influence of the SMBH, whose radius $r_\mathrm{h} = GM_\bullet/\sigma_\star^2 \approx 2\,\mathrm{pc}$ ($\sigma_\star \approx 100\,\mathrm{kms}^{-1}$ is the estimated velocity dispersion of stars in the nuclear star cluster), and therefore the perturbations caused by other bodies are small on the time-scale of the order of 100 yr we consider here.

In our runs, we compute the distance of every neutron star from an infalling spherical object, presumably a cloud or a star with an extended gaseous envelope,

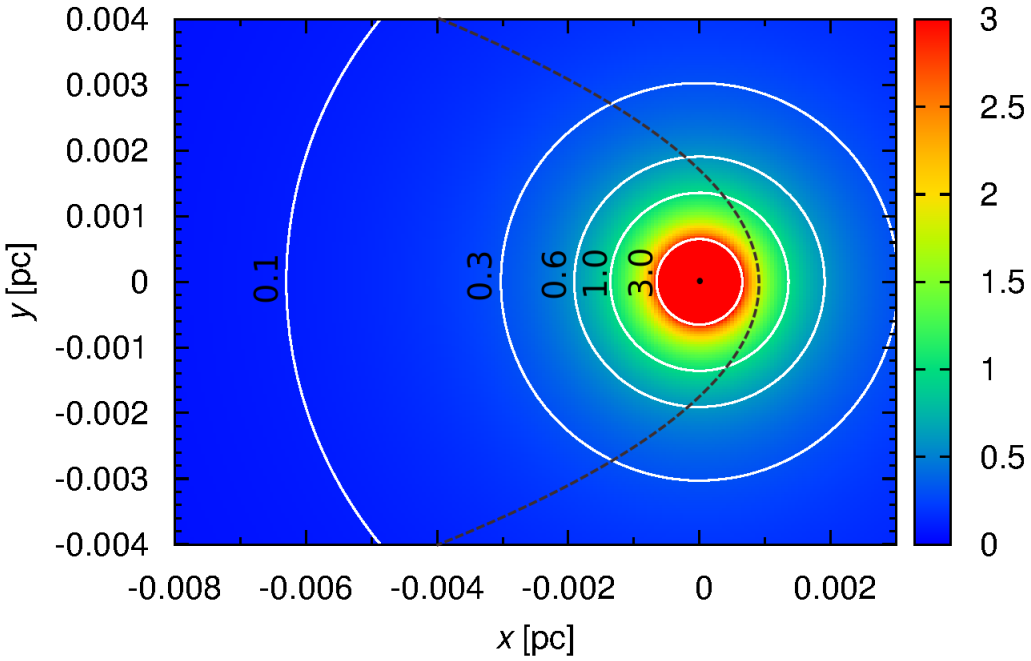

Figure 3.14: The number of neutron stars inside a spherical cloud moving on an elliptical trajectory. The distribution of neutron stars is according to Pfahl & Loeb (2004) (see Eq. (3.31)) with $N_{\rm NS} = 10^5$.

having the radius $R_{\rm o}$. We are looking for the MOID, which is determined in our model according to the tidal interaction that is thought to be of a high significance for distances $r_{\rm rel} \leq 3R_{\rm o}$ and the penetrating encounters are for $r_{\rm rel} \lesssim R_{\rm o}$.

The target object is approximated as a homogeneous sphere having the radius of $R_{\rm o} = 100\,{\rm AU}$ and it is assumed not to change its shape during the infall. This simplification may influence our statistics near the pericentre. In case of the cloud, both tidal stretching and hydrodynamic effects may be more profound due to an increasing density of ambient medium towards the centre. It is thought that the tidal stretching of the cloud just influences the character of the encounter. For instance, if the cloud is tidally stretched, some encounters may be closer in comparison with our model and vice versa. The number of encounters should not be influenced much, since the volume does not change significantly by stretching. Strong hydrodynamics effects may influence our statistics much more since the cloud may be dissolved after the pericentre passage and/or it may change its trajectory and inspiral towards the SMBH. In case of a mass-losing star embedded in a gaseous-dusty envelope, this approach may be valid even after the pericentre passage, provided that it does not change orbit significantly and maintains an extended envelope.

Keeping these caveats in mind, we check the MOID along the whole orbit of an extended object. In case of the gaseous clump, only the part of the trajectory from the apocentre to the pericentre is reasonable in this approximation due

to hydrodynamic affects that are expected to affect the orbital evolution in the post-pericentre phase. The entire orbit mapping may be, however, well-suited for a star with an extended outflowing envelope and/or a gaseous-dusty shell, as was discussed above. The statistics of random encounters of neutron stars with a circum-stellar matter was not discussed in-depth in the literature. In the disk population, such events are rare. However, close to the Galactic centre, penetrating encounters may be more frequent and thus worth considering.

The orbital elements of the extended object moving on a highly eccentric trajectory are adopted from Phifer et al. (2013) and Gillessen et al. (2013a). They were inferred from observations of Brγ emission and L'-band observations of the current passage of G2/DSO, respectively. The eccentricity of the nominal trajectory is ~ 0.9814 and ~ 0.9664, period ~ 276 and ~ 198 years, and semi-major axis $\sim 6807\,\mathrm{AU}$ and $\sim 5495\,\mathrm{AU}$ with the pericentre distance of $\sim 127\,\mathrm{AU}$ and ~ 185, respectively. In our analysis, we take $(i, \Omega, \omega) = (0, 0, 0)$ for the nominal trajectory. The number of objects that are uniformly distributed in the space of orbital elements is 15×10^6.

In Fig. 3.15 we plot the distribution of the orbital elements of interacting bodies only for L'-band data, since the results are qualitatively the same for the orbit with a higher eccentricity. The true anomaly of the target object and relative velocities as functions of semi-major axes of interacting bodies are plotted in Fig. 3.16.

By looking at plots in Figs. 3.15 and 3.16, we see features determined mostly by the high eccentricity of the orbit. We see in ai-plane that colliding objects have rather lower prograde or retrograte orbits with respect to the trajectory of the cloud: we see cumulations of inclinations for $i \in (0, 20)^\circ$ and $i \in (160, 180)^\circ$. In case of $a\omega$ plane, there is no such clumping and the distribution is approximately uniform for the argument of pericentre. Some clustering is apparent for the length of ascending node in $a\Omega$ plane. The plot of true anomaly versus semi-major axis, Fig. 3.16, shows that there are some direct hits (red, orange, green points). It is also clear from this figure that some objects move close to the cloud and/or penetrate it for a large span of the true anomaly ($\sim 100^\circ$), so tidal distortion of the cloud would take place in such a case. The plot of relative velocities versus semi-major axis, Fig. 3.16, shows that relative velocities are mostly higher than $\sim 1000\,\mathrm{km\,s^{-1}}$, reaching even several $10\,000\,\mathrm{km\,s^{-1}}$, and smaller than $\sim 10^5\,\mathrm{km\,s^{-1}}$. There are rare cases with lower velocities than $\sim 1000\,\mathrm{km\,s^{-1}}$, indicating a small potential for the gas to accrete onto neutron star and cause an observable flare in X-ray wavelengths.

Furthermore, we plot the temporal evolution of the relative number of direct hits, computed as the ratio between interactions with MOID $\leq R_0$ classified as direct (interacting with the gaseous envelope) and all close interactions with MOID $\leq 3R_0$. The plots are in Fig. 3.17. In both plots, the relative number fluctuates from ~ 0 to as much as $\sim 0.20 - 0.25$ meaning that approximately one fourth and fifth of interacting bodies directly hits the gaseous clump. Near the pericentre there is a peak of the relative number of direct hits with respect to immediate pre-pericentre and post-pericentre evolution, which is larger for the orbit with a higher eccentricity.

We also plot the temporal evolution of the relative velocity of interacting bodies (with respect to the target) for both all encounters (with MOID $\leq 3R_0$)

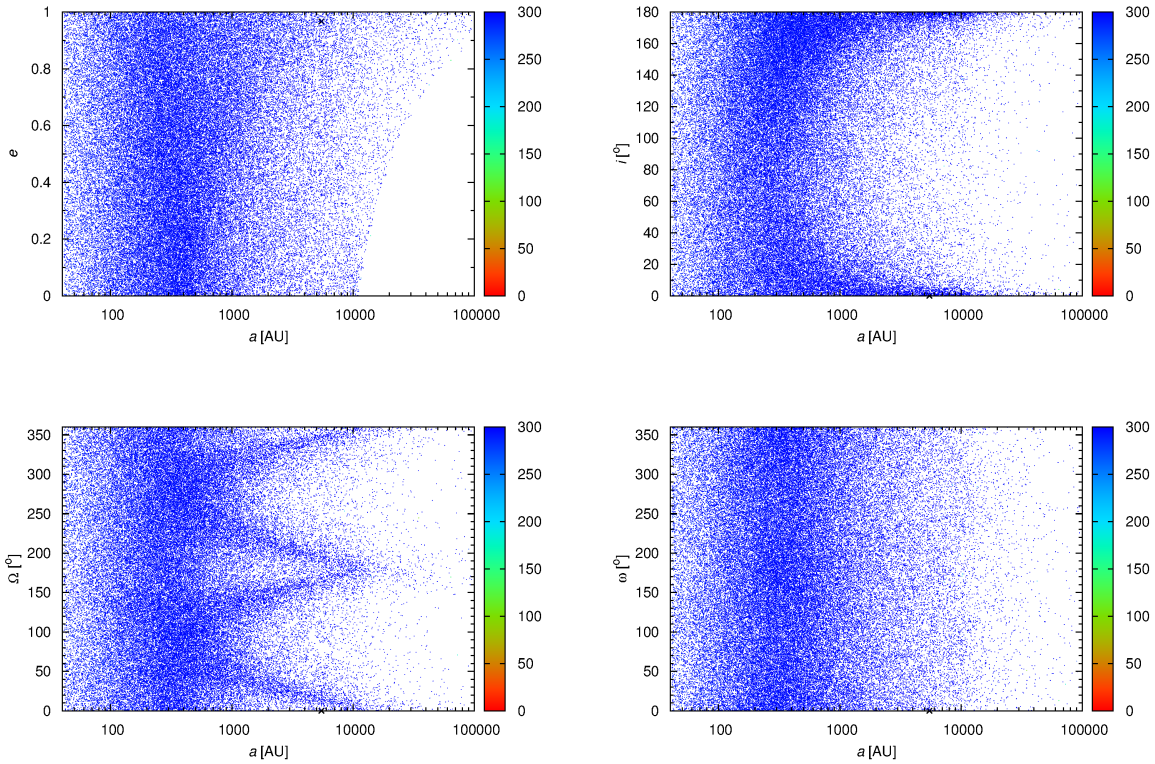

Figure 3.15: The plots of the eccentricity, the inclination, the length of ascending node, and the argument of pericentre as functions of semi-major axis for neutron stars interacting with the extended object moving on a highly eccentric trajectory with the MOID $\leq 3R_{\rm o}$. The MOID in AU is colour-coded according to the colour bar.

and for direct hits (MOID $\leq R_0$), see Fig. 3.18. The velocities are averaged over the time-step of the simulation, which is 0.01 yr The relative velocities are naturally the highest around the pericentre passage, $\sim 10^4\,{\rm km\,s^{-1}}$, for both a smaller and a higher eccentricity trajectory.

Estimates of accretion luminosity. In case of direct passages through the cloud or the gaseous envelope, we also estimate the bolometric accretion luminosity for neutron stars that have magnetic field small enough for the accretion flow not to be halted. We refer to such neutron stars as non-magnetized and they are frequently associated with old, isolated neutron stars beyond death lines, see Fig. 3.8. For the purpose of the estimate of accretion luminosity, we use the analytical Bondi-Hoyle-Lyttleton solution for the cylindrical accretion of stars propagating though the interstellar medium. The accretion rate for the star moving at velocity $v_\star$ with respect to the ISM having the density of $\rho_{\rm m}$ is given by (e.g., Lipunov,1992):

$$\dot{M}_{\rm BHL} = \eta 4\pi \frac{(GM_{\rm NS})^2}{(v_\star^2 + c_{\rm s}^2)^{3/2}} \rho_{\rm m}\,, \tag{3.32}$$

where $c_{\rm s}$ is the speed of sound in the cloud, $v_\star$ is the velocity of the star with respect to the medium, $M_{\rm NS}$ is the mass of the neutron star (we take $M_{\rm NS} =$

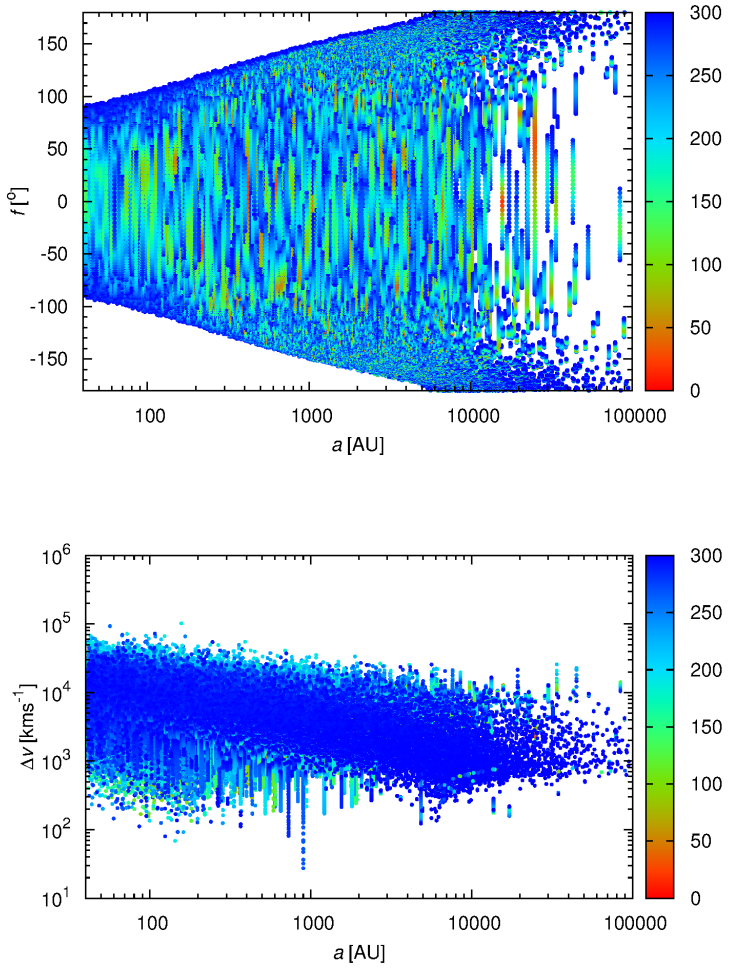

Figure 3.16: The plots of the true anomaly f of the target object (*Top panel*) and relative velocities Δv (*Bottom panel*) as functions of semi-major axis of interacting bodies. The MOID in AU is colour-coded according to the colour bar.

$1.4\,M_\odot$), and η is a dimensionless factor of the order of unity (we take $\eta = 1$). An important parameter is the velocity of the sound in the medium. To get an estimate, we adopt the initial density value of the G2 cloud from simulations of Schartmann et al. (2012), $\rho_\mathrm{m} \approx 10^{-18}\,\mathrm{g\,cm^{-3}}$. Concerning the temperature of the medium, it is thought that the ionized gas is in ionization equilibrium with the radiation field of nearby massive OB stars, which sets the temperature to $T \approx 10^4\,\mathrm{K}$. We assume that the gas is ideal, which yields the following estimate of the speed of sound:

$$c_\mathrm{s} = \left(\frac{\gamma P}{\rho}\right)^{1/2} = \left(\frac{\gamma kT}{\mu m_\mathrm{u}}\right)^{1/2} \approx 9\,\mathrm{km\,s^{-1}}\,, \tag{3.33}$$

where we set the adiabatic index γ as well as the relative atomic mass μ equal to one, assuming that it is composed primarily of hydrogen. We see in Fig. 3.18 that direct hits are supersonic, specifically from one to three orders of magnitude larger than the expected speed of sound in ionized hydrogen cloud/envelope. In

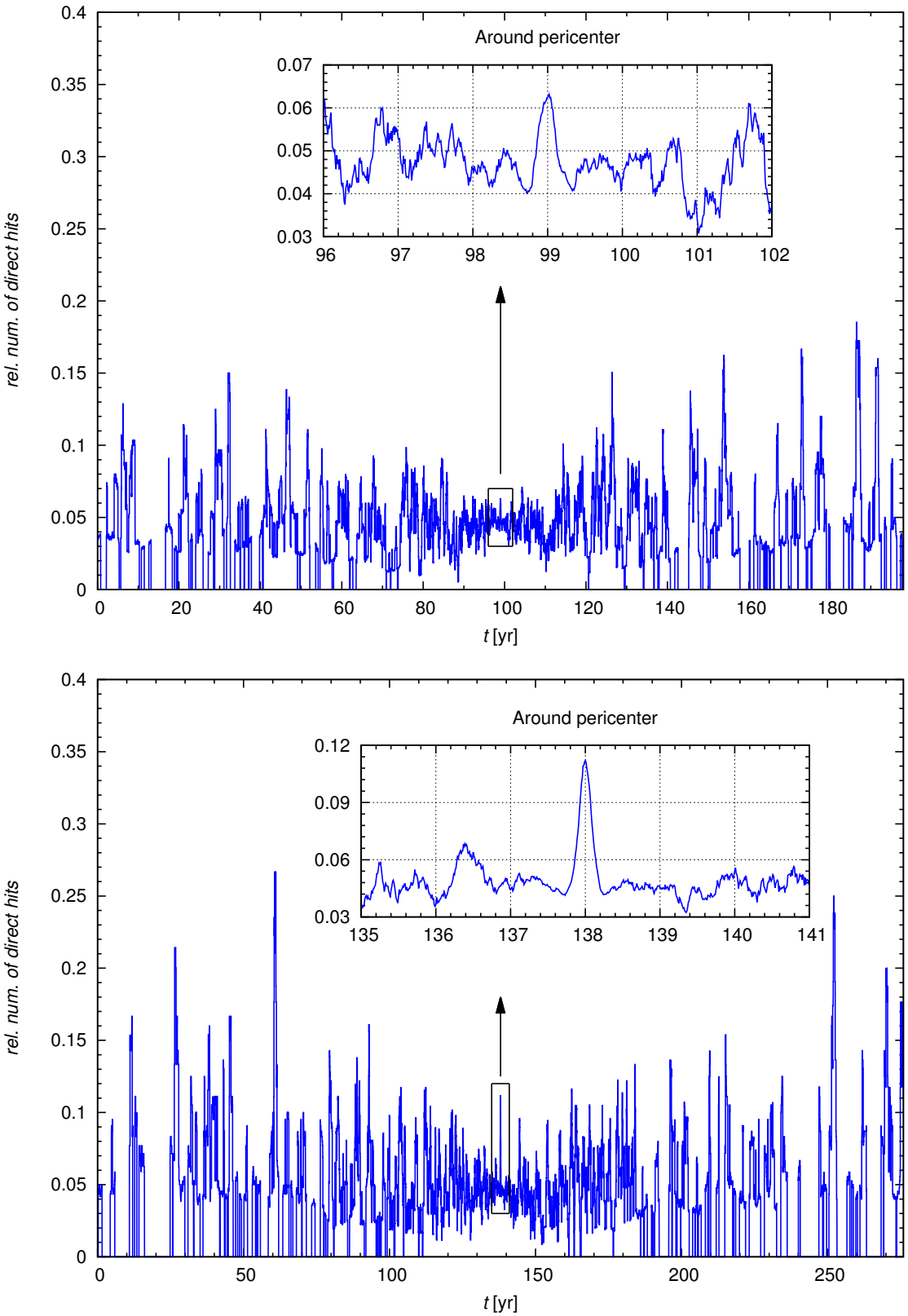

Figure 3.17: (*Top panel*) The temporal evolution of the relative number of direct hits for a lower eccentricity and semi-major axis, ~ 0.9664 and $\sim 5495\,\mathrm{AU}$, respectively. The time around pericentre passage, which is of interest, is in a magnified subplot (pericentre passage at 99 yr). (*Bottom panel*) The same evolution for a higher eccentricity and semi-major axis, ~ 0.9814 and $\sim 6807\,\mathrm{AU}$, respectively (pericentre at 138 yr).

most cases, the speed of sound may be neglected in (3.32). However, we we will keep this term in our computations since there are some rare occasions when $v_\star \lesssim 100\,\mathrm{km\,s^{-1}}$. It is also significant to compare gravitational capture radius $R_\mathrm{G} = 2GM_\mathrm{NS}/(v_\star^2+c_\mathrm{s}^2)$, which characterizes the range of gravitational interaction, and the typical radius of a neutron star $R_\mathrm{NS} \approx 10\,\mathrm{km}$. The gravitational capture radius becomes equal to neutron star radius R_NS at velocities:

$$v_\star = \left(\frac{2GM_\mathrm{NS}}{R_\mathrm{NS}} - c_\mathrm{s}^2\right)^{1/2} \approx 200\,000\mathrm{km\,s^{-1}}\,.$$

Above these velocities, gravitational capture radius becomes smaller than the radius of neutron star. Therefore this regime (Eddington accretion) may be effectively described by:

$$\dot{M}_\mathrm{E} = \pi R_\mathrm{NS}^2 \rho_\mathrm{m} v_\star\,. \tag{3.34}$$

On the other hand, there may be a hypothetical situation when the neutron star is embedded in a gaseous envelope and co-moves with it, so $v_\star = 0\,\mathrm{km\,s^{-1}}$. We stress again that in this analysis we neglect the effect of the magnetic field. The spherical Bondi accretion would then take place. It is described by the formula (e.g., Lipunov,1992):

$$\dot{M}_\mathrm{B} = 4\pi \left(\frac{2}{5-3\gamma}\right)^{(5-3\gamma)/[(2(\gamma-1)]} \frac{(GM_\mathrm{NS})^2}{c_\mathrm{s}^3}\rho_\mathrm{m}\,, \tag{3.35}$$

where the adiabatic index $\gamma \in (1, 5/3)$ and we set the whole dimensionless factor equal to one, which is the value of the limit $\gamma \to 5/3$. The Bondi-Hoyle-Lyttleton regime describes the spherical Bondi accretion for subsonic velocities of stars with respect to the gaseous medium ($v_\star < c_\mathrm{s}$).

Finally, we compute the bolometric luminosities across the large range of velocities ($v_\star \in (0, 10^5)\,\mathrm{km\,s^{-1}}$) for interactions of non-magnetized neutron stars with the cloud or envelope structure. The luminosity is computed $L_\mathrm{acc} = \eta_\mathrm{acc}\dot{M}c^2$, where $\eta_\mathrm{acc} = 1/2 \times R_\mathrm{s}/R_\mathrm{NS} \approx 0.1 \to 10\%$ for the Schwarzschild radius of approximately 3 km. The luminosity as a function of velocities of interacting stars is in Fig. 3.19.

Looking at Fig. 3.19, we see that the accretion luminosity in the subsonic regime is far above the Solar luminosity, specifically by five orders of magnitude. In the supersonic regime, the luminosity starts decreasing according to eq. (3.32) as $L_\mathrm{acc} \propto v_\star^{-3}$ and reaches the Solar luminosity at about $\sim 217\,\mathrm{km\,s^{-1}}$ and continues decreasing. At $\sim 193\,000\,\mathrm{km\,s^{-1}}$, the trend reverses and the luminosity increases linearly with the velocity, because the gravitational capture radius is effectively replaced by the radius of neutron star.

Finally, using the relations and parameters described above, we use the relative interaction velocities for direct hits (see Fig. 3.18) to compute accretion luminosities. The results for both smaller- and higher-eccentricity orbits of clouds are in Fig. 3.20.

In general, the bolometric accretion luminosities are the smallest around and at the pericentre, about three and four orders of magnitude smaller than the Solar luminosity ($\sim 10^{29}\,\mathrm{erg\,s^{-1}}$ and $\sim 10^{28}\,\mathrm{erg\,s^{-1}}$ for the smaller and the higher eccentricity, respectively) . This is simply explained by the highest velocities of

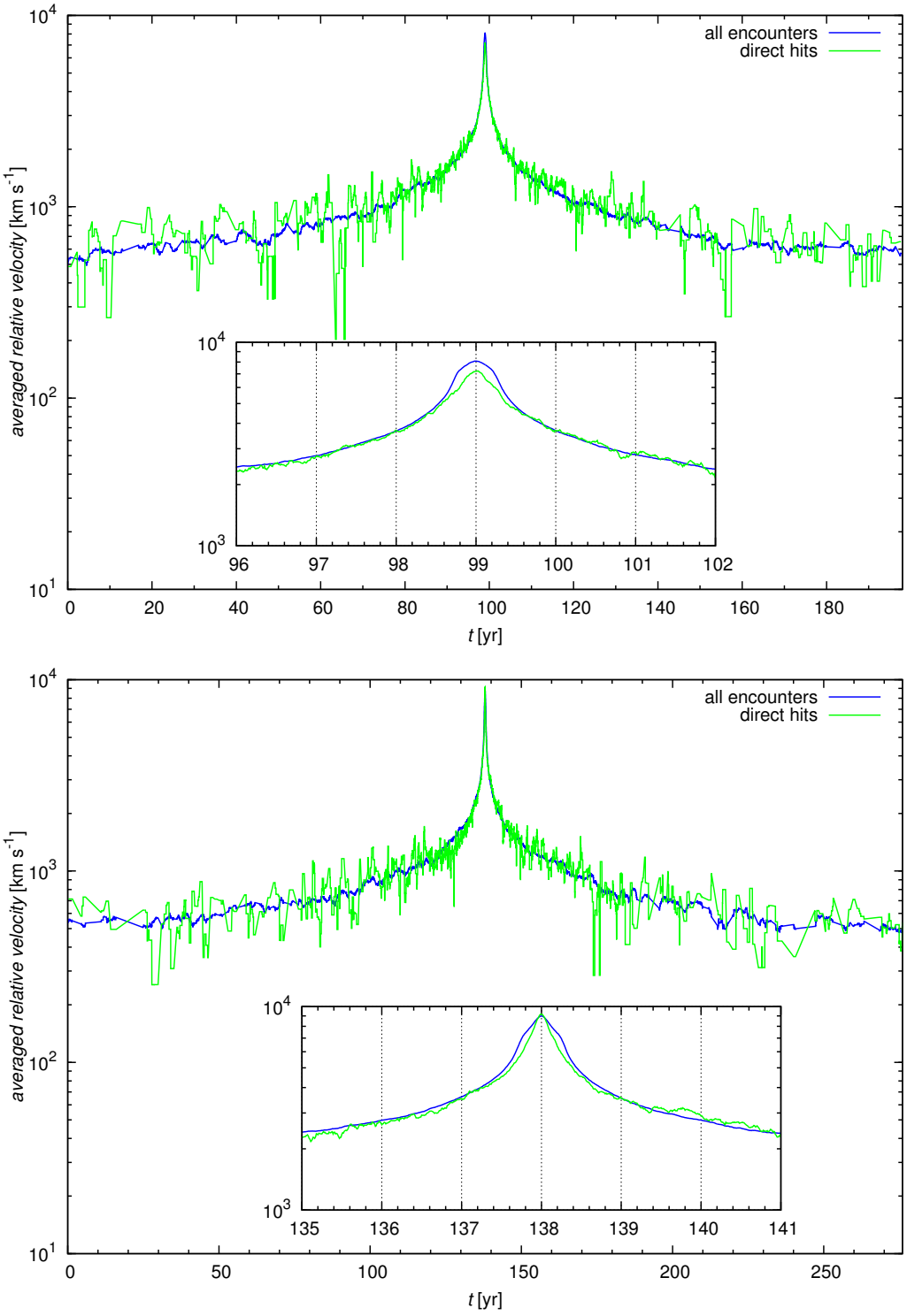

Figure 3.18: (*Top panel*) The temporal evolution of the relative velocities of interacting bodies for the orbit with a lower eccentricity and semi-major axis, ~ 0.9664 and $\sim 5495\,\mathrm{AU}$, respectively. The time around pericentre passage, which is of interest, is in a magnified subplot. The velocities are averaged over $0.01\,\mathrm{yr}$. Two cases are distinguished: all encounters (blue line) and direct hits (green). (*Bottom panel*) The same evolution for a higher eccentricity and semi-major axis, ~ 0.9814 and $\sim 6807\,\mathrm{AU}$, respectively.

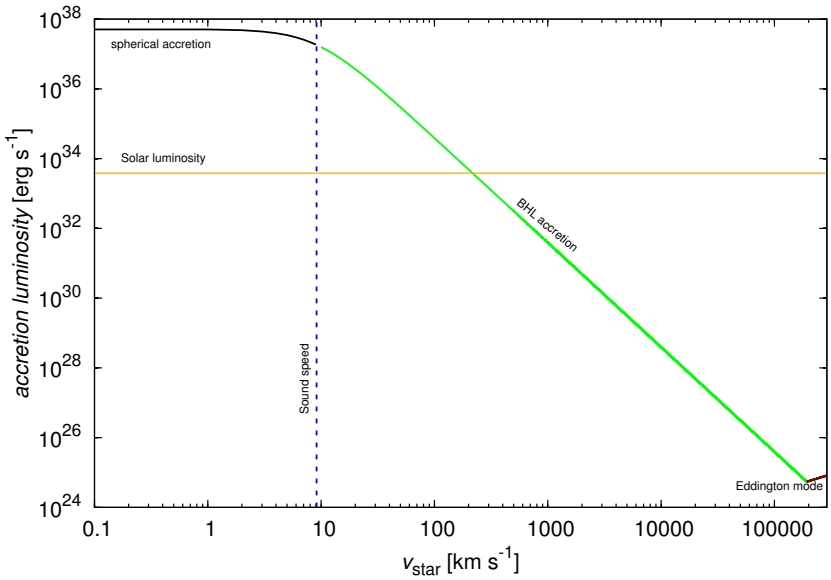

Figure 3.19: The bolometric accretion luminosity caused by the capture of cloud/envelope material by colliding non-magnetized neutron stars. The accretion modes change as the velocity increases. For velocities smaller than the sound speed in the cloud, spherical (Bondi) accretion takes place. For supersonic velocities, cylindrical (Bondi-Hoyle-Lyttleton) regime is established. In case of very high, relativistic velocities ($\approx 200\,000\,\mathrm{km\,s^{-1}}$), the effective gravitational capture radius is smaller than the radius of the neutron star (Eddington accretion).

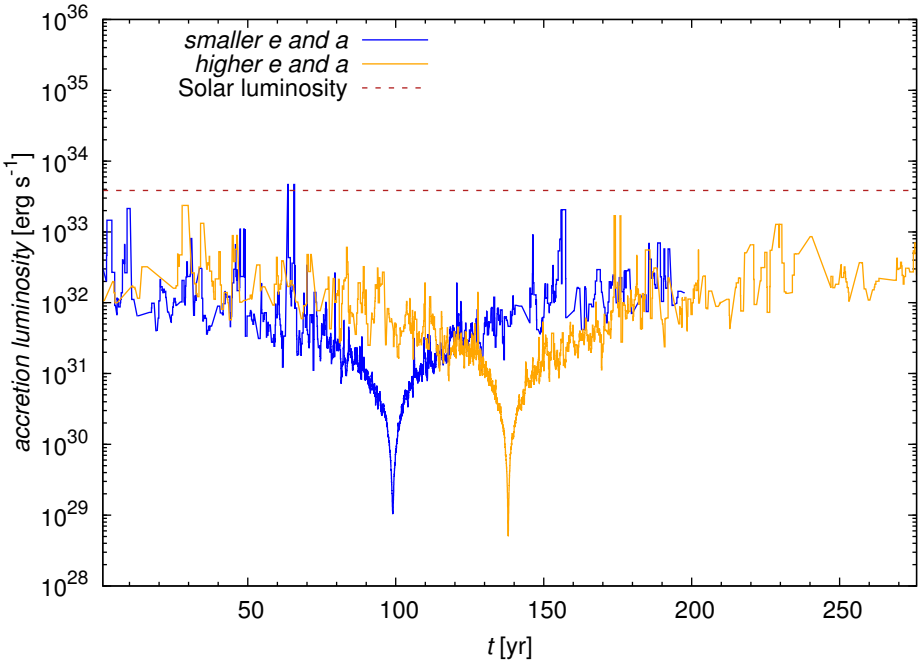

Figure 3.20: The temporal evolution of the bolometric accretion luminosity for averaged relative velocities of neutron stars in case of direct hits. The cases for smaller (blue) as well as higher (orange) eccentricity and semi-major axis are included for comparison.

eccentric clouds and neutron stars and hence, the highest relative velocities of interacting bodies (see Fig. 3.18). The accretion luminosities for the higher-eccentricity orbit are smaller during the pericentre passage for the same reason. At higher true anomalies (closer to the apocentre of the orbit), the luminosities are larger than at the pericentre, on average by two–three orders of magnitude ($\sim 10^{32}\,\mathrm{erg\,s^{-1}}$). There are some rare occasions when the Solar luminosity is reached and even exceeded, implying the relative velocities of interacting bodies around $\lesssim 200\,\mathrm{km\,s^{-1}}$.

3.4.2 Collisions with the 'Minispiral' – Sgr A West

Beyond the 'S'-cluster, denser HII regions may be observed in radio – see chapter 2 – as well as infrared wavebands. Stars are witnessed to interact with this medium, producing cavities, bow-shock structures where the ram pressures of the stellar wind as well as that of the surrounding medium are at balance (e.g., supergiants IRS7, IRS8, IRS9W, see Zhao et al., 2009; Zhao et al., 2010; comet-shaped bow-shock sources X3 and X7, Mužić et al., 2010). It is therefore plausible that members of the Galactic centre neutron star population also interact in different ways with the complex 'Minispiral' medium.

The gaseous material of the 'Minispiral' is mainly contained in three arms - the Nothern Arm, the Eastern Arm, and the Western Arc. We model it as an ensemble of spherical clumps moving along three bundles of Keplerian orbits, see Fig. 3.21. This simplification is justified by good agreement of observed radial velocities with those inferred from the Keplerian model (Zhao et al. 2009, 2010), although there are some deviations that are probably caused by the interaction of the 'Minispiral' with the winds of massive OB stars and other magnetohydrodynamical effects.

Collisions with the 'Minispiral' – geometrical approach. We map the orbital elements as well as relative velocities of colliding neutron stars with spherical clumps distributed along the three arms of the 'Minispiral', see Fig. 3.21. Each gaseous clump is assumed to have a radius of $0.04\,\mathrm{pc} \approx 1''$, which is a typical scale of observed structures in Sgr A West. Both neutron stars and the clumps are assumed to move on Keplerian orbits in the central potential of the Sgr A* SMBH and their orbital elements do not change during the simulation. This simplification is sufficient for a statistical description of interactions. Moreover, orbits of stars in the central parsec are well described by Keplerian orbits. This is also valid for the motion of the individual 'Minispiral' arms. There are deviations from the Keplerian motion that are larger for more distant orbits. In case of the 'Minispiral' arms, the deviations are caused by magnetohydrodynamical interaction with the surrounding medium.

We distribute 100 000 neutron stars uniformly in the space of orbital elements: $a \in (0.05, 1.00)\,\mathrm{pc}$, $e \in (0, 1)$, $i \in (0°, 180°)$, $\omega \in (0°, 360°)$, and $\Omega \in (0°, 360°)$. The 'Minispiral' is represented by 64 spherical clumps that are distributed along the individual arms in the following way:

- *Northern Arm*: 22 clumps; true anomalies range: $\phi \in (-168, 112)°$,
- *Eastern Arm*: 19 clumps; true anomalies range: $\phi \in (-101, 6)°$,

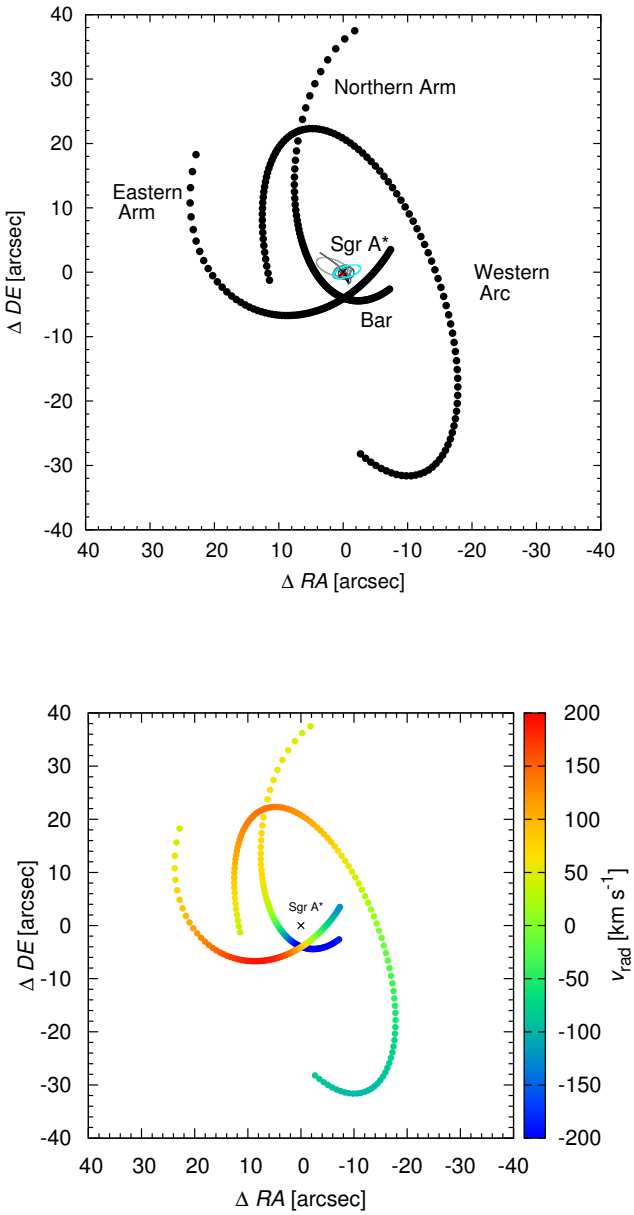

Figure 3.21: Keplerian model of the 'Minispiral': (*Top panel*) Four basic parts: the Northern Arm, the Eastern Arm, the Western Arc, and the Bar. Compact radio source Sgr A* is at the origin surrounded by 'S'-cluster. See 3-mm Fig. 2.7 for comparison. (*Bottom panel*) Radial velocity plot of the three arms; color bar units are in km/s.

- *Western Arc*: 23 clumps; true anomalies range: $\phi \in (-249, 44)^\circ$.

We flag the collisions when a neutron star is 0.04 pc or less from the centre of the clump. We let the system evolve for 1000 years to get enough points for colliding bodies in the space of orbital elements as well as their relative velocities. The time-step is 0.1 yr. Out of 100 000 neutron stars, the average number of collisions/interactions per unit of time is 1078 ± 125, so the probability of interactions is ≈ 0.01, which for conservative estimates of the number of neutron stars, $\sim 10\,000$, yields ≈ 100 interactions. About 1/10 out of the total number of neutron stars are expected to be pulsars beaming towards the Earth (Wharton

et al. 2012); hence $\approx$ 10 pulsars should interact with the 'Minispiral' gaseous environment.

The distribution of the orbital elements of colliding bodies is plotted in Fig. 3.22. We distinguish collisions with individual arms by colour: the Northern Arm (red), the Eastern Arm (green), and the Western Arc (blue). In general, the distribution of orbital elements covers a broad range. Colliding neutron stars have semi-major axes greater than 0.1 pc. The smallest semi-major axes have those neutron stars that collide with the Northern Arm, followed by bodies interacting with the Eastern Arm, and the largest semi-major axes have the ones colliding with the Western Arc. Concerning eccentricities, all values in the range $(0, 1)$ are represented, with the distribution in ae plane being narrower for smaller values of eccentricities, $e \lesssim 0.2$. Inclinations as well as arguments of pericentre are distributed uniformly. In case of the longitude of the ascending node Ω, the colliding objects with Ω close to the ascending or the descending node of individual 'Minispiral' arms prevail: for the Northern arm, $\Omega \approx 64°$ or $\Omega \approx 244°$, in case of the Eastern Arm, $\Omega \approx 138°$ or $\Omega \approx 318°$, and for the Western Arc, $\Omega \approx 71°$ or $\Omega \approx 251°$.

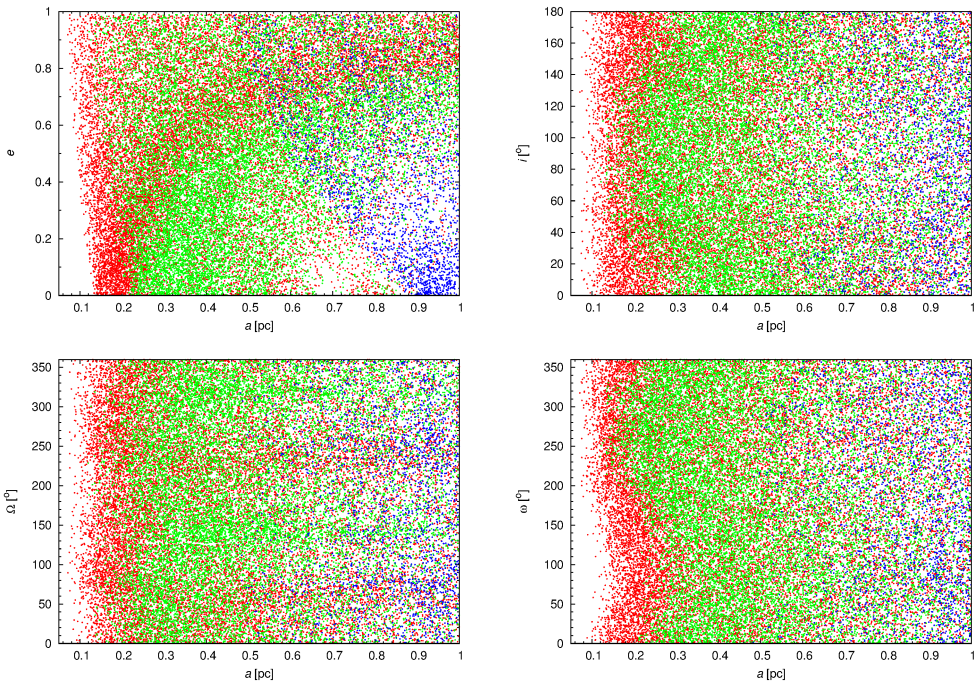

Figure 3.22: Distribution of the orbital elements of colliding bodies, from upper left to bottom right: (a, e), (a, i), (a, Ω), and (a, ω). Collisions with individual arms are distinguished in the following way: red points correspond to the Northern Arm, green points to the Eastern Arm, and blue points to the Western Arc.

We also monitor the relative velocities $v_\star$ of neutron stars passing through the gaseous medium of the 'Minispiral'. Consequently, we compute the expected bolometric luminosities assuming the axially-symmetric accretion flux, $L_{\rm acc} = \eta_{\rm acc}\dot{M}c^2$, with the accretion efficiency of $\eta_{\rm acc} = 1/2 \times R_{\rm s}/R_{\rm NS} \approx 0.1 \rightarrow 10\%$. We assume that isolated neutron stars are old enough for the magnetic field to be significantly reduced and thus not affecting the accretion flow in the vicinity of the

star. Hence, the accretion rate $\dot{M}$ may be approximated by the analytical Bondi-Hoyle-Lyttleton relation, eq. (3.32), where we take the mean values of electron temperature and density of the 'Minispiral' region from Zhao et al. (2010), $\overline{T}_{\rm e} \approx 6 \times 10^3\,{\rm K}$ and $\overline{n}_{\rm e} \approx \overline{n}_{\rm H} \approx 10^4\,{\rm cm}^{-3}$. The plots of relative velocity with respect to both the semi-major axis of colliding neutron stars and time are in Fig. 3.23. The plot of the bolometric accretion luminosity with respect to time is in Fig. 3.24. As expected, both the relative velocity and the accretion luminosity that are averaged over a time-step (0.1 yr) do not change with time considerably. We see in Fig. 3.23 that the highest relative velocities are for the Northern Arm, followed by the Eastern Arm, and the Western Arc. This is naturally translated into the accretion luminosities that are the largest for the interactions with the Western Arc. In all cases the bolometric luminosities are $\sim 10^{30} - 10^{32}\,{\rm erg\,s}^{-1}$, hence by at least an order of magnitude smaller than the Solar luminosity. Accreting neutron stars propagating through denser regions of the 'Minispiral' arms could be possibly detected as faint X-ray sources, provided that the sensitivity and the resolution is large enough.

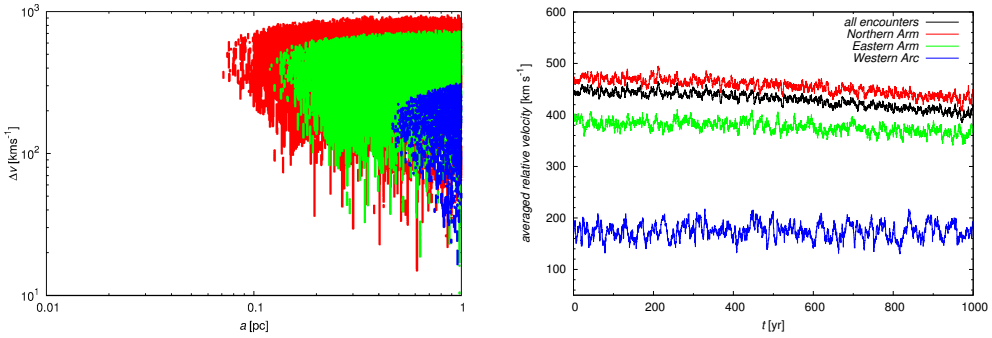

Figure 3.23: Relative velocities of interacting neutron stars as functions of semi-major axis (*Left panel*) and time (*Right panel*). Collisions with individual arms as well as all encounters are distinguished by colour according to the key in the right panel.

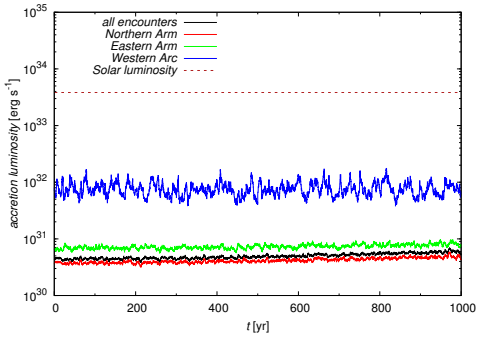

Figure 3.24: The Bondi-Hoyle-Lyttleton bolometric accretion luminosity as a function of time; collisions with individual arms as well as all encounters are distinguished by colour, see the key.

3.5 Interaction modes of magnetized neutron stars

In general, hydrogen gas near the Galactic centre, specifically that constituting the 'Minispiral', is often ionized by the radiation of hot O/B stars. All objects present propagate through this environment and can capture the material to some extent. When the accretion flows are optically thick, the radiation temperature $T_{\rm rad}$ is approximately equal to the black body temperature T_{bb} at local thermal equilibrium (LTE). On the other had, for optically thin flows, radiation easily escapes, so $T_{\rm rad} \approx T_{\rm th}$, where $T_{\rm th}$ is the thermal temperature corresponding to the release of thermal energy after the accretion of a proton-electron pair. So the radiation temperature is bounded by two extremes – black body and thermal temperature:

$$T_{\rm bb} \lesssim T_{\rm rad} \lesssim T_{\rm th}\,,$$
$$\left(\frac{L_{\rm Edd}}{\eta\sigma_{\rm SB}4\pi R_{\rm NS}^2}\right)^{\frac{1}{4}} \lesssim T_{\rm rad} \lesssim \frac{GM_{\rm NS}m_{\rm p}}{3k_{\rm B}R_{\rm NS}}\,,$$

where $L_{\rm Edd}$ is the Eddington luminosity, which represents the upper boundary for the steady accretion, $\sigma_{\rm SB}$ is the Stefan-Boltzmann constant, $m_{\rm p}$ is a proton mass, $k_{\rm B}$ is the Boltzmann constant, and η is the emissivity. Now we can easily estimate the energies of emitted photons $\epsilon = h\nu$:

$$2\,{\rm keV} \lesssim h\nu \lesssim 60\,{\rm MeV}\,.$$

We see that these energies fall into the X-ray and gamma band, so the accretion processes associated with neutron stars are studied at a high-frequency end of the electromagnetic spectrum.

The accretion flow in case of isolated, non-magnetized stars, neutron stars including, is either spherical for subsonic motion or cylindrical in case of supersonic motion, which is often valid for the Galactic centre environment. The associated accretion rate may be estimated by the analytic Bondi-Hoyle-Lyttleton relation, eq. (3.32). However, observed neutron stars have high magnetic fields, see Fig. 3.9. Hence, it appears that it is often not possible to neglect the effect of the magnetic field. It may indeed significantly alter both the inflow and the outflow of material.

The theory presented and subsequently applied in this subsection is mostly inspired by monographs of Lipunov (1992) and Shapiro & Teukolsky (1983).

Effect of magnetic field. Many observed neutron stars – pulsars – have considerable magnetic fields, most frequently of the order of 10^{12} Gauss, as is clearly seen in P–$\dot{P}$ diagram, Fig. 3.8. Warm ionized gas that is also detected close to the Galactic centre, specifically in Sgr A West region (e.g., Kunneriath et al., 2012 and references therein) has high electric conductivity that is proportional to its temperature, $\lambda_{\rm c} \approx 10^7\,T_{\rm e}^{3/2}\,{\rm cm}^{-1}$. Therefore, this plasma must effectively interact with the large magnetic field of neutron stars. Consequently, we need Maxwell's equations besides classical hydrodynamic equation describing gas dynamics in the potential of neutron star. In fact, if we are close to the neutron star

surface, we have to solve a system of relativistic magnetohydrodynamic equations (RMHD), which is often difficult for real systems.

In our analysis, we focus on the fundamental characteristics of the interaction of a rotating magnetized neutron star with the plasma in the surroundings. This interaction consists of two parts: *gravitational interaction* characterized by an accretion rate $\dot{M}$ of captured medium; *electromagnetic interaction* that is described by a magnetic dipolar moment μ and by a rotational period of a neutron star P. These three basic parameters, $\dot{M}$, μ, and P, are further complemented by the mass of neutron star $M_{\rm NS}$ and the relative velocity with respect to the medium v_∞. In fact, neutron stars are a part of the broader class of *gravimagnetic rotators* characterized by mass M, angular momentum $\mathbf{J} = I\mathbf{\Omega}$, and magnetic field, which is as the first approximation characterized by the dipole moment $\boldsymbol{\mu}$.

In order to simplify the problem, we consider the following assumptions:

(a) interaction takes place far from the neutron star surface, so relativistic approach is not necessary,

(b) electromagnetic part of the interaction is independent of the accretion flux parameters,

(c) the intrinsic magnetic field of neutron stars is a dipole field.

Let us make a few notes concerning assumptions (a), (b), and (c). Point (a) means that the interaction of interstellar plasma with the magnetic field or relativistic particle wind of the neutron star takes place at $r \gg GM_{\rm NS}/c^2$, which is often the case. Assumption (b) means that infalling plasma does not distort the intrinsic magnetic field of the neutron star much. Point (c) was already explained in section 3.1. We just repeat that due to the conservation of the magnetic flux, the ratio of quadrupole q and dipole components μ of the field scales with the stellar radius as $q/\mu \propto R$ during the core-collapse, so the field is effectively cleansed of higher multipole components. The dipole field is the most representative component far away from the surface, where the interaction with the ambient medium takes place. The closer to the surface matter gets, the more important the quadrupole component becomes.

Given assumptions (a), (b), (c), the problem becomes much simpler and many effects of the interaction are thus neglected. However, one still gets basic information about the character and the scale of the interaction if fundamental parameters of the neutron star and that of the ambient medium are given.

For a non-rotating neutron star, the harmonic surface current $j \approx \sin\theta$ induces the dipole field outside the sphere having the following form:

$$\mathbf{B}_{\rm d} = \frac{2\mu\sin\theta}{r^3}\mathbf{e}_{\rm r} - \frac{\mu\cos\theta}{r^3}\mathbf{e}_\theta\,, \tag{3.36}$$

where $\mathbf{e}_{\rm r}$ and $\mathbf{e}_\theta$ are unit vectors, μ denotes the dipole moment. The angle θ is measured from the axis perpendicular to the dipole field axis, see the sketch in Fig. 3.25. The magnetic field magnitude B_0 at the poles is twice as big as at the equator, which follows from the magnitude relation $B_{\rm d} = \mu/r^3(1+3\sin^2\theta)^{1/2}$. The magnetic dipole moment is given by the field magnitude at the poles B_0

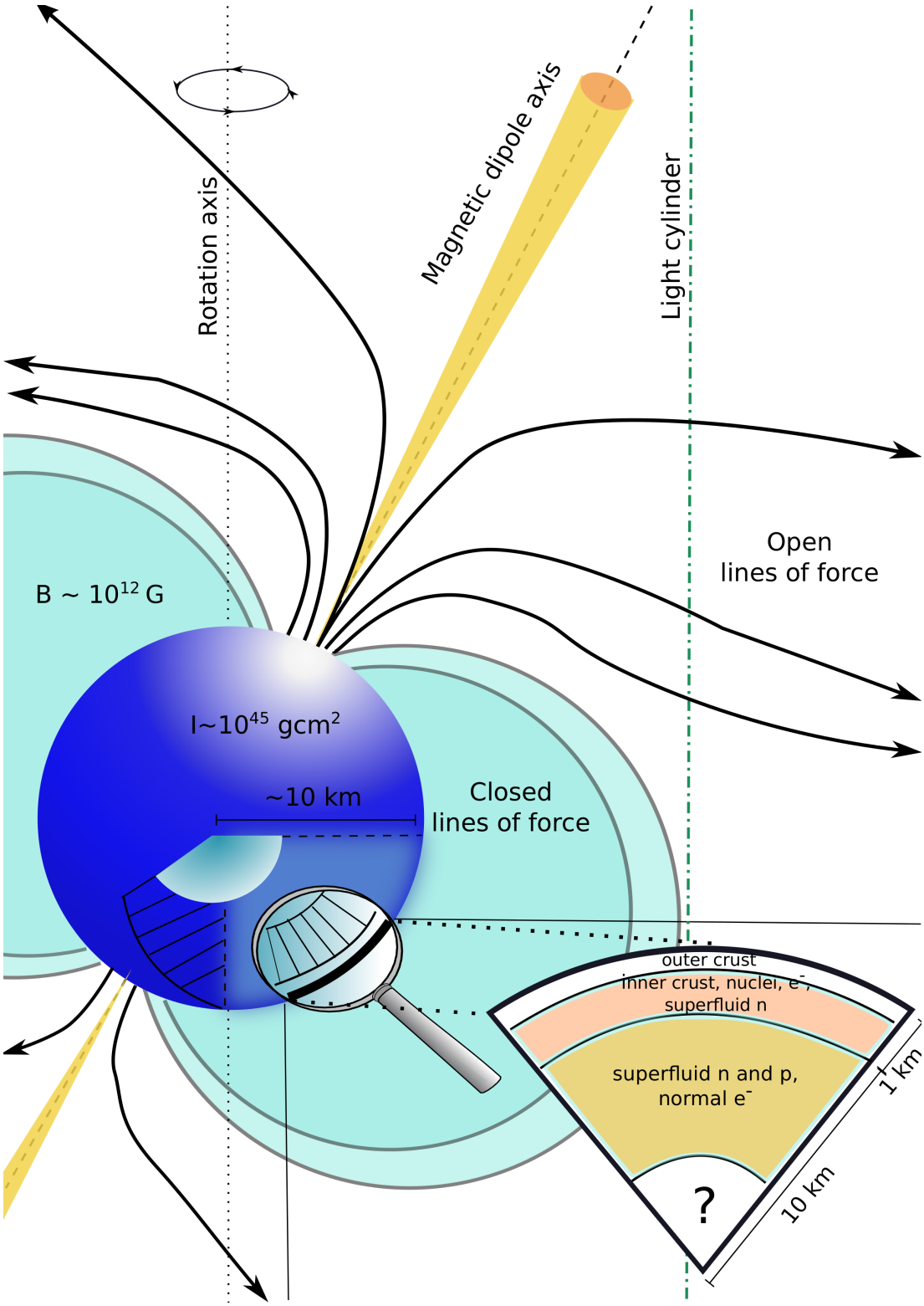

Figure 3.25: Sketch of a typical, canonical pulsar. In the lower right corner, a cross-section of the neutron star is depicted with two basic components: crust and superfluid neutron interior. Magnetic field lines are closed up to the light cylinder. Closer to the magnetic pole, field lines open and relativistic particles escape.

and the neutron star radius $R_{\rm NS}$, $\mu = 1/2 B_0 R_{\rm NS}^3$, yielding typical values $\mu \approx 1/2(2\times10^{12}\ {\rm Oe})\times10^{18}\,{\rm cm}^3 = 10^{30}\,{\rm Oe\,cm}^3$.[3]

In case of a rotating dipole, the electric component of the electromagnetic field also has to be considered. If the rotational axis of a neutron star is inclined with respect to the dipole axis by angle α, the neutron star emits electromagnetic dipole radiation at the rotational frequency Ω. In the frame of this model, there exists the distance $R_{\rm l} = c/\Omega$, below which the electromagnetic field is static and the electric component is given by $E \approx v/c\,B = (\Omega r/c)B = (r/R_{\rm l})B$. While approaching the radius of the light cylinder, $R_{\rm l}$, the electric component becomes comparable to the magnetic component. Upon the crossing of the light cylinder, the electromagnetic field is no longer static and it becomes a propagating electromagnetic wave. The magnetic dipole radiation carries away energy, see eq. (3.37), which may be rewritten using the magnetic dipole μ to

$$\frac{{\rm d}E_{\rm rad}}{{\rm d}t} = \frac{2}{3c^3}\mu^2\Omega^4\sin^2\alpha\,. \tag{3.37}$$

Gaseous environment and possible modes of accretion. A neutron star is assumed to pass through ideally conducting plasma with density ρ_∞, temperature T_∞, and sound speed c_∞ at infinity. We also consider relative motion of the star with respect to the surrounding medium $v_\star$. The plasma starts falling onto the neutron star, resulting from its attraction. We review from subsection 3.4.1 that in case of neutron stars with negligible magnetic field, the stationary flow of matter, or capture rate, is given by Bondi-Hoyle-Lyttleton relation (Bondi & Hoyle 1944; Bondi 1952; McCrea 1953):

$$\dot{M}_{\rm c} = \delta\frac{(2GM_{\rm NS})^2}{(v_\star^2+c_\infty^2)^{3/2}}\rho_\infty\,, \tag{3.38}$$

where δ is a dimensionless factor of the order of unity. Defining the capture cross-section $\sigma_{\rm G} = \delta\pi R_{\rm G}^2$, with $R_{\rm G}$ denoting the capture radius,

$$R_{\rm G} = \frac{2GM_{\rm NS}}{v_\star^2+c_\infty^2}\,, \tag{3.39}$$

we may use a convenient form of the capture rate:

$$\dot{M}_{\rm c} = \sigma_{\rm G}\rho_\infty v_\star\,. \tag{3.40}$$

In realistic astrophysical problems, quantities T_∞, ρ_∞, and c_∞ are taken at finite distances, $R \gg R_{\rm G}$.

Possible accretion modes may be divided in three distinct groups, see also Fig. 3.19:

(i) $v_\star \ll c_\infty$; spherical accretion, without angular momentum in accreting matter,

(ii) $v_\star \gg c_\infty$; cylindrical accretion – axially-symmetric accretion, without angular momentum in the accreting matter,

(iii) the disk accretion, infalling matter has a considerable angular momentum.

[3] 1 Oe is a unit of **H** field in cgs units. The equivalent in SI units is 1 A/m, $1\,{\rm A/m} = (4\pi\,10^{-3})$ Oe.

Stopping radius. Neutron stars as gravimagnetic rotators attract ionized matter due to gravitational forces on one hand and prevent it from accretion due to electromagnetic forces on the other. In the rotating dipole model, the electromagnetic field is stationary inside the light cylinder, $R_\mathrm{l} = c/\Omega$, and changes into freely propagating electromagnetic wave beyond it. The luminosity L_m of the magnetic dipole radiation may be estimated by eq. (3.37), $L_\mathrm{m} = \mathrm{d}E_\mathrm{rad}/\mathrm{d}t$. Goldreich & Julian (1969) found out that near the magnetic axis of the neutron star, which is inclined by a small angle with respect to the rotational axis, the electric component is directed along magnetic field, $E \approx (\Omega r/c)B_0$, and it accelerates charged particles beyond the light cylinder up to relativistic energies, which effectively forms *pulsar wind*. It is assumed that this wind becomes frozen in the surrounding medium and passes its impulse to it. The pressure of the wind may be estimated simply as $P_\mathrm{ej} = L_\mathrm{m}/(4\pi r^2 v_\mathrm{ej})$. On the other hand, it may happen that the accreted plasma penetrates into the region surrounded by the light cylinder. It is prevented from accretion onto the surface by the pressure of the static magnetic field, $P_\mathrm{m} = B^2/(8\pi r^6)$. To sum up, the pressure of electromagnetic forces is of a different character inside and outside the light cylinder, and it is described by the following relations:

$$P_\mathrm{m} = \begin{cases} \frac{\mu^2}{8\pi r^6} & \text{if } r \le R_\mathrm{l} \\ \frac{L_\mathrm{m}}{4\pi r^2 c} & \text{if } r > R_\mathrm{l}\,. \end{cases} \tag{3.41}$$

Using the light cylinder radius, R_l, we may rewrite the dipole radiation luminosity of the neutron star L_m, eq. 3.37, into the form:

$$L_\mathrm{m} = \kappa_\mathrm{t} \frac{\mu^2}{R_\mathrm{l}^3} \Omega\,, \tag{3.42}$$

where $\kappa_\mathrm{t} = 2/3 \sin^2\alpha$ is a dimensionless factor. Using eq. (3.42), the electromagnetic pressure acting on the surrounding gas expressed by (3.41) may be rewritten into following relations:

$$P_\mathrm{m} = \begin{cases} \frac{\mu^2}{8\pi r^6} & \text{if } r \le R_\mathrm{l} \\ \frac{\kappa_\mathrm{t}\mu^2}{4\pi R_\mathrm{l}^4 r^2} & \text{if } r > R_\mathrm{l}\,. \end{cases} \tag{3.43}$$

Electromagnetic pressure P_m is continuous for $\kappa_\mathrm{t} = 1/2$ at $r = R_\mathrm{l}$.

Matter being accreted onto the neutron star exerts pressure, which is approximately constant beyond the gravitational capture radius R_G and is equal to $1/2\rho_\infty v_\star^2$. For radii smaller than capture radius R_G, matter falls almost freely and exerts dynamic pressure $1/2\rho(r)v(r)^2$. Under the assumption of spherical accretion, $\dot{M}_\mathrm{c} = 4\pi r^2 \rho(r) v(r)$, which becomes $\dot{M}_\mathrm{c} = 4\pi R_\mathrm{G}^2 \rho_\infty v_\star$ beyond the capture radius, the accretion pressure P_a can be estimated as follows:

$$P_\mathrm{a} = \begin{cases} \frac{\dot{M}_\mathrm{c} v_\star}{8\pi R_\mathrm{G}^2} & \text{if } r > R_\mathrm{G} \\ \frac{\dot{M}_\mathrm{c} v_\star}{8\pi r^2} \left(\frac{R_\mathrm{G}}{r}\right)^{1/2} & \text{if } r \le R_\mathrm{G}\,. \end{cases} \tag{3.44}$$

The accretion pressure is a continuous function according to eq. (3.44).

Both the electromagnetic pressure P_m and the accretion pressure P_a as functions of distance are plotted in Fig. 3.26 for the following set of parameters:

$P = 1\,\mathrm{s}$, $B_0 = 2 \times 10^{12}\,\mathrm{G}$, $R_0 = 10^6\,\mathrm{cm}$, $n_\mathrm{H} = 10^4\,\mathrm{cm}^{-3}$, $T_\mathrm{e} = 6 \times 10^3\,\mathrm{K}$, $M_\mathrm{NS} = 1.4\,M_\odot$, $v_\star = 100\,\mathrm{km\,s}^{-1}$.

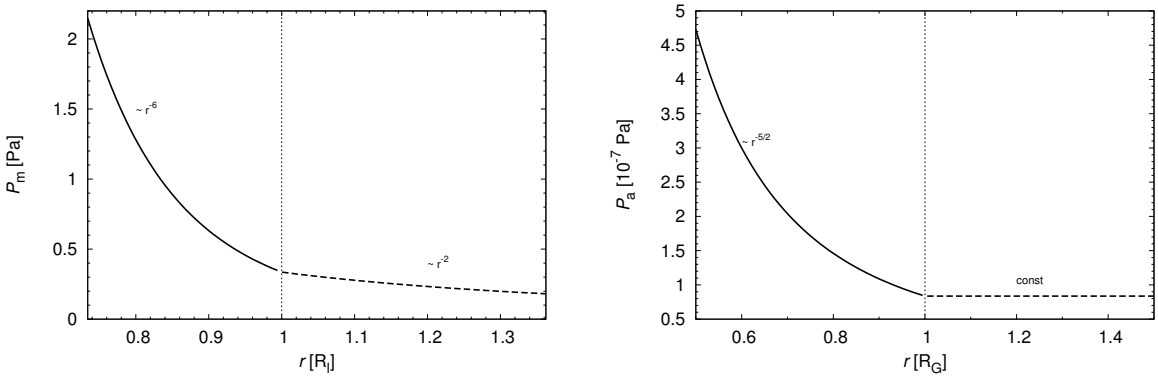

Figure 3.26: (*Left panel*) The pressure exerted by stationary magnetic field varies as $\sim r^{-6}$, whereas outside the light cylinder the pressure of relativistic particles that act on infalling plasma falls off with the distance as $\sim r^{-2}$. The distance is expressed in light radii (R_l). (*Right panel*) The pressure caused by accreted plasma is approximately constant beyond the gravitational capture radius, whereas for smaller radii gas falls freely and the pressure increases as $\sim r^{-5/2}$ while approaching the star. The units are expressed in gravitational capture radii (R_G).

The plasma being accreted by a neutron star is halted at the *stopping radius* where the pressure of electromagnetic forces is at balance with the pressure of accreted matter. The stopping radius may be derived from the following condition:

$$P_\mathrm{m} = P_\mathrm{a}\,. \tag{3.45}$$

If the pressure of electromagnetic forces is represented by the pressure of a static dipole field, then eq. (3.45) yields Alfvén radius, R_A. If the electromagnetic pressure P_m is related to the outflow of relativistic particles (pulsar wind), then the corresponding radius is the so-called Shvartsman radius, R_Sh. The stopping radius may be thus expressed as

$$R_\mathrm{st} = \begin{cases} R_\mathrm{A} & \text{if } R_\mathrm{st} \le R_\mathrm{l} \\ R_\mathrm{Sh} & \text{if } R_\mathrm{st} > R_\mathrm{l}\,. \end{cases} \tag{3.46}$$

For the case when $R_\mathrm{st} \le R_\mathrm{l}$, Alfvén radius is given by corresponding relations in eqs. (3.43) and (3.44), so again we get two cases for distances larger or smaller than the capture radius R_G:

$$R_\mathrm{A} = \begin{cases} \left(\frac{4\mu^2 G^2 M_\mathrm{NS}^2}{\dot{M}_\mathrm{c} v_\star^5}\right)^{1/6} & \text{if } R_\mathrm{A} > R_\mathrm{G} \\ \left(\frac{\mu^2}{\dot{M}_\mathrm{c}(2GM_\mathrm{NS})^{1/2}}\right)^{2/7} & \text{if } R_\mathrm{A} \le R_\mathrm{G}\,. \end{cases} \tag{3.47}$$

For $R_\mathrm{st} > R_\mathrm{l}$, relativistic pulsar wind interacts with accreted matter. By comparing dependencies in Fig. 3.26, we see that the accretion pressure increases as $\sim r^{-5/2}$ for $R_\mathrm{st} \le R_\mathrm{G}$ and thus more rapidly than the pressure of pulsar wind that decreases as $\sim r^{-2}$. Hence, for $R_\mathrm{st} \le R_\mathrm{G}$, no stable cavern can be maintained

by the ejection of matter. However, using eq. (3.43) for $r > R_{\rm l}$ and eq. (3.44) for $r > R_{\rm G}$, we may find the stopping radius for distances $R_{\rm st} > R_{\rm G}$. This radius is also known as Shvartsman radius and may be expressed in the following way:

$$R_{\rm Sh} = \left(\frac{2L_{\rm ej}}{\dot{M}_{\rm c} v_\star v_{\rm ej}} \right)^{1/2} R_{\rm G} \,,$$
$$R_{\rm Sh} = \left(\frac{8\kappa_{\rm t}\mu^2 (GM_{\rm NS})^2 \Omega^4}{\dot{M}_{\rm c} v_\star^5 c^4} \right)^{1/2} \quad \text{if} \quad v_{\rm ej} = c \,. \tag{3.48}$$

Let us note that the relations (3.47) and (3.48) are valid for the accretion rates below the Eddington limit for accretion, $G\dot{M}_{\rm c}M_{\rm NS}/R_{\rm st} < L_{\rm Edd}$. Supercritical regime occurs in disk accretion modes that do not develop in case when neutron stars are just passing through ionized plasma medium that has low angular momentum.

Corotation radius. The corotation radius of a rotating neutron star is another important distance scale. If accreting plasma penetrates beyond the light cylinder, it is stopped at Alfvén radius, $R_{\rm st} \approx R_{\rm A}$, where the plasma pressure and the pressure of static magnetic field are at balance. Further evolution of stopped plasma is given by the rotational velocity of the neutron star. Let us assume that the plasma becomes frozen at $R_{\rm st}$ in the magnetic field and corotates with it at angular velocity of the neutron star, Ω. The plasma clump will eventually reach the surface of the neutron star if the rotational velocity at the stopping radius $R_{\rm st}$ is smaller than the Keplerian velocity at the same distance:

$$\Omega R_{\rm st} < \left(\frac{GM_{\rm NS}}{R_{\rm st}} \right)^{1/2} . \tag{3.49}$$

On the other hand, if the condition (3.49) is not met, a centrifugal barrier develops that prevents plasma from further accretion. The critical, corotation radius $R_{\rm c}$ that separates the two modes is given by the equality in (3.49):

$$R_{\rm c} = \left(\frac{GM_{\rm NS}}{\Omega^2} \right)^{1/3} . \tag{3.50}$$

If $R_{\rm st} < R_{\rm c}$, rotation does not considerably effect the accretion flux. If $R_{\rm st} \geq R_{\rm c}$, stationary accretion is not allowed.

Interaction modes. The mode of interaction of magnetized rotating neutron stars as well as other gravimagnetic rotators is given by the relations between four fundamental distance scales: stopping radius $R_{\rm st}$, radius of light cylinder $R_{\rm l}$, gravitational capture radius $R_{\rm G}$. and corotation radius $R_{\rm c}$. Elementary combinatorics yields $4! = 24$ possible relations between these radii. However, when taking astrophysics into consideration, we get just a few modes. For instance, $R_{\rm l}$ is always greater than $R_{\rm c}$. We do not take supercritical regimes into account in our analysis, since it occurs in systems with disk accretion, and binary systems are also not considered. The classification of the interaction modes and thus types of neutron stars according to Lipunov (1992) is summarized in Table 3.7. The sketches of these basic regimes are in Fig. 3.27.

Name	Notation	Relation between distances	Observational effects
Ejector	E	$R_{\rm st} > \max\{\mathrm{R_G}, \mathrm{R_l}\}$	radiopulsars
Propeller	P	$R_{\rm c} < R_{\rm st} \leq \max\{\mathrm{R_G}, \mathrm{R_l}\}$	–
Accretor	A	$R_{\rm st} \leq R_{\rm G}$ and $R_{\rm st} \leq R_{\rm c}$	X-ray pulsars, X-ray bursters
Georotator	G	$R_{\rm G} < R_{\rm st} \leq R_{\rm c}$	–

Table 3.7: Summary of the interaction modes and thus types of neutron stars according to Lipunov (1992).

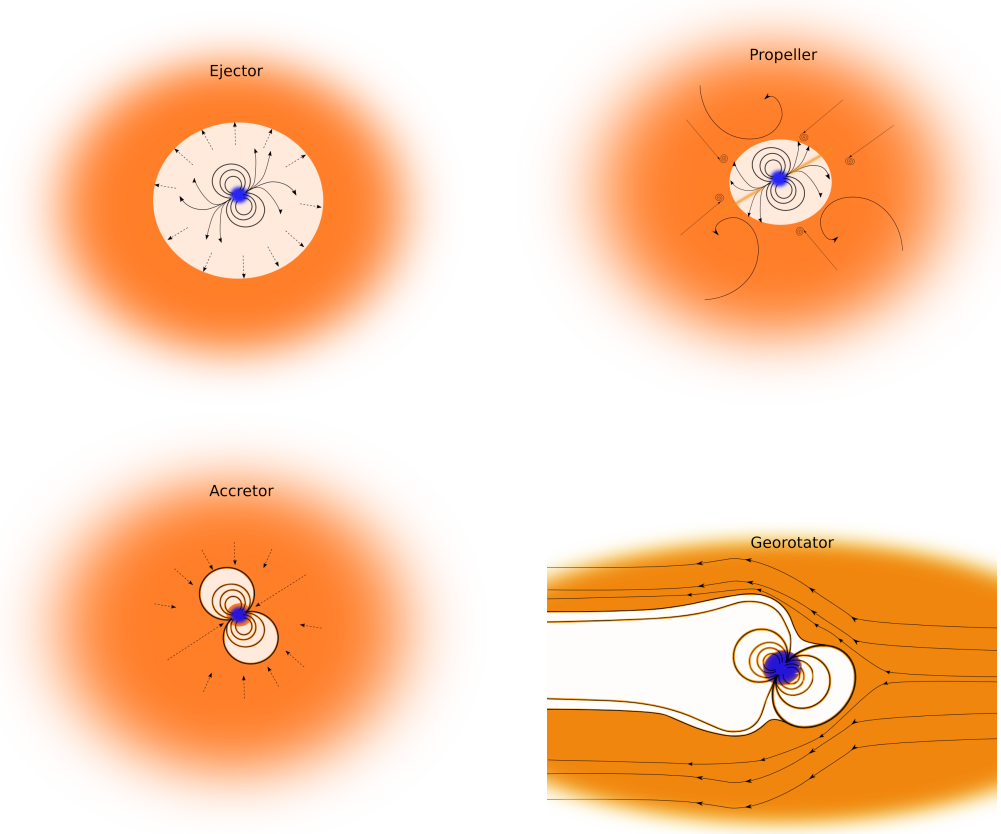

Figure 3.27: Illustrations of basic interaction modes of magnetized neutron stars; from top left to bottom right: ejector, propeller, accretor, and georotator.

3.5.1 Expected interaction modes in Sgr A West

We produce a synthetic population of million neutron stars according to the observed distribution of periods and magnetic fields, see Figs. 3.7 and 3.9. We do not consider a fraction of neutron stars that are in binary systems. They produce a second, smaller peak in the distributions. Synthetic Gaussian distributions of decadic logarithms of periods (in seconds) and that of surface magnetic fields (in Gauss) are plotted in Figure 3.28. The corresponding parameters, μ and σ, are in Table 3.8. The values of period and that of the surface magnetic field are independently attributed to each neutron star.

The three arms of the 'Minispiral' are modelled as clumps on three separate Keplerian orbits, as before. First, we fix the temperature of the ionized gas, we take $\overline{T}_{\rm e} = 6 \times 10^3\,\mathrm{K}$ according to Zhao et al. (2010). The density is continually

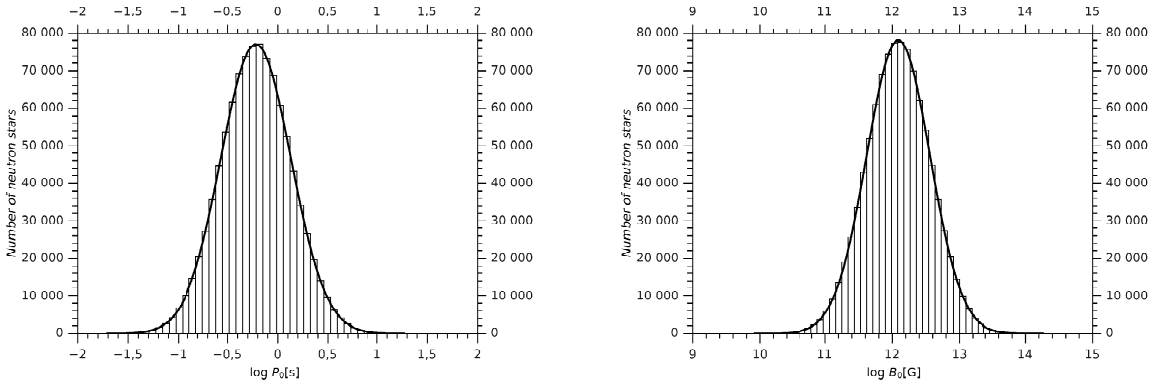

Figure 3.28: Synthetic distributions of the period and that of the surface magnetic field for the population of million neutron stars. The corresponding parameters, μ and σ, are in Table 3.8.

Quantity	μ	σ
Period	-0.2188 ± 0.0003	0.3488 ± 0.0004
Magnetic field	12.0900 ± 0.0005	0.4711 ± 0.0005

Table 3.8: Parameters of synthetic distributions of the period and that of the magnetic field that are plotted in Fig. 3.28.

increased by an order of magnitude, starting with $10^4\,\mathrm{cm}^{-3}$; we consider the densities of $(10^4, 10^5, 10^6, 10^7, 10^8, 10^9)\,\mathrm{cm}^{-3}$. Our Monte Carlo simulation yields $\sim 11\,700$ encounters per unit of time, which is consistent with the fraction of ~ 0.01 of the total number of the Galactic centre neutron stars that interact with the 'Minispiral' material. The interaction modes are scanned according to the classification in Table 3.7. We summarize the results via a series of histograms in Fig. 3.29. It is obvious that for densities that are derived from observations (10^4–$10^5\,\mathrm{cm}^{-3}$, Zhao et al., 2010; Kunneriath et al., 2012) ejector stage dominates ($\gtrsim 90\,\%$); for larger densities the fraction of propeller neutron stars increases and at $\sim 10^7\,\mathrm{cm}^{-3}$ it is the same as the fraction of ejectors and starts to prevail for higher densities, at which accretors become also more prominent. This may be explained by the dependence of the stopping radius, eqs. (3.47) and (3.48), on the accretion rate: for higher densities, $\dot{M}_\mathrm{c}$ increases and the stopping radius decreases. Hence, we naturally get a large fraction of propellers and accretors for high densities, which may be more relevant for AGN and the regions of dense gaseous-dusty tori than for low-luminosity AGN, of which the Milky Way centre serves as a paradigm. The distribution of ejectors, propellers, and accretors in the plane of period and magnetic field is in Fig. 3.30 for high densities, $\overline{n}_\mathrm{e} = 10^8\,\mathrm{cm}^{-3}$, in which accretor mode starts to be more prominent. It is apparent that the ejector regime prevails at short periods ($\sim 0.1\,\mathrm{s}$), for longer periods of $\sim 1\,\mathrm{s}$ propeller mode dominates, and accretors are prominent near death lines.

Second, we perform the simulation analogous to the first one, but this time we fix the density, $\overline{n}_\mathrm{e} = 5 \times 10^4\,\mathrm{cm}^{-3}$ (close to the values inferred from the interferometric observations, Zhao et al., 2010). The parameters related to the magnetic field and period distributions are kept the same. The electron temperature is varied from 1000 K up to 55 000 K. We just make a note that the motivation for

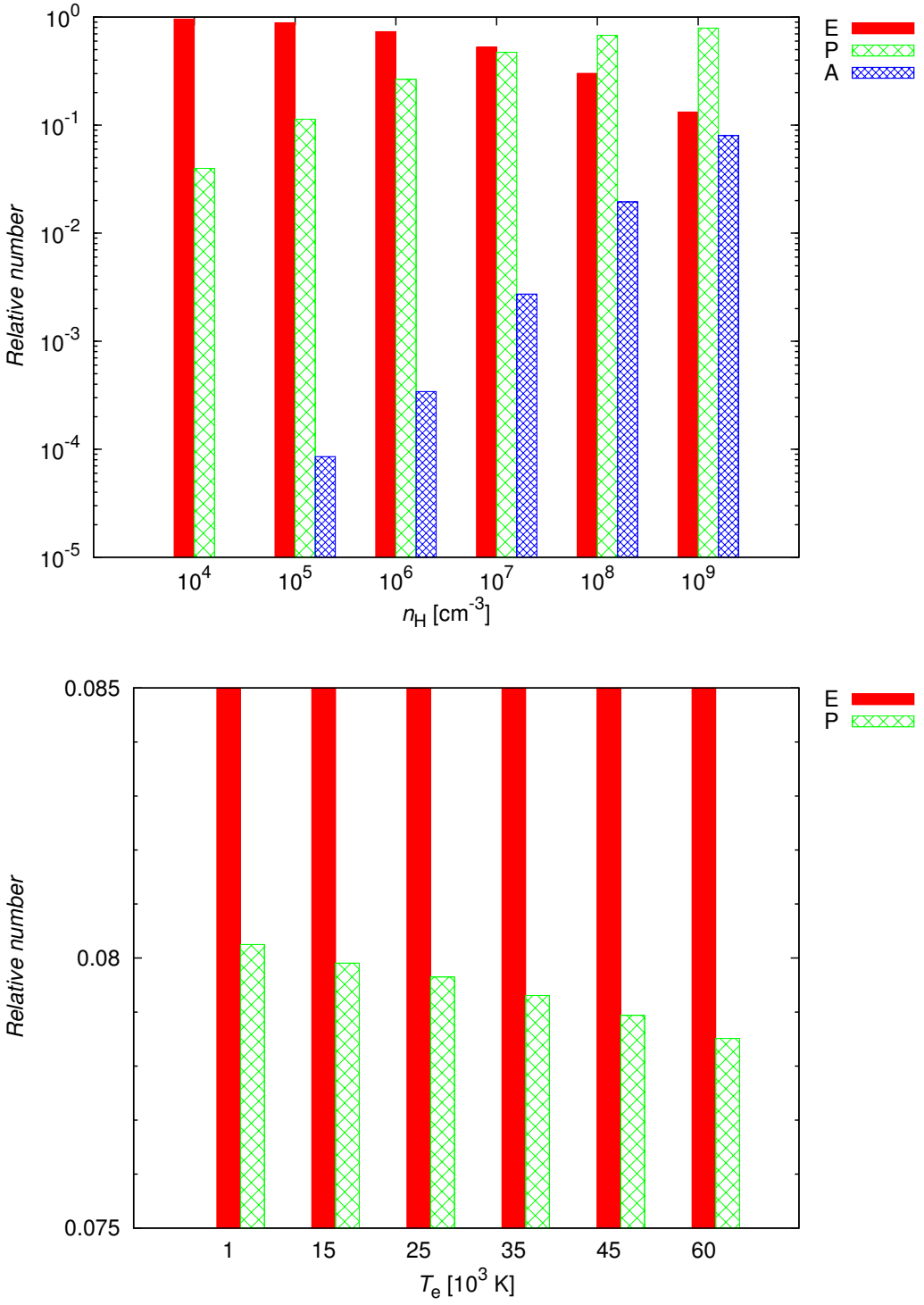

Figure 3.29: (*Top panel*) The distribution of interaction modes of the neutron stars that are found in the 'Minispiral' region. Three basic modes are monitored: ejector (E), propeller (P), and accretor (A). The distribution alters significantly as the density increases. The temperature is fixed at $\overline{T}_{\rm e} = 6 \times 10^3$ K. (*Bottom panel*) The distribution of interaction modes for the fixed density of $\overline{n}_{\rm e} = 5 \times 10^4\,{\rm cm}^{-3}$. We vary the temperature according to the description in the plot. Just two modes, ejector and propeller, are present. The relative number of ejector modes increases (0.9197, 0.9201, 0.9203, 0.9207, 0.9211, and 0.9215) with the increasing temperature.

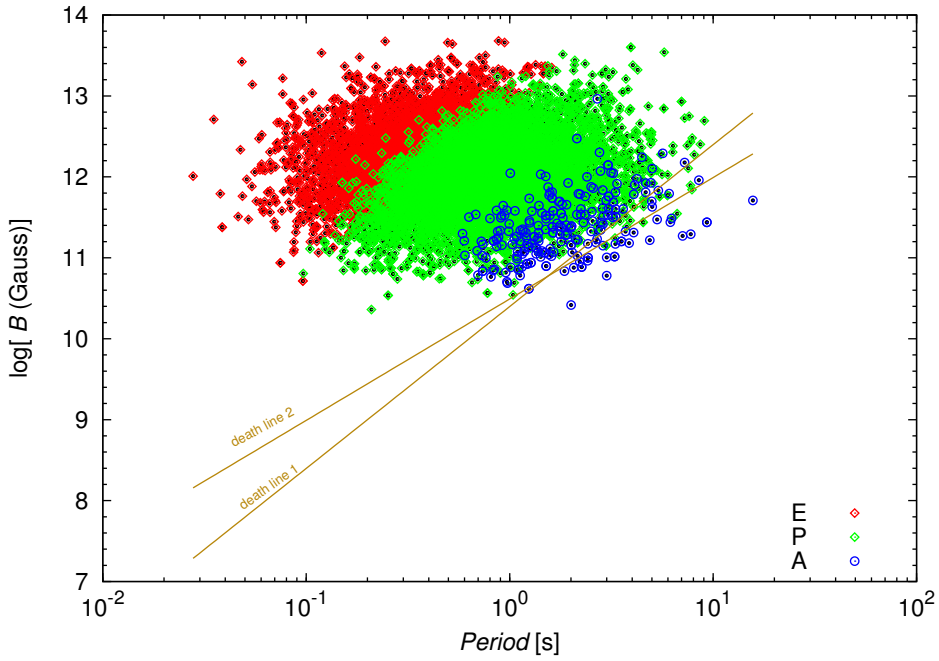

Figure 3.30: An exemplary distribution of neutron stars in P–B plane. The synthetic population of neutron stars interacts with the 'Minispiral' that is characterized by temperature and density. In this particular case, we consider the denser medium of density $\overline{n}_{\rm e} = 10^8\,{\rm cm}^{-3}$ and temperature $\overline{T}_{\rm e} = 6 \times 10^3\,{\rm K}$ to enhance the accretor mode. Three basic interaction modes are distinguished: ejector (E), propeller (P), and accretor (A). As in Fig. 3.8, we label two death lines.

these density and temperature variations is the fact that the 'Minispiral' consists of several streams and clumps of different temperature and density that can coexist. After several runs we find that the distribution of interaction modes does not vary much: ejectors represent $\gtrsim 92\,\%$ and propellers $\lesssim 8\,\%$ of those neutron stars that collide with the streams, see Fig. 3.29. For higher temperatures, accretion rate $\dot{M}_{\rm c}$ drops and the stopping radius increases, see eqs. (3.47) and (3.48). Hence, the number of propellers decreases, ejectors are more abundant, but the dependence on temperature is rather weak. No accretors appear, since we keep the density at $5 \times 10^4\,{\rm cm}^{-3}$ and we notice from the previous analysis summarized in Fig. 3.29 (top panel) that accretors appear at $\sim 10^7\,{\rm cm}^{-3}$.

Distribution of interaction modes for stratified clumps and different distributions. In our model, we implement clumps with variable density profile: they consist of four concentric shells with the corresponding outer radii $r_{\rm N} = \left(\frac{1}{2}\right)^{N-1} \times 0.08\,{\rm pc}$. The density increases towards the centre, starting with $10^4\,{\rm cm}^{-3}$ and $10^7\,{\rm cm}^{-3}$ in the core, increasing by one order of magnitude towards the core of each clump. This scheme ensures that most of the gaseous medium has number densities in the range $(10^4, 10^5)\,{\rm cm}^{-3}$, which are inferred from radio and infrared observations (see Kunneriath et al., 2012, Zhao et al., 2010 and references therein). We analyse interaction modes for four different distributions whose types and parameters are listed in Table 3.9. Distribution (1) is inferred

from the Gaussian fit of the main peak of both the period and the magnetic field distributions of observed neutron stars, see Fig. 3.7 and Fig. 3.9. Distribution (2) is a broader Gaussian distribution, (3) is a uniform distribution across a large span of values: $B_0 \in (10^7, 10^{15})\,\mathrm{G}$ and $P \in (10^{-3}, 10^2)\,\mathrm{s}$. Distribution (4) is a combined distribution of (1) and (3), where (3) uniformly fills an ellipse in PB_0 plane, satisfying condition:

$$\frac{(\log P - \mu_\mathrm{P})^2}{s_\mathrm{P}^2} + \frac{(\log B_0 - \mu_\mathrm{B})^2}{s_\mathrm{B}^2} \leq 1\,,$$

where s_P and s_B are corresponding semi-major axes, $s_\mathrm{P} = (\log P_\mathrm{max} - \log P_\mathrm{min})/2$ and $s_\mathrm{B} = (\log B_\mathrm{max} - \log B_\mathrm{min})/2$. The combined distribution is plotted in Fig. 3.31.

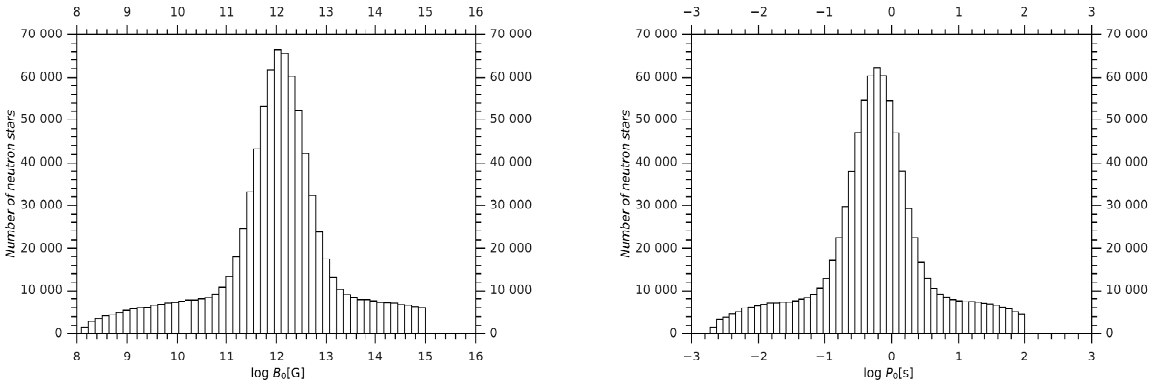

Figure 3.31: The combined distribution of magnetic field and period: it consists of Gaussian (1) and uniform distribution (3); for parameters see Table 3.9.

The distribution of interaction modes of neutron stars passing through the ionized 'Minispiral' arms is in Fig. 3.32. The notation used along the bottom horizontal axis $(1, 2, 3, 4)$ corresponds to different distributions listed in Table 3.9. In case of distribution (1), a narrow Gaussian inferred from the observed distribution of neutron stars, the ejector mode dominates, whereas propeller and accretor modes are represented by small amounts, $(E, P, A) \approx (95, 5, 3 \times 10^{-3})\%$. For the broader Gaussian distribution (2), the ejector mode decreases whereas propeller and accretor regimes increase, $(E, P, A) \approx (81.3, 18.4, 0.3)\%$. This trend continues in case of the uniform distribution (3), for which the accretor regime rises considerably, $(E, P, A) \approx (59.5, 20.4, 20.1)\%$. Finally, the combined distribution (4) with a Gaussian peak results in the dominant ejector mode again, $(E, P, A) \approx (82.1, 13.6, 4.3)\%$. In all cases, the ejector mode prevails by at least $\gtrsim 60\%$.

Furthermore, we plot the distribution of interaction regimes in PB_0 plane, distinguishing individual modes by colour: ejector (E) – red, propeller (P) – green, and accretor (A) – blue, see Fig. 3.33. The PB_0 plane is divided by a pair of two *death lines*, $B \approx 2.5 \times 10^{10} P^2$ (G) and $B \approx 3.1 \times 10^{10} P^{3/2}$ (G). Above these lines the production of electron and positron pairs in strong magnetic fields occurs and pulsars are active, whereas below these lines the pair production no longer proceeds and pulsars are turned off. The ejector mode dominates the

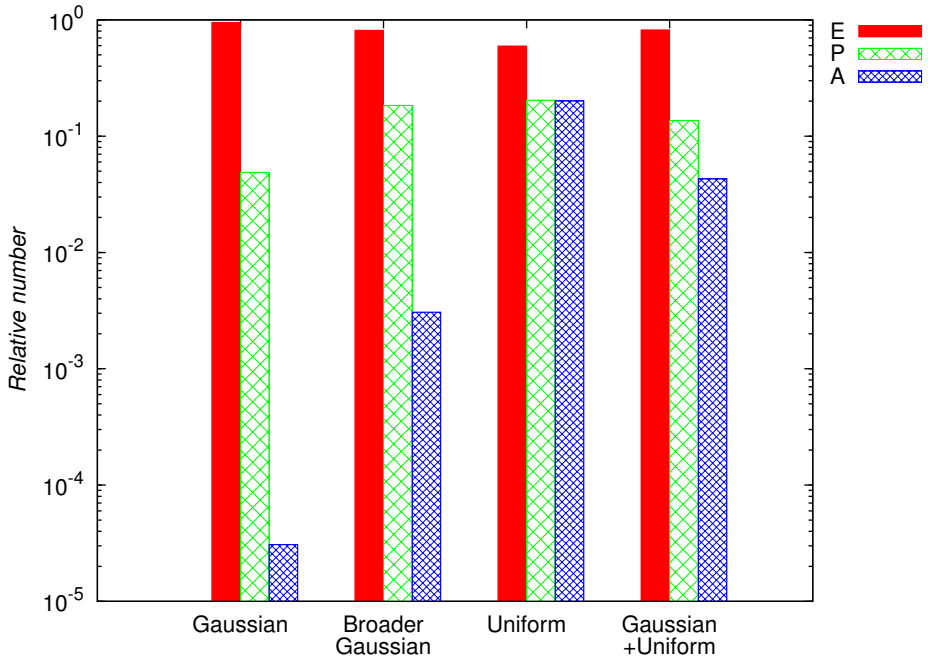

Figure 3.32: Distribution of interaction modes of neutron stars passing through the 'Minispiral' for four different distributions: (1) Gaussian, (2) broader Gaussian, (3) uniform distribution, and (4) combined distribution: Gaussian + uniform. Parameters of distributions are in Table 3.9.

Distribution number	Type	Parameters
1	Gaussian	$\mu_{\rm P} = -0.2188 \pm 0.0003$, $\sigma_{\rm P} = 0.3488 \pm 0.0004$ $\mu_{\rm B} = 12.0900 \pm 0.0005$, $\sigma_{\rm B} = 0.4711 \pm 0.0005$
2	Gaussian	$\mu_{\rm P} = -0.2178 \pm 0.0004$, $\sigma_{\rm P} = 0.7019 \pm 0.0005$ $\mu_{\rm B} = 12.0888 \pm 0.0006$, $\sigma_B = 0.85098 \pm 0.0008$
3	Uniform	$\log P_{\rm min} = -3$, $\log P_{\rm max} = 2$ $\log B_{\rm min} = 7$, $\log B_{\rm max} = 15$
4	Combined	$\mu_{\rm P} = -0.2189$, $\sigma_{\rm P} = 0.3478$ $\mu_{\rm B} = 12.09$, $\sigma_{\rm B} = 0.47$ $\log P_{\rm min} = -3$, $\log P_{\rm max} = 2$ $\log B_{\rm min} = 7$, $\log B_{\rm max} = 15$

Table 3.9: Distributions of the period and the magnetic field of neutron stars whose interaction regimes are plotted in Fig. 3.32.

region above both death lines, the propeller regime crosses these lines, and the accretor mode dominates the region below these lines.

Temporal evolution of the period: effect on the interaction regime. We add a simple temporal evolution to the rotational frequency Ω (or the rotational period P, $\Omega = 2\pi/P$) to each neutron star. We approximate the change in frequency by Taylor expansion, neglecting higher than third derivative of Ω:

$$\Omega = \Omega_0 + \dot{\Omega}|_0 \Delta t + \frac{1}{2}\ddot{\Omega}|_0 (\Delta t)^2 + \frac{1}{6}\dddot{\Omega}|_0 (\Delta t)^3 + \mathcal{O}\left(\Delta t^4\right) \tag{3.51}$$

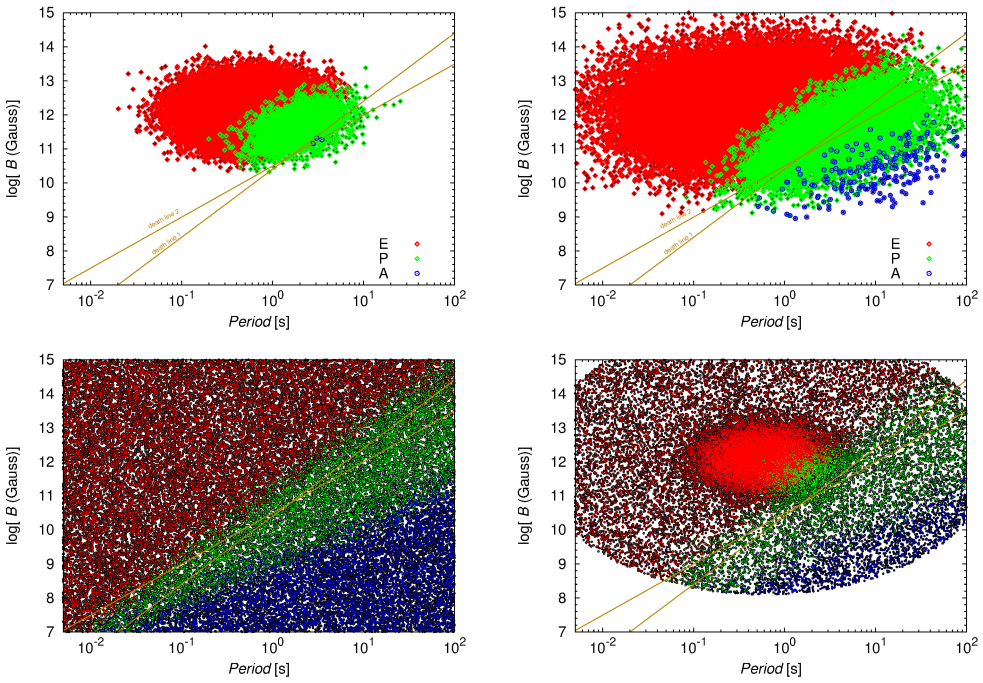

Figure 3.33: The distribution of interacting neutron stars in PB_0 plane. Interaction modes are distinguished by colour: ejector (E) – red, propeller (P) – green, and accretor (A) – blue. The following distributions are plotted: Gaussian distribution inferred from the distribution of observed neutron stars (1, top left), broader Gaussian distribution (2, top right), uniform distribution (3, bottom left), and the combination of Gaussian (1) and uniform distribution (3) (4, bottom right). The parameters of these distributions are listed in Table 3.9.

where Ω_0 is the current value of rotational frequency and $\dot{\Omega}|_0 < 0$ is the first derivative of frequency at a given time, $\ddot{\Omega}|_0 > 0$ is the second derivative, and $\dddot{\Omega}|_0 < 0$ is the corresponding third derivative. The dominant first frequency derivative is negative, hence the frequency becomes smaller and the period is prolonged. When looking for the first approximation of $\dot{\Omega}$, we make use of the magnetic dipole model. The radiation luminosity $\dot{E}_{\rm rad}$ of the rotating magnetic dipole is given by eq. (3.37) This energy originates from the kinetic rotational energy, $E_{\rm rot} = 1/2 I\Omega^2$, and its temporal change is given by $\dot{E}_{\rm rot} = I\Omega\dot{\Omega}$, hence $\dot{E}_{\rm rot} = -\dot{E}_{\rm rad}$. Another source of the loss of rotational energy are gravitational waves. The lowest-order gravitational radiation is of a quadrupole character. The theory of gravitational radiation implies that neutron stars have to be al least slightly deformed to have a time-varying quadrupole moment. Strong anisotropic magnetic fields in the interior of a neutron star can indeed induce such deformations. Therefore we approximate each neutron star as a homogeneous ellipsoid with the moment of inertia I and ellipticity ϵ that is given by the ratio of the difference in equatorial radii and the mean equatorial radius, $\epsilon = (a-b)/[(a+b)/2]$.

Finally, the energy losses $\dot{E}_{\rm GW}$ by gravitational waves caused by small asymmetry (i.e., $a \approx b$) of a neutron star may be expressed (e.g., Shapiro & Teukolsky, 1983):

$$\dot{E}_{\rm GW} = -\frac{32}{5}\frac{G}{c^5} I^2 \epsilon^2 \Omega^6$$
$$= 1.4 \times 10^{38} \left(\frac{I}{1.4 \times 10^{45} {\rm g\,cm^2}}\right)^2 \left(\frac{P}{0.0331\,{\rm s}}\right)^{-6} \left(\frac{\epsilon}{3 \times 10^{-4}}\right)^2 {\rm erg\,s^{-1}}. \quad (3.52)$$

Given these two sources of rotational energy loss – magnetic dipole radiation and gravitational waves – the conservation of energy yields:

$$I\Omega\dot{\Omega} = -\frac{2}{3c^3}\mu^2\Omega^4 \sin^2\alpha - \frac{32}{5}\frac{G}{c^5} I^2\epsilon^2\Omega^6\,. \quad (3.53)$$

From eq. 3.53 we may easily derive the relations for the first three derivatives of frequency $\dot{\Omega}$:

$$\begin{aligned}
\dot{\Omega} &= -\beta\Omega^3 - \gamma\Omega^5\,,\\
\ddot{\Omega} &= -\dot{\Omega}(3\beta\Omega^2 + 5\gamma\Omega^4)\,,\\
\dddot{\Omega} &= -\ddot{\Omega}(3\beta\Omega^2 + 5\gamma\Omega^4) - \dot{\Omega}^2(6\beta\Omega + 20\gamma\Omega^3)\,.
\end{aligned} \quad (3.54)$$

where β and γ stand for the following terms:

$$\begin{aligned}
\beta &= \frac{2}{3c^3}\frac{\mu^2}{I}\sin^2\alpha\,,\\
\gamma &= \frac{32}{5}\frac{G}{c^5} I\epsilon^2\,.
\end{aligned}$$

We analyse the evolution of interaction modes on the time-scale of 10^4–10^5 years, which is the approximate lifetime of the 'Minispiral' Zhao et al. (2009, 2010). The decay time of the magnetic field may be estimated as (Shapiro & Teukolsky 1983):

$$t_{\rm d} \approx \frac{\sigma L^2}{c^2}\,, \quad (3.55)$$

where σ is the conductivity and L is a characteristic length of the system. The conductivity σ may be estimated from fundamental constants $m_{\rm e}$, e, and c on dimensional grounds in the following way, $\sigma \approx (m_{\rm e}c^3)/e^2 \approx 10^{23}\,{\rm s^{-1}}$. We take $L \approx R_{\rm NS}$ and from eq. (3.55) we get $t_{\rm d} \approx 3.5 \times 10^6\,{\rm yr}$, which is by at least one order of magnitude longer than the time-scale that we consider here. Hence, we may consider the magnetic field strength to be constant.

We analyse the change of the rotational period and the period derivative using the sample of 50 neutron stars distributed according to Gaussian distribution (1) that is inferred from the observations of the disk population of neutron stars, see Table 3.9. The neutron stars are distributed in the space of orbital elements as before, but this time they have semi-major axis in range $a \in (0.05, 2.5)\,{\rm pc}$ and the radii of clumps are bigger, $\sim 4\,{\rm arcsec}$ to increase the probability of encounters; we investigate if the change of the interaction mode is due to the prolongation of the rotational period or if it is rather caused by density fluctuations in the gaseous

medium around the Galactic centre. Each gaseous clump of the 'Minispiral' comprises concentric shells characterized by the mean density and the mean temperature: $(10^4\,\mathrm{cm}^{-3}, 10^4\,\mathrm{K})$, $(10^5\,\mathrm{cm}^{-3}, 7.5\times10^4\,\mathrm{K})$, $(10^6\,\mathrm{cm}^{-3}, 5\times10^4\,\mathrm{K})$, and $(10^7\,\mathrm{cm}^{-3}, 2.5\times10^4\,\mathrm{K})$, from the outermost shell to the core of the clump, respectively. Outside the clumps, the density and the temperature profile are assumed to be radial and we take (Broderick & Loeb 2006; Broderick et al. 2011)

$$n_\mathrm{e}(r) = n_\mathrm{e}^0 \left(\frac{r}{r_\mathrm{s}}\right)^{-1.1}, \quad T_\mathrm{e}(r) = T_\mathrm{e}^0 \left(\frac{r}{r_\mathrm{s}}\right)^{-0.84}, \tag{3.56}$$

which are based on the models of the radiatively inefficient accretion flows and $n_\mathrm{e}^0 = 3.5\times10^7\,\mathrm{cm}^{-3}$, $T_\mathrm{e}^0 = 9.5\times10^{10}\,\mathrm{K}$.

The evolution during $10^5\,\mathrm{yr}$ and the interaction modes are plotted in period–period derivative diagram, see Fig. 3.34. Only ejectors (mainly pulsars) younger than $\sim 1\,\mathrm{Myr}$ show a distinct shift in position in $P\dot{P}$ plane. Such young pulsars are often located near supernova remnants in the disk population (see also Fig. 3.8). Neutron stars whose characteristic age given by eq. 3.14 is larger than $\sim 1\,\mathrm{Myr}$ do not show such a shift. One should realize that this is mainly given by the logarithmic nature of the standard $P\dot{P}$ diagram. However, it can be also deduced from our simple model of the period prolongation, see eq. 3.54, that the increase in period is larger for bigger magnetic fields (μ term) and shorter periods (larger rotational frequencies), which is often met for young pulsars embedded in supernova remnants. In our analysis we find out that the change of an interaction regime is not determined by the period prolongation on the time-scale of $10^5\,\mathrm{yr}$ but rather by density fluctuations of the gaseous medium in the vicinity of Sgr A*. We can clearly see it in Fig. 3.34, where three examples of neutron stars change their interaction mode from the ejector to the propeller mode and back due to encounters with the denser 'Minispiral' material. We note that only those neutron stars closer to the death lines, i.e. those that have smaller magnetic fields and/or longer periods, change their regime due to passages through a dense material. Neutron stars located in the upper left part of the $P\dot{P}$ diagram do not exhibit any alternation due to density fluctuations.

Consequently, we study if the distribution if interaction modes changes for an ensemble of $\sim 20\,000$ neutron stars on the time-scale of $5000\,\mathrm{yr}$. As before, they are distributed uniformly in the space of orbital elements with semi-major axes in range $a \in (0.05, 2.5)\,\mathrm{pc}$. The 'Minispiral' is modelled as an ensemble of clumps moving on three separate systems of Keplerian orbits. Outside these higher density regions, the environment is described by radial density and temperature profiles, eq. 3.56. Rotational periods and magnetic fields are distributed according to distribution (4), see Table 3.9, i.e. a combination of Gaussian and uniform distribution. The evolution in $P\dot{P}$ diagram is shown as a series of four plots, showing the initial distribution ($0\,\mathrm{yr}$), and subsequent distributions at $1000\,\mathrm{yr}$, $3000\,\mathrm{yr}$, and $5000\,\mathrm{yr}$, see Fig. 3.35. The only visible change is the shift of young ejectors–pulsars from the upper left part of the diagram to the right along the lines of constant magnetic field.

We see that there is no distinct change in the distribution of three interaction modes: ejector, propeller, and accretor. We also plot histograms, see Fig. 3.36, for the same years ($0\,\mathrm{yr}$, $1000\,\mathrm{yr}$, $3000\,\mathrm{yr}$, $5000\,\mathrm{yr}$) and three cases: all neutron stars (top panel), neutron stars that do not interact with the 'Minispiral' en-

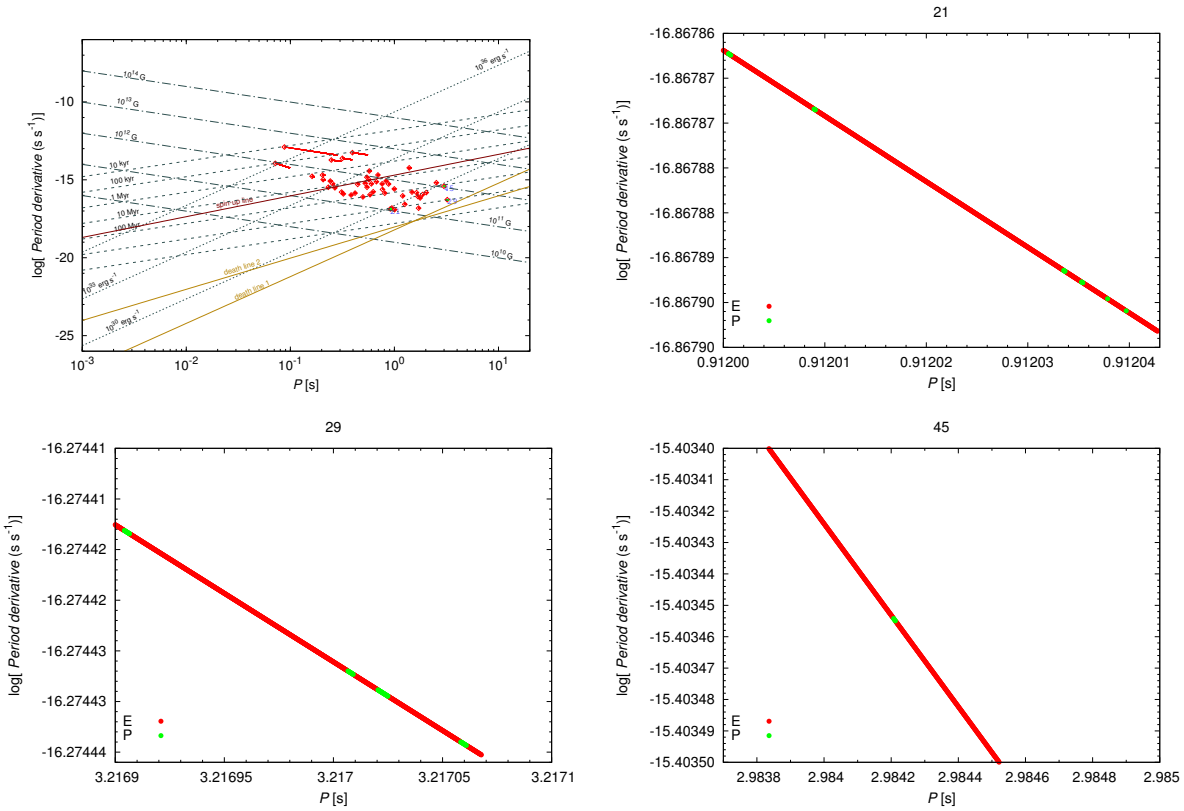

Figure 3.34: (*Top left*) Evolution of 50 neutron stars with different magnetic fields and periods in *Period–Period derivative* diagram. The shift is distinct only for the neutron stars with sufficiently strong magnetic fields and short periods. (*Top right, Bottom left, Bottom right*) Exemplary temporal evolutions of period and period derivative for three neutron stars. Period is prolonged, whereas period derivative decreases. Occasional changes of interaction modes are due to the encounters with the denser gaseous material.

vironment (middle panel), and neutron stars that do encounter denser regions of the 'Minispiral' (bottom panel). At each epoch $\sim$ 1% of neutron stars encounter denser medium; 2.2% at 0 yr, 2.0% at 1000 yr, 1.1% at 3000 yr, and 0.6% at 5000 yr. Therefore the overall distribution of interaction modes (top panel) is given mainly by non-interacting neutron stars (middle panel), i.e. those that propagate through the ambient medium characterized by radial profiles of density and temperature, see eq. 3.56. For the overall distribution and the distribution for non-interacting neutron stars we do not see any significant change with time, see Fig. 3.36. There are some distinct fluctuations in case of interacting neutron stars that also exhibit a decrease in ejector mode and an increase in propeller and accretor mode in comparison with non-interacting neutron stars.

We may conclude that density fluctuations change the distribution of interaction regimes, with denser medium making the propeller and the accretor mode more abundant. On the other hand, the established mode for neutron stars that propagate through sparse interstellar medium is determined mainly by their intrinsic properties, rotational period and the magnitude of magnetic field. On the time-scale of 10^3–10^4 yr the spin-down of neutron stars does not alter the overall distribution of interaction regimes.

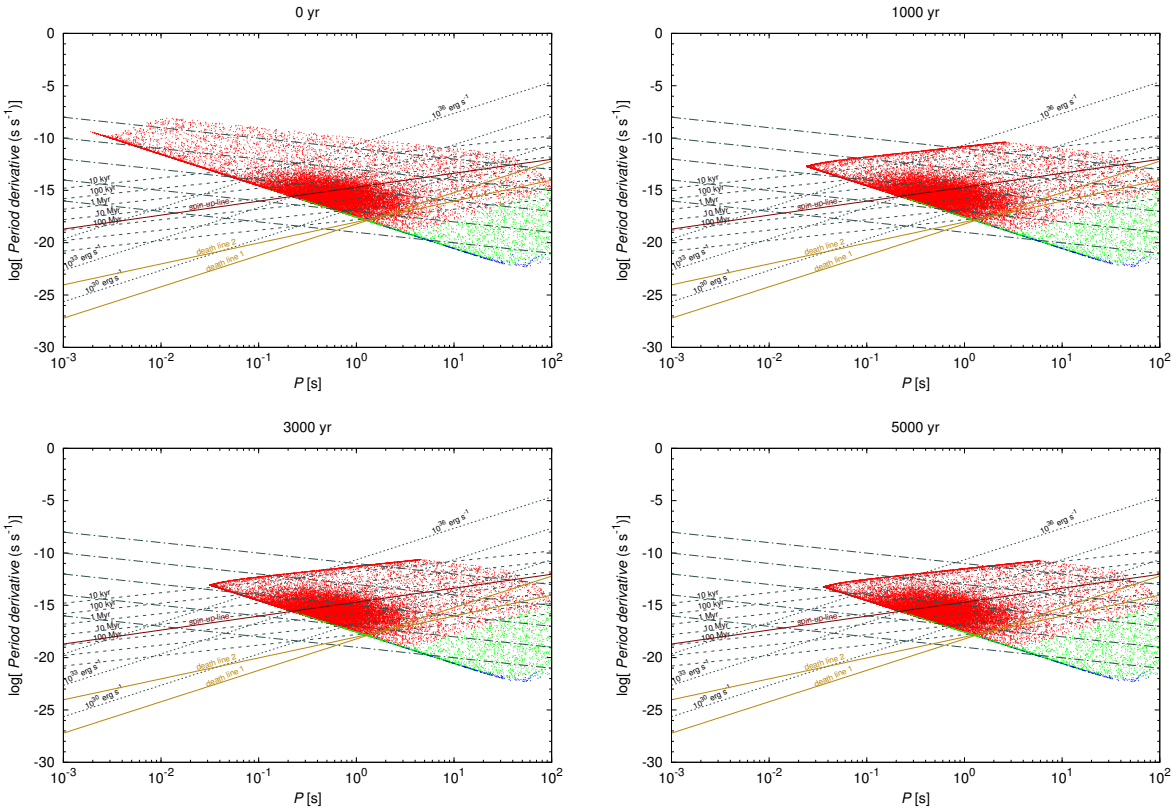

Figure 3.35: Distribution of interaction regimes (Ejector–red, Propeller–green, Accretor–blue) in $P\dot{P}$ diagram. Individual plots represent snapshots at different epochs: top left – 0 yr, top right–1000 yr, bottom left–3000 yr, bottom right–5000 yr.

3.5.2 Possible observable effects

Let us briefly discuss plausible observable consequences of each interaction mode: ejector, propeller, and accretor.

Ejectors manifest themselves mainly as radiopulsars. Given the predicted number of neutron stars in the central parsec of the Galactic centre, $\sim 10\,000$ according to section 3.2, the expected fraction of ejectors is $\sim 90\%$ (see Fig. 3.36) if the dominant population of neutron stars is the same as in the disk population. This fraction could be decreased if the population of old, isolated accreting neutron stars is more prominent. One should be aware of the fact that pulsars stay active for a certain amount of time, which can be approximated as $\tau \approx 100$ Myr, when they reach death lines and they turn off, see Fig. 3.8. Around death lines they become propellers and with further spin-down and magnetic field decay they start to accrete interstellar matter, see Figs. 3.33 and 3.35.

We take the beaming fraction of ejectors $f_\mathrm{b} = 0.2$ (Emmering & Chevalier 1989), i.e. pulsars that are expected to beam towards us, so potentially ~ 1800 pulsars could be detectable with sufficient sensitivity. However, as was already stressed in section 3.3, there is an apparent lack of pulsar detections in the Galactic centre region. The minimum detectable flux is given by relation (3.28); the pulsar searches in the Galactic disk are generally affected by high background temperature, which rises the minimum detectable flux. Moreover, all observa-

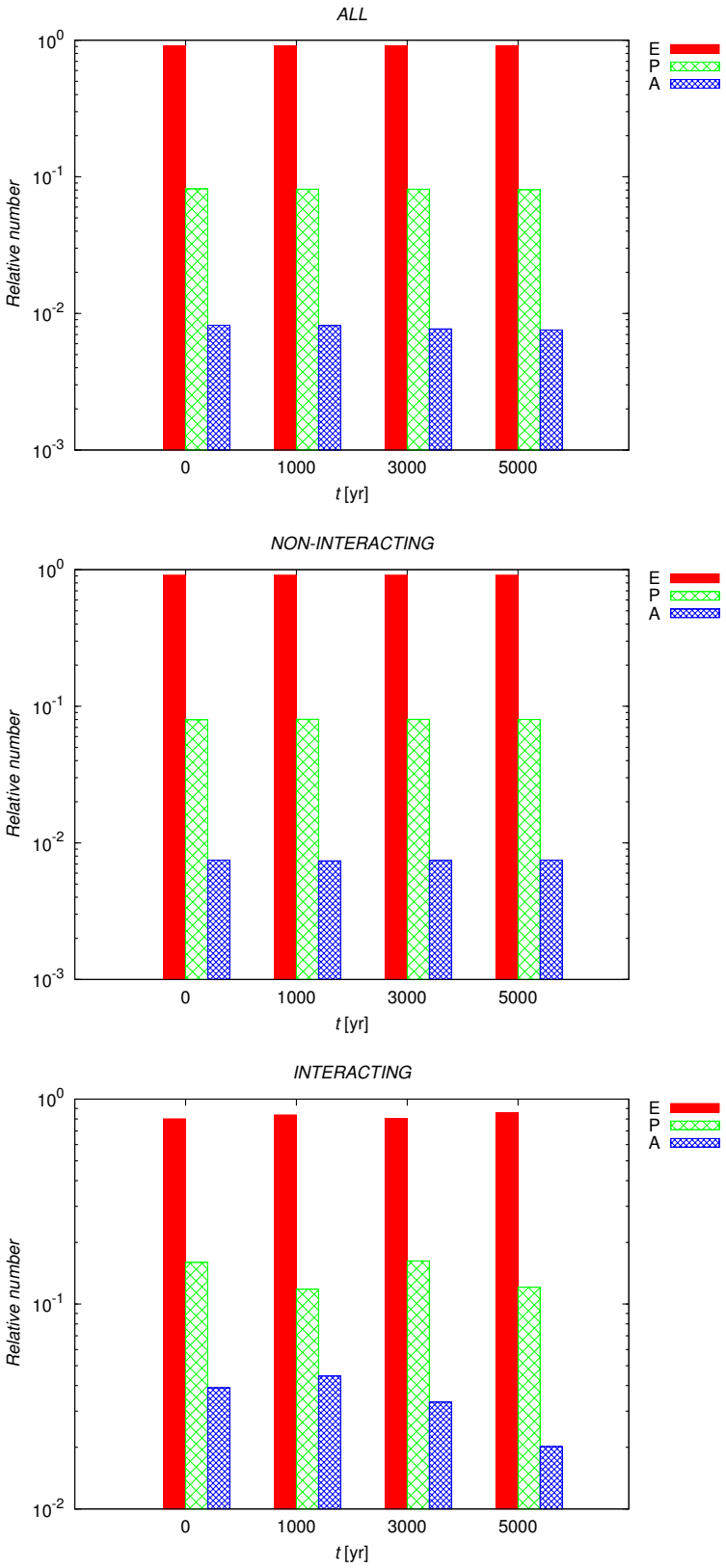

Figure 3.36: (*Top panel*) Distribution of interaction modes for all neutron stars at different epochs labelled along the horizontal axis. (*Middle panel*) Distribution of interaction modes for non-interacting neutron stars at different epochs. i.e. those that propagate through sparse and hot ambient medium. (*Bottom panel*) Distribution of interaction modes for interacting neutron stars at different epochs.

tions pointed at the Galactic centre region suffer from interstellar scattering resulting from turbulent plasma, which causes the temporal broadening of pulses to $\sim 2000\nu_{\rm GHz}^{-4}\,{\rm s}$ ($\nu_{\rm GHz}$ is the observing frequency in GHz). At usual observing frequencies $\sim 1\,{\rm GHz}$ it is not possible to detect even long-period pulsars and the surveys have to increase the frequency to $\sim 10\,{\rm GHz}$. However, since pulsars have spectral energy distribution in the power-law form $S_\nu \propto \nu^\alpha$, where $\alpha < 0$, flux decreases for higher frequencies. To sum up, the lack of observed radiopulsars in the Galactic centre may be explained by low sensitivity of current observing facilities. A major breakthrough is expected to come with the project of *Square Kilometre Array–SKA* with much higher sensitivity than current instruments. The mapping of the close vicinity of Sgr A* will be the role of *Event Horizon Telescope–EHT*, which may detect pulsars strongly bound to the supermassive black hole and the data could be then used to put the theory of general relativity to very precise tests.

Another way to detect ejectors–pulsars is to look for cavities, pulsar wind nebulae (PWN), and bow-shock structures formed when supersonic ejecting neutron stars emitting relativistic wind propagate through the denser medium of the 'Minispiral'. For the average electron temperature of the plasma in the 'Minispiral' region, $\overline{T}_{\rm e} \approx 6 \times 10^3\,{\rm K}$ (Zhao et al. 2010), the sound speed is $c_{\rm s} \approx (k\overline{T}_{\rm e}/m_{\rm H})^{1/2} \approx 7\,{\rm km\,s^{-1}}$. According to Fig. 3.23 of the semi-major axis–relative velocity plot, typical relative velocities of neutron stars that encounter high-density gas of the 'Minispiral' are larger than the sound speed of the interstellar medium by one–two orders of magnitude. Hence, motion is generally supersonic and bow-shock structures associated with neutron stars potentially form in the 'Minispiral' arms. The size of such a cavity is determined by the energy input, $\dot{E} \approx -\dot{E}_{\rm rot} = -I\Omega\dot{\Omega}$, from the central ejector as well as by the structure and properties of the surrounding medium. The velocity of the pulsar $\mathbf{v}_{\rm rel}$ with respect to the ambient medium also influences the size and orientation of the bow-shock structure. Along the relative velocity $\mathbf{v}_{\rm rel}$ the pressure of the wind of the ejector and the ram pressure of the ISM are at balance at the contact discontinuity. The distance of the contact discontinuity from the central ejector is given by *stand-off* distance (e.g., Brownsberger & Romani, 2014):

$$r_{\rm bs} = \left(\frac{\dot{E}}{4\pi c \rho_{\rm a} v_{\rm rel}^2} \right)^{1/2} , \tag{3.57}$$

where the density of the ambient medium (the 'Minispiral') is $\rho_{\rm a} \approx m_{\rm H} n_{\rm H}$ and we adopt the values from Zhao et al. (2010); Kunneriath et al. (2012); the major part of the 'Minispiral' gaseous clumps has $n_{\rm H} \approx 10^4 \div 10^5\,{\rm cm^{-3}}$, with the core of each clump of $10^7\,{\rm cm^{-3}}$. Although bow-shock structures and PWN are of different nature, equation (3.57) describes the characteristic size of both, i.e. the distance of the contact discontinuity from the central pulsar. In case of PWN, the termination shock is characterized by concentric tori and jets, as it is observed in the Crab nebula, for instance.

We compute the typical sizes of bow shocks and/or PWN for an ensemble of 10 000 neutron stars using eq. (3.57). Assuming that $\sim 90\%$ of interacting pulsars are ejectors, several hundred (in our exemplary runs ~ 400) bow-shock structures could be present in the 'Minispiral' region. However, most of them are

rather small (< 1 mas) and are below the detection limit. Propeller bow shocks are all below ~ 0.1 mas, whereas the bow-shock structures of ejectors have sizes above this value and up to ~ 1000 mas, see Fig. 3.37 for comparison; values along the horizontal axis are decadic logarithms of stand-off radii in milliarcseconds.

The number of large bow-shock structures (100mas $\lesssim r_{\rm bs} \lesssim 1000$ mas) is ~ 10 for ~ 500 neutron stars that interact with the 'Minispiral' out of $\sim 10\,000$ neutron stars that occupy the innermost parsec. The comparison of their sizes with the whole 'Minispiral' structure as seen from the Earth is in Fig. 3.38. The actual mm-image of the 'Minispiral' is in Fig. 3.37.

To sum up, the alternative way to look for ejecting neutron stars is to search for the signatures of their interaction with the 'Minispiral'. Common structures associated with supersonic pulsars are bow shocks. Our analysis shows that the number of relatively large structures in this region, $r_{\rm bs} \approx 100 \div 1000$ mas, can be of the order of ~ 10. They are expected to be sources of polarized non-thermal radiation, possibly detectable in X-ray, infrared, and radio wavelengths. Such comet-shaped sources are indeed evidenced in this region (Mužić et al. 2010). Further analysis is required to strengthen or reject their association with propagating neutron stars. Spectral features associated with bow-shock emission of magnetized neutron stars could be revealed with the improved resolution of ALMA.

In order for neutron stars to accrete the ambient matter they have to possess a weak magnetic field and rotate rather slowly to meet the basic conditions for accretors: $R_{\rm st} \leq R_{\rm G}$ and $R_{\rm st} \leq R_{\rm c}$, see Table 3.7 and Fig. 3.33. The magnetic field is of importance, i.e. it influences the flow of plasma, when the stopping radius is greater than the radius of the neutron star, $R_{\rm st} > R_{\rm NS}$. When we take Alfvén radius for the stopping radius, eq. (3.47), we arrive to the condition for the limiting value of both the dipole moment $\mu_{\rm min}$ and the magnetic field $B_{\rm min}$ (Lipunov 1992):

$$\begin{aligned} \mu_{\rm min} &\approx 10^{26} R_6^{7/4} \dot{M}_{17}^{1/2} M_{\rm NS}^{1/4} \,{\rm Oe\,cm^3}\,, \\ B_{\rm min} &\approx 10^{7} \dot{M}_{17}^{1/2} R_6^{5/4} M_{\rm NS}^{1/4} \,{\rm Oe}\,, \end{aligned} \tag{3.58}$$

where the corresponding quantities, $\dot{M}$, $R_{\rm NS}$, and $M_{\rm NS}$, are in cgs units. As was already discussed, most neutron stars have stronger magnetic fields, $B_0 \approx 10^{12}$ Gauss and the corresponding dipole moment $\mu \approx 10^{30}\,{\rm Oe\,cm^3}$. Hence, the magnetic field usually must be taken into account.

Accretors are generally associated with old, isolated neutron stars, with ages typically $\gtrsim 100$ Myr, which are below the death lines and capture the surrounding medium. Given the age of the Galactic centre $\sim 10^{10}$ yr, a non-negligible fraction of the population of neutron stars in the innermost parsec could be in an accreting stage. The largest fraction of accretors we obtained was for the uniform distribution of period and magnetic field between reasonable limits, distribution (4) in Table 3.9: $(E, P, A) \approx (59.5, 20.4, 20.1)\%$. They are expected to manifest themselves as weak X-ray sources. In case of the 'Minispiral', the bolometric luminosities computed according to the Bondi-Hoyle-Lyttleton formula, eq. (3.32) and Fig. 3.24, are in the range $\sim 10^{30}$–$10^{32}\,{\rm erg\cdot s^{-1}}$. To get an estimate, we consider X-ray luminosities to be of the same order for neutron stars as bolometric luminosities, smaller by a certain factor. Faint X-ray sources

have been indeed detected. Deep surveys using Chandra X-ray observatory have detected several point X-ray sources with luminosities $\sim 10^{32}$–$10^{35}\,\mathrm{erg\,s^{-1}}$ in a large field $\sim 2 \times 0.8$ square degree (Wang et al. 2002). A few sources with luminosities $\sim 3 \times 10^{30}$–$2 \times 10^{33}\,\mathrm{erg\,s^{-1}}$ have been also discovered in a deeper, smaller field of $17' \times 17'$ (Muno et al. 2003). Several weaker and stronger elongated X-ray sources with non-thermal spectra in the range 2–10 keV have been observed (Sakano et al. 2003; Park et al. 2004). Some of these sources are most probably associated with recycled millisecond pulsars in binary systems that are not considered here. Others may be manifestations of bow-shock structures and PWN mentioned earlier. However, some faint X-ray sources may correspond to old, isolated, accreting neutron stars passing at small relative velocities through the 'Minispiral' or Circum-nuclear disk in case of more distant sources.

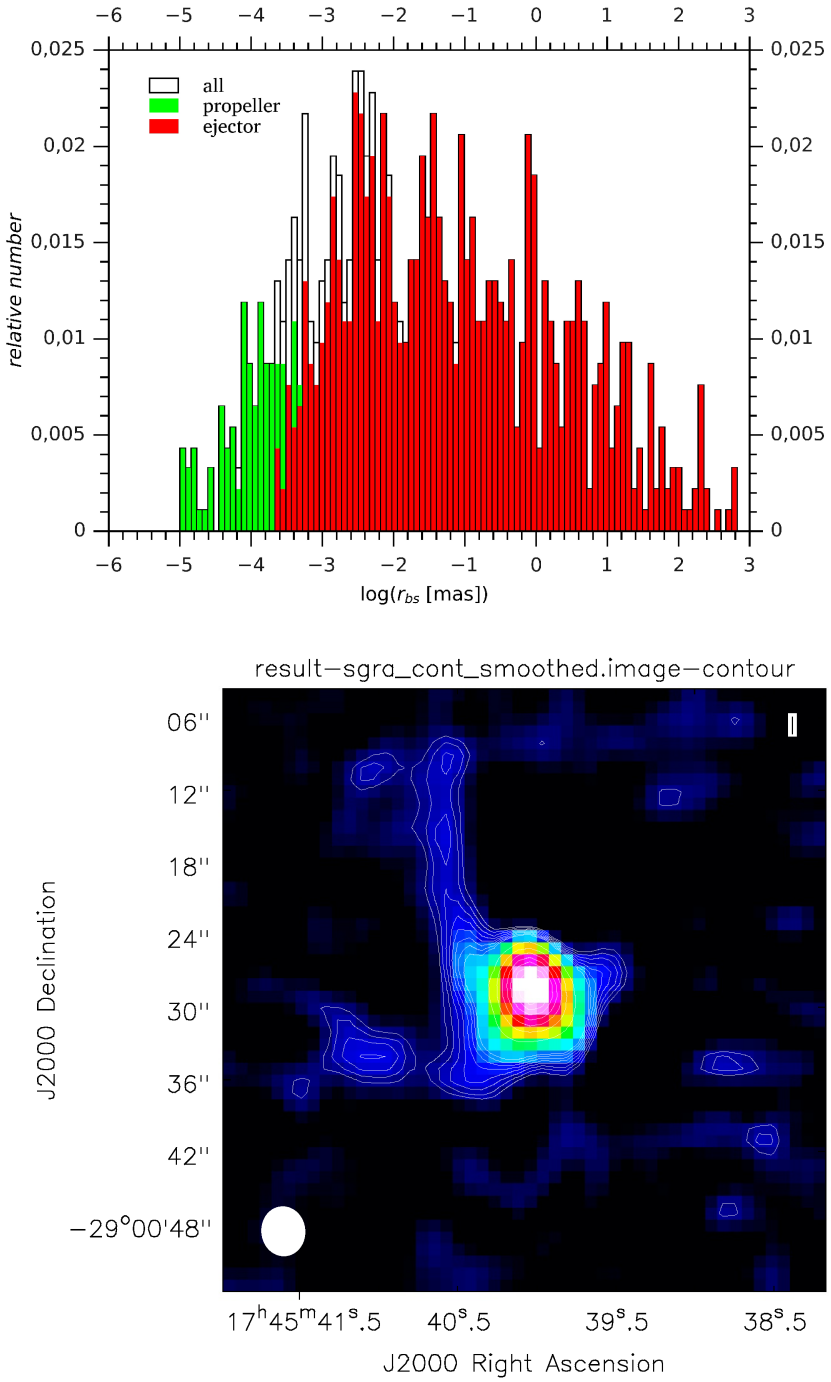

Figure 3.37: (*Top panel*) Histogram of sizes of bow-shock structures: propeller bow shocks (green) are concentrated towards the smaller sizes, whereas ejectors have larger bow shocks up to $\sim$ 1000 mas. Values along the horizontal axis are decadic logarithms of bow-shock sizes in milliarcseconds. Vertical axis represents relative numbers with respect to the total number of interacting neutron stars, $\sim$ 500. (*Bottom panel*) The continuum image of the 'Minispiral' at 3 mm by CARMA millimetre array; reanalysis of data from Kunneriath et al. (2012). The contour levels correspond to 0.01, 0.02, 0.03, 0.04, 0.05, 0.06, 0.07, 0.08, 0.09, 0.1, 0.15, 0.2, 0.25, 0.3, 0.35, 0.4, 0.45, 0.5, 0.55, 0.60, 0.65, 0.7, 0.8, 0.9, 1.0 Jy/beam. The beam is denoted by a white ellipse.

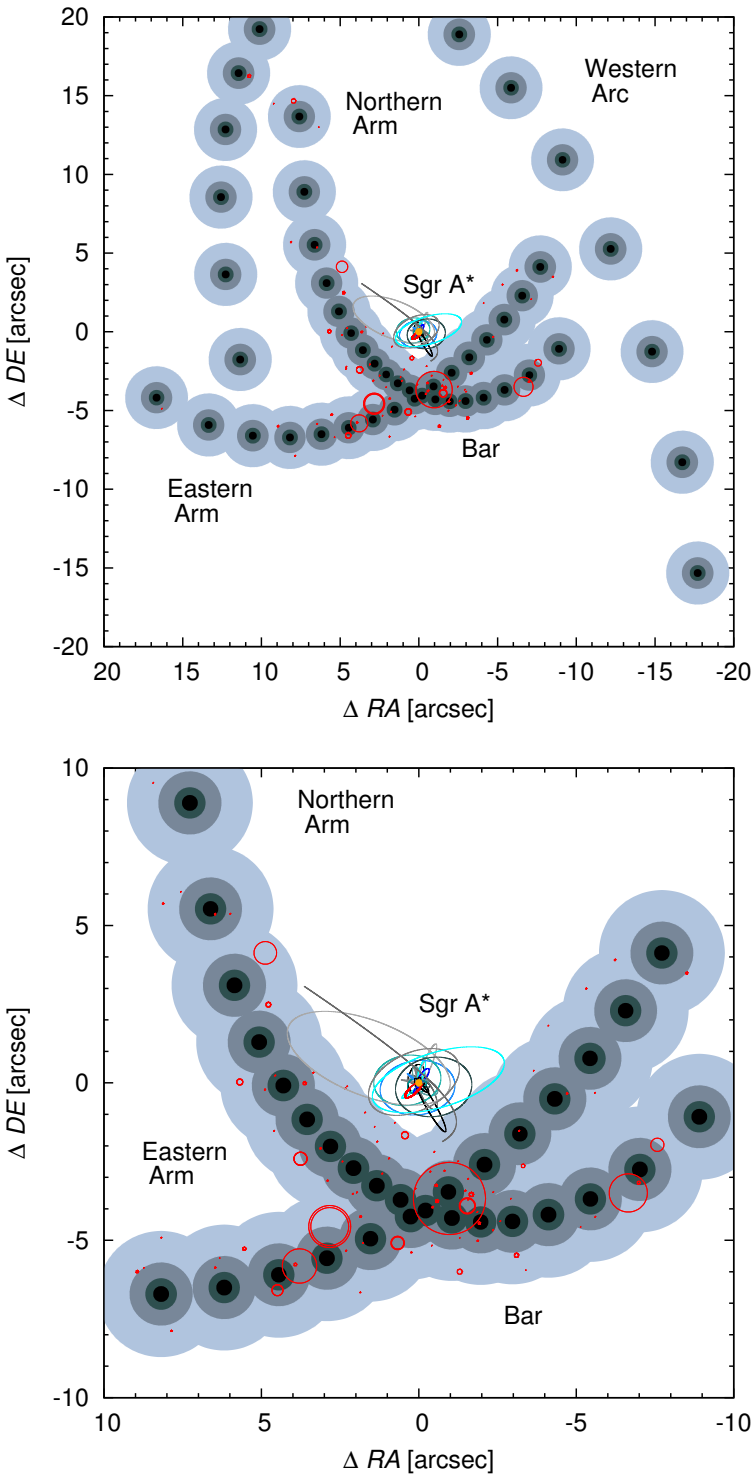

Figure 3.38: (*Top panel*) The model of the 'Minispiral' with three distinct arms, $40'' \times 40''$. Gray colours mark the concentric shells of different density and temperature used in our model. Red circles label the bow-shock structures and/or PWN associated with ejecting neutron stars interacting with the 'Minispiral'. (*Bottom panel*) The 'Minispiral' with two prominent arms: the Northern Arm and the Eastern Arm, $20'' \times 20''$. Orbits of several S-stars are sketched for illustration.

4. Clouds and stars on highly eccentric orbits

The main motivation for this section comes from the observational evidence of gaseous-dusty, infrared-excess S-cluster source G2 moving on a highly eccentric trajectory ($e \lesssim 1$) (Gillessen et al. 2012, 2013a,b; Eckart et al. 2013c; Phifer et al. 2013). However, the context is broader and the topic is associated with infrared and radio observations of dusty stellar sources in Sgr A, frequently forming bow-shock structures (e.g., X3 and X7, Mužić et al., 2010). The presented analysis aims to shed more light on the material transport and accretion flows in low-luminosity galactic nuclei, of which the Galactic centre serves as a paradigm. The transport of gaseous-dusty material in the Galactic centre is directly linked to the variability of its accretion flow. In fact, the current low-luminous regime may be temporary and there is an evidence of the higher activity in the past (e.g., *Fermi bubbles*, Su et al., 2010). It is therefore appropriate to consider the Galactic centre as a prototype of a low-luminosity active galactic nucleus (LLAGN).

The presence of individual gaseous-dusty clumps may be the result of collisions of streams in the 'Minispiral' region (Czerny et al. 2013b,a) and/or colliding winds of massive OB stars present in the central parsec (Gillessen et al. 2012, 2013a). This shocked and subsequently cooled material looses angular momentum and descends towards the SMBH on highly-eccentric orbits, where upon the pericentre passage it moves at velocities of a few $10^3\,\mathrm{km\,s^{-1}}$, see Fig. 1.2, which is a typical pericentre velocity of observed S-cluster members. Extended gaseous structures are subjected to tidal shearing as well as strong hydrodynamic drag approximately proportional to the square of the relative velocity with respect to the hot, ambient medium, $a_{\rm drag} \propto v_{\rm rel}^2$. Hence, core-less gaseous clumps are expected to disrupt and slowly descend towards the accretion zone of the SMBH where the trajectories of remaining gas and dust are circularized.

Highly-eccentric, plunging orbits of stars near massive black holes may be explained by two mechanisms:

- the Kozai mechanism (Kozai 1962; Šubr & Karas 2005; Karas & Šubr 2007),
- resonant relaxation (Rauch & Tremaine 1996; Hopman & Alexander 2006).

In the model where a spherical stellar cluster evolves in the sphere of influence of a massive black hole a secular evolution of stellar orbits via Kozai oscillations is induced by an axially symmetric, self-gravitating gaseous-dusty or stellar disc and/or torus. An important parameter is the ratio of the disc mass $M_{\rm d}$ and the SMBH mass $M_\bullet$, $\mu = M_{\rm d}/M_\bullet \ll 1$. If the radius of the disc is $R_{\rm d}$, then the time-scale of the oscillations of orbital elements due to the Kozai phenomenon is given by (e.g., Karas & Šubr, 2007):

$$T_{\rm K} \equiv \frac{\lambda}{2\pi\mu}\left(\frac{R_{\rm d}}{a}\right)^3 P \simeq 5.06\times10^3\left(\frac{M_\bullet}{10^6\,M_\odot}\right)\frac{\lambda}{\mu}\left(\frac{R_{\rm d}}{a}\right)^3\left(\frac{a}{10^7\,\mathrm{R_g}}\right)^{3/2}\ \mathrm{yr}\,, \quad (4.1)$$

where λ is a correction term of the order of unity and the scale $R_{\rm g} \equiv GM_\bullet/c^2 \simeq 1.5\times10^{11}(M_\bullet/10^6\,M_\odot)$; $10^7\,R_{\rm g} \approx 1.9\,\mathrm{pc}$ for the Galactic centre supermassive black

hole of $\sim 4 \times 10^6\, M_\odot$. The Kozai time scale is greater than the orbital period of individual stars of the nuclear cluster, $T_\mathrm{K} > P_\mathrm{orb}$, given the condition that $\mu \ll 1$. For the orbital period scale, the following relation holds:

$$P_\mathrm{orb} = 2\pi \left(\frac{a^3}{GM_\bullet}\right)^{1/2} \simeq 3.1 \times 10^4 \left(\frac{M_\bullet}{10^6\, M_\odot}\right) \left(\frac{a}{10^7\, R_\mathrm{g}}\right)^{3/2} \mathrm{yr}\,. \tag{4.2}$$

As is discussed by Karas & Šubr (2007), there are two disc/torus structures observed in the Galactic centre that can induce the Kozai oscillations. One is the Circum-Nuclear disk of molecular and atomic gas extending from $\sim 1.5\,\mathrm{pc}$ up to $3 \div 4\,\mathrm{pc}$ (Christopher et al. 2005) and the other is a disc of young stars closer to the Sgr A* ($\sim 0.03 \div 0.3\,\mathrm{pc}$, Levin & Beloborodov, 2003; Paumard et al., 2006).

However, Karas & Šubr (2007) show that the Kozai effect is more important for intermediate-mass black holes ($\sim 10^4\, M_\odot$) rather than supermassive ones. It might have played a significant role during the early phases of the Galaxy formation, when the central black hole was less massive and a compact accretion disc was present, causing stars to disrupt when plunging below the tidal-disruption radius during the high-eccentricity phases. Hopman & Alexander (2006) propose instead a more efficient mechanism of *resonant relaxation* of orbital angular momenta that is supposed to take place in the spherical potential of the supermassive black hole, where stars close to the SMBH are tightly bound. They move on Keplerian orbits that do not precess significantly given the condition that they are not too far from the SMBH where the precession is induced by the enclosed stellar mass as well as not too close where the relativistic precession occurs. When the precession time is long enough, the orbits remain fixed in space and the mutual interaction between stars causes the change of the direction (*vector resonant relaxation*) and the size (*scalar resonant relaxation*) of angular momenta or both. We discussed in section 1.2 that the Galactic nucleus has not reached a steady-state collisional equilibrium; the non-resonant two-body relaxation time scale is much longer than the age of observed young dynamic structures (Genzel et al. 2010). However, the fast vector resonant relaxation probably led to the randomization of the orbit orientations of 'S'-stars. The slower scalar relaxation has not influenced 'S'-stars much, but could contribute to their non-zero eccentricities, see Fig. 1.3.

Both the scalar resonant relaxation and the Kozai mechanism cause the decrease in angular momenta of stars orbiting the SMBH, thus deflecting them into the *loss cone* orbits from which they fall into the SMBH either directly (infall) or gradually (inspiral) and eventually become tidally disrupted. These processes can thus naturally provide additional material for accretion events and their further study will contribute to the explanation of the variability of low-luminosity nuclei missing compact accretion discs.

Many authors have studied the mechanism of the tidal disruption of stars upon their fly-by close to the SMBH and the corresponding accretion phenomena (e.g., Hills, 1975; Frank, 1978; Rees, 1988). However, a considerable amount of material may be provided for accretion when stars with extended gaseous-dusty envelopes and/or discs move on eccentric orbits near the SMBH and their pericentre distances are larger than the tidal-disruption radius (Hills 1975):

$$r_{\rm t} \approx R_\star \left(\frac{M_\bullet}{M_\star}\right)^{1/3} = 100 \left(\frac{R_\star}{R_\odot}\right) \left(\frac{M_\bullet}{10^6\,M_\odot}\right)^{1/3} \left(\frac{M_\star}{M_\odot}\right)^{-1/3} R_\odot\,, \tag{4.3}$$

where the stellar radius $R_\star$ and mass $M_\star$ are expressed in corresponding Solar values. Hence, the star itself is not disrupted, but a major part of the envelope is diverted from the original path and spirals towards the SMBH. If the material of the gaseous-dusty envelope is continuously replenished during one orbital period, the passages through the pericentre are expected to lead to repeated accretion events. The scenario of such a dust-enshrouded star near the SMBH is analyzed in Zajaček et al. (2014), on which this chapter is based.

4.1 Accretion phenomena

Most galaxies host supermassive black holes (SMBH; $10^6\,M_\odot \lesssim M_\bullet \lesssim 10^9\,M_\odot$) in their cores, where these accrete gas and dust in the form of an accretion flow from their immediate neighbourhood (Krolik 1999; Meier 2012). The example nearest to us is the compact radio source Sgr A*, which contains a black hole of mass $M_\bullet = 4.4 \times 10^6 M_\odot$ at distance 8.2 kpc in the centre of the Milky Way (Eckart et al. 2005; Melia 2007; Genzel et al. 2010).

The character of accretion and the corresponding accretion rate vary greatly over different galaxy types. It appears that the availability of mass supply and the accretion mode that is established in the course of evolution of the system are the main agents that determine the power output and the spectral energy distribution of supermassive black holes (Frank et al. 2002). In several ways, the Galactic centre can serve as a paradigm for low-luminosity nuclei.

Active galactic nuclei (AGN) and quasars host radiatively efficient types of disc accretion (i.e., the standard scheme of geometrically thin accretion discs, or slim discs; Shakura & Sunyaev 1973; Abramowicz et al. 1988) with accretion rates reaching and even exceeding the Eddington limit of $\dot{M}_{\rm Edd} \simeq L_{\rm Edd}/(0.1c^2)$, where

$$L_{\rm Edd} = \frac{4\pi G M_\bullet m_{\rm p} c}{\sigma_{\rm T}} \simeq 1.3 \times 10^{44}\,\frac{M_\bullet}{10^6 M_\odot} \quad [{\rm erg/s}], \tag{4.4}$$

with $m_{\rm p}$ proton mass, $\sigma_{\rm T}$ Thomson cross-section.

Low-luminosity nuclei exhibit significantly lower accretion rates, $\dot{M}_\bullet \ll \dot{M}_{\rm Edd}$ (Eckart et al. 2013a). This can be explained as a combination of a diminishing supply of material falling onto the black hole and the radiatively inefficient mode of accretion at certain stages. In this context, the present state of the Galactic centre represents an extreme example of an inactive nucleus: $\dot{M}_\bullet \simeq 10^{-8} M_\odot$ per year, which can be understood in terms of advection-dominated flow (Narayan & McClintock 2008).[1]

[1]For the supermassive black hole of Sgr A* in the Galactic centre, the quiescent bolometric luminosity is $L_{\rm bol} = \eta \dot{M}_\bullet c^2 \simeq 10^{36}$ erg s^{-1}. This corresponds to the dimensionless efficiency parameter for the conversion of accreted mass into radiation of about $\eta \simeq 10^{-3}$, although it can be as low as 10^{-5} at the present stage of the source. The accretion outflow of Sgr A* is radiatively inefficient compared with predictions from the standard accretion disc theory, where $\eta \simeq 0.06$–0.42 is the predicted range.

The temperature of the accreted material grows in the course of its infall in the gravitational field of the central black hole because the potential energy is converted into heat and is only partially released in the form of emerging radiation (e.g. Frank et al. 2002; Krolik 1999). While at the distance of several tens to hundreds Schwarzschild radii ($r_{\rm s} \equiv 2GM_\bullet/c^2 \doteq 2.95 \times 10^5\, M_\bullet/M_\odot$ cm) the medium consists of ionised gas of the accretion disc and hot, diluted corona, farther out the temperature drops below the critical value for dust sublimation, $T_{\rm sub} \simeq 1.5 \times 10^3$ K (Barvainis 1987; Krishna Swamy 2005). Therefore, at larger distances a clumpy torus can persist with a fraction of its mass in the form of dust (Krolik & Begelman 1988; Hönig & Kishimoto 2010).

An equilibrium can be reached through processes of dust sublimation (by strong irradiation from the central source and stars of the nuclear cluster), in competition with the replenishment of dust by stellar winds and the infall of clouds from the outer regions, where the circumnuclear torus is present (Antonucci 1993; Urry & Padovani 1995). The co-evolution of gas and dust phases within clouds falling onto a supermassive black hole is relevant for our understanding of mass transport in the innermost regions of galactic nuclei.

Recently, an infrared-excess source named G2/DSO has been discovered (Gillessen et al., 2012) and subsequently detected in L- and K-bands (Gillessen et al. 2013a; Phifer et al. 2013; Eckart et al. 2013b), see Figure 4.1.

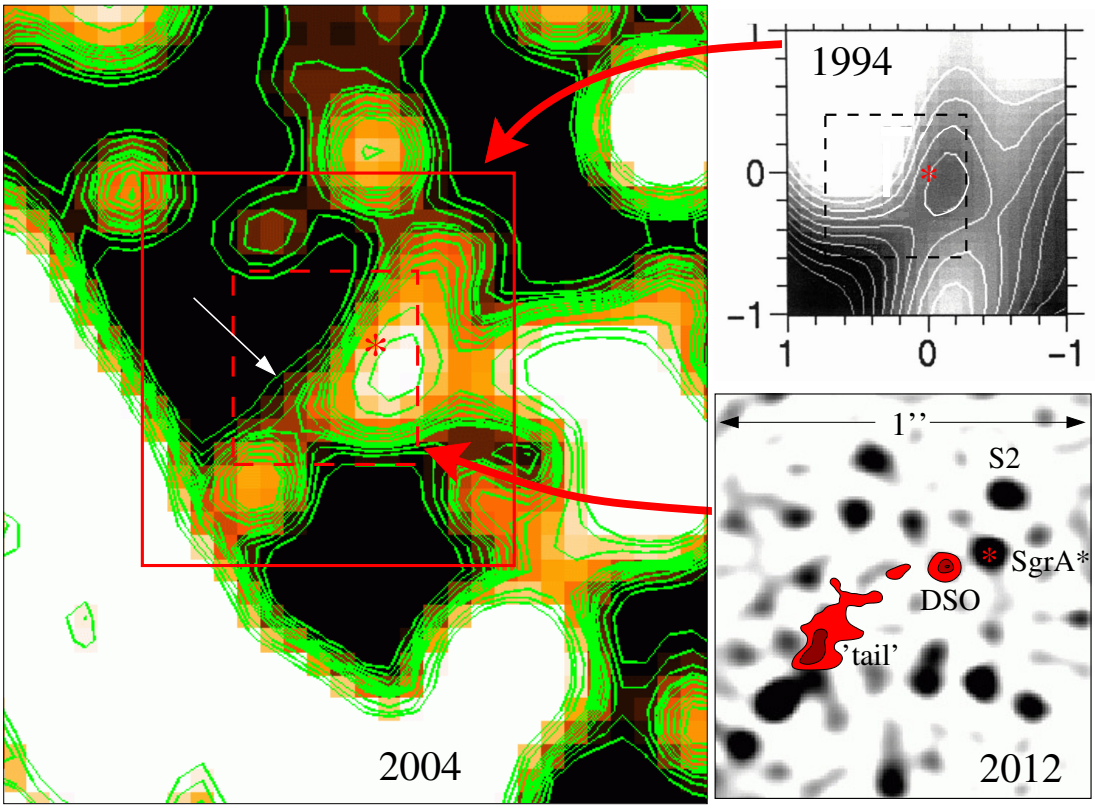

Figure 4.1: The 2004 VISIR and 1994 Palomar (Stolovy et al. 1996) 8.7 micron images, a source/flux ridge at the position of the DSO/G2 'tail' can be identified (white arrow). A 2012 NACO Ks-band image with the DSO and its 'tail' contours in red is shown. The image scales are given in arcseconds (figure adopted from Eckart et al., 2013b).

It may indeed be a manifestation of a common mechanism of material transport in low-luminosity nuclei. We analyse the scenario of an infrared-excess, dusty stellar source. As indicated in Shcherbakov (2014), the cloud component of the source is optically thin and diluted and not thick and dense. Therefore, it is valid to assume that the cloud component is mainly constituted by the gaseous wind driven by the radiation pressure of central star and the dust that is located and formed in such a wind. This is the reason that in the following analysis we assume the dust to be in contact only with stellar wind and the ambient atmosphere around Sgr A* through which G2/DSO travels.

The adopted scenario is not necessarily only connected to this single event. It may be applied to other observed infrared-excess stellar sources that have been shown to move through the gaseous medium near the Galactic centre (e.g., Moultaka et al., 2005, Mužić et al., 2010). Moreover, it may be relevant for modelling the environment in other low-luminosity active galactic nuclei.

In this analysis we adopt a simplified (toy) model: dust grains are treated as numerical particles under the influence of gravity of SMBH ($M = M_\bullet$) and the embedded star ($M = M_\star$), or the components of a binary ($M_\star^{(1)}$, $M_\star^{(2)}$), and the effect of an outflowing wind of gas. We focus on dust-enshrouded stars with different distributions of dust bound to the central star, and we explore the amount of material that is lost from the cloud to the black hole. Effects arise from the ambient pressure of a central wind, the wind pressure from the star, and a bow-shock forming at the interface of winds. The star moves at transonic speed near the pericentre.

In this way we address the question whether and how dust particles embedded in the wind envelope are affected by close passages near the SMBH. For most model parameters, most of the dusty material is stripped from the envelope already on the first transit. For low accretion rates, the dust component can survive down to quite small radii, especially in regions shielded by obscuration. Furthermore, if the Field criterion (Field 1965; Barai et al. 2012) is fulfilled for the thermal stability of a two-temperature medium, the dust may co-exist with the hot medium at the same radius. The dust component by itself would be unimportant, but it contributes significantly to the radiation in NIR and tracing it helps to understand the observed emission. Similar treatment of dust dynamics is often employed in other astrophysical systems (mainly protoplanetary discs and stellar atmospheres, see e.g., van Marle et al., 2011).

We model the encounters over a broad span of parameters. To present specific examples we use orbital parameters relevant for the Galactic centre G2/DSO infrared source (Gillessen et al. 2013b), and we also attempt to distinguish among different outcomes of the passages through the pericentre (Eckart et al. 2013c; Phifer et al. 2013).

Furthermore, we point out to the possibility that the stellar core may actually consist of two components of a binary star. This idea is suggested by models of the origin of S-stars in the Galactic centre as a product of three-body interaction during the pericentre passage of a binary star on a highly eccentric trajectory (Gould & Quillen 2003; Perets et al. 2007). Although the presence of a stellar core and its putative binary nature within the G2 cloud are on a purely hypothetical level, this scenario can connect, in a natural way, two apparently different aspects: the high eccentricity of the plunging trajectory, and the origin of the population

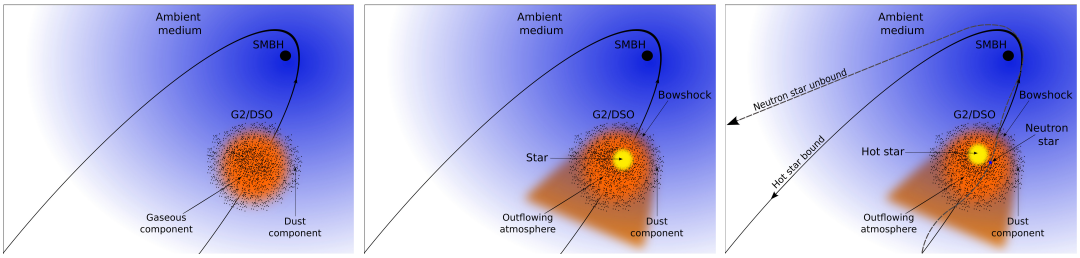

Figure 4.2: Three variants of the model setup for which the predictions are qualitatively different especially at the post-pericentre phase. The model ingredients include the central supermassive black hole (black circle), an infalling cloud made of gas and dust (red), an embedded star (yellow), and a hot diluted flow (blue). We consider the pericentre at about 10^3 Schwarzschild radii, so that the star is not expected to be tidally disrupted. However, the gaseous/dusty envelope is affected significantly. *Left panel:* a core-less cloud on an eccentric trajectory, interacting with the diluted ambient medium near the SMBH. *Middle panel:* the cloud enshrouds an embedded star. A radial wind of the outflowing gaseous atmosphere occurs and a bow-shock forms ahead of the stellar body. *Right panel:* binary system enclosed by a common envelope that becomes largely dispersed at the first pericentre passage. At the same time, the three-body interaction with the central SMBH causes the binary components to separate from the nominal trajectory.

of stars near the supermassive black hole. If there is indeed a star enshrouded by a dusty atmosphere, it was proposed that high eccentricity can be achieved by the Kozai mechanism (Šubr & Karas 2005) or by resonant relaxation (Hopman & Alexander 2006).

The geometrical setup and the main ingredients of our model are illustrated in figure 4.2. Three different flavours of the basic scenario were considered: a core-less cloud infalling onto the SMBH, a star embedded within the dusty envelope, and an embedded binary that becomes disrupted near the SMBH. We focus on the latter two scenarios. Our simplified approach is complementary to purely hydrodynamical situations that neglect the dust component (Anninos et al. 2012; Burkert et al. 2012; Ballone et al. 2013; Shcherbakov 2014), which is consistent with an optically thick, dense medium where the dust is dragged along with the gas. However, for optically thin atmospheres, dust dynamics needs to be treated separately.

In the following analysis, we do not treat Brγ production or the radiation processes in the bow-shock region (Sądowski et al. 2013). We do see, however, that the dusty envelope is stretched by the gravitational and drag forces (depending on the initial distribution of particles in phase space and the parameters of the wind outflow), which leads to the gradual offset between the dust component and the stellar core. We note that observationally any difference between the cloud location in L-band with respect to the location of K (Brγ) in the orbit is most likely due to uncertainties in the determination of the orbital positions; it may be heavily affected by different systematics in the two bands.

The chapter is organized as follows: in sect. 4.2 we set up the model and describe the numerical procedure to explore the mutual interaction between the

star and its environment. We discuss the dependence of the dust temperature on the distance and the luminosity of the central source. Then we consider the effect of the star enshrouded by an initially spherical dusty envelope and a remnant disc. In sect. 4.3, we present the results of the simulations including the wind blowing from the centre and the effect of the bow-shock region. We compare the difference between a disc-like Keplerian distribution and a Gaussian distribution of particles in the phase space. Finally, we determine the fraction of dust mass affected at subsequent encounters, and we show the offset that develops gradually between the centre of mass of the cloud and the nominal position of the star in the orbit. In sect. 4.4 we summarize and discuss our results, and we conclude in sect. 4.5.

4.2 Model setup, numerical scheme, and tests

4.2.1 Clouds infalling onto SMBH

Accretion tori are not smooth, instead, they often form individual clouds with a mixed composition of gas and dust phases (e.g., Cox 2005; Vladimirov et al. 2005). The patchy structure evolves by collisions, and some of the clumps can be set on a highly eccentric trajectory with the pericentre close to the central black hole. Interaction with the surrounding environment leads to the drift and gradual separation of different constituents of the cloud and deformation of its shape – dust and gas components of the cloud move with respect to each other, and with respect to the star (if embedded in the cloud core).

A bow shock develops around an embedded star and different species are transported across discontinuities in a different manner (smaller grains tend to be bound to the gas component, while the large grains are capable of penetrating into the interstellar medium; cf. MacGregor & Stencel 1992; van Marle et al. 2011; Keppens et al. 2012). If large portions of the medium are neutral, viscous forces play an important role, while in a fully ionised plasma the efficient mechanism of dust grain charging operates. Then the main parameter that defines the coupling between dust and gas is the Coulomb coupling parameter, which is the ratio of the Coulomb potential energy of the particle interaction to the kinetic energy of the thermal motion. Depending on the system parameters, both weak coupling and strong coupling have been observed in dusty plasmas.

The grain size is a dominant factor for the forces acting on the gas/dust mixture. The mutual coupling between these two components of the complex plasma (including the viscous forces) is thought to just increase the effective dust grain mass by the amount of gas that is dragged along in the coupling. The particle mass is not relevant within the strong gravitational field of the SMBH and/or the star, instead, it may only be relevant for the wind force acting on the dust. For a gas-to-dust ratio of 100:1, the effective increase of the grain mass load by two orders of magnitude would then correspond to the grain size variation by factor of about 5. This is well contained in the factor of a hundred in the grain sizes that we considered here. The relation between size and mass is uncertain because grains are most likely fluffy and not solid. Moreover, other factors are also connected with the grain size, for example, the typical electric charge that can develop by the interaction with the surrounding plasma and by photoionisation.

An infalling cloud passes through the external environment with physical properties spanning a wide range of values. We modelled the passages of stars with dusty envelopes through the pericentre by numerically integrating the trajectories of star(s) and that of dust particles that represent one of elementary constituents of the cloud. These are followed in the gravitational field of the SMBH, taking into account the hydrodynamical interaction with the diluted ambient wind. Gravitational effects need to be taken into account, but nonetheless, the Newtonian description is adequate for the gravitational field because we considered the motion with the pericentre at $\simeq 10^3 r_{\rm s}$, so not in the immediate vicinity of the black hole horizon, where the relativistic effects on the orbit evolution become important. The variety of factors listed above underline a potentially important influence of the grain properties for the gas/dust coupling and hence support our simulation approach.

We employed the integration package `Swift` (Levison & Duncan 1994), which has been designed to evolve a set of mutually gravitationally interacting bodies together with a group of test particles that are influenced by gravity of the massive bodies, but do not affect each other (or the massive bodies). In the numerical scheme we included the effect of radial wind outflow and that of ambient gaseous wind and employed a sufficiently accurate Bulirsch-Stoer integrator with an adjustable time-step.

The adopted procedure allowed us to follow a large number of numerical particles in the gravitational field, namely, a superposed gravitational field of the central SMBH and the embedded star. The gravity of the black hole plays a role in the motion of parcels because their mass is relatively large (like dust grains compared to gas atoms), but we modified the integration routine to also include the hydrodynamic drag that acts through the interaction of particles with the gaseous ISM as well as an outflowing stellar wind. The dust grain mass is a parameter that allowed us to study different cases, including a toy model where the grains represent super-particles of mass exceeding that of realistic cosmic dust.

4.2.2 Tidal stretching of a cloud

The simplest model of an infalling cloud is a swarm of non-interacting particles that do not interact with the surrounding environment. As will be shown, the ambient medium affects considerably the motion of both gas and dust. However, the temporal evolution of positions and velocities of elementary constituents of the cloud moving on a highly eccentric orbit will show how gravity alone effects the shape of a cloud in the phase space (with and without star embedded).

For the nominal trajectory of the object, we used the orbital elements derived using L'-band astrometry Gillessen et al. (2013a) (see Table 4.1). For comparison, we also use the recent values derived using Brγ astrometry (Phifer et al. 2013), L'-band, and Brγ based data Gillessen et al. (2013b).

The tidal force is given by $\delta a_{\rm G} = (-GM_\bullet/r^3) D_{\rm cloud}$, where $D_{\rm cloud}$ is the characteristic scale of the cloud and r the distance from the SMBH. The ratio of the tidal force to the acceleration in the potential of the SMBH is simply $\delta a_{\rm G}/a_{\rm G} \approx -D_{\rm cloud}/r$, which for $D_{\rm cloud} \approx 100\,{\rm AU}$ and the distance near the pericentre $r \approx 300\,{\rm AU}$ yields $\delta a_{\rm G}/a_{\rm G} \approx -1/3$, so tidal forces are of importance for

	Gillessen et al. (2013a) - L'	Phifer et al. (2013) -Brγ	Gillessen et al. (2013b) -L'	Gillessen et al. (2013b)-Brγ
Semi-major axis[mas]	666 ± 39	831 ± 223	684 ± 33	1048 ± 118
Semi-major axis[pc]	0.027 ± 0.002	0.033 ± 0.009	0.028 ± 0.001	0.042 ± 0.005
Eccentricity	0.9664 ± 0.0026	0.9814 ± 0.0060	0.9698 ± 0.0031	0.9762 ± 0.0074
Inclination [°]	109.48 ± 0.81	121 ± 3	110.2 ± 1.4	118.1 ± 2.0
Position angle of the ascending node [°]	95.8 ± 1.1	56 ± 11	94.5 ± 1.8	81.9 ± 4.3
Angle to periapse [°]	108.50 ± 0.74	88 ± 6	108.6 ± 1.2	97.2 ± 2.2
Epoch of periastron [yr]	2013.69 ± 0.04	2014.21 ± 0.14	2013.72 ± 0.05	2014.25 ± 0.06
Orbital period (yr)	198 ± 18	276 ± 111	206 ± 15	391 ± 66

Table 4.1: Orbital elements for the nominal trajectory of the cloud approaching the SMBH.

extended gaseous-dusty structures, such as clouds or envelopes around stars.

For illustration, we plot the temporal evolution of the velocity magnitude, the distance (Fig. 4.3), and the line-of-sight velocity component transformed to the local standard of rest (Fig. 4.4). In Figs. 4.3 and 4.4, we compare the evolution for the mean orbital elements determined by Gillessen et al. (2013a,b); Phifer et al. (2013).

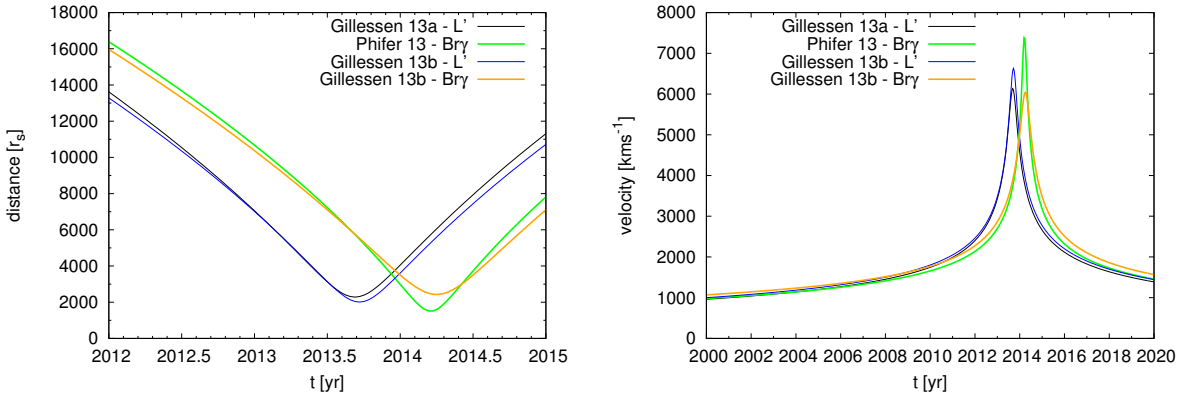

Figure 4.3: The temporal evolution of the distance of the cloud from the SMBH in Schwarzschild radii (left) and of the velocity magnitude (right). The orbital elements were taken from Gillessen et al. (2013a,b); Phifer et al. (2013).

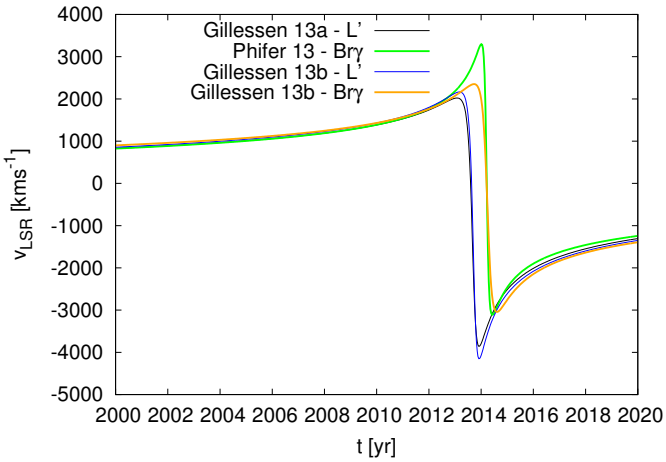

Figure 4.4: The temporal evolution of the line-of-sight velocity component transformed to the local standard of rest (LSR). The orbital elements were taken from Gillessen et al. (2013a,b); Phifer et al. (2013).

Model I: Large velocity dispersion

Our N-particle model consists of 10 000 particles. The initial conditions were set for the epoch 2000.0. We assume that the positions and the velocities are distributed according to the Gaussian distribution in the position-velocity phase space and the velocities are assumed to be isotropic. The initial FWHMs are 25 mas and 120 $\mathrm{km s^{-1}}$. In Fig. 4.5, we plot the evolution of the cloud in right ascension and declination coordinates.

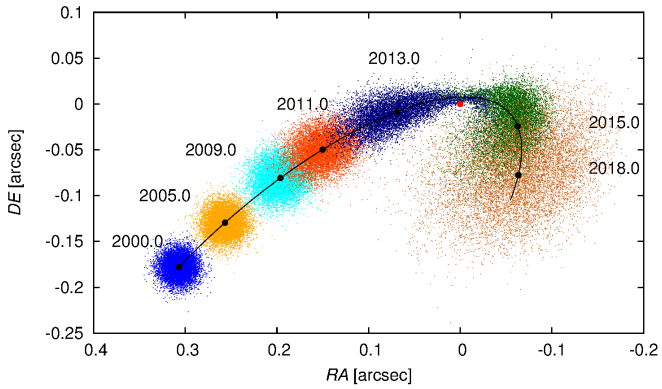

Figure 4.5: The evolution of the cloud along the nominal trajectory as seen from the Earth.

It is also useful to plot the projected distance of the cloud from the SMBH with respect to the line of sight velocity component since it enables one to see the rapid increase of velocity and its gradient while approaching the pericenter (see Fig. 4.6).

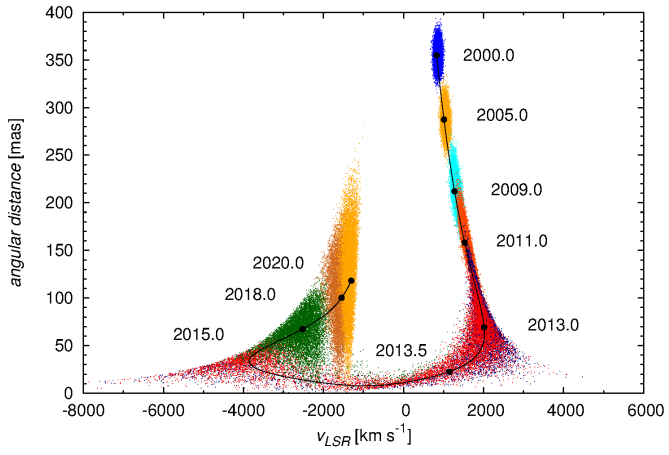

Figure 4.6: The position-velocity graph with a few marked positions on the nominal orbit for given years.

Model II: Small velocity dispersion

Case A: First, we investigate the case when a massive star could reside inside the cloud. As before, we start the integration in 2000.0. Our N-particle cloud consists of 5 000 particles and one star with the mass 10 $M_{\odot}$. We set up the parameters in such a way that the velocity of most particles is less than the escape velocity of the star at a given radius. The FWHMs of the Gaussian distributions are 25 mas and 12 kms^{-1}. We plot the evolution of the cloud-star system in right ascension and declination plane (see Fig. 4.7).

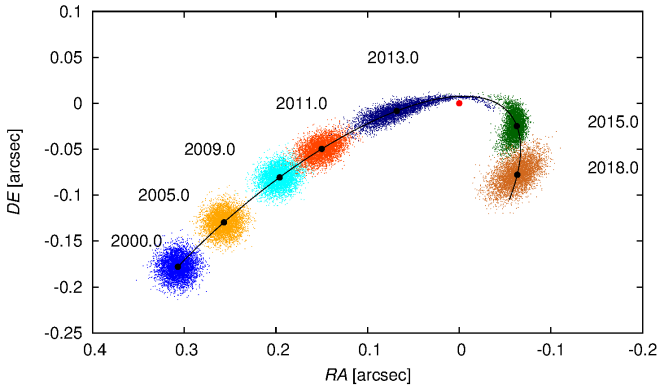

Figure 4.7: The evolution of the cloud-star system along the nominal trajectory as seen from the Earth.

As in case of a purely dust cloud, we plot the projected distance of the cloud from the SMBH with respect to the line of sight velocity component (see Fig. 4.8).

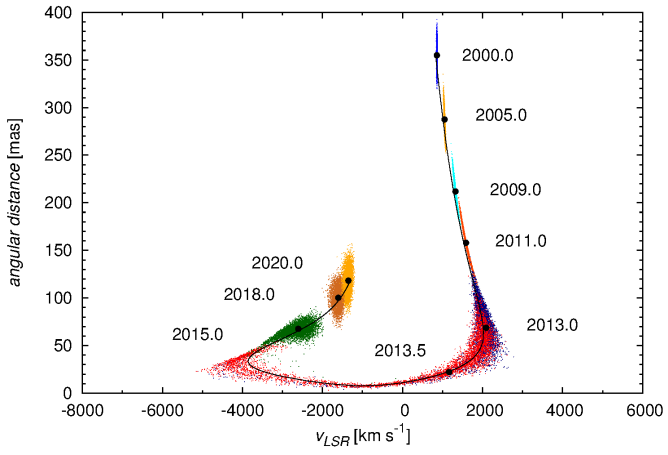

Figure 4.8: The position-velocity graph of the cloud-star system with a few labelled positions of the star for chosen years.

Case B: We investigate a dust cloud as before, but we start with a small velocity dispersion (FWHM 12 kms^{-1}). This time we study the evolution of the

cloud during the whole period. The results are plotted in the position-velocity graph (Fig. 4.9).

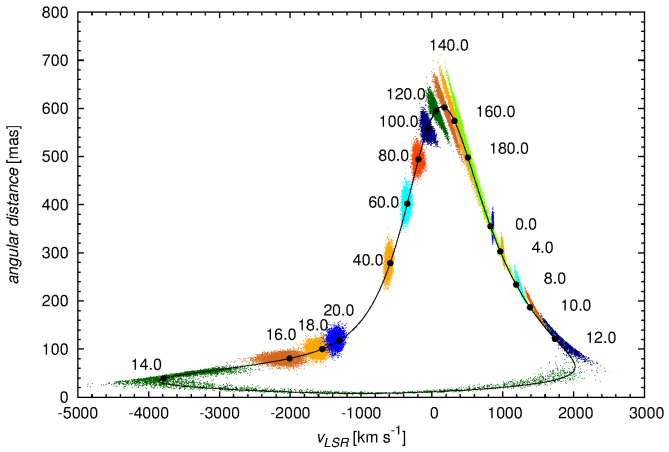

Figure 4.9: The position-velocity plot of the cloud with an initially small velocity dispersion (FWHM 12 kms^{-1}). The initial position is marked as 0.0 and the subsequent positions are labelled as elapsed years from the initial one.

Model III: Protoplanetary disc

Finally, we test the idea of a protoplanetary disc put forward by Murray-Clay & Loeb (2012). We produce a disc consisting of 5 000 particles with Keplerian velocities. The disc radius is 100 AU and has a uniform distribution of inclination, $(0, 30)^\circ$ and $(150, 180)^\circ$. The mass of the star is set to 10 $M_\odot$. The integration lasts from the epoch 2000.0 to 2020.0. In Fig.4.10, we plot the evolution of the disc-star system along the nominal trajectory.

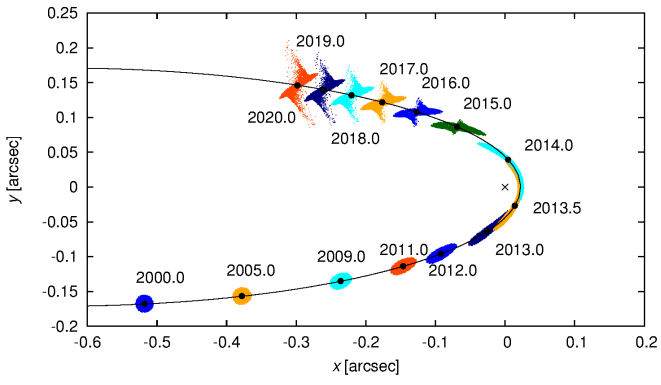

Figure 4.10: The evolution of the disc-star system along the nominal trajectory.

In all discussed cases we see that velocity dispersion increases up to the pericentre and then it decreases. This is a typical behaviour when only gravity determines the evolution. In case when non-gravitational forces are involved, mainly hydrodynamic drag of the ambient medium, extended gaseous-dusty structures

are affected the most at the pericentre due to the highest velocity - the cloud constituents are slowed down, lose kinetic energy, and spiral towards the SMBH.

4.2.3 Non-gravitational forces acting on dust

Although the stellar atmosphere consists largely of outflowing gas, here we concentrated mainly on the dust component. Both species interact with each other, but they can separate to a certain extent during the evolution. Observationally, the gas is expected to be revealed by Brγ spectral line emission, while the dust grains will contribute to the thermal continuum and can be detected by polarisation. This provides information about in situ conditions of the surrounding environment, but the predictions are currently uncertain due to incomplete knowledge about the nature and composition of G2/DSO.

In a galactic nucleus all objects interact with the hot plasma that is supplied by stellar winds, in particular, of hot, massive OB stars. The effects of this interaction depend on temperature and density profiles of the ISM. For the purpose of this work, we used semi-analytical relations for electron density $n_\mathrm{e}(r)$ and electron temperature $T_\mathrm{e}(r)$ radial profiles based on the models of radiatively inefficient accretion flows (Broderick & Loeb 2006; Broderick et al. 2011),

$$n_\mathrm{e}(r) = n_\mathrm{e}^0 \left(\frac{r}{r_\mathrm{s}}\right)^{-1.1}, \quad T_\mathrm{e}(r) = T_\mathrm{e}^0 \left(\frac{r}{r_\mathrm{s}}\right)^{-0.84}. \tag{4.5}$$

In these dependencies, we considered quantities n_e and T_e to adopt averaged values, $n_\mathrm{e}^0 = 3.5 \times 10^7\,\mathrm{cm}^{-3}$ and $T_\mathrm{e}^0 = 9.5 \times 10^{10}\,\mathrm{K}$. Electrons are decoupled from ions at small distances from the SMBH; ion temperatures are ~ 1 to 5 times higher than electron temperatures resulting from MHD simulations (e.g., Dexter et al. 2010). The density profile (4.5) is used in eq. (4.10) to estimate the ambient density $\rho_\mathrm{a} = m_\mathrm{H}\, n_\mathrm{H}$ (with $n_\mathrm{H} \approx n_\mathrm{e}$).

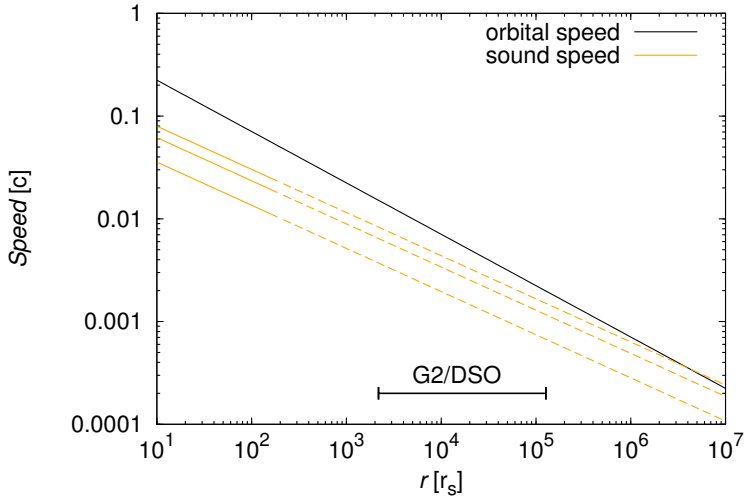

Figure 4.11: Comparing the orbital (Keplerian) velocity with the sound speed at corresponding radius from the central black hole (units of Schwarzschild radii). The range of G2/DSO is labelled. On the vertical axis, the unit of speed is the speed of light, c.

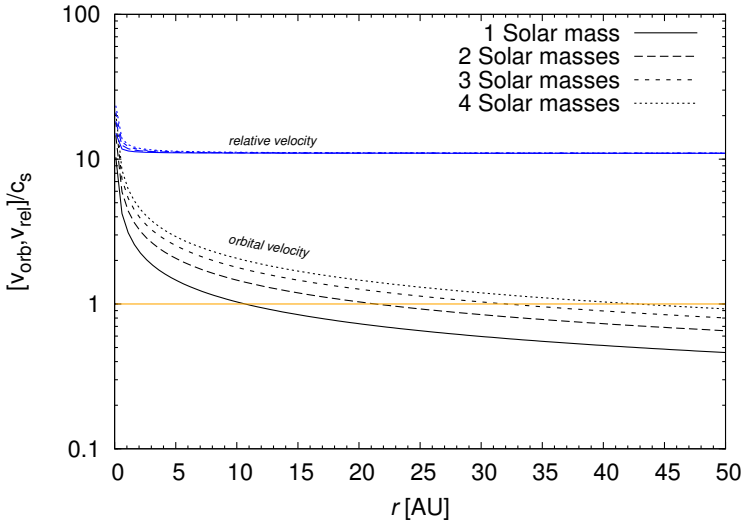

Figure 4.12: Ratio of orbital velocities (black lines) and relative velocities (blue lines) to the speed of sound as a function of distance from the star. Relative velocities are typically higher than the sound speed by about one order of magnitude for wind velocities of the order of $100\,\mathrm{km\,s^{-1}}$.

The profiles in eq. (4.5) were originally derived for the accretion flows up to $\sim 100\,r_\mathrm{s}$, whereas we considered the pericentre passages at a typical distance one order of magnitude larger, $r \sim 10^3\,r_\mathrm{s}$. However, the densities inferred from the one-dimensional model (used to fit Chandra X-ray data farther away from the Galactic centre; Quataert 2004) do not differ much when extrapolated from the inner flow to the region of our interest (factor of ~ 3; see Psaltis 2012, for comparisons).

In general, the equation describing the motion of dust particles in the gaseous environment (optically thin stellar atmospheres, protoplanetary discs) is

$$\frac{\mathrm{d}\mathbf{v}}{\mathrm{d}t} = \mathbf{a}_\mathrm{grav} + \mathbf{a}_\mathrm{drag} + \mathbf{a}_\mathrm{rad}\,, \tag{4.6}$$

where $\mathbf{a}_\mathrm{grav}$ represents gravitational interactions, $\mathbf{a}_\mathrm{drag}$ stands for the wind drag acceleration, and $\mathbf{a}_\mathrm{rad}$ is the acceleration due to radiation pressure.

The radiation pressure acceleration acting on a grain that is located at distance $r_\star$ from the star with flux $\Phi_\star = L_\star/(4\pi r_\star^2)$ may be expressed by (e.g., Bertotti et al., 2003)

$$\mathbf{a}_\mathrm{rad} = Q\frac{\Phi_\star \sigma_\mathrm{eff}}{mc}\left[\left(1 - \frac{\mathbf{r}_\star\cdot\mathbf{v}_\star}{r_\star c}\right)\frac{\mathbf{r}_\star}{r_\star} - \frac{\mathbf{v}_\star}{c}\right] + \mathcal{O}\left(\frac{v_\star^2}{c^2}\right)\,, \tag{4.7}$$

where the factor Q reflects the way the particle absorbs or reflects light, m denotes the dust mass, σ_eff its effective cross-section, $\mathbf{v}_\star$ is the velocity vector in the frame of the star, and c is the speed of light. The terms in the brackets represent the direct pressure, the change of radiation energy due to the Doppler effect, and the Poynting-Robertson drag, respectively. Eq. (4.7) is valid in a Newtonian approximation that is consistent with the pericentre passage of a star at the distance of $\sim 1000\,r_\mathrm{s}$ at most. However, in the immediate vicinity of the SMBH, it would be necessary to include the second and higher powers of $(v_\star/c)$ as well.

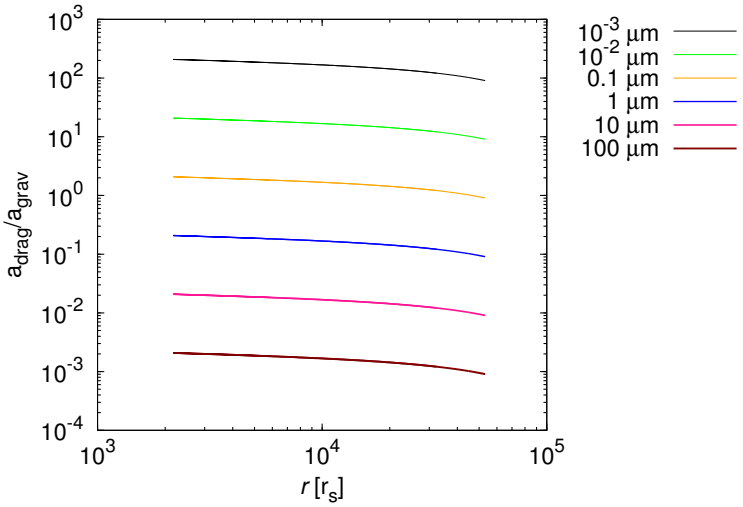

Figure 4.13: Ratio of the hydrodynamical drag to the gravitational acceleration across the range of radii. The two effects can be of comparable magnitude and, therefore, both need to be taken into account in the model of the orbit evolution.

The first two radial terms in eq. (4.7) effectively change the mass of the star, which itself is a free parameter in our model, and the non-radial Poynting-Robertson term causes the decrease in the semi-major axis and eccentricity of the orbit and contributes to the inspiral of dust towards the star on the Poynting-Robertson time scale $\tau_{\rm pr}$, which may be approximated using eq. (4.7) and setting the effective cross-section equal to the geometrical cross-section of the grain, $\sigma_{\rm eff} = \pi R^2$:

$$\begin{aligned}\tau_{\rm pr} &= \frac{16\pi c^2}{3Q} L_\star^{-1} R \rho_{\rm d} r^2 \\ &= 28 \times 10^2\,{\rm yr}\,\frac{1}{\rm Q}\left(\frac{\rm L_\star}{\rm L_\odot}\right)^{-1}\left(\frac{\rm R}{1\,\mu{\rm m}}\right)\left(\frac{\rho_{\rm d}}{1\,{\rm g cm^{-3}}}\right)\left(\frac{\rm r}{1\,{\rm AU}}\right)^2 . \end{aligned} \tag{4.8}$$

In our model, we worked with time scales of 100 yr, which are shorter than $\tau_{\rm pr}$ by one order of magnitude for distances of ~ 1 AU. For more distant orbits, the time scale is significantly prolonged because of its quadratic dependence on the distance.

The radiation pressure from other S-stars in the background also contributes, but it is at least two orders of magnitude weaker. For an estimate, we took $\sim$ 500 mas $\approx$ 4125 AU as an average distance of individual S-cluster members. The estimated number of $\sim$ 20-$M_\odot$ stars is $\sim$ 30 and we compared the effect of their radiation with a low-mass (LM) star of 2 $M_\odot$. Hence, the ratio of accelerations due to radiation, eq. (4.7), is

$$\frac{a_{\rm LM}}{a_S} \approx \frac{L_{\rm LM}}{30 L_{\rm S}} \left(\frac{r_{\rm S}}{r_{\rm LM}}\right)^2 \approx \frac{1}{30}\left(\frac{M_{\rm LM}}{M_{\rm S}}\right)^{3.5}\left(\frac{r_{\rm S}}{r_{\rm LM}}\right)^2 = \frac{1}{30}\left(\frac{2\,M_\odot}{20\,M_\odot}\right)^{3.5}\left(\frac{4125\,{\rm AU}}{1\,{\rm AU}}\right)^2 \approx 180\,. \tag{4.9}$$

Similarly, the Poynting-Robertson time scale, eq. (4.8), yields $\tau_{\rm pr} \approx 10^5\,{\rm yr}$ for the average distance of 500 mas and the luminosity of ~ 30 20-$M_\odot$ stars. Scoville & Burkert (2013) also estimated that although a production rate of Lyman continuum photons is high, very few of them are intercepted because of the small area of the bow shock formed ahead of the star. Hence, the effect of radiation pressure from background stars is weak on the time scale of $\sim 100\,{\rm yr}$ considered here.

The radiation drag in the vicinity of a putative star will only slightly affect individual orbits of grains on the time scale of a few orbital periods. The ensemble of particles behaves similarly with and without the radiation term involved, which shows that gravitational forces and hydrodynamical drag are dominant for their dynamics. To reduce computation costs, we omitted this term in most of our numerical calculations.

The acceleration caused by the drag for both supersonic (Stokes law) and subsonic (Epstein law) modes may be written in a closed form (e.g., Kwok, 1975, van Marle et al., 2011):

$$\mathbf{a}_{\rm drag} = -\eta_{\rm drag}\frac{\pi R^2}{m}\rho_{\rm a}\sqrt{v_{\rm rel}^2 + \overline{v}_{\rm t}^2}\,\mathbf{v}_{\rm rel}\,, \tag{4.10}$$

where $\mathbf{v}_{\rm rel} = \mathbf{v} - \mathbf{v}_{\rm g}$ is the relative velocity of grains with respect to the gas motion $\mathbf{v}_{\rm g}$. The mean thermal velocity, assuming Maxwellian distribution, is $\overline{v}_{\rm t} = (8/\pi)^{1/2} c_{\rm s}$, which is proportional to the sound speed $c_{\rm s} = \sqrt{kT/m_{\rm H}}$ (for ideal gas). The factor $\eta_{\rm drag}$ acquires the value 4/3 for the Epstein law and $1/2C_{\rm d}(Re)$ for the Stokes law, where the coefficient $C_{\rm d}(Re)$ depends on the Reynolds number Re (for an in-depth discussion see Perets & Murray-Clay, 2011). As shown in Fig. 4.11, orbital velocities within the inner $\sim 10^6$ Schwarzschild radii are supersonic, $v_{\rm orb} \approx \sqrt{GM_\bullet/r} > c_{\rm s}$, so the Stokes law is approximately valid. This is also true for grains embedded in the outflowing wind atmosphere close to the star, see Fig. 4.12. If we assume an isothermal atmosphere with $T \approx 10\,000{\rm K}$ that is in ionisation equilibrium with the environment, orbital velocities are approximately equal to the sound speed at distance $r_{\rm s} \approx GM_\star m_{\rm H}/(kT)$ and decrease. However, relative velocities with respect to radial outflow, in case of circular orbits of grains, are higher than the sound speed by about factor of 10 for typical terminal wind velocities of $100\,{\rm km\,s^{-1}}$. Assuming that grains have a spherical shape with diameter d and substituting the dust grain volume times density for the mass, we obtain $\mathbf{a} \approx -\frac{3}{4}C_{\rm d}(Re)(\rho_{\rm a}/\rho_{\rm d})d^{-1}v_{\rm rel}\mathbf{v}_{\rm rel}$ and we set $C_{\rm d} = 1$.[2]

[2]From subsonic to supersonic regimes, the drag coefficient changes typically by about a factor of two.

We note that the magnetic field frozen in the stellar wind and potentially that of the interstellar medium near the galactic nucleus as well may influence the motion of charged dust, mainly of a smaller size. This is mainly determined by the ratio of the charge of the grain q resulting from photo-charging and its mass m, q/m. When the main component of the field is radial, $\mathbf{B} = B_{\rm r}\hat{\mathbf{r}}$, and dust motion is azimuthal, $\mathbf{v} = v_\phi\hat{\boldsymbol{\phi}}$, the Lorentz acceleration, $a_{\rm L} = (q/m)v_\phi B_{\rm r}$ causes the grain inclination to increase or decrease, depending on the mutual orientations of the magnetic field and velocity vectors. The field orientation may flip after some time and may lead to oscillations around the orbital plane. Because of the many uncertainties concerning the magnetic field strength and the efficiency of photo-charging, we did not consider the magnetic field in our analysis.

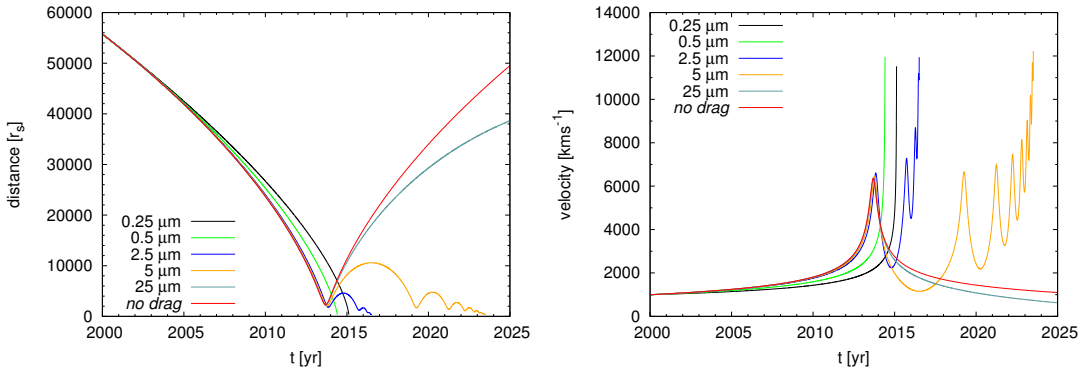

Figure 4.14: Single-particle approximation. *Left panel:* the temporal evolution of 3D distance (in Schwarzschild radii); the orbital parameters are set consistent with the G2/DSO in Galactic centre. Different particle (dust grain) sizes are considered, taking into account the effect of gravity and the hydrodynamical drag exerted by the ambient medium. *Right panel:* the corresponding velocity as a function of time. Hydrodynamical drag acts more efficiently on particles of larger size, causing their rapid in-spiralling and accretion onto the central black hole.

Despite the arguments for neglecting these terms and effects, this is just a crude model. Nonetheless, it allows us to reproduce the relevant trends in a semi-analytical way.

In figure 4.13 we plot the ratio of the magnitude of the acceleration due to the drag force (4.10) with respect to the gravitational acceleration across the range of radii. In this case we neglected the motion of ambient medium and set the relative velocity $v_{\rm rel}$ equal to the orbital speed. Although the ratio varies significantly (by six orders of magnitude), it is non-negligible for some typical particle sizes in the range $\sim 0.1\,\mu$m–$1\,\mu$m (for the smallest particles it exceeds the gravitational acceleration magnitude).[3]

[3]The effect might be more significant in AGN, where the typical density of the environment is higher than in inactive nuclei, but in that case strong irradiation leads to dust heating and destruction in a relatively large volume around the central source.

4.2.4 Dust heating and sublimation

As the cloud approaches the central region, the dust absorbs the radiation mainly at shorter wavelengths and heats up. The dust temperature grows to the sublimation temperature $T_{\rm sub}$ and eventually leads to sublimation.

We derive the relation for the equilibrium temperature of a dust grain located in the dust cloud that is at distance r from the central source of radiation. We assume that dust grains are optically thick to optical/UV/X-ray radiation that they absorb and optically thin to infrared radiation that they emit.

In standard models of dust heating and sublimation (Barvainis 1987), the grain is heated when exposed to optical/UV source with luminosity $L_{\rm uv}$. The grain then reradiates in the infrared part of spectrum, to which dust is optically thin, because the absorption efficiency Q_ν in infrared is much smaller than in short-wavelength parts of the spectrum. The absorption efficiency is modelled as a power-law function $Q_\nu = q_{\rm ir}\nu^\gamma$, where the exponent γ often acquires the value $\gamma \in (1, 2)$. For the estimate of the equilibrium temperature, we adopt the following parameters for dust grains (Draine & Lee 1984; Barvainis 1987):

Parameter	Value
Material	graphite
Evaporation temperature $T_{\rm evap}$	1500 K
$q_{\rm ir}$	1.4×10^{-24}
γ	1.6

Table 4.2: The values of basic parameters for a graphite grain (taken from Barvainis, 1987).

The radius of the grain is a free parameter in our analysis. It may acquire values from $\sim 50\,$nm up to a few micrometers, depending on the efficiency of dust coagulation to bigger particles.

For the monochromatic luminosity of a dust grain with radius a having temperature $T_{\rm gr}$ the following relation holds:

$$\begin{aligned} L_{{\rm ir},\nu} &= 4\pi a^2 \pi Q_\nu B_\nu(T_{\rm gr}) \\ &= 4\pi a^2 \pi q_{\rm ir} \nu^\gamma B_\nu(T_{\rm gr})\,, \end{aligned} \tag{4.11}$$

where $B_\nu(T_{\rm gr})$ is the Planck function.

The grain is exposed to radiation from a central source having the radiation energy density u_ν. It absorbs mostly the short-wavelength radiation (optical, UV, X-ray). The equilibrium temperature $T_{\rm gr}$ is reached when the rate at which the grain absorbs the energy equals the rate at which it radiates. Thus, assuming this condition, we get the equation:

$$\pi a^2 \int_0^\infty u_\nu c Q_{\rm uv} {\rm d}\nu = \int_0^\infty L_{{\rm ir},\nu} {\rm d}\nu\,. \tag{4.12}$$

We set $Q_{\rm uv} = 1$, so the absorption cross-section equals the geometrical cross-section. We assume that there is no absorption and emission of the radiation between the source and the surface of the cloud, so the intensity at the optical depth $\tau_{\rm uv}$ within the cloud is simply $I_\nu = I_{\nu,0} \exp(-\tau_{\rm uv})$. After inserting the luminosity relation (4.11) into (4.12), we finally get:

$$\frac{L_{\rm uv}\exp\left(-\tau_{\rm uv}\right)}{4\pi r^2} = 4\pi q_{\rm ir}\int_0^\infty \nu^\gamma B_\nu(T_{\rm gr})\mathrm{d}\nu\,, \tag{4.13}$$

where r represents the distance from the source. Now we will evaluate the integral on the right-hand side of the equation (4.13):

$$\int_0^\infty \nu^\gamma B_\nu(T_{\rm gr})\mathrm{d}\nu = \frac{2h}{c^2}\int_0^\infty \frac{\nu^{3+\gamma}}{\exp\left(\frac{h\nu}{kT}\right)-1}\mathrm{d}\nu\,. \tag{4.14}$$

After the standard substitution $x = \frac{h\nu}{kT}$ and taking the quantities independent of ν in front of the integral, (4.14) acquires the form:

$$\int_0^\infty \nu^\gamma B_\nu(T_{\rm gr})\mathrm{d}\nu = \frac{2h}{c^2}\left(\frac{k}{h}\right)^{4+\gamma} T_{\rm gr}^{4+\gamma}\int_0^\infty \frac{x^{3+\gamma}}{\exp\left(x\right)-1}\,. \tag{4.15}$$

The integral in (4.15) has the form of the Mellin transform[4], which yields the product of Gamma and Riemann zeta function $\Gamma(4+\gamma)\zeta(4+\gamma)$.

After inserting the analytic solution of the integral (4.15) into (4.13), we get the following equation:

$$\frac{L_{\rm uv}\exp\left(-\tau_{\rm uv}\right)}{4\pi r^2} = \frac{8\pi q_{\rm ir}h}{c^2}\left(\frac{k}{h}\right)^{4+\gamma} T_{\rm gr}^{4+\gamma}\Gamma(4+\gamma)\zeta(4+\gamma)\,. \tag{4.16}$$

Thus, the following relation holds for the temperature of the grain as a function of the distance from the source $T_{\rm gr}(r)$:

$$T_{\rm gr} = \left[\frac{L_{\rm uv}c^2}{32\pi^2 q_{\rm ir}h\Gamma(4+\gamma)\zeta(4+\gamma)}\exp\left(-\tau_{\rm uv}\right)\right]^{\frac{1}{4+\gamma}} r^{-\frac{2}{4+\gamma}}\left(\frac{h}{k}\right)\,. \tag{4.17}$$

We see that according to (4.17) the temperature of the grain does not depend on its size. When we express the luminosity in solar luminosity and the distance in parsecs and use the values of parameters from Table 4.2, the relation (4.17) may be rewritten to the useful form:

$$T_{\rm gr} = 9.627\left[\left(\frac{L_{\rm uv}}{L_\odot}\right)\left(\frac{1\mathrm{pc}}{r}\right)^2\exp\left(-\tau_{\rm uv}\right)\right]^{\frac{1}{5.6}}\ \mathrm{K}\,. \tag{4.18}$$

Sublimation radius. When the sublimation temperature of dust $T_{\rm sub}$ is known, we may easily derive the estimate of the sublimation radius $r_{\rm sub}$, at which the grain sublimes. From (4.17), after rearranging terms, we get:

$$r_{\rm sub} = \left[\frac{L_{\rm uv}c^2}{32\pi^2 q_{\rm ir}h\Gamma(4+\gamma)\zeta(4+\gamma)}\exp\left(-\tau_{\rm uv}\right)\right]^{\frac{1}{2}} T_{\rm sub}^{-\frac{4+\gamma}{2}}\left(\frac{h}{k}\right)^{\frac{4+\gamma}{2}}\,. \tag{4.19}$$

[4]The Mellin transform of $f(x)$ is defined as $\int_0^\infty f(x)x^{s-1}\mathrm{d}x$ for complex s. In our case $s = 4+\gamma$ and $f(x) = \frac{1}{\exp(x)-1}$, which yields the product of Gamma and Riemann zeta function $\Gamma(4+\gamma)\zeta(4+\gamma)$.

Again, after inserting the values from Table 4.2, we get a useful relation:

$$r_{\mathrm{sub}} = 567.285\, T_{\mathrm{sub}}^{-2.8} \left[\left(\frac{L_{\mathrm{uv}}}{L_{\odot}} \right) \exp\left(-\tau_{\mathrm{uv}}\right) \right]^{\frac{1}{2}} \mathrm{pc}\,, \tag{4.20}$$

where the sublimation temperature is expressed in Kelvins. We assume that below r_{sub} there is no dust or its existence is limited to obscured regions.

There are two basic constituents of cosmic dust – silicate and graphite grains. It has been determined that graphite grains have a higher sublimation temperature than silicate grains ($T_{\mathrm{evap}} \approx 1500\,\mathrm{K}$) (Barvainis 1987). In other works, it is assumed that the sublimation temperature is $T_{\mathrm{evap}} = 1000\,\mathrm{K}$ for all grains (Czerny & Hryniewicz 2011).

We estimate the optical and UV luminosity of a typical galactic nucleus. For the Galactic centre, $L_{\mathrm{uv}} \in (10^6, 10^7)\, L_{\odot}$ (Davidson et al. 1992). In order to compare the sublimation radius for different evaporation temperatures and optical depths of the cloud, we plot the sublimation radius versus luminosity of the central source representing typical luminosities in galactic nuclei, see Fig. 4.15.

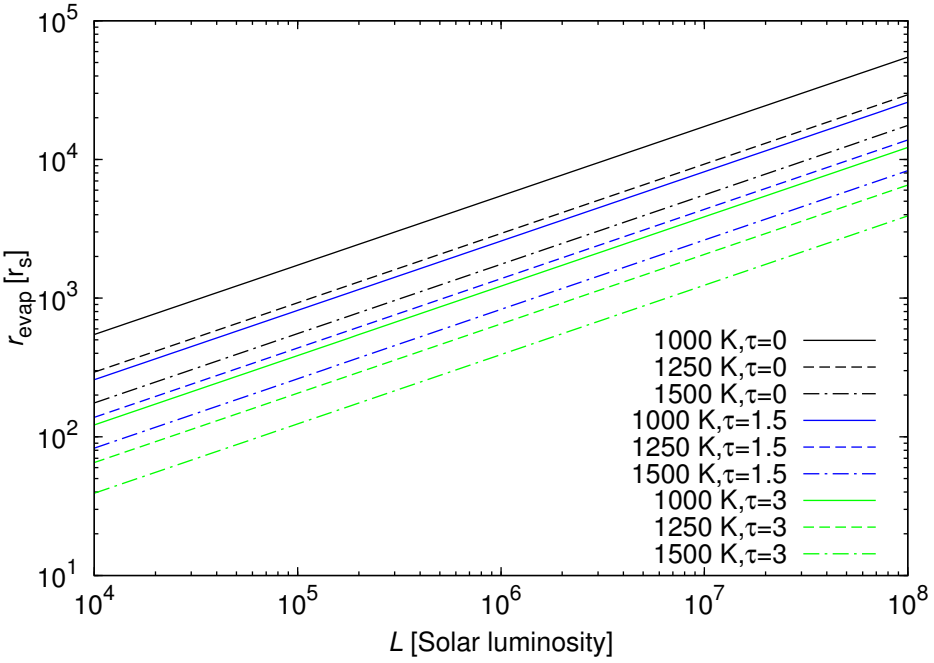

Figure 4.15: The evaporation radius versus the luminosity of a galactic nucleus. We vary the optical depth ($\tau \in \{0, 1.5, 3\}$) as well as the evaporation temperature ($T_{\mathrm{evap}} \in \{1000, 1250, 1500\}\,\mathrm{K}$).

Computing temperature of dust embedded in the cloud. As a simple application of relation (4.17) or rather (4.18), we compute the change of temperature with respect to the distance from the SMBH, while taking into account the optical depth τ_{uv} of the cloud material. We assume that the cloud moves only in the field of the SMBH on an elliptical orbit with the semi-major axis a and the eccentricity e, so the distance r as a function of the true anomaly θ is $r(\theta) = \frac{a(1-e^2)}{1+e\cos(\theta)}$. To get specific values, we adopt the orbital elements of G2/DSO

cloud from Gillessen et al. (2013a). We neglect the distance of a grain from the centre of mass of the cloud with respect to the distance r.

We plot the computed values $T_{\mathrm{sub}} = T_{\mathrm{sub}}(r, \tau_{\mathrm{uv}})$ in Fig. 4.16. The luminosity of a galactic nucleus is a parameter, for which we adopt $10^6\,\mathrm{L}_\odot$.

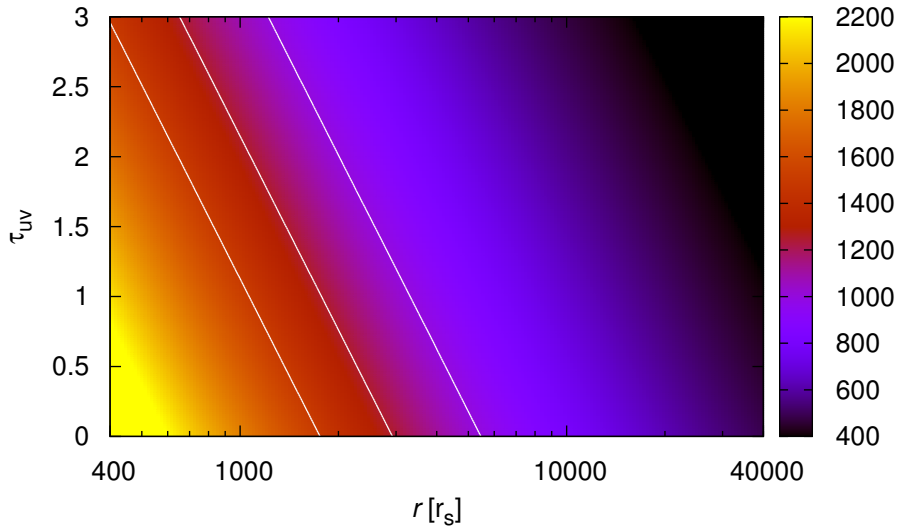

Figure 4.16: The dependence of the dust temperature (in Kelvins) on the distance r and the optical depth τ_{uv} within the cloud as expressed by the relation (4.18). For the luminosity of the center, we adopt $10^6\,\mathrm{L}_\odot$. The three lines mark the evaporation radii for 1000 K,1250 K, and 1500 K from the right to the left.

In Fig. 4.17, we plot the temporal evolution of the temperature of a dust grain for three values of the luminosity of the central source of radiation ($L_{\mathrm{uv}} \in \{10^5, 10^6, 10^7\}\,L_\odot$). Time 0.0 yr corresponds to the position of the cloud at the apocentre; the pericentre is reached at time 99 yr, where the temperature is the highest. Furthermore, there is a plot of the distance from the SMBH versus the time dependence with the scale of the equilibrium temperature of a dust grain. In this plot, we adopt the value of $10^6\,L_{\mathrm{uv}}$ for the central source luminosity. For both plots in Fig. 4.17, the optical depth τ_{uv} is set to zero, which means that we are considering an optically thin cloud or the surface layers of the cloud.

We see in Figs. 4.16 and 4.17 that below $10\,000\,\mathrm{r_s}$ the temperature of the grain in the surface layers of the cloud reaches about 800 K and increases to about 1000 K at $5000\,\mathrm{r_s}$. Naturally, the grains in the surface shell evaporate the first. On the other hand, deep in the cloud at $\tau_{\mathrm{uv}} \approx 3$, the grains survive even at the pericentre ($r \approx 2200\,\mathrm{r_s}$) with the temperature of about 800 K. However, if the cloud is completely optically thin to UV/optical radiation ($\tau_{\mathrm{uv}} \lesssim 1$), then the temperature of all grains is above 1000 K and may possibly evaporate. However, the evaporation temperature of graphite grains is higher than silicate grains ($T \approx 1500$ K,Barvainis (1987)), so these would survive the pericentre passage. Besides the uncertainty of the evaporation temperature of the dust, we have to be also aware of the uncertainty of the luminosity of the central source at shorter

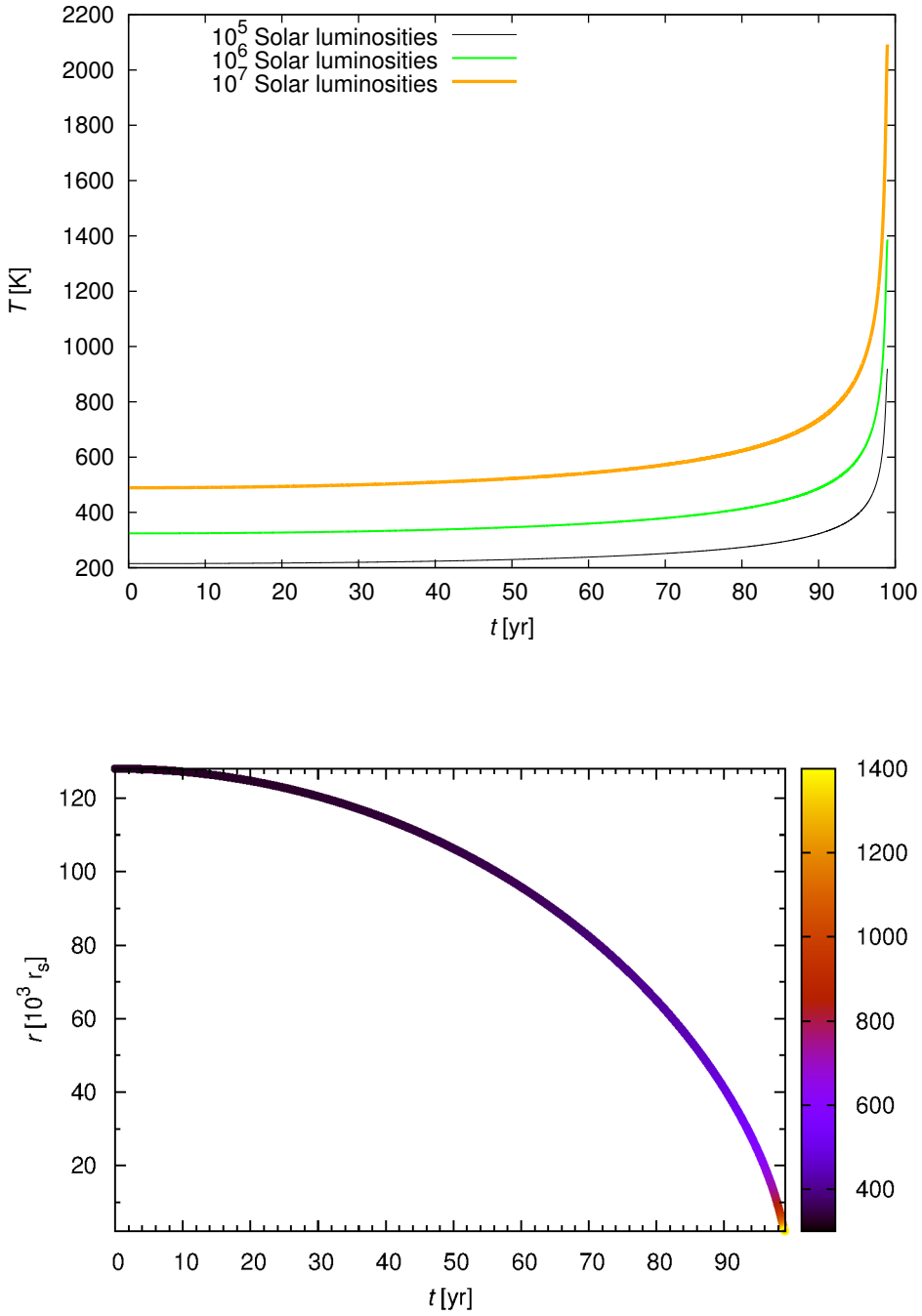

Figure 4.17: Top: The temporal evolution of the temperature of a dust grain for three values of the luminosity of the central source of radiation: $L_{\mathrm{uv}} \in \{10^5, 10^6, 10^7\}\, L_\odot$. Bottom: The distance from Sgr A* versus time plot with the colour-scale of temperature (in Kelvins) of a dust grain. In this case, $L_{\mathrm{uv}} = 10^6\, L_\odot$.

wavelengths, which may be greater or smaller than the adopted value by one order of magnitude. The one-order-of-magnitude change of luminosity changes the temperature by the factor $10^{1/5.6} \approx 1.5$, which is important, when we discuss the evaporation of dust grains (the grains having the temperature 800 K at a certain distance would have already 1200 K at the same distance for higher luminosity).

Case of the Galactic centre and implementation. When we take into account only the radiation of the central accretion flow, the sublimation radius is easily determined by eq. (4.20), which enables us to estimate the sublimation radius or inversely the temperature of dust at given r (again, realistic profiles must be more complicated; Kishimoto et al. 2011). Furthermore, in sources with radiatively efficient accretion, X-ray heating contributes significantly (Czerny & Hryniewicz 2011).

For the sublimation temperature $T_{\rm sub} \approx 1\,500\,{\rm K}$ (Barvainis 1987), low optical depth, and $L_{\rm uv} \approx 10^3\,L_\odot$, the relation (4.20) gives $r_{\rm sub} \approx 2.3 \times 10^{-5}{\rm pc} \approx 56\,{\rm r_s}$ as a lower estimate (we did not consider hot OB stars present near the centre, whose radiation probably heats the dust further). When the stellar populations are taken into account, the central luminosity can be estimated to a few $\sim 10^6\,L_\odot$ for the smooth distribution, and up to $10^7\ L_\odot$ for the clumpy structure (Davidson et al. 1992), which leads to $r_{\rm sub} \approx 2.3 \times 10^{-3}{\rm pc} \approx 5600\,{\rm r_s}$ as an upper limit for the sublimation radius.

Given the uncertainty, it is appropriate to refer to the sublimation zone extending from a few tens of Schwarzschild radii up to $\sim 5 \times 10^3\,r_{\rm s}$. To shorten the integration time of numerical experiments, we safely set the inner sublimation radius to $300\,r_{\rm s}$ in our test runs. Using the inverse relation $T = T(r, \tau_{uv})$ in eq. (4.18), we estimate the temperature profile of dust near the source of central luminosity $10^5\,L_\odot$, which is intermediate between the limits of 10^3 and $10^7\,L_\odot$ (see figure 4.18).

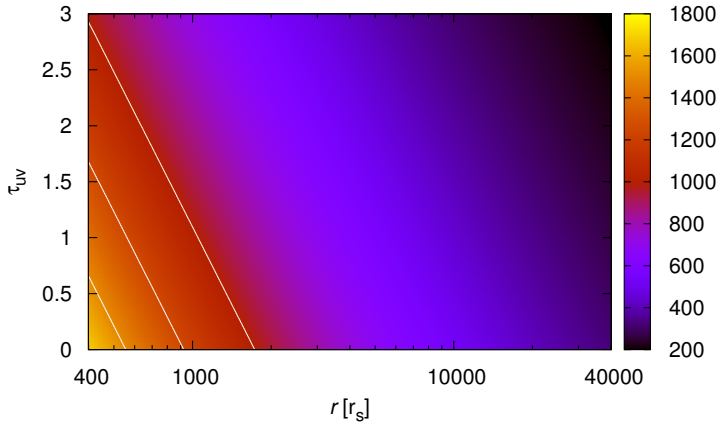

Figure 4.18: Colour-coded profile of temperature $T \equiv T(r, \tau_{uv})$ of dust for the central source of luminosity $10^5\,L_\odot$ near the central SMBH. From right to left, the three lines are isotherms corresponding to $T = 1000$ K, 1250 K, and 1500 K (dust sublimation temperature).

The passages with pericentre above $\simeq 1 \times 10^3\,r_{\rm s}$ (the case of G2/DSO, the Dusty S-cluster Object in the Galactic centre)[5] probably does not heat the dust to the sublimation temperature, which would only be reached at $\approx 600\,r_{\rm s}$. However, the mechanism of heating is more complicated not only because of the presence of stars, but also because of the shock heating that may contribute in case of transonic motion.

[5]The S-cluster is the 1″ diameter star cluster of high-velocity stars surrounding Sgr A* (Eckart & Genzel 1996; Ghez et al. 1998; Eckart et al. 2005; Melia 2007; Genzel et al. 2010).

4.2.5 Role of central star

It has often been advocated (e.g., Gillessen et al., 2013b) that the infalling DSO/G2 source may represent a core-less clump that has originated farther out at greater distance, $\gtrsim 10^4 r_\mathrm{s}$, and now is on the way toward the pericentre, where it will largely disintegrate and undergo accretion onto the SMBH. However, it may be also a dusty envelope that enshrouds a star. Extended shells surrounding stars near Sgr A* have been reported, see for example Moultaka et al. (2005).

Before the pericentre passage, the two cases are expected to produce a similar image and the corresponding spectrum to contain a thermal component from the dust. On the other hand, a transit through the pericentre must reveal the nature in a clearer way. Because we considered a pericentre distance of the order of $10^3 r_\mathrm{s}$, the star itself is not destroyed by tidal forces of the SMBH, instead, it continues to follow the eccentric ellipse. The diluted atmosphere is more visibly affected by its interaction with the ambient medium.

First, we compared the temporal evolution of the spatial distance and velocity with/without the hydrodynamical drag for the high-eccentricity orbits of a single particle. As a specific example, we used the L'-band based nominal orbital elements of G2/DSO (Gillessen et al. 2013a). The resulting evolution is plotted in figure 4.14; it appears to be consistent with eccentricities and semi-major axes of dust grains gradually decreasing, as they move in the ambient medium.

Next, we considered a cloud of particles with a certain initial distribution of positions and velocities and included different effects acting on the motion. Gillessen et al. (2012, 2013a) studied the evolution of such a cloud of particles in the field of the Sgr A* SMBH. We revisited their simulations by including the interaction with different prescriptions for the ambient wind. In our simulations, for example, 2000 particles were initially distributed according to a spherically symmetric Gaussian distribution in the position–velocity phase space. We used the same L'-band-based orbital elements for the G2/DSO cloud as above.

The evolution in the orbital plane and in the velocity–distance plane are plotted in figure 4.19 (left panels) for selected epochs since the start of the simulation. The initial FWHM of the phase-space distribution was set to be 25 mas for positions (the value adopted from Gillessen et al. 2013b), and 5 km/s as a typical turbulent velocity within the cloud. These simulations reveal that because of the drag of the ambient ISM and gravity of the SMBH, most particles continue to spiral in towards the centre. The cloud as a whole becomes progressively stretched by the tidal forces, and the velocity dispersion rises abruptly as particles approach the SMBH.

Secondly, we examined the evolution with an embedded star, whose mass has been set to $M_\star = 2M_\odot$. Dust grains ($d = 5\,\mu$m) initially obey a uniform distribution of semi-major axes in the range $(0.1, 50)$ AU, eccentricities in the range $(0, 0.1)$, and inclinations within $(0°, 180°)$.[6] The distribution of velocities is Keplerian. Fig. 4.19 also shows the evolution of such a stellar source (right panels).

The particles start to trail behind the star because of the drag. In combination with the tidal effects, the position and the velocity dispersion gradually increase

[6]Inclination values lower than 90° correspond to a prograde (direct) orbit, values exceeding 90° are reserved for the retrograde sense of motion.

up to the pericentre. During the post-pericentre phase the velocity dispersion first decreases, then increases again while particles spiral inwards to the SMBH. In Fig. 4.19 we clearly see how the attraction of the star influences some of the particles (cp. the epoch 15.05). A small fraction of particles remain bound to the star; specifically for this run, about 5‰ particles remained bound to the star; this number did not change after the second pericentre passage.

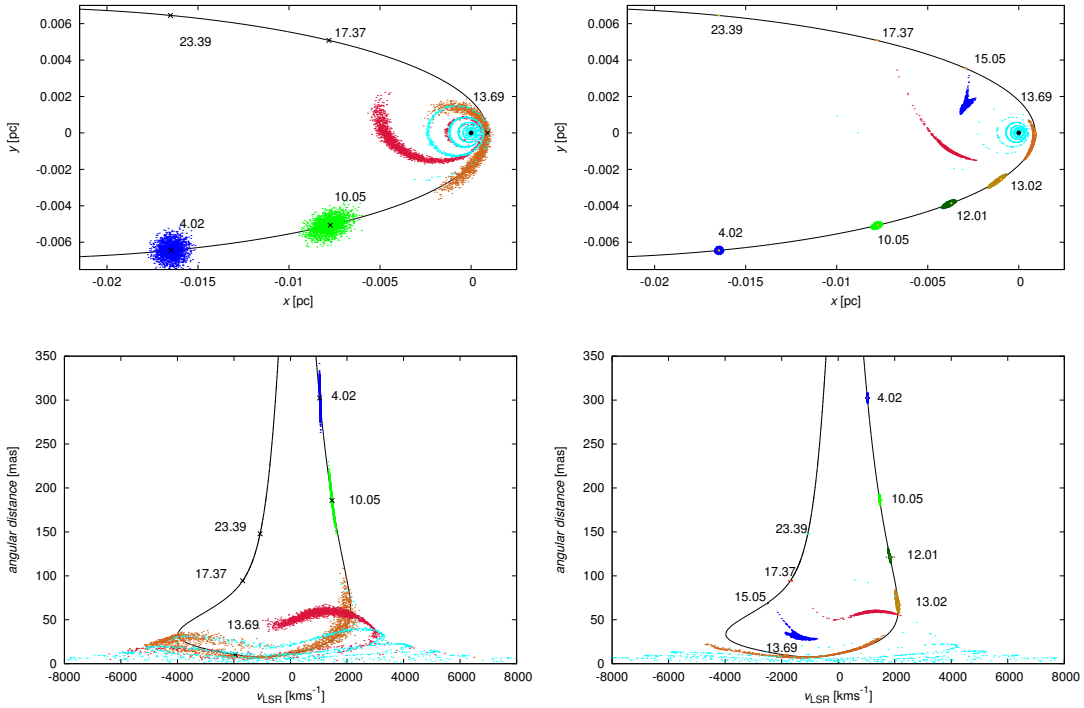

Figure 4.19: Numerical representation of the dust/gas cloud in terms of elementary parcels, trajectories of which are integrated in the gravitational field and influenced by the hydrodynamical drag. *Top left:* the evolution of the cloud in the orbital plane for selected epochs since the start of the simulation. Snapshots of the cloud are distinguished by different colours and shown at several moments of time (time marks correspond to years since the initial moment of integration). The cloud particles are characterised by the Gaussian dispersion around the nominal trajectory in the phase space (the black curve). *Bottom left:* representation of the evolution from the top–left panel is shown in the velocity–distance plane. The velocity is transformed into the local standard of rest. The angular distance is expressed in milliarcseconds. *Top right:* the evolution as in the top-left panel, but for a cloud with an embedded star in the core. *Bottom right:* the track in the velocity–position plane corresponding to the trajectory from the top–right panel.

4.2.6 Dust truncation radius

To estimate the dust mass diverted from the initial nominal trajectory of the cloud at its pericentre passages, it is useful to consider the Hill radius of the binary system star–SMBH. At the pericentre,

$$r_{\mathrm{H}} = a(1-e)\left(\frac{M_\star}{3M_\bullet}\right)^{1/3}, \tag{4.21}$$

which for the mass $M_* = 2M_\odot$ and the position at the pericentre yields $\sim 1\,\mathrm{AU}$; inside this sphere of influence the particles remain bound to the star, while outside it the particles are captured by the SMBH.

The sphere of influence increases after each pericentre passage, as illustrated in figure 4.20, where we plot the Hill radius evolution over an interval of time. We varied the eccentricity, but other orbital parameters remained fixed ($M_\bullet = 4.4\times10^6 M_\odot$ for Sgr A* SMBH). Highly eccentric trajectories ($e \gtrsim 0.9$) are prone to a significant mass loss when the atmosphere of the star undergoes the Roche-lobe overflow onto the black hole.

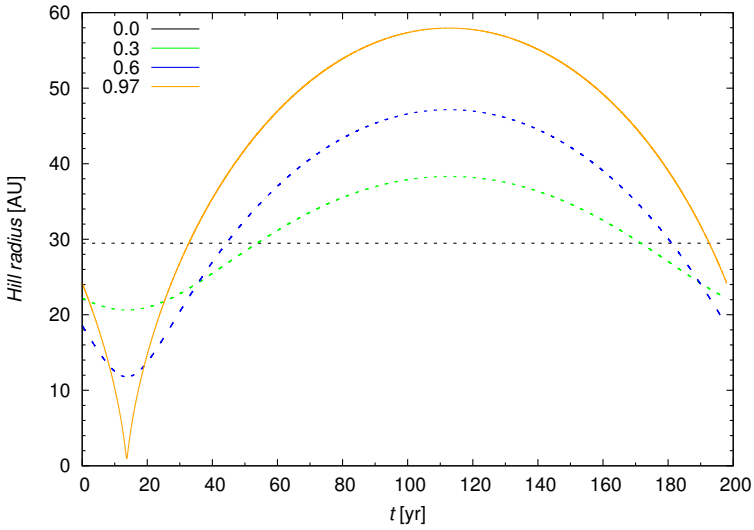

Figure 4.20: Critical Hill radius $r_{\mathrm{H}}(t)$ for four different eccentricities: $e = 0.0$, 0.3, 0.6, and 0.97. Enhanced accretion occurs when some of the dust particles move beyond r_{H}.

The Hill radius expressed by eq. (4.21) employs only tidal shearing. However, in our case the motion of dust is influenced by drag from the wind outflow, and this may indeed decrease the critical radius at which orbits of grains become unstable and consequently leave the circumstellar environment. Following the analysis of Perets & Murray-Clay (2011), we define the wind-truncation radius at which the gravitational acceleration acting on the grain $GM_\star/r_\star^2$ is equal to the acceleration a_{drag} resulting from the wind drag:

$$r_{\mathrm{w}} = \left(\frac{GM_\star}{a_{\mathrm{drag}}}\right)^{1/2}. \tag{4.22}$$

After inserting the drag term (4.10) into (4.22), we obtain

$$r_{\mathrm{w}} = \left(\frac{GM_\star m}{\eta_{\mathrm{drag}}\pi R^2 \rho_\star (v_{\mathrm{rel}}^2 + \overline{v}_{\mathrm{t}}^2)^{1/2} v_{\mathrm{rel}}}\right)^{1/2}. \tag{4.23}$$

To derive an estimate, we assumed the Stokes law and rewrote eq. (4.23) as a function of grain diameter d and distance from the star $r_\star$,

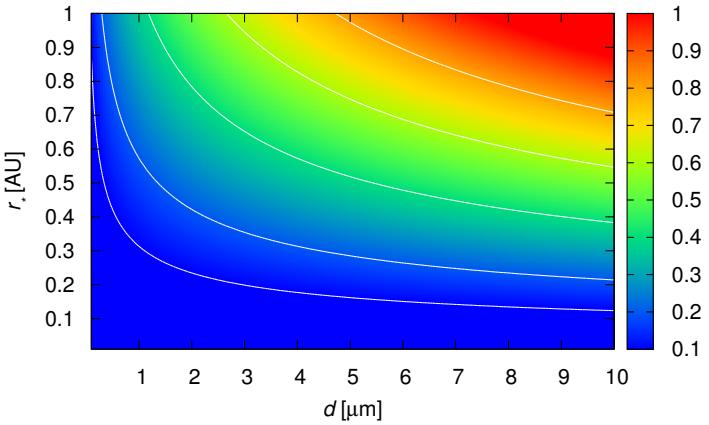

Figure 4.21: Colour-coded plot of the wind-truncation radius (colour bar units in AU). Each point in the graph estimates the truncation radius from the equilibrium between gravitational and drag forces for a given distance from the star and a grain diameter. The contours stand for values 0.1, 0.2, 0.4, 0.6, and 0.8 AU.

$$r_{\rm w}(d, r_\star) = \left(\frac{4}{3}\frac{GM_\star}{C_{\rm d}}\rho_{\rm d}\right)^{1/2}\left(\frac{d}{\rho_\star v_{\rm rel}^2}\right)^{1/2}, \tag{4.24}$$

where both the stellar wind density $\rho_\star$ and the relative velocity of grains with respect to the wind $v_{\rm rel}$ are functions of the distance from the star. We rewrote eq. (4.24) into a convenient form, taking $\rho_{\rm d} = 2\,260\,{\rm kg\,m^{-3}}$ for the density of dust (e.g., Barvainis, 1987) and assuming the density of spherical wind outflow $\rho_\star = \dot{m}_{\rm w}/(4\pi r_\star^2 v_{\rm w})$,

$$r_{\rm w} = 0.28\left(\frac{M_\star}{M_\odot}\right)^{1/2}\left(\frac{d}{\mu{\rm m}}\right)^{1/2}\left(\frac{v_{\rm rel}}{100\,{\rm km\,s^{-1}}}\right)^{-1}\left(\frac{v_{\rm w}}{100\,{\rm km\,s^{-1}}}\right)^{1/2} \times\left(\frac{\dot{m}_\star}{10^{-8}\,M_\odot{\rm yr^{-1}}}\right)^{-1/2}\left(\frac{r_\star}{\rm AU}\right)\,{\rm AU}\,. \tag{4.25}$$

In Fig. 4.21, we plot the wind-truncation radius as a function of both the grain diameter (in μm) and the distance from 2 $M_\odot$-star (in AU) with the typical mass-loss rate of $10^{-8}\,M_\odot\,{\rm yr^{-1}}$ and the terminal wind speed of $100\,{\rm km\,s^{-1}}$. The wind drag generally causes the stability region to shrink below the Hill radius (in our case ~ 1 AU at the pericentre), mainly affecting small grains $\lesssim 1\,\mu$m.

4.3 Results of simulations

4.3.1 Effects of wind and a bow shock – the case of G2/DSO

Comet-shaped features have been observed near the Galactic centre that point to the role of the radial outflow in the form of a wind from the central region (Mužić et al. 2010). The source of the wind can be hot stars and/or the accretion

flow in the vicinity of the SMBH. A similar effect is expected to occur in our model as well. One of the differences that distinguishes the core-less cloud from a dust-enshrouded star is the size of the bow shock (e.g., van Marle et al. 2011; Araudo et al. 2013). In the case of a star, the bow shock is formed by the wind interaction; a powerful wind outflow (as in the case of massive stars) develops the stagnation point radius at a much larger radius than the size of the star. On the other hand, in the case of a core-less cloud the bow shock is only slightly larger than the size of the cloud.

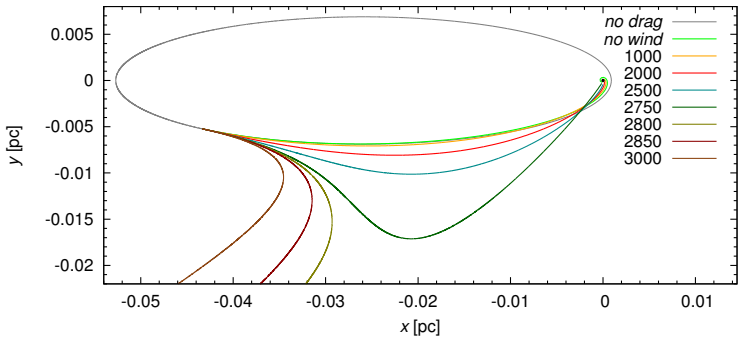

Figure 4.22: Trajectory of a single dust grain ($d = 1\,\mu$m) for different cases of the central wind outflow velocity. The grey ellipse corresponds to the nominal trajectory, neglecting the drag by the wind. The values of the outflow velocity are expressed in km/s in the legend.

We included the radial wind outflow by setting $\mathbf{v}_{\rm rel} = \mathbf{v} - \mathbf{v}_{\rm w}$ in eq. (4.10), where $\mathbf{v}$ stands for the velocity of numerical particles with respect to the SMBH, and $\mathbf{v}_{\rm w}$ is the wind velocity (we assumed a spherical outflow at $r \lesssim 1''$). The particles feel the wind drag; the computed trajectories for particles of $d = 1\,\mu$m are shown in figure 4.22. The initial conditions were the same for all cases and were computed according to the nominal orbital elements of the G2/DSO object. For small and moderate wind velocities ($\lesssim 1000\,$km/s), the trajectory is only slightly affected. The time of pericentre passage is delayed and the rate of spiralling inwards increases because there is an additional non-radial term (due to the aberration). For $v_{\rm w} \gtrsim 2800\,$km/s the particles are blown away with the wind. Mužić et al. (2010) found evidence of the presence of wind speed from the centre that are of this order of magnitude.

Consequently, we compared the evolution of a bound star–gas–dust system with and without the effect of a spherical wind from the centre. Particles ($d = 2.5\,\mu$m) were initially distributed uniformly around the star ($M_\star = 3\,M_\odot$ in this example). The range of inclination was set from 0° to 180°, semi-major axes spanned the interval $(0.001, 10)\,$AU, and eccentricities varied from 0 to 0.1. The resulting evolution is plotted in figure 4.23. The wind slows the particles down and the initial shape of the shell is more stretched than in the no-wind case.

If a wind-blowing star moves supersonically through ISM, a bow shock is formed. The effect has also been confirmed at 0.2 pc distance from the Galactic centre (Mužić et al. 2010). Here we employed a two-dimensional model of the bow shock,

$$R(\theta) = R_0 \csc\theta \sqrt{3(1 - \theta\cot\theta)}\,, \tag{4.26}$$

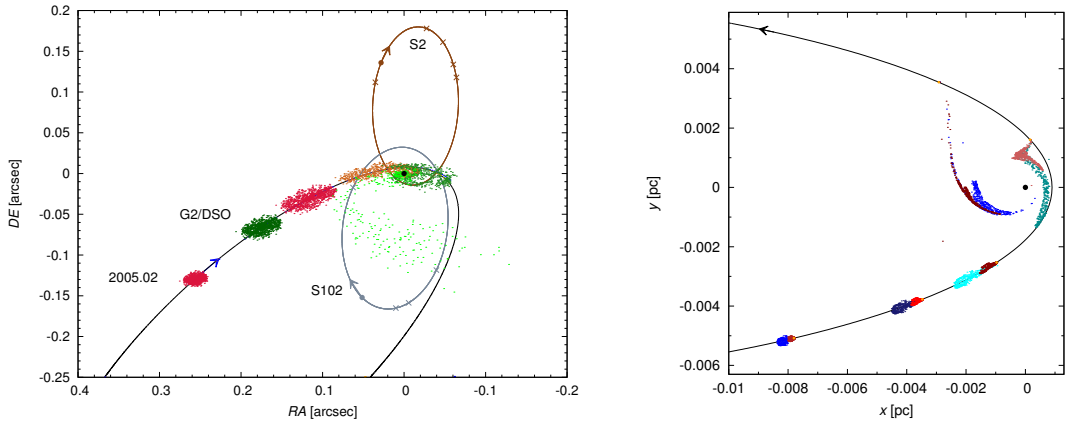

Figure 4.23: *Left panel:* a sketch of the orbit orientation on the sky, consistent with the current nominal trajectory of the G2/DSO (i.e., arriving from the south-east direction and going into pericentre from the north, then leaving towards the south-east, showing the offset from the SMBH position in the origin). Two eccentric orbits of the S-stars are also indicated. *Right panel:* two cases of the possible evolution a gaseous/dusty stellar envelope, initially bound to the star: (i) with a radial wind blowing from the centre ($v_{\rm w} = 1000$ km/s; bluish colours), and (ii) without the outflowing wind (reddish colours). Here the same nominal trajectory as in the left panel is plotted, now with respect to the (x, y) orbital plane. See the text for details.

which we rotated around the symmetry axis to obtain the correct orientation of the shock in 3D. In eq. (4.26), R_0 stands for the stand-off distance, where the ram pressures of the ambient medium and the stellar wind are at balance (Wilkin 1996),

$$R_0 = \left(\frac{\dot{m}_{\rm w} v_{\rm w}^{\star}}{4\pi \rho_{\rm a} v_{\rm rel}^2} \right)^{1/2} , \tag{4.27}$$

where $\dot{m}_{\rm w}$ is the stellar mass-loss rate, $v_{\rm w}^{\star}$ is the terminal velocity of the stellar wind. We used eq. (4.5) to find $\rho_{\rm a}$, and $v_{\rm rel} = |\mathbf{v} - \mathbf{v}_{\rm w}|$ at a specific point on the orbit. The symmetry axis of the bow shock is aligned with the direction of the relative velocity, $\mathbf{v}_{\rm rel}$, as expected. For illustration, we plot the evolution of the size and orientation of the bow shock along a highly eccentric orbit. We use the parameters of a young, low-mass T Tauri star (Scoville & Burkert 2013): $\dot{m}_{\rm w} = 10^{-8}\, M_{\odot}\,{\rm yr}^{-1}$, $v_{\rm w}^{\star} = 200\,{\rm km\,s}^{-1}$, and $M_{\star} = 2\,M_{\odot}$. We prescribe $0\,{\rm km\,s}^{-1}$, $500\,{\rm km\,s}^{-1}$, $1000\,{\rm km\,s}^{-1}$ for the wind-outflow from the centre, see Fig. 4.24.

We assumed that the wind-blowing star has a spherical wind with the constant magnitude equal to its terminal velocity. In our numerical scheme, particles outside the bow shock feel the drag and wind from the ambient medium near the nucleus. Inside the bow shock, the drag is approximately proportional to the second power of the relative velocity with respect to the circumstellar environment with the radial outflow, and to the circumstellar density $\rho_{\star}$, $\rho_{\star} = \dot{m}_{\rm w}/(4\pi r_{\star}^2 v_{\rm w}^{\star})$. In further examples we used the parameters relevant for a young, low-mass (T Tauri) star (Scoville & Burkert 2013): $\dot{m}_{\rm w} = 10^{-8}\, M_{\odot}\,{\rm yr}^{-1}$, $v_{\rm w}^{\star} = 200\,{\rm km/s}$, but the procedure may be also applied to more evolved stellar types.

Now we also included the effect of the bow shock on the cloud evolution. In our example we set the mass of an embedded star to $M_{\star} = 2M_{\odot}$ and compared two

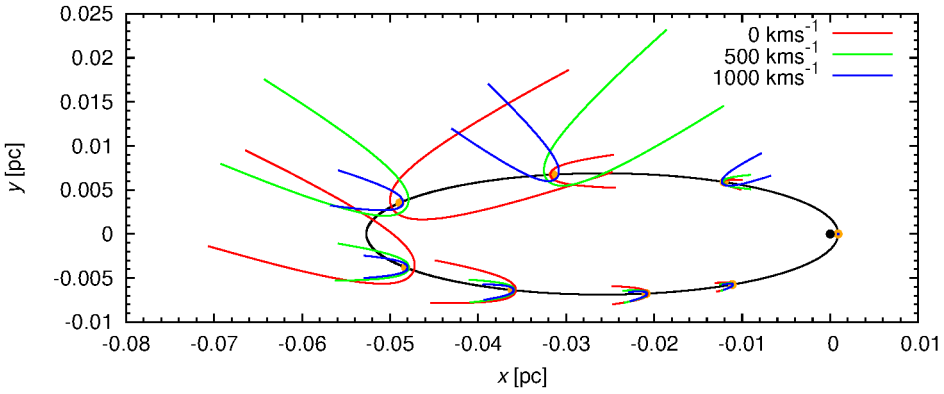

Figure 4.24: The evolution of the bow-shock size and orientation along a highly eccentric trajectory with the orbital elements of G2/DSO source. We adopt the mass-loss rate and the terminal wind speed of a young, low-mass T Tauri star.

cases (figure 4.25): first, the wind blowing from the centre at velocity of 500 km/s, and, second, the other case with 1000 km/s wind. In each, case particles have a uniform distribution of semi-major axes in the interval $(0.1, 50)$ AU, inclination $(0°, 180°)$, and eccentricity $(0, 0.1)$. We note that the character and orientation of the bow-shock sources can in principle be tested observationally via polarimetry (Buchholz et al. 2013; Valencia-S et al. 2012), although we did not attempt this here.

The evolution is similar in the two cases – the material outside the bow shock spirals towards the SMBH because of the drag, while inside the bow shock the cloud elements continue to move through the circumstellar environment. Figure 4.25 shows a very narrow shape of the bow shock near the pericentre. At this stage, many particles are torn away from the star, which is enhanced by both stellar wind and the outflow from the centre (see subsection 4.2.6). However, a fraction that occupies the bow-shock region continues to orbit. In the case of strong wind from the centre, the particles are dragged more efficiently, so that a long tail forms behind the star. As mentioned above, only a diminishing part of the initial material survives the repeating passages through pericentre. The cloud is progressively stretched and accreted, and its centre drifts away from the position of the embedded star.

We also plot the changing division between the predicted position of the star and the centre of mass of the cloud (Fig. 4.25, bottom row). The mutual separation tends to grow with time (apart from fluctuations) till the pericentre passage, then decreases again as the fraction of the cloud unbound to the star sublimates or becomes accreted onto the black hole. This offset is expected to be detectable in the NIR band if sufficient resolution is reached to resolve the cloud structure.

4.3.2 Spherical cloud vs. disc-like structure

Near a protostar or T Tauri star, two types of dust/gas environment can be considered: a spherical cloud with an approximately Gaussian distribution in the position–velocity phase space, and a disc-like configuration with a Keplerian distribution of bulk velocity. The latter case represents a protoplanetary or a debris disc. Murray-Clay & Loeb (2012) proposed such a disc as the origin of the

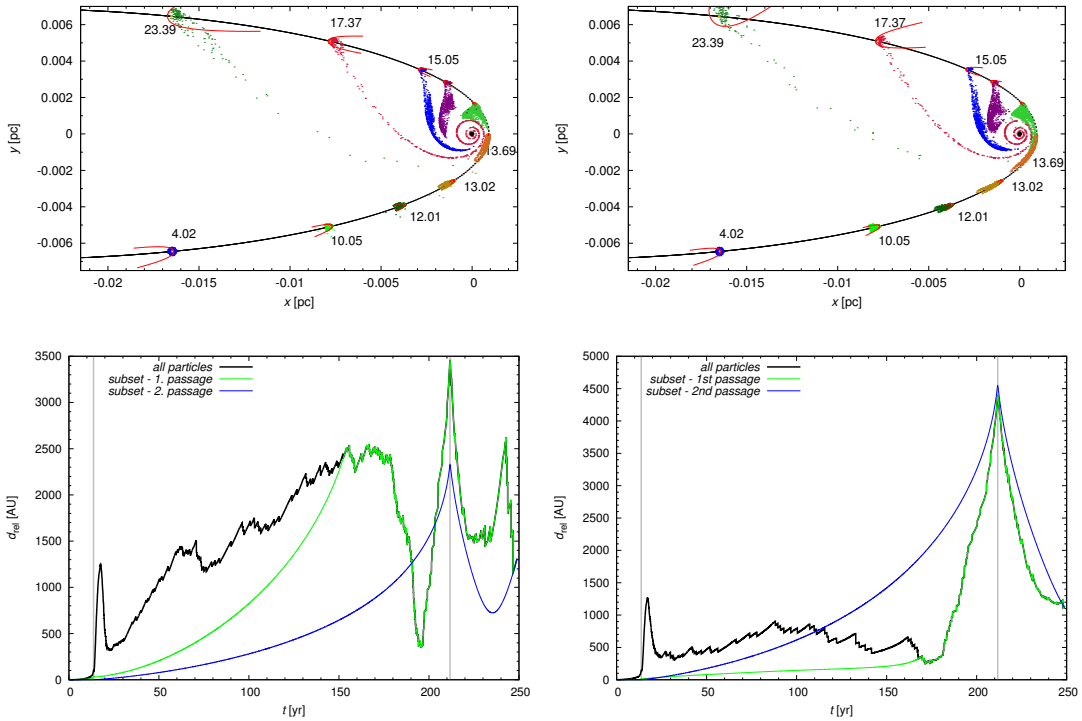

Figure 4.25: Evolution of the star with a dusty envelope together with an instantaneous orientation of the bow shock (top panels). *Top left:* star mass $M_\star = 2M_\odot$. The velocity of the wind from the centre is $v_\mathrm{w} = 500\,\mathrm{km/s}$. *Top right:* same parameters as in the left panel except for $v_\mathrm{w} = 1000\,\mathrm{km/s}$, showing the change of orientation of the bow shock. In both cases, the mass transfer peaks with a slight delay after the pericentre passage. Corresponding to the two panels in the top row, an offset is shown between the star position along its nominal orbit from the centre of mass of the cloud in the bottom panels. Different curves show the offset computed for all particles forming the cloud (black curve), a subset of particles in the cloud that survive the first passage through the pericentre (green curve), and a subset of those that also survive the second passage. Moments of pericentre passages are indicated by vertical lines. The separation of 1000 AU corresponds to $\simeq 0.12$ arcsec at the distance to Sgr A*. *Bottom left:* $v_\mathrm{w} = 500\,\mathrm{km/s}$. *Bottom right:* $v_\mathrm{w} = 1000\,\mathrm{km/s}$.

cloud near SMBH. We compared the evolution of the two geometries.

In both cases, dust grains are distributed around a $2M_\odot$ star with the parameters from the previous section. For the Gaussian velocity dispersion cloud, the initial FWHM was taken to be equal to 100 AU ($\approx 12\,\mathrm{mas}$) and $5\,\mathrm{km/s}$, respectively. Particles in the disc were distributed uniformly, with semi-major axes in the range $(0.1, 50)\,\mathrm{AU}$, low eccentricity in the range $(0, 0.1)$, and inclinations in the range $(0, 30)^\circ$ and $(150, 180)^\circ$ (taking into account both direct and retrograde orbits with respect to the orbit of the star).

In figure 4.26 we plot a typical evolution in the orbital plane for the chosen epochs (top panels) as well as the distribution in the position–velocity diagrams (bottom panels). These simulations indicate that a Gaussian cloud is not as much affected by the star as the particles in the disc. It is also evident that in case of

the disc structure, more particles survive the pericentre passage and continue to orbit the star.

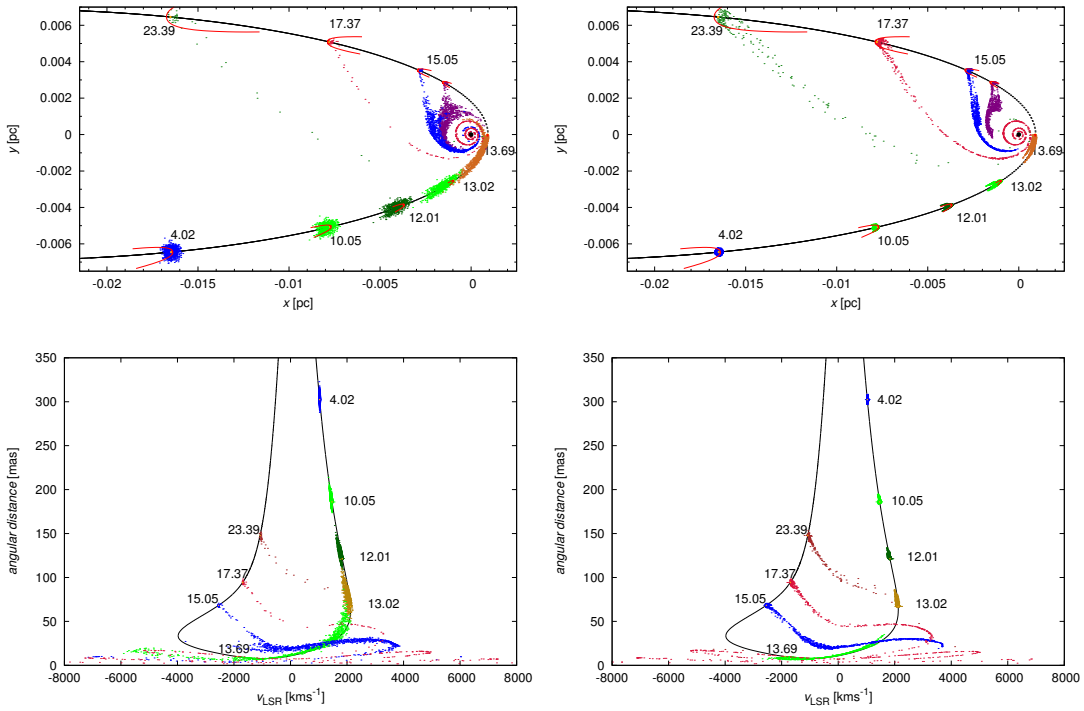

Figure 4.26: Analogy to Fig. 4.19 for the case with the bow-shock. *Top left:* the evolution of an initially spherical Gaussian envelope in the presence of a star for chosen epochs since the start of the simulation. *Bottom left:* representation of the evolution from the top–left panel is shown in the velocity–distance plane. The angular distance is expressed in miliarcseconds. *Top right:* as in the top-left panel, but for a star-disc system. *Bottom right:* the track in the velocity–position plane corresponds to the trajectory from the top–right panel.

4.3.3 Fraction of mass influenced at subsequent encounters

High-eccentricity passages are more likely to be non-repeating events if the cloud does not host a body inside its volume (see Fig. 4.19). The material of the cloud becomes dispersed and largely accreted onto the SMBH at the first pericentre passage. However, in the scenario with a shell surrounding a stellar object, a fraction of material remains bound to the star while only the rest is rerouted towards the black hole. In Table 4.3, we summarise the typical results of computations of the percentage of the captured material for the first and the subsequent pericentre passages.

As soon as the star/cloud on its trajectory reaches the critical radius for the mass overflow, the percentage of captured mass is high ($\gtrsim 90\%$ at the first pericentre passage). For the Gaussian distribution in the position–velocity phase space, it is near or equal to 100% in both the bow-shock and no-bow-shock cases.

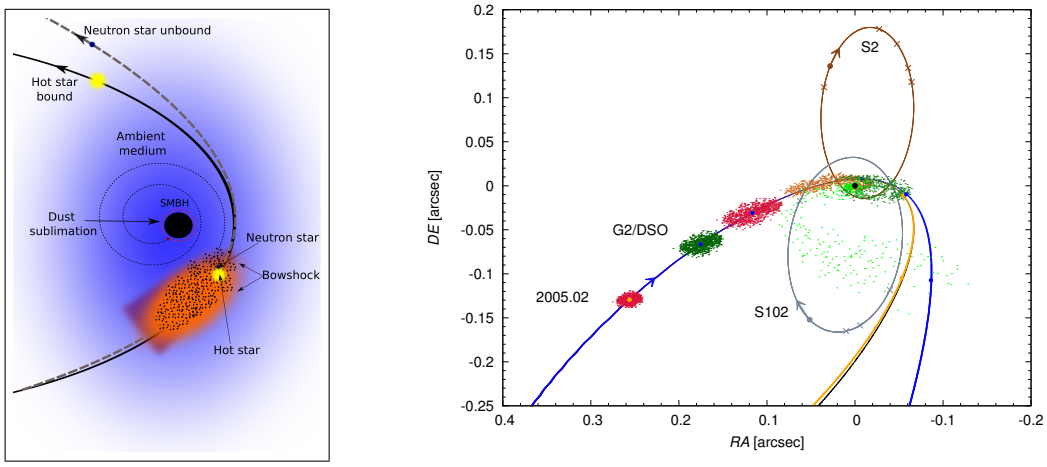

Figure 4.27: Sketch of the model geometry for a binary with a common envelope (in the left panel) and the orientation consistent with the G2/DSO nominal trajectory on the sky (in the right panel). The two components (i.e., hot star+neutron star in this example) deviate from each other, the first one being bound and the other one unbound at the moment of pericentre passage. The cloud is then dispersed in the ambient medium and eventually accreted onto the SMBH.

When the bow shock is included and particles follow the bulk Keplerian distribution in a disc, more particles remain bound after the first pericentre crossing than the no-bow-shock scheme predicts (the bow-shock region protects some particles from being diverted from the cloud orbit near the pericentre). This is connected with the character of the drag forces on both sides of the bow shock in our model and also agrees with previous results concerning the fate of a pressure supported gas cloud, which appears to be particularly prone to complete destruction near the pericentre. However, one should bear in mind that we work with a four-parametric model. At the second pericentre passage, the total amount of the captured material is generally much smaller than at the first passage, nevertheless, the percentage fluctuates significantly in terms of the immediate mass of the cloud.

We also tested a potential difference between the stability of direct (prograde) and retrograde discs. From the classical three-body theory, one can derive the difference between the critical Hill radii of direct and retrograde orbits, r_d and r_r, respectively, resulting from the Coriolis term (Innanen 1979):

$$\frac{r_\mathrm{r}}{r_\mathrm{d}} = \left[\frac{5+e+2(4+e)^{1/2}}{3+e}\right]^{2/3}, \tag{4.28}$$

which leads to the ratio of $r_\mathrm{r}/r_\mathrm{p} \approx 1.9$ for the eccentricity $e \approx 1$, which is our case. Hence, retrograde discs may not be as truncated as direct discs; the upper limit to the prolongation of their critical radius is the factor of ~ 1.9. This is consistent with our test runs involving only gravity. A direct disc around a 2-$M_\odot$ star with the semi-major axes in the range $(0.05, 10)$ AU, low inclinations $(0, 10)°$, and low eccentricities $(0, 0.01)$ dissolves after one revolution after the first pericentre passage, forming families of orbits along the original trajectory and trajectories with smaller semi-major axes, with some particles escaping the system. A few of them remain in orbit of the star inside the Hill radius. A retrograde disc with

Table 4.3: Typical examples from different runs for the fraction of material deflected from the original trajectory during the first and second pericentre passages (evaluated with respect to the total number of particles in the cloud at the corresponding stage). Columns of model characteristics specify the initial distribution of particle positions and velocities (disc-like Keplerian vs. spherical Gaussian), presence or absence of the bow-shock effect and wind, assumed mass of the star in the cloud core, and size of the dust grains.

Run	Model characteristics				Note	Mass capture [%]	
	Initial distribution	Bow shock	$M_\star/M_\odot$	Grain size [μm]		1st passage	2nd passage
1	disc-like (dr)	no	3	2.5	–	99.2	0.0
2	spherical	no	3	2.5	–	100.0	0.0
3	disc-like (dr)	no	3	2.5	–	99.4	0.0
4	disc-like (dr)	no	3	5	–	99.6	0.0
5	disc-like (dr)	no	2	5	–	99.6	50.0
6	disc-like (dr)	no	2	5	–	99.5	0.0
7	disc-like (dr)	no	3	2.5	(i)	95.2	12.5
8	disc-like (dr)	no	3	2.5	(i), (ii) 1000 km/s	94.4	14.3
9	disc-like (dr)	yes	2	2.5	(ii) 500 km/s	86.6	83.6
10	disc-like (dr)	yes	2	2.5	(ii) 1000 km/s	88.6	58.8
11	spherical	yes	2	2.5	(ii) 500 km/s	99.2	100.0
12	disc-like (dr)	yes	2	2.5	(ii) 500 km/s	91.3	65.5
13	disc-like (dr)	yes	2	0.6	(ii) 500 km/s	91.3	71.3
14	disc-like (dr)	yes	2	0.1	(ii) 500 km/s	98.1	100.0
15	disc-like (dr)	yes	2	2.5	(ii) 500 km/s	87.3	90.6
16	sphere+disc (dr)	yes	3	2.5	(ii), 1000 km/s, rad	93.3	68.7
17	disc-like (d)	yes	2	2.5	(ii), 1000 km/s, rad	88.6	74.8
18	disc-like (r)	yes	2	2.5	(ii), 1000 km/s, rad	90.6	89.8

Notes: (i) dust region extending from $r = 0.001\,\mathrm{AU}$; (ii) central outflow wind v_w included; "rad" denotes radiation pressure from the star;
(d,r,dr) denotes only direct orbits, only retrograde orbits, and both, respectively.

Additional (non-essential) parameter is the number of numerical particles in each run (typically of the order of 10^3).

the same distribution of orbital elements remains more compact and detached particles spread mostly along the original trajectory. However, when drag forces from both the stellar wind and the central outflow are involved, there is no difference in terms of stability between direct and retrograde discs (see runs 17 and 18 in Table 4.3). This is because the stability of discs is no longer determined by the gravitational Hill radius, but by the smaller wind-truncation radius (see subsection 4.2.6).

These results demonstrate that in the most cases the stellar envelope is significantly affected around the pericentre, and the diverted part eventually becomes largely dispersed during the accretion event. The outcome is similar to the case of a gaseous cloud, treated in the hydrodynamical regime (Anninos et al. 2012; Burkert et al. 2012), although a small fraction of the dusty envelope can survive to the following revolution.

4.3.4 Binary embedded within common envelope

The high eccentricity of the G2/DSO trajectory suggests that it might be possible to connect this object with hypothetical events of the three-body interaction (Hills 1988) involving the SMBH as the origin of stars on bound orbits near SMBH

(Gould & Quillen, 2003, see figure 4.27). In this tentative scenario a binary system is disrupted during the pericentre passage. As a result of this interaction, one of the remnant bodies remains on a circularised orbit, whereas the other component gains orbital energy and is ejected (Löckmann et al. 2008; Bromley et al. 2012). For realistic estimates of disruption rates, see Perets et al. (2007).

Might the infalling cloud contain such a binary stellar system? The initial eccentric trajectory of the binary centre of mass was set in agreement with the infalling cloud within which it remain embedded. The orbital parameters of the binary system are expected to be disturbed at the moment of close encounter with the SMBH and the observational resolution about the nature of the object should emerge soon after the pericentre passage. We can illustrate two qualitatively different options for the possible outcome of the post-pericentre evolution: (i) both components remain bound to the SMBH; (ii) one component is ejected from the system on a hyperbolic trajectory at the expense of the orbital energy of the other component.

Table 4.4: Two exemplary cases of an embedded binary evolution. The true anomaly is the initial value, $\dot{m}_{\rm w}$ stands for the mass-loss rate. Additional wind parameters v_c and $v_{\rm w}^{\star}$ denote the terminal velocities of the assumed spherical wind from the centre and the star, respectively.

Parameter	Case A	Case B
Mass of the binary components $[M_\odot]$	4.0 1.4	3.0 1.4
True anomaly [°]	120.0	80.0
Semi-major axis [AU]	3.0	2.0
Eccentricity	0.05	0.05
$\dot{m}_{\rm w}$ $[M_\odot\,{\rm yr}^{-1}]$	10^{-7}	
v_c $[{\rm km\,s}^{-1}]$	500	
$v_{\rm w}^{\star}$ $[{\rm km\,s}^{-1}]$	700	

Note: In these examples we performed integration runs with 1000 numerical particles representing the material of an initially spherical cloud, whereas the circumbinary disc population consisted of 500 particles with semi-major axes uniformly distributed from 10 AU to 50 AU, inclinations up to 30°, and eccentricities ranging from 0.0 to 0.1. The spherical cloud population adopts a Gaussian distribution in the phase space with the initial FWHMs of 12.5 mas and 5 km/s. In both examples, the integration starts at the true anomaly of $-167°$ for the barycentre position.

For each case we performed a number of simulations with a different set-up of free parameters, namely, the masses $M_\star^{(i)}$ of the two components and the osculating elements of the embedded binary system. The primary component $M_\star^{(1)}$ represents a hot, wind-blowing star, the secondary $M_\star^{(2)}$ is thought to be a neutron star (for definiteness of the simulation).

The gaseous-dusty envelope enshrouding the whole binary was modelled in the same way as in previous examples, that is, in terms of dust particles that experience the hot atmosphere of the SMBH, the stellar wind from the primary and the bow-shock effect. The initial conditions and parameters are summarised

in Table 4.4. In general, the fraction of cloud initial mass that is retained after the pericentre passage is diminished by the presence of the binary star in the core compared with an otherwise similar set-up with a single stellar object embedded inside.

In Fig. 4.28 we plot the temporal evolution of velocities, distances, and the mutual distance for both components in Case A as well as Case B. It is obvious that during the pre-pericentre phase, the components orbit around the common centre of mass, while at the pericentre they become unbound and move independently with different semi-major axes and eccentricities

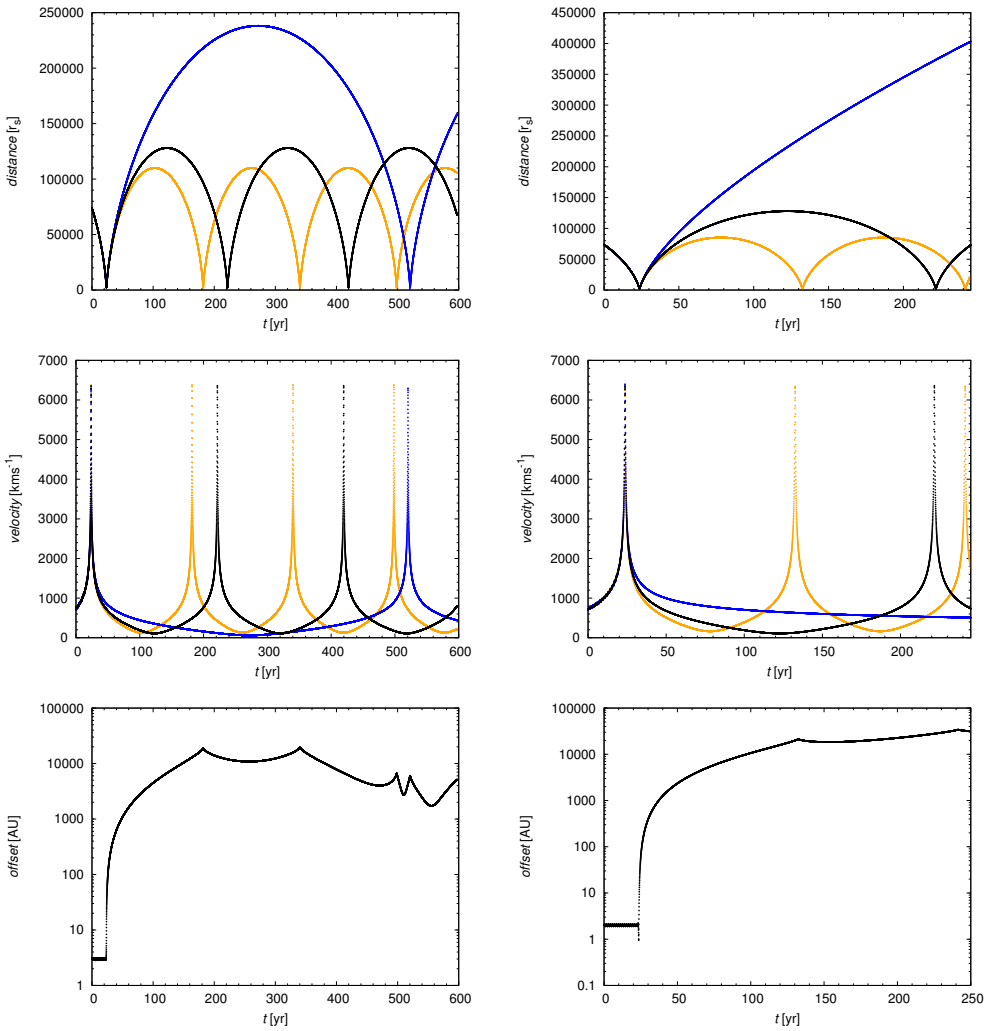

Figure 4.28: Temporal evolution (from top to bottom) of the distances of each component from the SMBH, velocities with respect to the SMBH, and mutual distance between components. The hot, heavier star is depicted by orange points, neutron star by blue points, and the nominal trajectory of G2/DSO by a black line. The evolution qualitatively differs for a different set of parameters, depending mainly on the initial distance between components and the ratio of the component masses $M_\star^{(i)}$. *Left panel:* $M_\star^{(1)} = 4.0 M_\odot$, $M_\star^{(2)} = 1.4 M_\odot$. *Right panel:* $M_\star^{(1)} = 3.0 M_\odot$, $M_\star^{(2)} = 1.4 M_\odot$.

The evolution of the binary enshrouded by a common gaseous-dusty envelope is depicted in figure 4.29, showing the part of the orbit around the pericentre,

where the envelope is affected the most and is finally disrupted, as components become unbound.

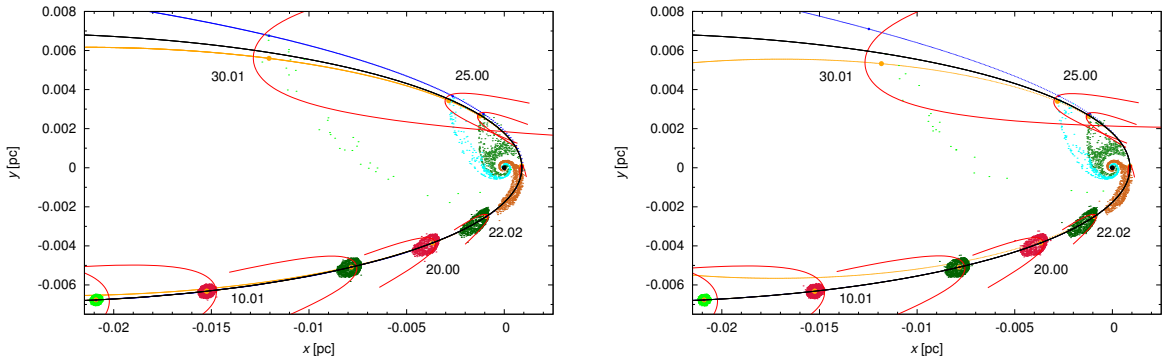

Figure 4.29: Evolution of the binary system enshrouded by a common wind envelope with significant dust content. The hot primary is labelled by an orange line, whereas the neutron star by a blue line. The nominal trajectory, which components follow at the beginning of the simulation, is black. The qualitatively different cases are depicted with the different ratio of the masses of components $M_\star^{(i)}$. *Left panel:* $M_\star^{(1)} = 4.0 M_\odot$, $M_\star^{(2)} = 1.4 M_\odot$. *Right panel:* $M_\star^{(1)} = 3.0 M_\odot$, $M_\star^{(2)} = 1.4 M_\odot$.

In figure 4.30 we show the distance–velocity plots, the temporal evolution of the binary semi-major axis a, and eccentricity e. At the pre-pericentre phase, the components orbit the common centre of mass, while at the pericentre they become unbound with respect to each other and start to move independently with different semi-major axes and eccentricities. We note, however, that this is a multi-parametric system where the outcome of the evolution depends on a mutual interplay of different parameters.

The disruption event occurs when the secondary is outside the tidal-shearing radius, which may be again estimated using the Hill radius of the primary, eq. (4.21). For cases A and B, we derived $r_\mathrm{H} \sim 1.3\,\mathrm{AU}$ and $\sim 1.2\,\mathrm{AU}$, respectively. Following the discussion in the previous subsection, the disruption radius for the binary orbiting the black hole approximated by eq. (4.21) is effectively enlarged if the secondary orbits the primary in a retrograde sense.

The observation of a single event of the binary disruption while passing close to the SMBH is improbable and should be regarded only as a speculative scenario. However, other proposed scenarios for the G2/DSO infrared source, such as isothermal clouds or the disruption of a star, are also rare given the rate at which streams and winds collide or stars disrupt to produce such a cloud. Moreover, the nature of the binary content in the Galactic centre is still unclear (Antonini & Perets 2012). Hence, all the estimates of binary replenishment in the central region are crude. The binary scenario can be easily rejected/confirmed by observations based on the post-pericentre evolution of the trajectory of the G2/DSO infrared source.

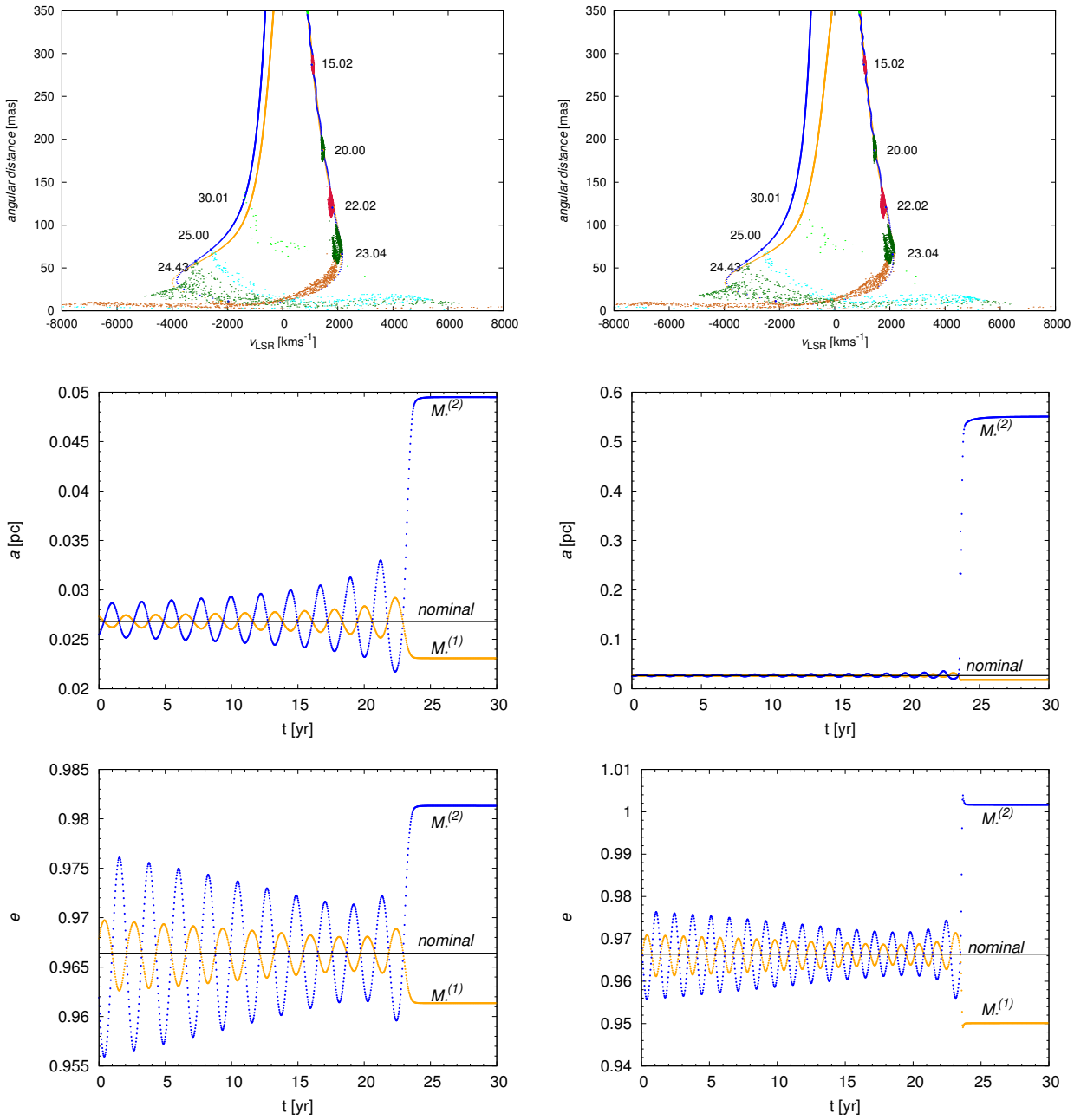

Figure 4.30: Evolution of the cloud with an embedded binary, components of which become unbound via the three-body interaction at the pericentre passage near the central SMBH. The initial trajectory of the binary barycentre corresponds to the nominal trajectory of the G2/DSO (black solid line), whereas the post-pericentre stage depends strongly on the path of the individual components emerging from the system. Two exemplary cases are shown in different columns, corresponding to the choice of the component masses $M_\star^{(i)}$. *Left panel:* $M_\star^{(1)} = 4.0 M_\odot$, $M_\star^{(2)} = 1.4 M_\odot$. *Right panel:* $M_\star^{(1)} = 3.0 M_\odot$, $M_\star^{(2)} = 1.4 M_\odot$.

4.4 Discussion of the results

We examined the pericentre passages and gradual destruction of dusty envelopes of stars that move supersonically through the immediate vicinity of the SMBH. Motivation for this topic arises because stars are shown to interact with the

ionised medium close to Sgr A*, forming bow-shock structures (e.g., Mužić et al., 2010, and references therein). Here we focused on stars with a significant dust content that interacts with an optically thin wind outflow. Examples of such stars may also be found in the disc population of the Galaxy, specifically Herbig Ae/Be-type stars, see for instance Boersma et al. (2009).

The potential importance of the subject is heightened by the current passage of the infrared-excess G2/DSO source near Sgr A*. We focused on stellar-origin scenarios in which a star is enshrouded by a dusty shell. We revisited a simplified core-less scenario for comparisons of time scales and position-velocity distributions, although we did not perform detailed hydrodynamical simulations. The adopted approach is in several aspects complementary to hydrodynamical and MHD schemes, and it appears relevant for exploration of the dust component. We computed the evolution in the presence of the star and the SMBH and also included additional effects within an approximation:

- hydrodynamical drag due to the plasma environment in the SMBH inner accretion zone;
- radially directed wind outflowing from the centre;
- wind-shearing in the immediate circumstellar environment;
- bow-shock formation due to supersonic motion through the ISM.

We plotted the results showing the shape of a Keplerian disc-like system and a Gaussian envelope at different epochs. We computed the line-of-sight velocities (transformed to the local standard of rest) and the angular distance–velocity plots.

The idea of stars embedded in clouds of gas and dust does not have to be limited to our Galaxy. It has been explored by various authors (e.g., Zurek et al. 1994; Armitage et al. 1996; Šubr & Karas 1999; Vilkoviskij & Czerny 2002, and references therein) in the context of repetitive interactions of stars of the nuclear cluster with the material of the accretion disc or a dusty torus in AGN.

The mini-spiral of the Galactic centre is a potential source of matter for infalling clouds. This structure contains a mixture of hot, warm, and cold phases. Under such conditions the accreted medium consists of complex plasma with a non-negligible content of dust (Chan et al. 1997). Located at a distance about 0.1–0.2 pc (projected distance ~ 0.06 pc) from the supermassive black hole, this feature can be understood as consisting of three independent clumpy streams of mainly gaseous material at roughly Keplerian motion around the centre (Zhao et al. 2010; Kunneriath et al. 2012). The streams collide, and their mutual interaction may cause the loss of angular momentum and an occasional inflow of the clumpy material towards the black hole (Paumard et al. 2005; Czerny et al. 2013a). In this scenario, the distribution of angular momentum determines the probability of setting the clouds on a plunging orbit (Czerny et al. 2013b).

One can thus expect that the current example of G2/DSO in the centre of the Milky Way may be a signature of a common mechanism that transports the gaseous clumpy medium and stars to the immediate vicinity of the central SMBH on sub-parsec scales.

4.5 Summary

We modelled the fate of an infalling star with an extended envelope near the SMBH. The complex medium was treated in terms of numerical particles with their mass and size as parameters, interacting with the ambient environment. The mass of dust particles is typically large enough so that the gravitational influence on the grains needs to be taken into account close to the SMBH and the mass-losing star.

We assumed an orbit pericentre of the order of $10^3 r_\mathrm{s}$, so that the star itself was not tidally disrupted. However, the surrounding cloud was affected very significantly (core-less clouds are influenced even more, and they are basically destroyed on the first encounter with the black hole). We noticed a significant mass-loss from the cloud at the first pericentre passage in all considered cases ($\gtrsim 90\%$). During the second passage the mass loss fluctuates. In other words, if the star is enshrouded in a dusty shell before the first pericentre passage, it becomes stripped of most of the envelope, unless the material is continuously replenished. If a binary star is embedded within the envelope, there is a chance that the two components separate during the pericentre passage, revealing the nature of the cloud core.

During the pericentre passage, the centre of mass of the cloud separates from the stellar core inside the cloud, but then it returns to the star as the unbound particles are destroyed by sublimation or become accreted onto the black hole. The presence of the bow shock around a star somewhat diminishes the amount of captured particles (Table 4.3), and a greater fraction of the cloud can survive to the following pericentre passage. On the other hand, the presence of a binary tends to dissolve the cloud more efficiently at the moment of close encounter with the SMBH. The characteristics of motion across the bow shock depend strongly on parameters, mainly the mass-loss rate and the stellar-wind velocity, so the predictions are uncertain and the outcome of the simulations vary. In addition, there are still uncertainties in the density and temperature profiles of the flow near the Galactic centre. However, the comparison of our simulations with post-pericentre observations can help to set better constraints.

Conclusion

In the first part of the thesis (Chapter 1), which is a brief review of the literature on the Galactic centre, we focused on the evidence that Sgr A* is a supermassive black hole of $\sim 4 \times 10^6\,M_\odot$ based on the proper motion and radial velocity measurements of gas and stars in the close vicinity of the central dark mass. Specifically, we discussed the importance of the observations of stars that belong to the Nuclear star cluster. We paid attention to the Nuclear star cluster as a whole, discussing stellar populations of late-type and early-type stars. We briefly discussed relaxation processes, namely non-resonant two-body relaxation that could have affected the disk of young massive stars. The Bahcall-Wolf-like cusp also seems to be missing, which is proved by the apparent dearth of late-type stars in the inner $\sim 0.5\,\mathrm{pc}$. However, faster scalar and vector resonant relaxations could have significantly affected late-type as well as early-type stars, probably causing the orbits of S-stars to be randomly inclined. Finally, we concentrated on the gaseous-dusty environment, mainly distinct structures of Circum-nuclear disk containing molecular and atomic gas and ionized 'Minispiral'.

Chapter 2 shows the importance of radio-interferometry in unveiling the structure of the gaseous medium in the inner $\sim 25''\,(1\,\mathrm{pc})$ of the Galactic centre. The most distinct feature is the 'Minispiral', which is asymmetrically distributed around Sgr A*. It consists of three arms whose motion is approximately Keplerian. In this chapter we reproduced the image of the structure of the 'Minispiral' from the radio interferometric observations at mm wavelengths.

Consequently, in Chapter 3 we focused on the population of neutron stars in the innermost parsec. We estimated that $\sim 10^4$–10^5 neutron stars are present in the central parsec based on the assumed IMF that we vary and the enclosed dynamical mass. These neutron stars interact with individual gaseous-dusty clumps, similar to the currently observed dusty S-cluster object (G2/DSO). For the uniform distribution of neutron stars the cumulative number of encounters from the apocentre to the pericentre is low (< 1). However, the mean number of encounters is of the order of unity for the radial distribution $\propto r^{-3/2}$. In principle, the current passage of G2 infrared source near the SMBH ($\sim 150\,\mathrm{AU}$ pericentre distance) might be potentially used to constrain the distribution of compact remnants. However, we found that the accretion luminosity is generally low, specifically below $10^{30}\mathrm{erg\,s^{-1}}$ at the pericentre due to large relative velocities, $\sim 10^4\,\mathrm{km\,s^{-1}}$.

The 'Minispiral' arms seem to be a more promising target concerning both the number of encounters as well as the observable effects. In Chapter 3 we approximated the velocity profile of the gas along the arms with the Keplerian model (Zhao et al. 2009, 2010) and we adopted the mean density and temperature from the observations at radio- and mm-wavelenghts (Zhao et al. 2010; Kunneriath et al. 2012). We used Monte Carlo approach to study the interactions between neutron stars that are uniformly distributed in the space of orbital elements and the 'Minispiral'. Neutron stars with the smallest semi-major axes interact with the Northern Arm, followed by the Eastern Arm, and the most distant neutron stars interact with the Western Arc. A large fraction of colliding objects has longitudes of ascending node close to the longitude of the ascending and descend-

ing nodes of individual arms. Their inclinations are distributed approximately uniformly. The fraction of interacting neutron stars is $\sim 1\%$–10% depending on the assumed size of the gaseous clumps of the 'Minispiral'; based on the observations we set the length-scale of individual 'Minispiral' clumps 1–2 arcsec. The relative velocities of neutron stars with respect to the 'Minispiral' gas lie in the range ~ 200–$1000\,\mathrm{km\,s^{-1}}$, being the largest for the Northern Arm, followed by the Eastern Arm, and the smallest for the Western Arc.

Most importantly, we study the distribution of three main interaction modes of neutron stars: ejector (E), propeller (P), and accretor (A). We find out that for the typical densities of the 'Minispiral' arms, $\sim (10^4 - 10^5)\,\mathrm{cm^{-3}}$, and the distribution of periods and magnetic fields typical for the observed population of neutron stars in the Galaxy, the ejector mode is the most prominent ($\sim 90\%$), followed by the propeller ($\sim 10\%$), the fraction of accretors is negligible. For higher densities, the fraction of propellers and accretors increases. For densities larger than $10^8\,\mathrm{cm^{-3}}$ the propeller mode is the most prominent one. Although these densities are higher than average densities in the 'Minispiral' arms, they may be relevant for putative higher-density clumps in localized regions, and generally in active galactic nuclei, where dusty tori and compact accretion discs exist with higher densities. Hence, the distribution of interaction modes varies across types of galactic nuclei.

The dependence of the distribution of interaction modes on the mean temperature is rather weak in the range $\sim (10^3, 10^4)\,\mathrm{K}$. We found a small decrease of the propeller regime for the higher mean temperature, which is expected. The distribution of interaction modes naturally depends on the assumed distribution of the rotational periods and the dipole magnetic field of neutron stars. We investigated the distribution for the Gaussian distribution inferred from the observations of the disk population, for the broader Gaussian distribution, the uniform distribution, and the combination of both the Gaussian and the uniform distribution. Although we found differences, the fraction of individual interaction modes may be ranked in the following way: $E > P \gtrsim A$.

The prolongation of rotational period due to the dipole radiation and the gravitational-wave losses does not change the initial distribution on the scale of $\sim 10^4$–10^5 years. However, the interaction mode of a single neutron star may change due to fluctuations in the gaseous medium surrounding the Galactic centre. From an observational point of view, ejectors may manifest themselves as radiopulsars and they can potentially form larger bow-shock structures in the 'Minispiral' arms (~ 10 bow-shock and/or PWN objects with typical sizes of $\sim 100\,\mathrm{mas}$–$1000\,\mathrm{mas}$). The propeller cavities are too small for detection. Old ($\tau \gtrsim 100\,\mathrm{Myr}$), isolated neutron stars may manifest themselves as faint X-ray sources ($\sim 10^{30}$–$10^{32}\,\mathrm{erg\,s^{-1}}$) when accreting a denser ambient medium.

Finally, Chapter 4 is dedicated to one particular but important aspect of matter transport in low-luminosity galactic nuclei. We focus on the clouds and dust-enshrouded stars (and binaries) moving on orbits with low angular momentum, thus sweeping very close ($\sim 1000\,\mathrm{r_s}$) to the SMBH but still far enough to prevent stars from the tidal disruption. The main motivation for this study is the current passage of the dusty S-cluster object G2 around Sgr A*. However, it is not necessarily relevant only for this single event. Several infrared-excess stars are indeed evidenced to move through the gaseous medium near the Galactic centre

(e.g., Moultaka et al., 2005, Mužić et al., 2010). In our analysis we determine the fraction of the total mass of the dust component that is diverted from the original, elliptical path during the passages through the pericentre. We find that the main part of the dust ($\gtrsim 90\%$ of its mass) is significantly affected upon the first crossing. The fraction of mass captured at the second passage fluctuates but generally decreases to very low values. Encounter of a core-less cloud with the SMBH is, most likely, a non-repeating event: the cloud becomes tidally stretched, partially mixed with the ambient medium, and then partially accreted onto the SMBH.

However, in the case of a dust-enshrouded star, part of the envelope survives the pericentre passage. The offset between the centre of mass of the diverted part and the star can be as large as ~ 0.3 arcsec. Such a large difference can be potentially detected in NIR bands. Finally, we examine a speculative scenario of a binary star (hot, mass-losing star + neutron star) embedded within a common wind envelope that becomes dispersed at the pericentre passage. In addition, there are still uncertainties in the density and temperature profiles of the flow near the Galactic centre. The comparison of our simulations with post-pericentre observations can help to set better constraints. The most important results of this analysis were accepted for publication in Astronomy & Astrophysics journal, see Zajaček et al. (2014).

Bibliography

Abramowicz, M. A., Czerny, B., Lasota, J. P., & Szuszkiewicz, E. 1988, ApJ, 332, 646

Allen, D. A., Hyland, A. R., & Hillier, D. J. 1990, MNRAS, 244, 706

Allen, D. A. & Sanders, R. H. 1986, Nature, 319, 191

Anninos, P., Fragile, P. C., Wilson, J., & Murray, S. D. 2012, ApJ, 759, 132

Antonini, F. & Perets, H. B. 2012, ApJ, 757, 27

Antonucci, R. 1993, ARA&A, 31, 473

Araudo, A. T., Bosch-Ramon, V., & Romero, G. E. 2013, MNRAS, 436, 3626

Armitage, P. J., Zurek, W. H., & Davies, M. B. 1996, ApJ, 470, 237

Baade, W. & Zwicky, F. 1934, Physical Review, 46, 76

Bahcall, J. N. & Wolf, R. A. 1976, ApJ, 209, 214

Bahcall, J. N. & Wolf, R. A. 1977, ApJ, 216, 883

Balick, B. & Brown, R. L. 1974, ApJ, 194, 265

Ballone, A., Schartmann, M., Burkert, A., et al. 2013, ApJ, 776, 13

Barai, P., Proga, D., & Nagamine, K. 2012, MNRAS, 424, 728

Bartko, H., Martins, F., Fritz, T. K., et al. 2009, ApJ, 697, 1741

Bartko, H., Martins, F., Trippe, S., et al. 2010, ApJ, 708, 834

Bartos, I., Haiman, Z., Kocsis, B., & Márka, S. 2013, Physical Review Letters, 110, 221102

Barvainis, R. 1987, ApJ, 320, 537

Becklin, E. E., Gatley, I., & Werner, M. W. 1982, ApJ, 258, 135

Becklin, E. E., Matthews, K., Neugebauer, G., & Willner, S. P. 1978, ApJ, 219, 121

Becklin, E. E. & Neugebauer, G. 1968, ApJ, 151, 145

Becklin, E. E. & Neugebauer, G. 1975, ApJL, 200, L71

Bertotti, B., Farinella, P., & Vokrouhlický, D., eds. 2003, Astrophysics and Space Science Library, Vol. 293, Physics of the Solar System - Dynamics and Evolution, Space Physics, and Spacetime Structure (Boston/Dordrecht/London: Kluwer Academic Publishers)

Binney, J. & Tremaine, S. 2008, Galactic Dynamics: Second Edition (Princeton: Princeton University Press)

Blum, R. D., Ramírez, S. V., Sellgren, K., & Olsen, K. 2003, ApJ, 597, 323

Boersma, C., Peeters, E., Martín-Hernández, N. L., et al. 2009, A&A, 502, 175

Bondi, H. 1952, MNRAS, 112, 195

Bondi, H. & Hoyle, F. 1944, MNRAS, 104, 273

Bower, G. C., Falcke, H., Herrnstein, R. M., et al. 2004, Science, 304, 704

Bower, G. C., Goss, W. M., Falcke, H., Backer, D. C., & Lithwick, Y. 2006, ApJL, 648, L127

Broderick, A. E., Fish, V. L., Doeleman, S. S., & Loeb, A. 2011, ApJ, 738, 38

Broderick, A. E. & Loeb, A. 2006, ApJL, 636, L109

Broderick, A. E., Loeb, A., & Narayan, R. 2009, ApJ, 701, 1357

Bromley, B. C., Kenyon, S. J., Geller, M. J., & Brown, W. R. 2012, ApJL, 749, L42

Brownsberger, S. & Romani, R. W. 2014, ApJ, 784, 154

Buchholz, R. M., Schödel, R., & Eckart, A. 2009, A&A, 499, 483

Buchholz, R. M., Witzel, G., Schödel, R., & Eckart, A. 2013, A&A, 557, A82

Burkert, A., Schartmann, M., Alig, C., et al. 2012, ApJ, 750, 58

Chan, K.-W., Moseley, S. H., Casey, S., et al. 1997, ApJ, 483, 798

Chatzopoulos, S., Fritz, T., Gerhard, O., et al. 2014, ArXiv 1403.5266

Chennamangalam, J. & Lorimer, D. R. 2013, ArXiv 1311.4846

Christopher, M. H., Scoville, N. Z., Stolovy, S. R., & Yun, M. S. 2005, ApJ, 622, 346

Clénet, Y., Rouan, D., Gratadour, D., et al. 2005, A&A, 439, L9

Cox, D. P. 2005, ARA&A, 43, 337

Cuadra, J., Nayakshin, S., Springel, V., & Di Matteo, T. 2006, MNRAS, 366, 358

Czerny, B. & Hryniewicz, K. 2011, A&A, 525, L8

Czerny, B., Karas, V., Kunneriath, D., & Das, T. K. 2013a, in IAU Symposium, ed. C. M. Zhang, T. Belloni, M. Méndez, & S. N. Zhang, Vol. 290 (Cambridge: Cambridge University Press), 199–200

Czerny, B., Kunneriath, D., Karas, V., & Das, T. K. 2013b, A&A, 555, A97

Dale, J. E., Davies, M. B., Church, R. P., & Freitag, M. 2009, MNRAS, 393, 1016

Davidson, J. A., Werner, M. W., Wu, X., et al. 1992, ApJ, 387, 189

Davidson, K. & Ostriker, J. P. 1973, ApJ, 179, 585

de la Fuente Marcos, R. & de la Fuente Marcos, C. 2013, MNRAS, 435, L19

Deegan, P. & Nayakshin, S. 2007, MNRAS, 377, 897

Deneva, J. S., Cordes, J. M., & Lazio, T. J. W. 2009, ApJL, 702, L177

Dexter, J., Agol, E., Fragile, P. C., & McKinney, J. C. 2010, ApJ, 717, 1092

Do, T., Ghez, A. M., Morris, M. R., et al. 2009, ApJ, 703, 1323

Do, T., Lu, J. R., Ghez, A. M., et al. 2013a, ApJ, 764, 154

Do, T., Martinez, G. D., Yelda, S., et al. 2013b, ApJL, 779, L6

Doeleman, S. S., Weintroub, J., Rogers, A. E. E., et al. 2008, Nature, 455, 78

Draine, B. T. & Lee, H. M. 1984, ApJ, 285, 89

Eatough, R., Karuppusamy, R., Kramer, M., et al. 2013a, The Astronomer's Telegram, 5040, 1

Eatough, R. P., Kramer, M., Klein, B., et al. 2012, ArXiv 1210.3770

Eatough, R. P., Kramer, M., Klein, B., et al. 2013b, in IAU Symposium, Vol. 291, IAU Symposium, ed. J. van Leeuwen (Cambridge: Cambridge University Press), 382–384

Eckart, A., Britzen, S., Horrobin, M., et al. 2013a, in Proceedings of Science, Vol. 004, Nuclei of Seyfert Galaxies and QSOs

Eckart, A. & Genzel, R. 1996, Nature, 383, 415

Eckart, A. & Genzel, R. 1997, MNRAS, 284, 576

Eckart, A., Genzel, R., Ott, T., & Schödel, R. 2002, MNRAS, 331, 917

Eckart, A., Horrobin, M., Britzen, S., et al. 2013b, ArXiv 1311.2753

Eckart, A., Moultaka, J., Viehmann, T., Straubmeier, C., & Mouawad, N. 2004, ApJ, 602, 760

Eckart, A., Mužić, K., Yazici, S., et al. 2013c, A&A, 551, A18

Eckart, A., Schödel, R., & Straubmeier, C. 2005, The Black Hole at the Center of the Milky Way (London: Imperial College Press)

Eisenhauer, F., Genzel, R., Alexander, T., et al. 2005, ApJ, 628, 246

Ekers, R. D., van Gorkom, J. H., Schwarz, U. J., & Goss, W. M. 1983, A&A, 122, 143

Emmering, R. T. & Chevalier, R. A. 1989, ApJ, 345, 931

Falcke, H., Melia, F., & Agol, E. 2000, ApJL, 528, L13

Ferrand, G. & Safi-Harb, S. 2012, Advances in Space Research, 49, 1313

Field, G. B. 1965, ApJ, 142, 531

Forrest, W. J., Shure, M. A., Pipher, J. L., & Woodward, C. E. 1987, in American Institute of Physics Conference Series, Vol. 155, The Galactic Center, ed. D. C. Backer, 153–156

Frank, J. 1978, MNRAS, 184, 87

Frank, J., King, A., & Raine, D. J. 2002, Accretion Power in Astrophysics: Third Edition (Cambridge: Cambridge University Press)

Fritz, T. K., Chatzopoulos, S., Gerhard, O., et al. 2013, ArXiv 1311.5258

Genzel, R., Eckart, A., Ott, T., & Eisenhauer, F. 1997, MNRAS, 291, 219

Genzel, R., Eisenhauer, F., & Gillessen, S. 2010, Reviews of Modern Physics, 82, 3121

Genzel, R., Schödel, R., Ott, T., et al. 2003, ApJ, 594, 812

Genzel, R., Thatte, N., Krabbe, A., Kroker, H., & Tacconi-Garman, L. E. 1996, ApJ, 472, 153

Genzel, R. & Townes, C. H. 1987, ARA&A, 25, 377

Ghez, A. M., Becklin, E., Duchjne, G., et al. 2003a, Astronomische Nachrichten Supplement, 324, 527

Ghez, A. M., Duchêne, G., Matthews, K., et al. 2003b, ApJL, 586, L127

Ghez, A. M., Klein, B. L., Morris, M., & Becklin, E. E. 1998, ApJ, 509, 678

Ghez, A. M., Morris, M., Becklin, E. E., Tanner, A., & Kremenek, T. 2000, Nature, 407, 349

Ghez, A. M., Salim, S., Hornstein, S. D., et al. 2005, ApJ, 620, 744

Giacconi, R., Gursky, H., Paolini, F. R., & Rossi, B. B. 1962, Physical Review Letters, 9, 439

Gillessen, S., Eisenhauer, F., Fritz, T. K., et al. 2009a, ApJL, 707, L114

Gillessen, S., Eisenhauer, F., Trippe, S., et al. 2009b, ApJ, 692, 1075

Gillessen, S., Genzel, R., Fritz, T. K., et al. 2013a, ApJ, 763, 78

Gillessen, S., Genzel, R., Fritz, T. K., et al. 2013b, ApJ, 774, 44

Gillessen, S., Genzel, R., Fritz, T. K., et al. 2012, Nature, 481, 51

Goldreich, P. & Julian, W. H. 1969, ApJ, 157, 869

Gould, A. & Quillen, A. C. 2003, ApJ, 592, 935

Guesten, R., Genzel, R., Wright, M. C. H., et al. 1987, ApJ, 318, 124

Haller, J. W., Rieke, M. J., Rieke, G. H., et al. 1996, ApJ, 456, 194

Hamaker, J. P., Bregman, J. D., & Sault, R. J. 1996, A&AS, 117, 137

Hartmann, D. H. 1995, ApJ, 447, 646

Heger, A., Fryer, C. L., Woosley, S. E., Langer, N., & Hartmann, D. H. 2003, ApJ, 591, 288

Hewish, A., Bell, S. J., Pilkington, J. D. H., Scott, P. F., & Collins, R. A. 1968, Nature, 217, 709

Hills, J. G. 1975, Nature, 254, 295

Hills, J. G. 1988, Nature, 331, 687

Högbom, J. A. 1974, A&AS, 15, 417

Hönig, S. F. & Kishimoto, M. 2010, A&A, 523, A27

Hopman, C. & Alexander, T. 2006, ApJ, 645, 1152

Hyman, S. D., Lazio, T. J. W., Kassim, N. E., et al. 2005, Nature, 434, 50

Innanen, K. A. 1979, AJ, 84, 960

Jackson, J. M., Geis, N., Genzel, R., et al. 1993, ApJ, 402, 173

Johnston, S., Kramer, M., Lorimer, D. R., et al. 2006, MNRAS, 373, L6

Karas, V. & Šubr, L. 2007, A&A, 470, 11

Kato, S., Fukue, J., & Mineshige, S. 2008, Black-Hole Accretion Disks — Towards a New Paradigm — (Kyoto: Kyoto University Press)

Kennea, J. A., Burrows, D. N., Kouveliotou, C., et al. 2013, ApJL, 770, L24

Keppens, R., van Marle, A. J., & Meliani, Z. 2012, in Astronomical Society of the Pacific Conference Series, Vol. 459, Numerical Modeling of Space Plasma Flows, ed. N. V. Pogorelov, J. A. Font, E. Audit, & G. P. Zank, 73

Kishimoto, M., Hönig, S. F., Antonucci, R., et al. 2011, A&A, 536, A78

Kocsis, B. & Tremaine, S. 2011, MNRAS, 412, 187

Kormendy, J. & Richstone, D. 1995, ARA&A, 33, 581

Kozai, Y. 1962, AJ, 67, 591

Krabbe, A., Genzel, R., Eckart, A., et al. 1995, ApJL, 447, L95

Krishna Swamy, K. S. 2005, Dust in the Universe: Similarities and Differences, World Scientific Series in Astronomy and Astrophysics, Vol. 7. (Singapore: World Scientific Publishing)

Krolik, J. H. 1999, Active Galactic Nuclei: From the Central Black Hole to the Galactic Environment (Princeton: Princeton University Press)

Krolik, J. H. & Begelman, M. C. 1988, ApJ, 329, 702

Kroupa, P. 2012, ArXiv 1210.1211

Kunneriath, D., Eckart, A., Vogel, S. N., et al. 2012, A&A, 538, A127

Kwok, S. 1975, ApJ, 198, 583

Lacy, J. H., Townes, C. H., Geballe, T. R., & Hollenbach, D. J. 1980, ApJ, 241, 132

Lacy, J. H., Townes, C. H., & Hollenbach, D. J. 1982, ApJ, 262, 120

Lauer, T. R., Ajhar, E. A., Byun, Y.-I., et al. 1995, AJ, 110, 2622

Levin, Y. & Beloborodov, A. M. 2003, ApJL, 590, L33

Levison, H. F. & Duncan, M. J. 1994, Icar, 108, 18

Lindqvist, M., Habing, H. J., & Winnberg, A. 1992a, A&A, 259, 118

Lindqvist, M., Winnberg, A., Habing, H. J., & Matthews, H. E. 1992b, A&AS, 92, 43

Lipunov, V. M. 1992, Astrophysics of Neutron Stars (Berlin/Heidelberg: Springer-Verlag)

Lo, K. Y. & Claussen, M. J. 1983, Nature, 306, 647

Löckmann, U., Baumgardt, H., & Kroupa, P. 2008, ApJL, 683, L151

Lorimer, D. R. & Kramer, M. 2004, Handbook of Pulsar Astronomy, ed. R. Ellis, J. Huchra, S. Kahn, G. Rieke, & P. B. Stetson

Lu, J. R., Ghez, A. M., Hornstein, S. D., Morris, M., & Becklin, E. E. 2005, ApJL, 625, L51

Lu, J. R., Ghez, A. M., Hornstein, S. D., et al. 2009, ApJ, 690, 1463

Lynden-Bell, D. 1969, Nature, 223, 690

Lynden-Bell, D. & Rees, M. J. 1971, MNRAS, 152, 461

MacGregor, K. B. & Stencel, R. E. 1992, ApJ, 397, 644

Maillard, J. P., Paumard, T., Stolovy, S. R., & Rigaut, F. 2004, A&A, 423, 155

Manchester, R. N., Hobbs, G. B., Teoh, A., & Hobbs, M. 2005, The Australia Telescope National Facility Pulsar Catalogue, http://www.atnf.csiro.au/research/pulsar/psrcat/

Maness, H., Martins, F., Trippe, S., et al. 2007, ApJ, 669, 1024

Marr, J. M., Wright, M. C. H., & Backer, D. C. 1993, ApJ, 411, 667

Martins, F., Genzel, R., Hillier, D. J., et al. 2007, A&A, 468, 233

Martins, F., Hillier, D. J., Paumard, T., et al. 2008, A&A, 478, 219

McCrea, W. H. 1953, MNRAS, 113, 162

McGinn, M. T., Sellgren, K., Becklin, E. E., & Hall, D. N. B. 1989, ApJ, 338, 824

McLaughlin, M. A., Lyne, A. G., Lorimer, D. R., et al. 2006, Nature, 439, 817

McNamara, D. H., Madsen, J. B., Barnes, J., & Ericksen, B. F. 2000, PASP, 112, 202

Meier, D. L. 2012, Black Hole Astrophysics: The Engine Paradigm (Berlin: Springer)

Melia, F. 2007, The Galactic Supermassive Black Hole (Princeton: Princeton Ubiversity Press)

Melia, F. & Falcke, H. 2001, ARA&A, 39, 309

Merritt, D. 2010, ApJ, 718, 739

Merritt, D. 2013, Dynamics and Evolution of Galactic Nuclei (Princeton: Princeton University Press)

Meyer, F. & Meyer-Hofmeister, E. 2012, A&A, 546, L2

Meyer, L., Ghez, A. M., Schödel, R., et al. 2012, Science, 338, 84

Mezger, P. G., Duschl, W. J., & Zylka, R. 1996, A&ARv, 7, 289

Miralda-Escudé, J. 2012, ApJ, 756, 86

Miralda-Escudé, J. & Gould, A. 2000, ApJ, 545, 847

Mori, K., Gotthelf, E. V., Zhang, S., et al. 2013, ApJL, 770, L23

Morris, M. 1993, ApJ, 408, 496

Moultaka, J., Eckart, A., & Mužić, K. 2012, Journal of Physics Conference Series, 372, 012019

Moultaka, J., Eckart, A., Schödel, R., Viehmann, T., & Najarro, F. 2005, A&A, 443, 163

Muno, M. P., Baganoff, F. K., Bautz, M. W., et al. 2003, ApJ, 589, 225

Muno, M. P., Clark, J. S., Crowther, P. A., et al. 2006, ApJL, 636, L41

Muno, M. P., Pfahl, E., Baganoff, F. K., et al. 2005, ApJL, 622, L113

Murray-Clay, R. A. & Loeb, A. 2012, Nature Communications, 3

Mužić, K., Eckart, A., Schödel, R., et al. 2010, A&A, 521, A13

Najarro, F., Hillier, D. J., Kudritzki, R. P., et al. 1994, A&A, 285, 573

Najarro, F., Krabbe, A., Genzel, R., et al. 1997, A&A, 325, 700

Narayan, R. & McClintock, J. E. 2008, NewAR, 51, 733

Nayakshin, S. & Sunyaev, R. 2005, MNRAS, 364, L23

Ostriker, J. P., Rees, M. J., & Silk, J. 1970, Astrophysical Letters, 6, 179

Özel, F., Psaltis, D., Narayan, R., & Santos Villarreal, A. 2012, ApJ, 757, 55

Park, S., Maeda, Y., Muno, M. P., et al. 2004, in Bulletin of the American Astronomical Society, Vol. 36, AAS/High Energy Astrophysics Division #8, 949

Paumard, T., Genzel, R., Martins, F., et al. 2006, ApJ, 643, 1011

Paumard, T., Maillard, J.-P., & Morris, M. 2005, in Growing Black Holes: Accretion in a Cosmological Context, ed. A. Merloni, S. Nayakshin, & R. A. Sunyaev (Berlin: Springer), 197–202

Paumard, T., Maillard, J. P., Morris, M., & Rigaut, F. 2001, A&A, 366, 466

Peebles, P. J. E. 1972, General Relativity and Gravitation, 3, 63

Perets, H. B., Hopman, C., & Alexander, T. 2007, ApJ, 656, 709

Perets, H. B. & Murray-Clay, R. A. 2011, ApJ, 733, 56

Perger, M., Moultaka, J., Eckart, A., et al. 2008, A&A, 478, 127

Pfahl, E. & Loeb, A. 2004, ApJ, 615, 253

Phifer, K., Do, T., Meyer, L., et al. 2013, ApJL, 773, L13

Piddington, J. H. & Minnett, H. C. 1951, Australian Journal of Scientific Research A Physical Sciences, 4, 459

Psaltis, D. 2012, ApJ, 759, 130

Quataert, E. 2004, ApJ, 613, 322

Rauch, K. P. & Tremaine, S. 1996, NewA, 1, 149

Rea, N., Esposito, P., Pons, J. A., et al. 2013, ApJL, 775, L34

Rees, M. J. 1988, Nature, 333, 523

Reid, M. J. & Brunthaler, A. 2004, ApJ, 616, 872

Reid, M. J., Menten, K. M., Zheng, X. W., et al. 2009, ApJ, 700, 137

Rieke, G. H. & Rieke, M. J. 1988, ApJL, 330, L33

Sakano, M., Warwick, R. S., Decourchelle, A., & Predehl, P. 2003, MNRAS, 340, 747

Salpeter, E. E. 1955, ApJ, 121, 161

Sanders, R. H. & Lowinger, T. 1972, AJ, 77, 292

Sądowski, A., Narayan, R., Sironi, L., & Özel, F. 2013, MNRAS, 433, 2165

Schartmann, M., Burkert, A., Alig, C., et al. 2012, ApJ, 755, 155

Schmidt, M. 1963, Nature, 197, 1040

Schödel, R., Feldmeier, A., Kunneriath, D., et al. 2014, ArXiv 1403.6657

Schödel, R., Merritt, D., & Eckart, A. 2009, A&A, 502, 91

Schödel, R., Ott, T., Genzel, R., et al. 2002, Nature, 419, 694

Scoville, N. & Burkert, A. 2013, ApJ, 768, 108

Shakura, N. I. & Sunyaev, R. A. 1973, A&A, 24, 337

Shapiro, S. L. & Teukolsky, S. A. 1983, Black holes, white dwarfs, and neutron stars: The physics of compact objects

Shapley, H. 1918a, PASP, 30, 42

Shapley, H. 1918b, ApJ, 48, 154

Shcherbakov, R. V. 2014, ApJ, 783, 31

Shen, Z.-Q., Lo, K. Y., Liang, M.-C., Ho, P. T. P., & Zhao, J.-H. 2005, Nature, 438, 62

Spitzer, L. 1978, Physical processes in the interstellar medium (New York: New York Wiley-Interscience)

Spitzer, L. 1987, Dynamical evolution of globular clusters (Princeton: Princeton University Press)

Stolovy, S. R., Hayward, T. L., & Herter, T. 1996, ApJL, 470, L45

Stovall, K., Creighton, T., Price, R. H., & Jenet, F. A. 2012, ApJ, 744, 143

Su, M., Slatyer, T. R., & Finkbeiner, D. P. 2010, ApJ, 724, 1044

Šubr, L. & Haas, J. 2014, ArXiv 1404.0380

Šubr, L. & Karas, V. 1999, A&A, 352, 452

Šubr, L. & Karas, V. 2005, A&A, 433, 405

Šubr, L., Schovancová, J., & Kroupa, P. 2009, A&A, 496, 695

Taylor, J. H. & Manchester, R. N. 1977, ApJ, 215, 885

Trumpler, R. J. 1930, PASP, 42, 214

Urry, C. M. & Padovani, P. 1995, PASP, 107, 803

Valencia-S, M., Bursa, M., Karssen, G., et al. 2012, Journal of Physics Conference Series, 372, 012073

van Marle, A. J., Meliani, Z., Keppens, R., & Decin, L. 2011, ApJL, 734, L26

Vilkoviskij, E. Y. & Czerny, B. 2002, A&A, 387, 804

Vladimirov, S. V., Ostrikov, K., & Samarian, A. A. 2005, Physics and Applications of Complex Plasmas (London: Imperial College Press)

Vollmer, B. & Duschl, W. J. 2001, A&A, 377, 1016

Wang, Q. D., Gotthelf, E. V., & Lang, C. C. 2002, Nature, 415, 148

Wharton, R. S., Chatterjee, S., Cordes, J. M., Deneva, J. S., & Lazio, T. J. W. 2012, ApJ, 753, 108

Wilkin, F. P. 1996, ApJL, 459, L31

Wollman, E. R., Geballe, T. R., Lacy, J. H., Townes, C. H., & Rank, D. M. 1977, ApJL, 218, L103

Yusef-Zadeh, F., Arendt, R., Bushouse, H., et al. 2012, ApJL, 758, L11

Zajaček, M., Karas, V., & Eckart, A. 2014, ArXiv 1403.5792

Zane, S., Turolla, R., & Treves, A. 1996, ApJ, 471, 248

Zhao, J.-H., Blundell, R., Moran, J. M., et al. 2010, ApJ, 723, 1097

Zhao, J.-H., Morris, M. R., Goss, W. M., & An, T. 2009, ApJ, 699, 186

Zurek, W. H., Siemiginowska, A., & Colgate, S. A. 1994, ApJ, 434, 46

A. Calibration script in CASA

```
#******CALIBRATION***CARMA************************************
# Michal Zajacek (2013/2014)



#**********importing uv fits to measurement set**************

msfile = "minispiral3.ms"
importuvfits(fitsfile="fits/c0337.1C_100GC6.fits",vis=msfile)

listobs(vis='minispiral3.ms',listfile='listobs.dat')

plotants(vis='minispiral3.ms', figfile='plotants_3.png')

#*************flagging*****************************************


flagdata(vis='minispiral3.ms', flagbackup = F, mode = 'shadow')
flagdata(vis='minispiral3.ms',mode='manual', autocorr=True)
flagmanager(vis = 'minispiral3.ms', mode = 'save', versionname = 'Apriori')


#***********Bandpass calibration*********************************

# examing phase vs. freq and time for bandpass calibrator 3C273

for ant in range(1,16):
        a=str(ant)
        plotms(vis='minispiral3.ms', xaxis='freq', yaxis='phase',
               selectdata=True,field='1',avgtime='1E6',avgscan=T,
               coloraxis='baseline',antenna=a,
               plotfile='phasefreq_3c273/phasefreq_3c273_ant'+a+'.png',
               expformat='png')

for ant in range(1,16):
       a=str(ant)
       plotms(vis='minispiral3.ms', xaxis='time', yaxis='phase',
              selectdata=True,field='1',spw='0',avgchannel='90',
              avgscan=T,coloraxis='baseline',
              overwrite=T,plotfile='phasetime_3c273/phasetime_3c273_ant'+a+'.png',
              expformat='png')

#Solutions for phase

gaincal(vis='minispiral3.ms', caltable='cal-minispiral3.G1',spw='0',field='1',
        selectdata=T,solint='int',refant='3',calmode='p')

plotcal(caltable = 'cal-minispiral3.G1', xaxis = 'time', yaxis = 'phase',
    poln='X', plotsymbol='o', plotrange = [0,0,-180,180],
     figfile='cal-phase_vs_time_XX.G1.png')

plotcal(caltable = 'cal-minispiral3.G1', xaxis = 'time', yaxis = 'phase',
    poln='Y', plotsymbol=':', plotrange = [0,0,-180,180],
     figfile='cal-phase_vs_time_YY.G1.png')
```

```
plotms(vis='minispiral3.ms',xaxis='freq',yaxis='phase',averagedata=T,
       avgtime='1e8',avgscan=T,avgbaseline=T,field='1')

#Generating bandpass calibration table

bandpass(vis = 'minispiral3.ms', caltable = 'cal-minispiral3.B1',
         gaintable = 'cal-minispiral3.G1',field = '1', minblperant=3,
         minsnr=2, solint='inf', combine='scan,obs',bandtype='B', fillgaps=1,
         refant = '3', solnorm = T)

#****************GAIN CALIBRATION***********************************

#***************setting absolute flux scale*************************

setjy(vis='minispiral3.ms', field='6', standard='Butler-JPL-Horizons 2010',
      spw='0',usescratch=False)

# Solving simultaneously for phase and amplitude

gaincal(vis='minispiral3.ms', caltable = 'cal-minispiral3.G2', spw ='0',
        field = '3,6', minsnr=1.0, solint= 'inf', selectdata=T, solnorm=False,
        refant = '3',gaintable = 'cal-minispiral3.B1', calmode = 'ap')


fluxscale( vis="minispiral3.ms", caltable="cal-minispiral3.G2",
        fluxtable="cal-minispiral3.G2.flux", reference="6",
        transfer="3")

#********Applying calibrations****************************************
applycal( vis='minispiral3.ms', flagbackup=F, field='4,3',
    interp=['nearest','nearest'], gainfield = ['3', '1'],
    gaintable=['cal-minispiral3.G2.flux', 'cal-minispiral3.B1'])


# We have to apply calibration solutions to 1 3C273

applycal(vis='minispiral3.ms', flagbackup=F, field='1',
    interp=['nearest', 'nearest'], gainfield = ['3', '1'],
    gaintable=['cal-minispiral3.G2.flux', 'cal-minispiral3.B1'])

# We have to apply cal solutions to 6 - Neptune

applycal(vis='minispiral3.ms', flagbackup=F, field='6',
    interp=['nearest', 'nearest'], gainfield = ['6', '1'],
     gaintable=['cal-minispiral3.G2.flux', 'cal-minispiral3.B1'])
```